Contribution of Demand Side Management to Angular and Frequency Stability of Transmission Networks

A thesis submitted to The University of Manchester for the degree of

Doctor of Philosophy

In the Faulty of Science and Engineering

2022

Mr Mengxuan Wang, BSc, MSc

Department of Electrical and Electronic Engineering

Blank Page

List of Contents

Word Count: 62,030

List of Figures

List of Tables

Nomenclature

List of Symbols

T	Torque
J	Moment of Inertia
t	Time
ω	Angular Speed
P	Real Power
Q	Reactive Power
S	Apparent Power
H	Inertia Time Constant
δ	Electrical Position of Rotors/Confidence Level
K	Damping Power Coefficient
I	Identity Matrix/Current
U	Voltage/Utilisation Rate
λ	Eigenvalues
σ	Damping/Standard Deviation
ξ	Damping Ratio
a	Acceleration
f	Frequency
R	Resistance
X	Reactance
Z	Impedance
n	Number of Variables
C	Capacity of Lines/Generator Operating Costs
w	Weighting Factors
x	Variable
F/D	Flexibility
E	Sample Mean Error

O	Operating Points
N	Number of Iterations
μ	Mean Value
$\Gamma(\cdot)$	Gamma Function
Φ^{-1}	Inverse Gaussian Conditional Probability Distribution
Δ	Operator Representing the Variations

Subscripts and Superscripts

a	After/Acceleration
b	Before
B	Base Value/Bus
m	Mechanical/Maximum Value
e	Electrical
pu	Per Unit
D	Damping
S	Synchronising
0	Initial Value
n	Number of Variables, n=1,2,3…
i	Number of Variables, n=1,2,3…
j	Number of Variables, n=1,2,3…
c	Fault Clearance
Crit	Critical
G/g	Generator
limit/lim	Limit
max	Maximum Value
min	Minimum Value
t	Time Instant
base	Base Value
Z/cz	Constant Impedance Load
I	Constant Current Load

P/cp	Constant Power Load
nadir	Frequency Nadir
np	Normalised with Respect to The Most Probable Value
nm	Normalised with Respect to The Maximum Value
fd	Field Winding on the d-Axis
1d	Damping Winding on the d-Axis
1q/2q	Damping Winding on the q-Axis
RES	Renewable Energy Sources
d	With Demand Side Management
w	Without Demand Side Management
pv	Real Power Coefficient of Voltage
qv	Reactive Power Coefficient of Voltage
pf	Real Power Coefficient of Frequency
qf	Reactive Power Coefficient of Frequency

Acronyms

4TNE	4 Transmission Network Equivalent
AAI	Average Acceleration Index
AC	Alternating Current
ACI	Acceleration Index
AEP	American Electric Power
AGC	Automatic Generation Control
AVR	Automatic Voltage Regulator
BESS	Battery Energy Storage System
CLASS	Customer Load Active System Services
CPP	Critical Peak Pricing
DC	Direct Current
DFIG	Double-Fed Induction Generator
DLC	Direct Load Control
DN	Distribution Network

DR	Demand Response
DRX	Demand Response Exchange
DRXO	Demand Response Exchange Operator
DSM	Demand Side Management
ED	Euclidean Distance
EDR	Emergency Demand Response
EDSM	Emergency Demand Side Management
ENTSO-E	European Network of Transmission System Operators for Electricity
ESO	Electricity System Operator
EV	Electric Vehicle
FCC	Full Converter Connected
FN	Frequency Nadir
FRI	Frequency Response Index
FRT	Fault Ride Through
FVSI	Fast Voltage Stability Index
FZ	Frequency Zenith
GB	Great Britain
GEV	Generalised Extreme Value
GSP	Grid Supply Point
HILP	High Impact Low Porbability
HVDC	High Voltage Direct Current
I	Constant Current
IBT	Inclining Block Tariff
IC	Industrial Customer
ICT	Information and Communication Technologies
IEC	International Electrotechnical Commission
IM	Induction Motor
IQR	Interquartile Range
KPI	Key Performance Indicator
LFC	Load-Frequency Control
LHS	Latin Hypercube Sampling
LUF	Line Utilisation Factor

MCS	Monte Carlo Simulation
MLL	Maximum Loading Limit
NEDS	Normalised Euclidean Distance of Stability
NERC	North American Electric Reliability Corporation
NETS	New England Test System
NYPS	New York Power System
OPF	Optimal Power Flow
P	Constant Power
PAR	Peak to Average Ratio
PCA	Principal Component Analysis
PCICSI	Parallel Circuit Inspired Composite Stability Index
PDF	Probability Density Function
PG&E	Pacific Gas & Electric Company
PJM	Pennsylvania, New Jersey and Maryland Interconnection
PMSG	Permanent Magnet Synchronous Generators
PMU	Phasor Measurement Unit
PSS	Power System Stabiliser
p.u.	Per Unit
PV	Photovoltaic
PVI	Real Power Flow Violation Index
QVI	Reactive Power Flow Violation Index
RAI	Rotor Angle Index
RES	Renewable Energy Sources
R-K	Runge-Kutta
RMS	Root Mean Squared
RoCoC	Rate of Change of Current
RoCoF	Rate of Change of Frequency
RoCoS	Rate of Change of Speed
RTP	Real-Time Pricing
SCIG	Squirrel-Cage Induction Generator
SDI	Speed Deviation Index
SEDC	Smart Energy Demand Coalition

SMIB	Single Machine Infinite Bus
TCSC	Thyristor Controlled Series Capacitor
TKE	Transient Kinetic Energy
ToU	Time-of-Use
TPE	Transient Potential Energy
TSI	Transient Stability Index
TWh	Terawatt Hour
UFLS	Under Frequency Load Shedding
USLS	Under Speed Load Shedding
UVLS	Under Voltage Load Shedding
VVI	Voltage Violation Index
WECC	Western Electricity Coordinating Council
Z	Constant Impedance

Abstract

Demand side management (DSM) has become one of the most popular solutions to enhance and improve operational flexibility of future power systems, which are characterised by ever-growing variability and uncertainty caused by the integration of renewable energy source (RES)-based power generation and the evolution of customer appliances. By manipulating power consumption patterns of demand, DSM pushes systems to new operating points with altered stability performance. Hence, comprehensive power system stability assessments are essential to assess the impact of advanced DSM on power system flexibility and stability. The first part of this thesis focuses on comprehensive power system stability assessment from both angular (including small disturbance and large disturbances) and frequency stability aspects simultaneously based on proposed composite stability indices. Proposed composite stability indices are adopted to assess the impacts of integration of RES-based generation and different load models on combined system stability performance by considering simultaneously the distances to corresponding stability limits while relying on calculations of widely adopted stability indices for different stability aspects. Thus, proposed composite stability indices provide an efficient assessment and comprehensive measure of system stability performance and can facilitate the understanding of the impacts of existing and future technologies and stability enhancement solutions on the combined stability performance of the power system. The second part of this thesis adopts proposed composite stability indices to investigate the impacts of advanced DSM on combined system stability performance at transmission level based on a Monte Carlo Simulation (MCS)-based probabilistic analysis method, taking account of uncertainties from RES-based generation, system demand and system faults. The advanced DSM, developed based on typical flexible processes from large industrial customers and distribution networks and corresponding demand payback effects, changes not only magnitudes, but also load compositions of power system demand. Critical factors (e.g., models of system demand) that affect the impact of advanced DSM on combined system stability are also identified by a rage of case studies developed with different operating conditions (e.g., RES baseline). The second part of this thesis aims to deliver a more comprehensive and inclusive understanding of the advanced DSM such that future DSM programs can be planned and implemented more efficiently without endangering power system stability performance.

Declaration

No portion of the work referred to in this thesis has been submitted in support of an application for another degree or qualification of this or any other university or other institute of learning.

Copyright Statement

Acknowledgement

I can never thank enough my supervisor, Professor Jovica V. Milanovic, for his patience, support, help and trust over the past six years. His selfless support has made my research career to be enjoyable and priceless.

My special thanks also extend to my colleagues in the C26 of the Ferranti Building. It is a great honour to be involved in, and work with such a united, selfless and powerful research team. All discussions between us and advice from my colleagues have pushed me closer to a greater success.

I would also like to thank the EU Horizon 2020 project CROSSBOW and MIGRATE, for providing me great opportunities to develop my research and communication skills. Working experiences for these two international research projects helped me to establish a 'link' between academia and industrial. More importantly, with the help of these two projects and The University of Manchester, I can fund my PhD career.

Moreover, I'm extremely grateful for all my friends around me, especially Miss Yitian Dai and Mr Wang Chai, who bring me joys and happiness even in the 'darkest night'.

Finally, I can never thank enough for the supports from my parents and my wife. Your supports have made me fearless to pursue my dream even thousands of miles away from home.

Through the dark nights, I see the way to be shined.

In Manchester, 29th April 2022.

To Yuqing Zhang

1 Introduction

1.1 Introduction

This chapter introduces the background information and motivations of the research, followed by introductions of the two main areas covered in this thesis. The overall aims and objectives of the research are presented after the overview and discussion of the past work in related areas. Finally, it discusses the main contributions of the research and presents an overview of the thesis.

1.2 Research Context

The dependency of modern civilisation on electricity has increased significantly over the past decade due to the rapid electrification in various areas, including public and private transportation, and the popularisation of smart electric domestic appliances. According to recent statistical surveys, the global electricity net consumption has increased by about 37% (from 17,444 Terawatt hour (TWh) to 23,845 TWh), while the global consumption of primary energy (e.g., coal, gas and wind) increased by about 19% (from 145,881 TWh to 173,340 TWh) from 2009 to 2019 [1, 2]. Because more and more portions of primary energy are consumed to generate electricity, decarbonisation in electrical power systems has become much more important than ever before. In response to the heightened awareness of sustainable development and the ever-

growing penalty for high greenhouse gas emissions, the integration of renewable energy sources (RES) based generators (e.g., wind turbines, photovoltaics and hydro storage plants) interests both policy makers and power system operators. In the UK, electricity supplied by wind and solar energy has increased by about 780% (from 8 TWh to 70 TWh) over the past decade (i.e., 2010 - 2020) [3], and thus future power systems are expected to be operated with rapidly increasing levels of RES-based generation.

Although the integration of RES-based generators reduces the consumption of fossil fuels and subsequently, greenhouse gas emissions, it introduces new challenges to power system operator, such as harmonic injection caused by electronic-based interfaces, intermittent power output caused by unstable availability of primary sources and reduced system inertia caused by the decommissioning of conventional coal-fired synchronous generators. In addition to the above-mentioned challenges from the supply side, the operation of future power systems is also challenged by new power consumption patterns, such as spatial and temporal variations of electric vehicle (EV) charging and smart domestic appliances which support remote control. Future power systems are expected to exhibit high variability and uncertainty from both supply and demand sides, and thus the requirement for increased power system flexibility has arisen.

Power system flexibility is a new concept that has emerged recently, focusing on the ability of power systems to maintain balance between supply and demand, considering high variability and uncertainty that arise from the integration of RES-based generation [4, 5]. A balance between power supply and demand is fundamental for the safe and reliable operation of power systems. Traditionally, mismatches between power supply and demand are compensated from the supply side, while the demand side is considered passive (i.e., uncontrollable). The capacities of operating reserves (also known as spinning reserves) and standing reserves (also known as non-spinning reserves) have been reduced due to the integration of RES-based generation and decommissioning of conventional coal-fired synchronous generators. Thus, the ability of the traditional method to support power system flexibility has become insufficient, facing the ever-growing flexibility requirement. Therefore, new technologies have emerged and are used to enhance power system flexibility. In addition to enhancing power system

flexibility from the supply side, such as implementing synthetic inertia of wind turbines and fast-acting governors, power system demand has become much more flexible and active (i.e., controllable) in recent decades due to the rapid development of information and communication technologies (ICT) and the liberalisation of the electricity market, thus providing new solutions, for instance, demand side management (DSM), for power system flexibility enhancement.

Following the energy issues raised in the 1970's [6], the term 'Demand Side Management (DSM)' was proposed publicly in the 1980's by Clark W. Gellings, and involved contrivances and programs that can affect electricity usage by altering the consumption pattern of customers to achieve desired changes in the load shape [6, 7]. In the early stage, the scope of DSM is restricted to electrical load management, strategic conservation and power marketing [6]. With the restructuring of modern power systems and the increasing willingness of customers to play a more active role in the electricity market, the price-responsive demand response (DR) has become one of the most important parts of DSM [8]. Similar to the DSM, DR can be defined as "changes in electric usage by the end-user from their usual consumption patterns in response to changes in the price of electricity overtime, or to incentive payments designed to induce lower electricity use at times of high wholesale market prices or when system reliability is jeopardised" [9]. Typical measures of DR include peak curtailment (i.e., reducing electricity consumption during peak demand periods) and valley filling (i.e., increasing electricity consumption during off-peak demand periods). Although DSM is a more general concept encompassing DR, energy efficiency, energy conservation, etc., this thesis focuses on assessing the impacts of short-term (either half-hourly or hourly) demand variations on combined system stability performance, and thus the term 'DSM' refers to 'DR' in this thesis [10].

Implementation of DSM can benefit power system operations, both economically and technically. By shifting load demand from peak hours to off-peak hours, the difference between peak demand and off-peak demand is reduced, resulting in significant savings of capital expenditure and generation costs for peak demand [11]. A recent study has shown that 10% of annual generation cost is spent to supply the highest 1% of peak demand throughout the year [12]. On the other hand, as the power demand values of

peak hours and off-peak hours become closer to each other, the need for system reserve capacity is reduced and consequently, power system stability is improved. DSM is expected to be one of the most efficient methods for power system stability and flexibility enhancement in future power systems with high RES penetration and high variability and uncertainty.

1.3 Motivation

DSM provides a new solution to enhance and improve power system flexibility by enabling customers to compensate mismatches between power supply and demand. By manipulating power consumption patterns in order to obtain either economic or technical benefits, DSM moves the power system from one operating point (defined as a specific equilibrium point of a power system with the balanced electricity generation and consumption in this thesis) to another, consequently changing the dynamic response of the system to physical disturbances. When DSM programs are set up to respond to price signals (i.e., customers alter their power consumption patterns according to different tariffs, e.g., time of use pricing), the new operating point can be either further away from the stability limits (i.e., more robust to various disturbances) or closer to the stability limits (i.e., more vulnerable to various disturbances). (The definition of stability limits is provided in Section 1.4). When the power system is operated further away from the stability limit, power system flexibility and stability are improved simultaneously because mismatches between power supply and demand can be compensated with reduced probability to violate any stability limits. On the contrary, when the power system is pushed closer to the stability limit by DSM, power system flexibility is reduced as fewer options are available for compensating mismatches between power supply and demand and maintaining system stability simultaneously.

In the case of DSM programs triggered by technical signals, for instance, under-frequency load shedding (UFLS) [13] and under-voltage load shedding (UVLS) [14], power system is moved to a new operating point where one certain aspect of system stability is improved, while the impact on remaining stability aspects is neglected. Such operating points, caused by incomprehensive DSM decisions, might be more vulnerable to certain

disturbance(s) that finally leads to system instability, blackouts and huge financial losses. Power system stability performance of post-DSM conditions is essential in DSM planning and decision-making processes. Therefore, this thesis assesses the contribution of DSM to multiple aspects of system stability (i.e., system angular and frequency stability) simultaneously.

The participants of modern demand response exchange (DRX) market are usually coordinated by a demand response exchange operator (DRXO), who purchases DSM from individual customers of the power system or aggregators representing a group of customers with limited negotiation ability [10]. Through DRXO, DSM are sold to system operators, electricity market operators, etc. Although DSM products are mainly supplied and collected at distribution level, the impact of DSM, either beneficial or detrimental, can propagate to transmission level where poor stability performance may lead to more severe consequences. Therefore, this thesis focuses on assessing the impact of DSM on combined system angular and frequency stability at transmission level.

In transmission networks, electricity is mainly supplied to distribution networks (DNs) through grid supply point (GSP) and to large industrial customers (ICs) that are connected at transmission level [15]. There are 225 GSPs in England and Wales, and another 280 GSPs in Scotland [16]. Theoretically, DSM products can be supplied to the UK transmission network by distribution networks through all these GSPs. Due to the high demand flexibility of large industrial customers, which will be further discussed in Section 1.5.1 and intensive number of GSPs connected to distribution networks, this thesis focuses on the DSM products and programs provided by distribution networks and large industrial customers connected at transmission level. Unlike power system flexibility, demand flexibility is considered as the proportion of controllable demand with respect to the total power consumption.

1.4 Power System Stability

Power system stability is an intrinsic attribute of power system operation; it refers to “the ability of an electric power system, for a given initial operating condition, to regain

a state of operating equilibrium after being subjected to a physical disturbance, with most system variables bounded so that practically the entire system remains intact" [17]. According to different characteristics of power system instability, system stability can be further divided into several stability categories (i.e., stability aspects), including rotor angle stability (including small disturbance stability and large disturbance stability), frequency stability, voltage stability, converter-driven stability and resonance stability [17].

When the power system is subjected to a disturbance, either small (e.g., switch on/off domestic appliances) or large (e.g., fault on transmission lines and loss of main transformers), the performance of different aspects of system stability varies to different extents and such variations can be assessed by changes in corresponding stability indicators (i.e., stability indices). If the disturbance is severe enough, the power system loses the ability to regain operating equilibrium and thus becomes unstable; these phenomena are usually indicated by system stability indices that vary beyond the corresponding maximum (or minimum) allowable value, which can also be called the stability limit.

In an alternating current (AC) power system, synchronous generators produce electricity through interactions between rotating rotor magnetic field and stationary stator windings (Faraday's Laws of Electromagnetic Induction). To generate balanced current in three phases at constant frequency, the rotors of synchronous generators are expected to rotate at constant speed (known as rated speed or synchronous speed) determined by the system rated frequency (either 50 Hz or 60 Hz) and the number of magnetic poles of the rotor. According to Newton's Second Law of Motion-Force and Acceleration [18], the relationship between the acceleration torque and speed of a rotating object follows (1.1), where T_a is the acceleration torque in N·m, J is the moment of inertia in kg·m^2, ω is the angular speed of rotation in rad/s and t is the time in seconds.

$$T_a = J \frac{d\omega}{dt} \tag{1.1}$$

With regard to generator rotors, the acceleration torque equals the difference between mechanical torque supplied by the prime mover (i.e., turbine) and the electromagnetic

torque acting on the rotor. Hence, the rotation of rotors follows (1.2) where T_m and T_e are mechanical torque and electromagnetic torque in N·m, respectively. ω_m represents the mechanical speed of rotor in rad/s.

$$T_m - T_e = J \frac{d\omega_m}{dt} \tag{1.2}$$

By introducing inertia constant H, which is defined as the ratio of stored energy of rotor to generator rating and shown as (1.3) where S_B and ω_m^{syn} are the generator rating in V·A and rated mechanical speed of rotor rotation in rad/s [19], equation (1.2) can be transferred to (1.4).

$$H = \frac{1}{2} \times \frac{J\left(\omega_m^{syn}\right)^2}{S_B} \tag{1.3}$$

$$T_m - T_e = \frac{2H}{\left(\omega_m^{syn}\right)^2} \times S_B \times \frac{d\omega_m}{dt} \tag{1.4}$$

In order to convert (1.4) into per unit (p.u.) system, noting that the base value for torque $T_{base} = S_B/\omega_m^{syn}$ and ω_m^{syn} is the rated mechanical speed of the rotor, both sides of (1.4) are divided by T_{base}, leading to (1.5).

$$T_m^{pu} - T_e^{pu} = 2H \times \frac{d\omega_{pu}}{dt} \tag{1.5}$$

In (1.5), ω_{pu} is the mechanical speed of rotor in p.u., it also equals the electrical speed of the rotor in p.u.; in other words, $\omega_{pu} = \omega_e/\omega_e^{syn}$ where ω_e and ω_e^{syn} are the electrical speed and rated electrical speed of the rotor in rad/s, respectively. Assuming δ to be the electrical position of the rotor rotating at an electrical speed of ω_e compared to the reference rotating at rated electrical speed ω_e^{syn}, then δ at time t can be derived following (1.6) where δ_0 is the initial position of the rotor (i.e., position at t = 0).

$$\delta = \left(\omega_e - \omega_e^{syn}\right) \times t + \delta_0 \tag{1.6}$$

Differentiating both sides of (1.6) with respect to the time results in:

$$\frac{d\delta}{dt} = \omega_e - \omega_e^{syn} \tag{1.7}$$

Further derivation leads to:

$$\frac{d^2\delta}{dt^2} = \frac{d\omega_e}{dt} \tag{1.8}$$

Recalling that $\omega_{pu} = \omega_e/\omega_e^{syn}$, therefore:

$$\frac{d\omega_{pu}}{dt} = \frac{1}{\omega_e^{syn}} \times \frac{d\omega_e}{dt} \tag{1.9}$$

Combining (1.5), (1.8) and (1.9):

$$T_m^{pu} - T_e^{pu} = \frac{2H}{\omega_e^{syn}} \times \frac{d^2\delta}{dt^2} \tag{1.10}$$

Multiplying both sides of (1.10) by ω_{pu}:

$$P_m^{pu} - P_e^{pu} = \frac{2H}{\omega_e^{syn}} \omega_{pu} \frac{d^2\delta}{dt^2} \tag{1.11}$$

Rearranging (1.11):

$$\frac{2H}{\omega_e^{syn}} \omega_{pu} \frac{d^2\delta}{dt^2} = P_m^{pu} - P_e^{pu} \tag{1.12}$$

Another damping power, which can be modelled as a component proportional to the speed deviation in (1.13), is usually considered for better representation of generator dynamic behaviour [19]. In (1.13), K_D, P_m^{pu} and P_e^{pu} represent the damping power coefficient, mechanical power supplied by the prime mover in p.u. and the electrical power injected to the network in p.u., respectively, and $\frac{1}{\omega_e^{syn}}\frac{d\delta}{dt}$ is the speed deviation in p.u. derived from (1.7).

$$\frac{2H}{\omega_e^{syn}} \omega_{pu} \frac{d^2\delta}{dt^2} = P_m^{pu} - P_e^{pu} - \frac{K_D}{\omega_e^{syn}} \frac{d\delta}{dt} \tag{1.13}$$

Equation (1.13) is known as the swing equation that describes the dynamic behaviour of

rotor during disturbances and hence, is widely adopted by studies regarding system dynamic performance [21 – 23]. Based on the swing equation, when the power system requires more electricity than generator supplies ($P_m^{pu} < P_e^{pu}$), the rotor is decelerated with respect to the rated speed, and consequently, generates electricity at lower frequency than rated. When the turbine supplies more power to the generator than the power system requires ($P_m^{pu} > P_e^{pu}$), the rotor is accelerated with respect to the rated speed, and the electricity is generated at higher frequency.

As the prime movers usually rotate at high speed and have large inertia, they require a long time to respond to control signals. Consequently, mechanical power (P_m^{pu}) is usually assumed to be fixed during the transient process [20]. Dynamic response of the rotor is mainly affected by electrical power (P_e^{pu}), which can be further modelled as two components, namely the synchronising component and damping component, as shown in (1.14) [19].

$$\Delta P_e^{pu} = \omega_{pu}(T_S \Delta\delta + T_D \Delta\omega) \tag{1.14}$$

where:

$T_S \Delta\delta$: Synchronising torque component in phase with rotor angle perturbation.

T_S: Synchronising torque coefficient.

$T_D \Delta\omega$: Damping torque component in phase with rotor speed deviation.

T_D: Damping torque coefficient.

ω_{pu}: Rotation speed of rotor in p.u.

An insufficient synchronising component leads to continuous rising or decreasing of the rotor angle (i.e., aperiodic drift) and an insufficient damping component leads to oscillations with increasing amplitude (i.e., oscillatory instability).

Due to the high computational cost of performing accurate probabilistic assessments of the combined system stability (especially for large disturbance and frequency stability) and different time frames associated with voltage stability, this thesis focuses on rotor angle stability, including small disturbance stability and large disturbance stability (also known as the transient stability), and system frequency stability. Furthermore, converter-driven and resonance stability [17] have been excluded because they are

newly introduced stability aspects and hitherto there are no widely adopted stability indices to assess them.

1.4.1 Small Disturbance Stability

Small disturbance stability is one of the sub-categories of rotor angle stability and it can be defined as the ability of synchronous machines to maintain synchronism when the system is subjected to a small disturbance [17]. Such disturbances occur continuously in power system operation and result in various electromechanical oscillations, characterised by different causes and frequencies. Typical electromechanical oscillation modes include local oscillation mode (i.e., one generation unit oscillates with respect to the rest of the system) with frequencies ranging from 1 to 2.5 Hz, inter-area oscillation mode (i.e., a group of generation units oscillate with respect to another group of generation units) with frequencies ranging from 0.1 to 1 Hz, control model (i.e., oscillations of controllers) with frequencies smaller than 0.1 Hz, etc. [24]. Poorly damped electromechanical oscillations are the main reasons for small disturbance instability in modern power systems.

System small disturbance stability is usually assessed by modal analysis because the equations of system dynamic response can be linearised in the case of small disturbance [19]. To perform modal analysis, a power system is firstly represented by n first order differential equations in matrix form, shown as (1.15) and (1.16).

$$\dot{x} = f(x, u) \tag{1.15}$$

$$y = g(x, u) \tag{1.16}$$

In the above equations, x is a nth order column vector representing state variables, u is a rth order column vector representing system inputs, y is a mth order column vector representing system outputs and $\dot{x}$ is the first order derivative of vector x with respect to time. Then, when a small disturbance (i.e., Δx and Δu) is introduced to the system with initial operating point x_0 and u_0, (1.15) can be rewritten as (1.17).

$$\dot{x} = f(x + x_0, u + u_0) \tag{1.17}$$

Equations (1.15) and (1.16) can be linearised as (1.18) and (1.19) by expressing (1.16) as Taylor's series expansion.

$$\Delta\dot{x} = A\Delta x + B\Delta u \tag{1.18}$$

$$\Delta y = C\Delta x + D\Delta u \tag{1.19}$$

With

$$A = \begin{bmatrix} \frac{df_1}{dx_1} & \cdots & \frac{df_1}{dx_n} \\ \vdots & \ddots & \vdots \\ \frac{df_n}{dx_1} & \cdots & \frac{df_n}{dx_n} \end{bmatrix} \qquad B = \begin{bmatrix} \frac{df_1}{du_1} & \cdots & \frac{df_1}{du_r} \\ \vdots & \ddots & \vdots \\ \frac{df_n}{du_1} & \cdots & \frac{df_n}{du_r} \end{bmatrix}$$

$$C = \begin{bmatrix} \frac{dg_1}{dx_1} & \cdots & \frac{dg_1}{dx_n} \\ \vdots & \ddots & \vdots \\ \frac{dg_m}{dx_1} & \cdots & \frac{dg_m}{dx_n} \end{bmatrix} \qquad D = \begin{bmatrix} \frac{dg_1}{du_1} & \cdots & \frac{dg_1}{du_r} \\ \vdots & \ddots & \vdots \\ \frac{dg_m}{du_1} & \cdots & \frac{dg_m}{du_r} \end{bmatrix}$$

where A is the $n \times n$ state matrix, B is the $n \times r$ input matrix, C is the $m \times n$ output matrix and D is the $m \times r$ feedforward matrix. Finally, small disturbance stability can be assessed by the roots characteristic equation of system first approximation, i.e., the eigenvalues of matrix A according to Lyapunov's first method [19, 25]. The system is small disturbance stable when all the eigenvalues of the system state matrix have negative real parts. The system is small disturbance unstable with at least one of the eigenvalues having positive real parts.

1.4.2 Large Disturbance Stability

Power system large disturbance stability is also known as transient stability; the terms 'large disturbance stability' and 'transient stability' are used interchangeably in this thesis. As well as small disturbance stability, transient stability is the other sub-category of rotor angle stability, and it refers to the ability of synchronous machines to maintain synchronism when the system is subjected to a large disturbance, such as faults on transmission lines and disconnection of transformers [17].

System transient instability is usually caused by insufficient or negative synchronising power (torque) and characterised by large aperiodic drifts of the rotor angle which is more commonly seen during the first swing period [17]. As governor and damper windings can help to damp rotor angle oscillation during the subsequent swings, first swing stability has become one of the most important parts to ensure transient stability [26]. For a single machine infinite bus (SMIB) system, the first swing stability can be determined based on the equal area criterion [27, 28].

The equal area criterion can be derived based on the swing equation excluding the damping components (i.e., equation (1.12)). Because the rotor speed in p.u. (i.e., ω_{pu}) is equal to one under normal operating conditions and it is close to one when the system is subjected to a disturbance [19, 20], ω_{pu} is neglected from (1.12) and the swing equation can be rewritten (in, strictly speaking, approximate, but widely adopted form) as:

$$\frac{2H}{\omega_e^{syn}}\frac{d^2\delta}{dt^2} = P_m^{pu} - P_e^{pu} \tag{1.20}$$

where H is inertia constant in MW·s/MVA, ω_e^{syn} is the rated electrical speed of rotor in rad/s, δ is rotor angle in radians, t is time in seconds, P_m^{pu} and P_e^{pu} are mechanical power and electrical power in p.u., respectively. Rearranging (1.20) leads to:

$$\frac{d^2\delta}{dt^2} = \frac{\omega_e^{syn}}{2H}\left(P_m^{pu} - P_e^{pu}\right) \tag{1.21}$$

Multiplying both sides of (1.21) by $2d\delta/dt$:

$$\frac{2d\delta}{dt}\frac{d^2\delta}{dt^2} = \frac{2d\delta}{dt}\frac{\omega_e^{syn}}{2H}\left(P_m^{pu} - P_e^{pu}\right) \tag{1.22}$$

Rearranging (1.22):

$$\frac{d}{dt}\left[\frac{d\delta}{dt}\right]^2 = \frac{\omega_e^{syn}}{H}\left(P_m^{pu} - P_e^{pu}\right)\frac{d\delta}{dt} \tag{1.23}$$

Integrating both sides of (1.23):

$$\left[\frac{d\delta}{dt}\right]^2 = \int \frac{\omega_e^{syn}}{H} \left(P_m^{pu} - P_e^{pu}\right) d\delta \quad (1.24)$$

When the mechanical power (P_m^{pu}) is greater than the electrical power (P_e^{pu}) during the disturbance, the acceleration energy ($A1$) for generator rotor can be calculated following (1.25), where δ_0 is the initial rotor angle and δ_c is the rotor angle at disturbance clearance in radians.

$$A1 = \int_{\delta_0}^{\delta_c} \frac{\omega_e^{syn}}{H} \left(P_m^{pu} - P_e^{pu}\right) d\delta \quad (1.25)$$

Likewise, the deceleration energy ($A2$) of the generator rotor after the disturbance clearance can be calculated following (1.26), where δ_c is the rotor angle at disturbance clearance and δ_m is the maximum allowable rotor angle in radians.

$$A2 = \int_{\delta_c}^{\delta_m} \frac{\omega_e^{syn}}{H} \left(P_m^{pu} - P_e^{pu}\right) d\delta \quad (1.26)$$

To regain stability after the disturbance clearance, the rotor acceleration energy ($A1$) cannot be greater than the rotor deceleration energy ($A2$) (i.e., $A1 \leq A2$). The disturbance clearing angle δ_c which satisfies $A1 = A2$ is also known as the critical clearing angle and denoted by δ_{crit}. Because P_m^{pu} is usually assumed to be constant during the transient process, system transient stability performance is highly related to factors, such as the type of disturbance, location of disturbance and time of disturbance clearance, that affect system electrical power (P_e^{pu}) during and after disturbances.

In large power systems with multiple generators, transient stability can be monitored by measuring the rotor angle and rotor speed. The power system can be considered large disturbance stable if all rotor angles oscillate within an allowable range and with decaying amplitude.

1.4.3 Frequency Stability

Power system frequency stability concerns the ability of an electric power system to

maintain steady frequency at all buses when the system is subjected to a disturbance. As discussed previously, system frequency fluctuates from the rated value (either 50 Hz or 60 Hz) when a mismatch exists between power generation and demand. If such a mismatch cannot be compensated fast enough, system frequency will continue to increase or decrease and finally lead to severe consequences.

A lot of power system components, such as synchronous generators, transformers and motors, require a stable frequency to operate normally. Regarding electricity generation, a low system frequency can lead to the maloperation of associated devices like pumps and consequently, endanger boilers. Moreover, a steam turbine that operates at low speed also suffers high pressure on blades and even resonance. Therefore, generators will be disconnected from the power system for the purpose of self-protection if system frequency cannot be restored to the rated value within the required time [29]. In terms of power transmission and distribution, electrical equipment, such as reactors and transformers, suffer high iron losses due to eddy current effects when the system frequency is higher than the rated value [30]. For motors integrated in the system from the demand side, operation with frequencies lower than the rated value results in overexcitation and overheating if the voltage is not reduced correspondingly [31].

Unfortunately, power system supply and demand are always changing in daily operation, which makes it extremely difficult to match system supply and demand exactly. Hence, system operators usually define an acceptable frequency range, which is 49.5 Hz to 50.5 Hz for British power systems [32]. In order to achieve faster identification and more efficient responses to frequency excursion, system frequency is measured in real-time by phasor measurement units (PMUs) and adjusted by hierarchical controls [33]. A typical representation of hierarchical frequency control is shown in Fig. 1.1, where frequency responses are segmented by different response times.

The inertial response refers to the inherent inertia nature of rotating mass [34 – 36], followed by primary control actions that aim to regain balance between supply and demand. However, primary control does not restore system frequency back to the rated value; this task is performed by secondary control, which is also referred to as load-frequency control (LFC) or automatic generation control (AGC) [37]. Finally, tertiary

control is introduced to relieve previous frequency controls (i.e., primary control and/or secondary control) and re-dispatch generators by performing regulating bids [38].

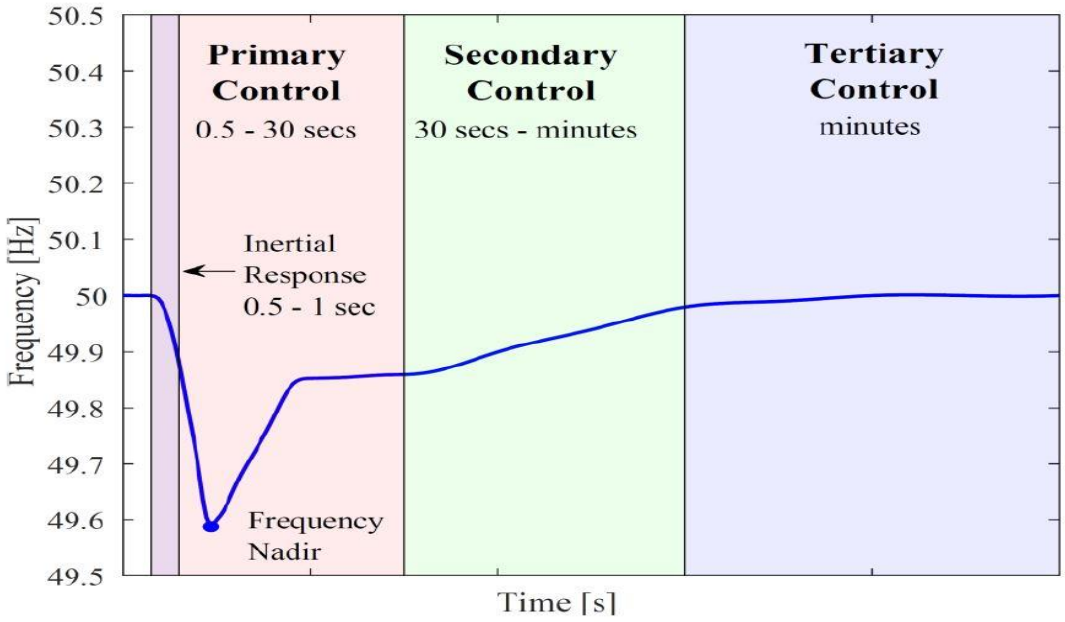

Figure 1.1 Hierarchical frequency control of power systems (adopted from [34])

1.5 Demand Side Management

1.5.1 State of the Art – Application of Demand Side Management

Based on different motivation and trigger criteria, DSM can be divided into two categories, namely explicit DSM (also known as incentive-based DSM) and implicit DSM (also known as price-based DSM) [39]. In explicit DSM programs, DSM providers are paid directly for altering a certain amount of corresponding power consumptions for a pre-agreed time period, while DSM providers can voluntarily change their power consumption patterns in response to price signals in the case of implicit DSM programs.

Due to the higher expected revenues and larger availability compared with implicit DSM programs, explicit DSM programs have been deployed widely during the last decade [40, 41]. According to the survey performed by Federal Energy Regulatory Commission of US in 2014, a total of 2.8 GW demand, from more than 5.4 million customers, can be curtailed for the purpose of peak demand reduction if all explicit DSM programs are

called in North American Electric Reliability Corporation (NERC) region [42]. Furthermore, the survey also indicates that nearly half (1.3 GW out of 2.8 GW) of potential load reduction is provided by industrial customers [42]. Similar DSM programs can also be found in other countries, based on the report published by Smart Energy Demand Coalition (SEDC) in 2015; interruptible load programs have been deployed in Germany since 2013 with a total contracted capacity of 900 MW [43]. This capacity increases to around 2 GW and 4 GW in the case of Spain and Italy, respectively [43]. In Asia, interruptible load programs have been applied in Singapore and Bangladesh to confront critical peak demand or sudden outage of generators [44, 45].

As well as curtailing load demand during peak hours, explicit DSM programs can be utilised to provide ancillary services, such as frequency and voltage regulations. It has been demonstrated in the Customer Load Active System Services (CLASS) project that around 3 GW of active power and 2 GVar of reactive power can be available for system frequency and voltage regulations, respectively, across the UK if voltage control devices can be applied widely at distribution network substations [46]. Moreover, a total of 872 MW demand has been contracted to provide system frequency control (67 MW for primary control, 400 MW for secondary control and 305 MW for tertiary control) [43]. Similar DSM programs for frequency control can also be found in Belgium (around 350 MW), Finland (around 500 MW), France (around 40 MW), etc. [43, 47].

Regarding implicit DSM programs, the application of DSM is highly related to the dynamic pricing mechanism (also known as tariff) offered to the customers. Typical tariffs include, but are not limited to:

- *Time-of-use tariffs (ToU)*. TOU reflects the variation of electricity supply cost with respect to the time throughout a day (or a year) by charging customers at different rates [48]. A typical TOU consists of peak, shoulder-peak and off-peak rates [49].

- *Critical Peak Pricing (CPP)*. CPP involves replacing the normal peak price by a much higher peak price to discourage customers from consuming electricity during peak hours. The number of CPP deployment per year can be decided by

contracts.

- *Inclining Block Tariff (IBT).* IBT aims to increase the average price of electricity for customers with high power consumption. To be more specific, electricity consumption is segmented into several blocks at the beginning of the charging period. When the power consumed by the customer exceeds the threshold of the first block, the customer will be moved into the second block where the electricity price is higher than the first block. Further increased power consumption moves the customer into the third block where the electricity price is even higher than the second one, and so on.

- *Real-Time Pricing (RTP).* RTP provides a dynamic electricity price for customers which will be updated hourly or even sub-hourly. RTP can be considered as the most popular pricing scheme among all tariffs as customers can manipulate their consumption patterns according to more accurate price signals; however, it requires fast and intensive communication infrastructure [49].

The implementation of implicit DSM programs can also be found in power system operations worldwide. In California, for instance, Pacific Gas & Electric Company (PG&E) provides a peak day pricing program for its customers to encourage load conservation and load shifting during critical peak demand periods by awarding discounts on normal electricity prices [50]. Similarly, several transmission and distribution service providers in Texas, such as City Public Service Board of San Antonio (CPS Energy), American Electric Power (AEP) Texas and Austin Energy Company, have introduced corresponding DSM programs to encourage target customers (e.g., industrial and agricultural end-users) to reduce their electricity consumption during peak demand periods by offering various economic incentives [51, 52].

Outside the US, implicit DSM programs have also interested many system operators and services provides. In the UK, “Low Carbon London” project aims to enrol more industrial and commercial customers to provide DSM by introducing various tariffs [53]. Endeavour Energy, a distribution network operator in Australia, has introduced several DSM programs (e.g., “Energy Savers Program”, “PeakSaver” and “CoolSaver”) to reduce peak

demand by directly controlling the air conditioning appliances of customers [50]. To motivate customer participation, a flat electricity price rate and a certain amount of free air conditioning services are provided to enrolled customers [54].

1.5.2 Demand Side Management Potential and Future Application

Knowing the contribution of DSM to power system operation, system operators worldwide have presented corresponding requirements and investment plans of future DSM programs. As one of the leading countries in DSM implementation, the UK has recognised the urgent need for novel ancillary services provided by DSM, such as dynamic regulation (a pre-fault service developed to regulate small and continuous frequency deviations) [55] and dynamic containment (a post-fault service developed to contain frequency within a pre-defined range after a significant frequency deviation) [56], and increased frequency response capacity [57, 58]. In order to implement DSM programs more efficiently in future power systems, the availability and the flexibility of future system demand needs to be studied and estimated accurately. In this thesis, DSM potential refers to the total capacity of flexible demand to participate various DSM programs (e.g., peak curtailment and valley filling).

The DSM potential of Swedish industrial customers is estimated in [59] by investigating five selected industries, accounting for 7% of the total Swedish industrial electricity consumption (between 5 GW to 8 GW). The results show that 147.9 MW and 104.6 MW of selected industries can be curtailed and shifted, respectively [59]. Consequently, the total DSM potential for whole Swedish industrial customers is estimated to be around 0.5 – 2 GW (up to about 12% of installed generation capacity in Sweden) [59]. Regarding the residential customers in Sweden, which holds a significant share (about 30%) of the total Swedish electricity consumption, the potential for load shifting (i.e., moving electricity consumption from demand peak to demand valley) has been estimated for domestic washing machines, dishwashers and dryers at national level in [60]. The result indicates that the peak demand can be reduced by 1.1%, 1.5%, 2.3% and 1.6% in winter,

spring, summer and autumn, respectively [60].

The DSM potential for direct load control (DLC) and curtailable air conditioning has been estimated in [61] for Shanghai, China, based on three development scenarios with different customer participation rates. The estimation results are illustrated in Fig. 1.2, from where it can be seen that the estimated DSM potential may vary significantly between different scenarios. The available capacity for DLC and curtailable air conditioning in 2030 has been estimated as 214 MW (0.3 % of the predicted peak demand in 2030) in the basic scenario, while the estimation results increase significantly to 790 MW (1% of the predicted peak demand in 2030) and about 2.5 GW (4% of the predicted peak demand in 2030) in the case of the moderate scenario and top performance scenario, respectively [61].

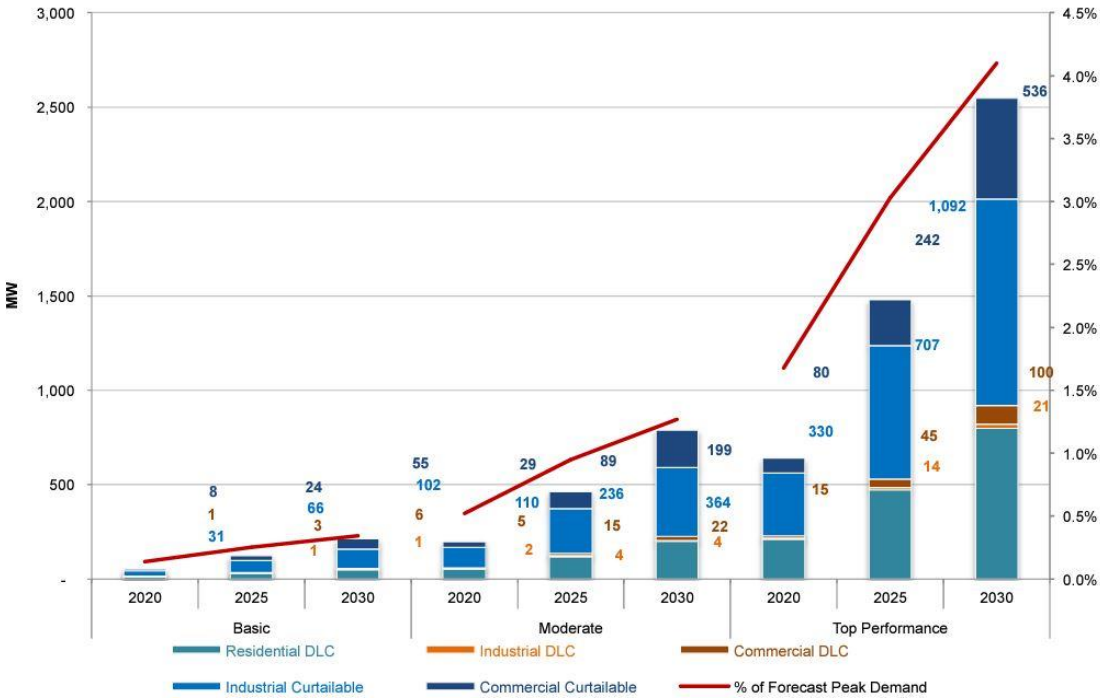

Figure 1.2 Estimated capacities for DLC and curtailable air conditioning in Shanghai, China (adopted from [61])

In the case of the UK, the technical potential (i.e., the maximum DSM capacity achievable by neglecting various existing barriers) for peak curtailment by non-domestic buildings has also been estimated based on three scenarios, namely the conservative scenario (a scenario developed based on a cautious estimation of demand flexibility), moderate scenario (a scenario developed based on an intermediate estimation of demand

flexibility) and stretch scenario (a scenario developed based on an optimistic estimation of demand flexibility) in [62]. The assessment performed in [62] covers multiple flexible demands, such as non-domestic refrigeration and lighting loads, and results in an estimated DSM potential of 1.2 GW (about 8% of estimated peak demand), 2.5 GW (about 17% of estimated peak demand) and 4.4 GW (about 30% of estimated peak demand) for the conservative scenario, moderate scenario and stretch scenario, respectively. Likewise, the study performed in [63] estimates the technical potential of curtailable and shiftable load covering all load sectors (e.g., industrial and residential) to be about 33% (18 GW out of 54 GW) of winter peak demand in the UK.

It can be noted from the above-mentioned DSM potential estimations that the majority of the assessments are performed based on multiple scenarios and focused on the technical potential of DSM; these are caused by existing barriers that limit DSM implementation. Typical barriers include, but are not limited to, barriers to regulatory framework, to market entry criteria, to investment cost and to market roles and interaction implications [50].

In order to implement DSM more efficiently in future power systems, intensive efforts have been made to remove DSM barriers and promote customer participation. For instance, Australian Energy Market Commission allows customers with lower power demands to provide ancillary services such that greater numbers of customers can participate in various DSM programs to maintain system security [64]. Similarly, PJM (Pennsylvania, New Jersey and Maryland Interconnection), a regional transmission organisation in US, has opened most of its ancillary service markets to DSM since 2006 [65].

1.6 Review of Past Work

1.6.1 Probabilistic Power System Stability Assessment

Power system stability has become one of the major concerns of power system operation since the 1920s when the system was mainly challenged by long transmission distances and insufficient synchronising torque of synchronous generators [66]. With the

rapid evolution of both power systems (e.g., more generators and more interconnections), mathematics (e.g., more accurate modelling of power system components) and computer techniques (e.g., more powerful analysing tools), power system stability assessment has become much more accurate and complex.

Traditional power system stability assessment usually adopts deterministic analysis method based on the worst operating point by totally neglecting the possibility of its occurrence [67, 68]. It is more computational efficient and guarantees a large stability margin, but it can result in huge investment and operation costs. Furthermore, deterministic analysis requires preciously defined input and system models to deliver accurate results, which fails to capture high variability and uncertainty exhibited in modern and future power systems [68]. To capture the high operational uncertainties, the probabilistic analysis method, which has been widely applied in generation adequacy assessment, power system planning, system reliability assessment, forecasting and short-term operation [69], is used in power system stability assessment.

Unlike the deterministic analysis method, the probabilistic analysis method requires statistical distributions as the input and delivers a range of possible outcomes as the result [70]. Moreover, the probabilistic analysis method is also capable of identifying the probability of a concerned output exceeding a certain value, which can be helpful in, for instance, assessing the impact of RES-based generation on system harmonic performance and investigating the impact of DSM on power system stability [71]. Although the probabilistic analysis method significantly increases the computational cost of stability assessment, it delivers more reasonable and realistic results.

Monte Carlo simulation (MCS), which was developed during the World War II for nuclear weapons, has been adopted widely in the probabilistic analysis of power systems [72]. MCS delivers a statistical estimation of output through the random sampling of input variables, according to the corresponding probability distribution such as normal distribution, uniform distribution etc., and performing deterministic simulation for each set of sampled input [73]. A standard MCS is performed based on the following steps:

1. Sample input variables n times randomly based on corresponding probability distributions and generate n sets of input variables.

2. Perform deterministic simulations for each set of input variables.

3. Obtain n sets of output variables and calculate required statistics.

In the case of power system stability assessment, input variables of MCS can be considered as system operational variability and uncertainty (e.g., intermittent power output of RES-based generation and uncertain system demand), while the outputs of MCS are stability performance indicated by various indices. Because the results of MCS are sets of system stability indices obtained from multiple deterministic simulations, the estimated system stability performances are usually represented by statistical values (e.g., mean values and most probable values) of stability indices.

The implementation of the MCS-based probabilistic analysis method in power system stability assessment can be found in many past works. The authors of [74] compare nine widely adopted numerical sensitivity analysis methods to identify the most critical parameter affecting small disturbance stability by performing MCS with the consideration of multiple operational uncertainties, such as wind speed, load demand and modelling parameters of automatic voltage regulator (AVR), modelled as probability distributions. Likewise, MCS is used in [75] to verify the accuracy of the proposed Gram-Charlier expansion approximation method to assess small disturbance stability performance of a grid connected photovoltaic (PV) system. The impact of placement and tuning of power system stabiliser (PSS) on small disturbance stability is determined by the MCS-based model analysis in [76], where the limitations of the deterministic analysis method have also been emphasised.

Similarly, MCS is adopted in [77] to study the impact of intermittency of wind generation on system transient stability. To be more specific, the uncertainly of wind speed, which has been assumed to follow a Weibull distribution, has been converted to distributions of evaluation indices (i.e., angle-based margin index and critical clearing time of faults) of transient stability by MCS. The wind farm under study has been modelled as a combination of double-fed induction generators (DFIG) and permanent magnet synchronous generators (PMSG) considering the wake effect. In addition to focusing on uncertainty associated with wind generation only, probabilistic transient stability assessment performed in [78] also covers operational uncertainties of system loading

and system faults. The MCS-based framework proposed in [78] has been validated to be capable of identifying the most critical generators in the system and assessing the impacts of various factors (e.g., disconnection of synchronous generators and change in system topology) on transient stability. Regarding system frequency stability, a novel control strategy of EV charging/discharging is proposed in [79] to enable frequency response services by EVs in future RES rich power systems. MCS is utilised to assess system frequency stability performance considering uncertain battery capacity, energy consumption per kilometer and travelling distance of EVs. Finally, MCS is adopted in [80] to investigate the risk of severe blackouts caused by cascading outages and frequency deviations.

Although the MCS-based probabilistic analysis method is more suitable to be used in complex system where input variables exhibit high variability and uncertainly, the implementation of MCS can still be limited by high computational cost. The authors of [81] and [82] have attempted to improve the traditional MCS. A quasi-MCS is introduced in [81], and it has been proved to be more efficient (i.e., less computational cost and more accurate results) than traditional MCS in probabilistic small disturbance stability analysis by replacing random sampling with Sobol sequence-based sampling [81]. Similarly, a latin hypercube sampling (LHS), which samples each subdivision of each input variable once, is utilised in [82] instead of random sampling defined in the traditional MCS. The novel methodology requires only 3.5% of the samples needed for traditional MCS to accurately estimate the probability of small disturbance instability with high system variability and uncertainty [82].

1.6.2 Impacts of Demand Side Management on Power System Stability

As discussed previously, DSM programs can be implemented in response to either stability enhancement requirements or price signals. In the former situation, DSM programs are expected to support and enhance one or several aspects of power system stability by compensating imbalance between power generation and demand from the

demand side. Typical DSM programs for stability enhancement include UFLS, UVLS, etc. Because such DSM programs are usually implemented with a specific objective (i.e., improve certain aspect(s) of power system stability), the impacts of DSM are usually assessed based on corresponding aspect(s) of power system stability.

For instance, a decentralised DSM strategy, which relies on controlling thermostatic domestic appliance (i.e., a combination of fridges and freezers) to provide primary operating reserve, is proposed and investigated based on different operating scenarios (e.g., seasonal variations) of the Irish power system in [83]. The impact of the novel DSM strategy is studied by the time responses of system frequency stability when the system is subjected to losses of synchronous generators with different capacities. Similarly, a novel emergency DSM (EDSM) program is developed based on existing UFLS and emergency DR (EDR) programs in [84]. The EDSM has proved to be more efficient (smaller frequency deviations with lower amounts of load shedding) than existing DSM programs by comparing corresponding system frequency responses when the test system (i.e., IEEE New England 39-bus system) is facing a small (about 8.5% of rated system demand) and a large (about 22.1% of rated system demand) power deficit. Similarly, an EDR-based under speed load shedding (USLS) scheme, which is triggered by the estimated recovery time of the induction motor speed, is introduced in [85]. The novel DSM scheme aims to achieve fast voltage recovery with lower amounts of load shedding, and thus the impact of the USLS is determined by focusing on the time responses of bus voltages after various system faults. In [86], the traditional UVLS is improved by introducing a hybrid control algorithm covering genetic algorithms and particle swarm optimisation. The research focuses on system voltage stability in contingency states quantified by the fast voltage stability index [87] and proves that the UVLS is a primary and economic way to enhance system voltage stability and avoid voltage collapses.

In the majority of the cases when the DSM is triggered by a price signal, it is expected that DSM curtails peak demand or shifts demand from peak hours to off-peak hours to achieve the desired load profile with lower generation costs and reserve costs. Although the DSM is not implemented to enhance one or multiple aspects of system stability, it affects all aspects of system stability performance simultaneously by moving the power

system to a new operating point. The impact of such DSM on system stability can still be assessed based on individual aspects of system stability.

In [88], customers are encouraged to discharge their battery energy storage systems (BESS) during peak hours, in order to reduce the need for system load shedding, by a frequency linked tariff where the electricity price is determined based on real time system frequency. The impact of the new DSM program is determined by using the time responses of critical bus voltages based on an IEEE 33-bus radial distribution network. Likewise, the authors of [89] present an advanced DSM strategy based on a particle swarm optimisation algorithm to support system voltage stability indicated by steady state load margins. The proposed DSM strategy reschedules load shifting whenever the steady state load margin after DSM is lower than 95% of the steady state load margin before DSM [89]. System demands (loads) have been modelled as composite load (i.e., a parallel connection of static ZIP load and induction motor (IM) with the consideration of corresponding flexibility (controllability) and payback profile; the simulations are also performed based on a modified IEEE 33-bus radial distribution network.

In terms of rotor angle stability, an optimal DSM program is presented in [90] where the amount of load shifting is optimised with the objective function of minimising the electricity cost to customers, based on the existing ToU tariff in the Danish spot market. When the time domain transient stability assessment was conducted, based on a simplified equivalent representation of the Western Danish power system with a three-phase short circuit fault, it was found that the optimal DSM program significantly improves system transient stability indicated by maximum rotor angle deviation and critical clearing time of fault. A more recent study, performed based on the IEEE 295-bus distribution network, investigates the impact of DSM on small disturbance stability by shifting different types of loads (e.g., domestic static ZIP load and domestic IM) from the peak hours to the off-peak hours [91]. Unlike most of the previous studies that focus on the beneficial impact of load shedding during peak hours, the detrimental impact of load reconnection during off-peak hours has also been studied and quantified in [91].

Additionally, a modified electricity tariff, which can be considered as an implicit (price-based) DSM program, has been introduced in [92] to encourage the participation of

demand side components (e.g., EV and BESS), and its impact on frequency stability is investigated by comparing frequency deviations with modified tariffs and traditional model predictive control. The results obtained based on a microgrid with RES-based generations illustrate that the proposed modified tariff is an effective solution to improving system frequency stability and reducing the peak to the average ratio (PAR) of the load profile.

All above-mentioned studies were performed focusing on one particular aspect of power system stability neglecting the impact of DSM on other aspects of power system stability. The power system stability performance of the new operating point after DSM can also be assessed from multiple stability aspects in order to gain deep insight into the impact of DSM on system stability.

A hierarchical power flow control algorithm, which coordinates the transmission network, distribution network and individual building management system, is proposed in [93] to support and enhance power system small disturbance and frequency stability. The proposed control algorithm enables stability enhancement from both generation side (i.e., synchronous generators) and demand side (i.e., DSM provided by building management system), and improves stability performance by increased system damping and frequency recovery ability. In [94], the impacts of DSM on voltage stability and frequency stability have been assessed simultaneously in an interconnected microgrid with connections of various RES-based generators. According to the transient responses of bus voltage and system frequency, it is noted that DSM can result in different impacts on different aspects of system stability. More specifically, DSM is more effective at regulating system frequency than bus voltage [94]. Moreover, the authors of [95] rank load demand (active power) of all demand buses affecting voltage and small disturbance stability by applying a Morris screening-based sensitivity analysis with the consideration of parameter correlation. It has been found that altering the active power at a certain location, which is the typical consequence of DSM programs, could affect system voltage and small disturbance stability to different extents. A similar study performed in [96] extends the parameter ranking (including active power demand) to both the rotor angle, voltage and frequency stability and a similar conclusion (i.e., changing active power at a certain location could affect different aspects of system stability very differently) has

been obtained.

1.6.3 Summary of Past Work

In summary, the assessment of the impact of DSM on system stability usually focuses on one particular stability aspect in the case of explicit DSM as the demand is manipulated with a clear stability enhancement target ([83 – 87]). DSM is considered as a solution for stability enhancement and improvement, and thus it is usually triggered by a critical operating point as the consequence of various system disturbances. Implicit DSM, which is typically triggered by finical incentives and price signals, is more likely to benefit power systems by resulting in desired load shape and subsequently, reduced generation and operation costs. However, whenever consumption patterns and compositions of demand are manipulated, the power system is transferred to a new operating point where system stability performance is significantly or completely changed; therefore, investigations into implicit DSM can be performed based on one ([88 – 92]) or multiple ([93 – 96]) aspects of power system stability.

System stability assessment based on the new operating point after implementation of DSM is essential because it could affect the decision of DSM deployment and the dispatch of power generations. Investigating the impact of DSM on one particular stability aspect based on corresponding stability indices can be insufficient and incomprehensive as DSM deployment affects all stability aspects simultaneously; the operation of power systems is endangered when any aspect of system stability is in critical situation. Furthermore, studies performed in [94 - 96] illustrated that the same DSM program can lead to very different impacts on different aspects of system stability, which emphasises the importance of simultaneous assessment of multiple stability aspects to obtain a more comprehensive understanding of DSM programs and more efficient DSM implementations.

Although many studies performed in the past have covered multiple stability aspects, the impact of DSM was quantified by multiple stability indices, indicating the performance of the corresponding stability aspect, meaning that the analysis was time-

consuming and complex. A more detailed review of power system stability indices can be found in Chapter 2 of this thesis. To the best of the author's knowledge, there are no published research or application results assessing the overall impact of DSM on multiple stability aspects by composite stability index.

It can also be noted from the past work that majority of the studies, except the study in [91], only focus on the impact of load shedding deployed during peak hours, while neglecting the impact of load reconnection (demand payback effect) during off-peak hours. A comprehensive assessment of the impact of DSM should cover system stability performance as the result of both load shedding during peak hours and load reconnection during off-peak hours.

1.7 Aims and Objectives of the Research

A comprehensive and accurate (to an extent) assessment of the impact of DSM (especially in the case of implicit DSM programs) on stability performance is essential to guide DSM deployment decisions and investment plans. Inappropriate DSM implementations, as the result of limited understanding or inaccurate modelling of DSM, could endanger system stability by forcing the system to operate closer to the stability limit and reducing customer satisfaction through the potential deployment of further DSM programs (e.g., UFLS and UVLS). Therefore, every effort in this research was made to develop an efficient tool to estimate the overall impact of DSM on combined system stability (system stability performance assessed from multiple aspects simultaneously) under various system operating and modelling conditions. Furthermore, this research also attempts to address the critical factors and the extents to which these factors could affect the overall impact of DSM on combined system stability.

The overall aim of this research is to develop a framework and algorithms to efficiently assess and quantify the overall impact of advanced DSM (a price signal-based load shifting with the consideration of different demand flexibility and demand payback requirement of flexible demands) on combined system stability, encompassing small disturbance stability, transient stability and frequency stability at transmission level; and

identify the critical factors that affect the impact of advanced DSM. In this thesis, the term 'advanced DSM' refers to more comprehensive and realistic modelling of DSM programs, i.e., including demand composition, controllability, modelling of payback effect, for power system dynamic studies. The impact of advanced DSM is expected to cover both load shedding around peak hours and load reconnection around off-peak hours and to be quantified by a generalised tool which can also be adopted to assess the contributions of other existing and novel technologies and operational practices on combined system stability.

To achieve the overall aim of this research, the following objectives have been identified:

- To perform comprehensive literature reviews on the state of the art of DSM application in modern power systems, accurate modelling of advanced DSM deployment and power system stability assessment from different stability aspects.
- To modify existing IEEE test systems and establish a simplified equivalent representation of four interconnected real world transmission networks suitable for power system stability assessments in the environment of DigSilent PowerFactory.
- To model a load shifting-based advanced DSM according to the system under study, with the consideration of different demand flexibility (defined as the capacity of demands to change their power consumption patterns in response to either control or price signals) based on their location and nominal size, accurate modelling of flexible demands based on their type and composition, and demand payback profiles based on surveys reported in open literature.
- To perform MCS-based probabilistic analyses based on selected test systems before and after deployment of advanced DSM for small disturbance stability, transient stability and frequency stability with probabilistic modelling of several critical operational uncertainties. The impact of advanced DSM shall be derived by comparing stability performance before and after the DSM implementation.
- To develop and validate an efficient way to evaluate multiple stability aspects simultaneously; the proposed evaluation method is expected to clearly indicate the

distance of the current operating point to the stability limit, which is considered as the combined system stability performance of that operating point, and identify any unstable operating points.

- To illustrate and quantify the impact of advanced DSM on combined system stability with different system operating and DSM modelling conditions using the proposed evaluation method and identify the critical factors that may affect the impact of advanced DSM on combined system stability.

- To investigate the system dynamic responses immediately after the system is subjected to DSM deployment (i.e., considering DSM deployment as disturbance), to validate the practicability of advanced DSM.

1.8 Contributions

The research performed in this thesis mainly contributes to power system stability assessment from multiple stability aspects simultaneously, and investigations of the impact of advanced DSM on multiple stability aspects at transmission level. Detailed contributions of this research are summarised as follows, where the references after each paragraph represent relevant thesis-based publications in the proceedings of international conferences or in the international journals. A full list of the author's thesis-based publications is provided in Appendix-B

1. Two composite stability indices, namely normalised Euclidean Distance for stability (NEDS) and parallel circuit inspired composite stability index (PCICSI), are proposed to evaluate combined system stability performance by measuring the distance of the current operating point to the combined stability limits. All composite stability indices aim to balance the different and even opposite impacts on different stability aspects and provide an efficient tool to investigate the impact of new technologies on combined system stability. Proposed composite stability indices and the methodology for developing them have the capability to be extended to include other stability or performance indices without significant loss of generality, corresponding verifications are considered as a future work of this thesis [B1, B11].

2. The comprehensive modelling of advanced DSM is developed in this thesis taking into account the dominated load characteristics (i.e., the characteristics of loads that consumes the largest amount of electrical power) and demand payback effects. To model the capacity and flexibility of DSM as realistically as possible, several flexible DSM processes from both large IC and DN load categories have been considered in this thesis and modelled as either constant power loads or corresponding dominated load characteristics. The implementation of advanced DSM is performed with the consideration of different demand flexibility and demand payback effects of each flexible DSM process. The developed DSM programs can reduce the difference between the demand peak and demand valley without creating a new demand peak and demand valley [B2, B12].

3. Development of the probabilistic framework to assess multiple aspects of power system stability. The developed MCS-based probabilistic stability assessments consider several system operational uncertainties (e.g., wind speed and load demand) as inputs, and perform random sampling of all input variables defined based on corresponding widely adopted probability distributions. Then, repeatable deterministic analyses are performed for each input set, and the system stability performance are indicated by selected statistical values of the output sets. The impacts of, for instance, RES-based generation and DSM, can be assessed by comparing the selected statistical values obtained from different operating conditions [B3, B6, B7, B10].

4. Simultaneous assessment of rotor angle and frequency stability to study the impact of RES-based generation and different load models on combined system stability using the proposed composite stability indices (i.e., NEDS and PCICSI) based on MCS-based probabilistic stability assessments. The results validate the accuracy and practicability of the proposed composite stability indices, and it has been found that PCICSI is better at evaluating the variations of combined system stability and identifying unstable cases within the system. Hence, PCICSI is adopted for subsequent studies, focusing on the impact of advanced DSM on combined system stability [B1, B11].

5. The impact of advanced DSM (including load shedding during peak hours and load reconnection, due to required demand payback effects during off-peak hours) on multiple aspects of power system stability are investigated either separately (quantified by corresponding stability indices) or simultaneously (quantified by proposed composite stability index) at transmission level. Furthermore, various factors, including, but are not limited to, DSM capacity, location of flexible demand, RES penetration level and load model, that may affect the impact of advanced DSM on combined system stability have been studied through MCS-based probabilistic stability assessments under different operating conditions. By performing discretely (i.e., either half-hourly or hourly) stability assessments and comparing combined system stability performances under different operating conditions, critical factors, which result in both quantitative and qualitative changes in the impact of advanced DSM, have been identified [B2].
6. Investigating system dynamic responses immediately after implementation of advanced DSM (manipulating load consumption patterns and load compositions) to validate the practicability of advanced DSM. The locations of critical generators are identified. The impact of introducing time delays between DSM programs, a potential solution to improving system stability performance immediately after implementations of advanced DSM, has been investigated, focusing on the time responses of the generator rotor angle and terminal frequency [B12].

1.9 Overview of the Thesis

The remaining seven chapters of this thesis with their main contents are introduced briefly as follows:

Chapter 2 – Composite Indices for Simultaneous Assessment of Multiple Aspects of Power System Stability

Chapter 2 first introduces stability indices widely adopted in power system stability assessment regarding small disturbance stability, transient stability and frequency stability, and gives a brief introduction of stability indices adopted in this research and

corresponding stability limit. After a review of existing composite stability indices focusing on a particular stability aspect, two proposed composite stability indices, developed based on selected individual stability indices from multiple stability aspects, are presented and discussed in this chapter. This chapter also provides theoretical analyses of the advantages and limitations of proposed composite stability indices.

Chapter 3 – Modelling of Test Power Systems

This chapter provides an introduction to three power networks adopted in this research with detailed discussions of modelling of important system components (i.e., synchronous generators, RES-based generators and system demands).

Chapter 4 – Modelling of Load Composition and Advanced Demand Side Management

This chapter starts with a discussion of the modelling methodology of load compositions when a composite load model is adopted to model system demands. Then, this chapter focuses on discussing the modelling of advanced DSM, including the capacities of each flexible DSM process, locations of flexible DSM assets and demand payback effects. Finally, the implementation of advanced DSM and its impact on the system loading curves are discussed in this chapter.

Chapter 5 – Probabilistic Assessment of Power System Stability

A comprehensive discussion of MCS-based probabilistic analysis method adopted in this research is provided in this chapter. It first introduces all the considered operational uncertainties, including a discussion about the corresponding probability distributions. This is followed by a detailed description of the Monte Carlo stopping rule. Finally, the chapter presents and discusses all the steps involved within MCS-based probabilistic stability assessments.

Chapter 6 – Assessment of Power System Stability Using Proposed Composite Stability Indices.

This chapter presents the results of the implementation and validation of proposed composite stability indices (NEDS and PCICSI) based on three test power systems. The

impacts of RES-based generation and different load models on individual stability aspects and combined system stability are quantified by individual stability indices and proposed composite stability indices, respectively. The performances of composite stability indices based on different system models are discussed individually in different sections, such that a clear comparison can be performed to identify the advantages and limitations of all proposed indices. A composite stability index with greater accuracy and applicability is identified and will be used for subsequent studies.

Chapter 7 – The Impacts of Advanced Demand Side Management on Angular and Frequency Stability.

This chapter focuses on illustrating the impact of advanced DSM on the system rotor angle and frequency stability by comparing system stability performances before and after advanced DSM deployment. Firstly, the impact of advanced DSM on individual stability aspects are discussed based on corresponding stability indices. Then, the composite stability index selected in Chapter 6 is utilised to quantify the impact of advanced DSM on combined system stability. Moreover, the impacts of some important factors (i.e., RES penetration level, load model, DSM capacity and location of flexible demand) have been studied to investigate how and to what extent they could affect the impact of advanced DSM on combined system stability. Finally, the last part of this chapter discusses system dynamic responses when the system is subjected to advanced DSM deployment (i.e., considering DSM deployment as a disturbance) to validate the practicability of advanced DSM.

Chapter 8 – Conclusion and Future Work

This final chapter summarises the major contribution of the research and identifies the possible improvement that can be made to this research as well as the areas that could be explored in future studies.

2 Composite Indices for Simultaneous Assessment of Multiple Aspects of Power System Stability

2.1 Introduction

This chapter discusses stability indices that have been widely adopted to assess small disturbance stability, transient stability and frequency stability. Two proposed composite stability indices, which assess multiple aspects of system stability simultaneously and rely on calculations of distances of selected stability indices to corresponding limits, are introduced and discussed based on a review of various composite stability indices developed in the past. The chapter also identifies and analyses the advantages and limitations of the proposed composite stability indices using simple examples.

2.2 Stability Indices for Individual Stability Aspects

2.2.1 Stability Indices for Small Disturbance Stability Assessment

Recalling from Section 1.4.1 that small disturbance stability can be assessed by linearised dynamic responses as the system is subjected to a small disturbance. By representing linearised power systems as (2.1) and (2.2), where A is the $n \times n$ state matrix, B is the $n \times r$ input matrix, C is the $m \times n$ output matrix and D is the $m \times r$

feedforward matrix, and applying Lyapunov's first method [19, 25], system small disturbance stability performance can be characterised by eigenvalues of the state matrix (i.e., matrix A).

$$\Delta\dot{x} = A\Delta x + B\Delta u \tag{2.1}$$

$$\Delta y = C\Delta x + D\Delta u \tag{2.2}$$

The eigenvalues (λ) of state matrix A can be obtained when non-trivial solutions (i.e., $\emptyset \neq 0$) exist for (2.3), where $\emptyset$ is a vector with a size of $n \times 1$.

$$A\emptyset = \lambda\emptyset \tag{2.3}$$

Rewritten (2.3) as:

$$(A - \lambda I)\emptyset = 0 \tag{2.4}$$

where I is the identity matrix with a size of $n \times n$. Because $\emptyset \neq 0$, equation (2.5) must be satisfied to solve (2.4).

$$det(A - \lambda I) = 0 \tag{2.5}$$

By solving (2.5), n solutions of λ (i.e., $\lambda = \lambda_1, \lambda_2, \ldots, \lambda_n$) can be obtained and they are the eigenvalues of state matrix A. Eigenvalues can be either real or complex numbers. The complex eigenvalues always appear in conjugate pairs. A real eigenvalue corresponds to a non-oscillatory drift with a decreasing amplitude when the eigenvalue is negative, an increasing amplitude when the eigenvalue is positive or a fixed amplitude when the eigenvalue is equal to zero. Regarding complex eigenvalues, each conjugate pair of complex eigenvalues represents a periodic oscillation mode with a decreasing amplitude when the real parts of eigenvalues are negative, an increasing amplitude when the real parts of eigenvalues are positive or a fixed amplitude when the real parts of eigenvalues are zero. In both cases (real and complex eigenvalues), the amplitude of oscillation decreases or increases faster with a larger magnitude of the real part of eigenvalues.

A general representation of eigenvalues (λ) is given as (2.6), where σ (real part of

eigenvalues) and ω (imaginary part of eigenvalues) are damping in s^{-1} and oscillation frequency in rad/s, respectively. An example is presented in Fig. 2.1 to illustrate the relationship between eigenvalues and oscillation modes; the oscillation mode presented in the subplot (a) has a damping (σ) of – 0.3 s^{-1} and a frequency of 1.59 Hz, while the oscillation mode presented in the subplot (b) has a damping of 0.3 s^{-1} and a frequency of 1.59 Hz.

$$\lambda = \sigma \pm j\omega \tag{2.6}$$

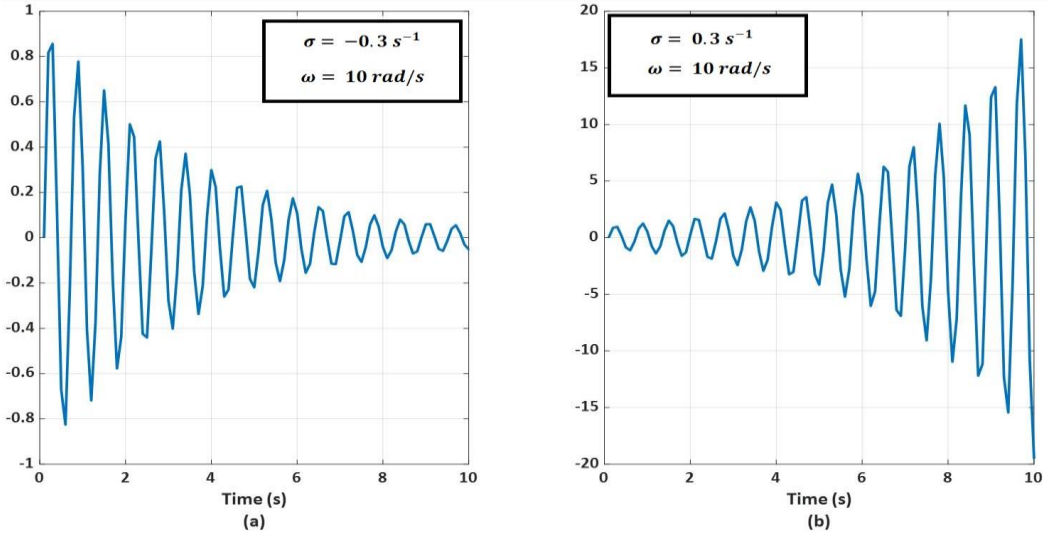

Figure 2.1 Two oscillation mode examples with a decreasing amplitude (a) and an increasing amplitude (b)

Instability of system small disturbance stability can be characterised by the critical conjugate pair of eigenvalues of the linearised system state matrix corresponding to the most critical electromechanical mode moving from the left-hand side (with negative values of σ) to the right-hand side (with positive values of σ) of the complex plant [17, 97]. Therefore, a negative damping (σ) of the conjugate eigenvalues corresponding to the most critical electromechanical mode indicates a stable operating point, while a positive damping of the most critical electromechanical mode indicates an unstable operating point in terms of small disturbance stability. The small disturbance stability limit (i.e., the boundary between stable operating points and unstable operating points) based on damping can be adopted as σ = 0 [98].

In addition to the damping, system small disturbance stability can also be assessed by the damping ratio (ξ) as shown in (2.7), where all variables have the same definitions as

(2.6). According to (2.7), positive values of ξ can be obtained from oscillations with decreasing amplitudes; on the contrary, oscillations with increasing amplitudes lead to negative values of ξ [99]. Consequently, stable operating points are indicated by positive damping ratios corresponding to the most critical electromechanical mode and the larger the value of the damping ratio, the more stable the system is. The small disturbance stability limit based on the damping ratio can be adopted as ξ = 0.

$$\xi = \frac{-\sigma}{\sqrt[2]{\sigma^2 + \omega^2}} \tag{2.7}$$

In real power system assessment and planning, the minimum damping ratio of all oscillation modes is expected to be larger than a certain value (e.g., 3% [100] or 5% [101]) to guarantee a safe stability margin. Although both the damping and damping ratio can assess small disturbance stability with clearly defined stability limits, this thesis uses damping of the most critical electromechanical mode to assess small disturbance stability because it provides a more direct illustration and requires fewer calculations. To sum up:

Small disturbance stability is assessed by the damping of the most critical electromechanical mode with stability limit defined as σ = 0 in this thesis. The larger magnitude the negative damping has, the more stable the system is.

2.2.2 Stability Indices for Transient Stability Assessment

Transient stability concerns the dynamic responses of rotor angles when the system is subjected to a large disturbance such that the dynamic equations cannot be linearised. As transient stability is characterised by the large rotor angle excursions and non-linear power-angle relationship, it is typically studied by numerical integration methods such as Euler Method and Runge-Kutta (R-K) Method [17].

For a SMIB system, transient stability indices are usually derived based on the equal area criterion as discussed in Section 1.4.2. Recalling from Section 1.4.2 that the acceleration ($A1$) and deceleration ($A2$) areas of rotor angle can be calculated following (2.8) and (2.9), respectively. Where H is inertia constant in MW·s/MVA, ω_e^{syn} is rated electrical

speed of rotor in rad/s, P_m^{pu} and P_e^{pu} are mechanical power and electrical power in p.u., respectively. The initial rotor angle, disturbance clearing rotor angle and maximum allowable rotor angle are represented by δ_0, δ_c and δ_m, respectively. Transient stability can then be assessed by disturbance clearing rotor angle (δ_c) and subsequently, disturbance clearing time (t_c).

$$A1 = \int_{\delta_0}^{\delta_c} \frac{\omega_e^{syn}}{H} \left(P_m^{pu} - P_e^{pu}\right) d\delta \tag{2.8}$$

$$A2 = \int_{\delta_c}^{\delta_m} \frac{\omega_e^{syn}}{H} \left(P_m^{pu} - P_e^{pu}\right) d\delta \tag{2.9}$$

Corresponding transient stability limits (i.e., critical disturbance clearing angle δ_{crit} and critical disturbance clearing time t_{crit}) are obtained assuming $A1 = A2$. If the disturbance is cleared at an angle (time) smaller than the critical disturbance clearing angle (time), the system is considered transient stable, otherwise, the system is considered transient unstable. However, it can be noted from (2.8) and (2.9) that such stability limits highly depend on the initial operating point (i.e., the operating point before disturbance) of the system, disturbance location, disturbance type, etc. In other words, general transient stability limits, which are suitable for transient stability assessment with various generator models and disturbance types, cannot be defined based on the critical disturbance clearing angle and clearing time.

In modern interconnection-rich power systems with many synchronous generators, the application of equal area criterion is limited by complex system topologies and high correlations between system components; therefore, system transient stability performance can be assessed based on stability indices derived from rotor angle excursions ($\delta(t)$) of a single synchronous generator. For instance, the maximum rotor angle deviation ($\Delta\delta_{ij}^{max}$), maximum rotor speed deviation ($\Delta\omega_{ij}^{max}$) and maximum rotor acceleration (a_{ij}^{max}) can be derived according to (2.10), (2.11) and (2.12), respectively, for generator i in a power system with N_g generators and a specific disturbance j. In (2.10) to (2.12), the initial rotor angle is indicated by δ_{ij}^0, the rotor angle and rotor speed at time instant t are represented by $\delta_{ij}(t)$ and $\omega_{ij}(t)$, respectively.

$$\Delta\delta_{ij}^{max} = \max\left(\left|\delta_{ij} - \delta_{ij}^{0}\right|\right), i = 1, 2, \dots, N_g \quad (2.10)$$

$$\Delta\omega_{ij}^{max} = \max\left(\left|\frac{\delta_{ij}(t) - \delta_{ij}(t - \Delta t)}{2\pi f \Delta t}\right|\right), i = 1, 2, \dots, N_g \quad (2.11)$$

$$a_{ij}^{max} = \max\left(\left|\frac{\omega_{ij}(t) - \omega_{ij}(t - \Delta t)}{\Delta t}\right|\right), i = 1, 2, \dots, N_g \quad (2.12)$$

Although all the above-mentioned indices assess transient stability of the concerned synchronous generator in such a way that better stability performance is indicated by lower index values, they cannot capture the dynamic responses of other generators and assess overall stability performance of the whole power system. Hence, some other transient stability indices have been developed based on rotor angle responses of multiple, if not all, synchronous generators. The transient potential energy (TPE) proposed in [102] assesses system transient stability and identifies the critical generator set by calculating the accumulated potential energy of any generator pair G_a and G_b (i.e., $a, b \in [1, 2, \dots, N_g]$) for a time interval ($t - t_0$) after the disturbance clearance. The TPE is calculated following (2.13), where t_0 and Δf_{ab} are the times of the disturbance clearance and frequency difference between G_a and G_b, respectively.

$$TPE = \int_{t_0}^{t} (\Delta P_{G_a} - \Delta P_{G_b})\ \Delta f_{ab}\ dt \quad (2.13)$$

Similarly, the transient kinetic energy (TKE), which is defined as (2.14), assesses system transient stability by calculating the kinetic energy of all generators immediately after the clearance of disturbance j [103]. In (2.14), the angular momentum of the rotor at rated speed and speed deviation of generator i are represented by J_i and $\Delta\omega_{ij}$, respectively.

$$TKE = \sum_{i=1}^{N_g} \frac{1}{2} J_i \Delta\omega_{ij}^2 \quad (2.14)$$

Moreover, the transient stability index (TSI), as shown in (2.15), is another widely adopted index to assess and quantify the whole system transient stability by comparing the maximum rotor angle deviation (δ_{max}^{j}) after the disturbance j and the maximum

allowable angle deviation (δ_{limit}) between any two generators in the system [104, 105]. The angle deviation limit can be pre-defined as either 180^o in the centre of inertia reference frame [106, 107] or 360^o when rotor angle separation between individual generators is concerned [104, 105].

$$TSI = \frac{\delta_{limit} - \delta_{max}^{j}}{\delta_{limit} + \delta_{max}^{j}} \times 100 \tag{2.15}$$

Power systems are considered transient stable when the maximum angle deviation (δ_{max}^{j}) does not exceed the limit; in other words, when the TSI ranges from 0 to 100. However, if TSI becomes negative as a result of angle deviation exceeding the limit, power systems are considered transient unstable. Therefore, the transient stability limit based on TSI can be defined as TSI = 0 and TSI assesses transient stability performance in such a way that the closer the TSI is to 100, the more stable the system is.

In this thesis, TSI is adopted to assess system transient stability for its ability to cover rotor angle responses of all synchronous generators and its precisely defined general transient stability limit which is suitable to be used regardless of system topologies and disturbance types. The maximum allowable angle deviation with a value of 360^o has been adopted to calculate TSI. To sum up:

Transient disturbance stability is assessed by the TSI with stability limit defined as TSI = 0 in this thesis. The closer the TSI is to 100, the more stable the system is.

2.2.3 Stability Indices for Frequency Stability Assessment

Like transient stability, frequency stability is characterised by the frequency excursions toward either larger or smaller values than the rated frequency (50 Hz or 60 Hz) when the system is subjected to an imbalance between power generation and demand. Consequently, frequency stability indices are derived based on the time responses of system frequency. Recalling from Section 1.4.3 that system frequency increases when the power generation is larger than the demand (i.e., over-generation), while it decreases when the power generation is smaller than the demand (i.e., over-demand),

examples of frequency excursions regarding over-generation and over-demand situations are shown in subplots (a) and (b) of Fig. 2.2, respectively, with a rated frequency of 50 Hz.

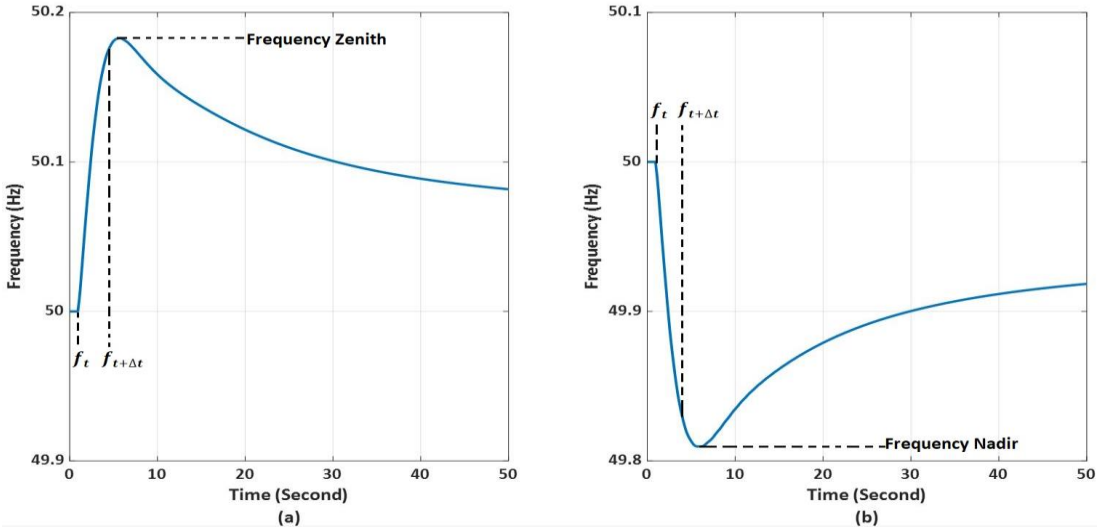

Figure 2.2 Frequency excursion examples in the case of over-generation (a) and over-demand (b)

As shown in Fig. 2.2, the maximum frequency value in the case of over-generation frequency excursions (Fig. 2.2 (a)) and the minimum frequency value in the case of over-demand frequency excursions (Fig. 2.2 (b)) are called frequency zenith and frequency nadir, respectively. As two of the most intuitive frequency stability indices, frequency zenith and frequency nadir assess frequency stability in such a way that better stability performance is represented by smaller frequency zenith values (i.e., closer to the rated frequency) and larger frequency nadir values (i.e., closer to the rated frequency). Additionally, the rate of change of frequency (RoCoF) is also widely adopted to assess frequency stability performance by measuring the speed of frequency rise or drop. RoCoF (in Hz/s) is usually obtained by measuring frequency changes within a pre-determined measurement time window, as shown in (2.16) where f_t is the frequency value at the beginning of the measurement window and Δt is the size of the measurement window [108]. Better frequency stability is indicated by smaller absolute values of RoCoF.

$$RoCoF = \frac{f_{t+\Delta t} - f_t}{\Delta t} \tag{2.16}$$

Regarding frequency stability limits, they can be properly defined based on both frequency zenith, frequency nadir and RoCoF. Because all disturbances adopted in this thesis for frequency stability assessment, either disconnection of synchronous generators or reconnection of demands, lead to over-demand situation and subsequently, frequency drop, only frequency nadir limit will be considered in this section. System stability limits defined for frequency nadir and RoCoF vary depending on system topology, coordination of control and protection devices and response of system components. According to the Grid Code published by the National Grid Electricity System Operator (ESO) of Great Britain (GB), system frequency could fall to 47 Hz in exceptional circumstances [109]; therefore, system apparatus (e.g., synchronous generators) must be operated for at least 20 seconds each time the system frequency falls into the range from 47 Hz to 47.5 Hz. Because the length of the MCS-based probabilistic stability assessments for frequency stability is shorter than 20 seconds in this thesis, and no extra frequency controls (e.g., UFLS and AGC) have been modelled in test power systems, the lowest frequency value in the Grid Code (i.e., 47 Hz) has been selected as the frequency nadir limit. Frequency excursions are therefore controlled mainly depending on the inertia responses and reserve capacities of synchronous generators. It is worth mentioning here that the frequency nadir limit is also selected such that reasonable numbers of stable and unstable operating points can be defined. The value of this limit can be adjusted if appropriate frequency controls are considered and modelled.

The frequency stability limit based on RoCoF, which is also defined by the National Grid ESO of GB, varies from $\pm$0.125 Hz/s for system with distributed generators to $\pm$1 Hz/s for existing power systems [110]. However, future GB power systems are more likely to use the RoCoF limit of $\pm$0.5 Hz/s due to the reduced system inertia [110].

This thesis adopts both frequency nadir and RoCoF for frequency stability assessment. RoCoF limit with the value of -1 Hz/s is used in this thesis based on a measurement window of 100 ms (i.e., Δt = 100 ms) [111]. To sum up:

Frequency stability is assessed by both frequency nadir and RoCoF with stability limit defined as 47 Hz and -1 Hz/s, respectively. More stable systems are indicated by larger

values of frequency nadir and smaller absolute values of RoCoF.

2.2.4 Composite Stability Indices for Individual Stability Aspects

Individual stability indices are usually developed focusing on specific characteristics or time scales of system dynamic responses; these indices may exhibit limited ability to capture and illustrate the dynamic responses of the whole system and correlations between system components. With the ever-growing integrations of RES-based generators, high voltage direct current (HVDC) transmission lines and flexible demands, which can affect multiple stability aspects simultaneously, power system stability assessments must be performed more efficiently and more comprehensively. Hence, composite stability indices have been developed to capture more features of system dynamic responses that used to be neglected previously or analysed separately. This sub-section introduces several composite stability indices proposed recently to assess system voltage, transient and frequency stability.

A composite index, which is developed based on the fast voltage stability index (FVSI) and line utilisation factor (LUF), is proposed in [112] to optimise the placement of thyristor-controlled series capacitor (TCSC) such that system voltage stability and power transfer capability can be improved with minimum power losses. The FVSI is a stability index to assess voltage stability based on a transmission line between sending end a and receiving end b, and it can be calculated as (2.17), where Q_b is the reactive power at the receiving end b, V_a is the voltage at the sending end a, Z and X are line impedance and line reactance, respectively [113].

$$FVSI_{ab} = \frac{4Z^2 Q_b}{V_a^2 X} \tag{2.17}$$

The LUF, as defined by (2.18), is developed to calculate the congestion level of the selected transmission line. In (2.18), the maximum power rating and the actual power rating of the transmission line between sending end a and receiving end b are represented by MVA_{ab}^{max} and MVA_{ab}, respectively. The proposed composite index

with equally weighted FVSI and LUF is given by (2.19).

$$LUF_{ab} = \frac{MVA_{ab}}{MVA_{ab}^{max}} \tag{2.18}$$

$$Composite\ \ Index_{ab} = 0.5\ \times\ FVSI_{ab} + 0.5\ \times\ LUF_{ab} \tag{2.19}$$

In [114], a maximum loading limit (MLL) index is proposed covering system voltage stability and power flow reliability to calculate the voltage stability margin of each bus and identify the critical bus accordingly. The voltage stability is assessed by the voltage violation index (VVI), which is given by (2.20), to determine the voltage violence from the base case. In (2.20), N_B is the total number of system buses, n is the exponent of penalty function, V_a^{base} and V_a^{max} are the voltages of bus a in the base case and maximum loading case, respectively.

$$VVI = \sum_{a=1}^{N_B} \frac{1}{2n} (V_a^{base} - V_a^{max})^{2n} \tag{2.20}$$

Power flow reliability is assessed by the real power flow violation index (PVI) and reactive power flow violation index (QVI) in [114]. Real and reactive power violation indices can be defined as (2.21) and (2.22), respectively. In (2.21) and (2.22), real and reactive power flows of transmission line l in the base case are represented by P_l^{base} and Q_l^{base}, respectively, while real and reactive power flows of the same transmission line when bus a is loaded at the maximum level are represented by $P_{l,a}^{max}$ and $Q_{l,a}^{max}$, respectively. C_l^{max} indicates the maximum capacity of transmission line l and N_L represents the total number of transmission lines in the system. Finally, the proposed composite index for bus a (MLL_a) is computed following (2.23).

$$PVI = \sum_{l=1}^{N_L} (P_l^{base} - P_{l,a}^{max}) /\ C_l^{max} \tag{2.21}$$

$$QVI = \sum_{l=1}^{N_L} (Q_l^{base} - Q_{l,a}^{max}) /\ C_l^{max} \tag{2.22}$$

$$MLL_a = VVI + PVI + QVI \tag{2.23}$$

Moreover, the authors of [115] present a composite index consisting of four selected sub-indicators (i.e., acceleration index (ACI), average acceleration index (AAI), speed deviation index (SDI) and rotor angle index (RAI)) to assess system transient stability by adopting a principal component analysis (PCA) based method. Individual sub-indicators for a specific generator i are derived following (2.24), (2.25), (2.26) and (2.27) for ACI, AAI, SDI and RAI, respectively. In (2.24) to (2.27), integrations are performed for rotor angle acceleration at time instant t indicated by $a_i(t)$, rotor speed deviation at time instant t indicated by $\Delta\omega_i(t)$ and rotor angle difference from the reference generator at time instant t indicated by $\delta_i(t)$ with a time period of T assuming system disturbance is introduced at $t = 0$.

$$ACI_i = \int_0^T a_i(t)dt \tag{2.24}$$

$$AAI_i = \frac{1}{T}\int_0^T a_i(t)dt \tag{2.25}$$

$$SDI_i = \int_0^T \Delta\omega_i(t)\,dt \tag{2.26}$$

$$RAI_i = \int_0^T \delta_i(t)dt \tag{2.27}$$

Correlated sub-indicators are then transformed into less correlated principal components by PCA method [116]. The weight factors for each sub-indicator and each principal component are given as (2.28) and (2.29), respectively. Where g_{ki} is the rotated factor loading, representing the loading of sub-indicator k in the jth principal component, obtained from orthogonal rotation of principal components [115] and e_j represents the eigenvalue of the jth principal component. The intermediate composite indicator for jth principal component (ICI_j) is derived following (2.30) based on all sub-indicators represented by I_k and corresponding weight factors (w_{kj}). Finally, the proposed composite index is obtained by combining all principal component-based ICIs and corresponding weight factors (a_j), as shown in (2.31).

$$w_{kj} = \frac{g_{ki}}{e_j} \tag{2.28}$$

$$a_j = \frac{e_j}{\sum_j e_j} \tag{2.29}$$

$$ICI_j = \sum_{k=1}^{4} w_{kj} I_k \tag{2.30}$$

$$Composite\ \ Index = \sum_j a_j\, ICI_j \tag{2.31}$$

Composite stability indices developed for frequency stability assessment can be found in [117] and [118]. A key performance indicator (KPI) is developed in [117] by simply dividing RoCoF by the frequency nadir (FN), as given in (2.32), to assess the frequency stability performance of power systems with high wind generations. In [118], a composite index, called frequency response index (FRI), is proposed to evaluate system frequency stability combining the system governor ramp rate, system inertia and power imbalance. The inertia constant (H_s) of a power system with N_g generators is given as (2.33) where the inertia constant and rated apparent power of generator i are represented by H_i and S_i, respectively. The system governor ramp rate for a specific disturbance j (C_s^j) is calculated as (2.34) where t_{nadir}^j and $\Delta P(t_{nadir}^j)$ are the time instants of the frequency nadir and system governor response at the same time instant. Finally, FRI, with respect to disturbance j, is calculated as (2.35) where ΔP_d^j is the power imbalance between generation and demand caused by the disturbance, and H_s^j is the system inertia constant during the disturbance.

$$KPI = \frac{RoCoF}{FN} \tag{2.32}$$

$$H_s = \frac{\sum_{i=1}^{N_g} H_i \times S_i}{\sum_{i=1}^{N_g} S_i} \tag{2.33}$$

$$C_s^j = \frac{\Delta P\left(t_{nadir}^j\right)}{t_{nadir}^j} \tag{2.34}$$

$$FRI^j = \frac{C_s^j H_s^j}{\Delta P_d^j} \tag{2.35}$$

It can be noted from the above discussions that all composite stability indices introduced focus on evaluating the stability performance of one specific stability aspect. Even though the accuracy and efficiency of single aspect stability assessments can be improved by the utilisation of composite stability indices, the stability performances of the system with respect to other stability aspects are still not addressed. Considering that multiple aspects of system stability are usually affected simultaneously, there is a need to develop composite stability indices assessing multiple aspects of system stability simultaneously.

2.3 Stability Indices for Multiple Stability Aspects

This thesis proposes two composite stability indices to assess small disturbance stability, transient stability and frequency stability simultaneously by calculating stability distances to corresponding stability limit that rely on selected stability indices for different stability aspects. Voltage stability has not been incorporated so far mainly because it involves different time scales (typically minutes), different models (typically simplified generator representation and inclusion of tap-changing transformers and other voltage regulation devices) and different types of analysis (typical gradual load increase). Continuation load flow analysis and observing bus loadability limit could be potentially used but that would assume that during the load increase at one or more buses, the DSM actions (connection or disconnection of loads and load payback effects) would not happen. The inclusion of voltage stability in composite stability indices is an area for future research. All selected stability indices and corresponding stability limits are summarised in Table 2.1.

Table 2.1 Selected stability indices and corresponding stability limit

Stability Aspect	**Stability Index**	**Stability Limit**
Small disturbance stability	Damping (σ)	σ=0 s^{-1}
Transient stability	TSI	TSI=0
Frequency Stability	Frequency nadir (FN)	FN=47 Hz
	RoCoF	RoCoF= -1 Hz/s

It can be seen from Table 2.1 that this thesis considers not only individual stability indices from multiple stability aspects, but also multiple stability indices (i.e., FN and RoCoF) from one single stability aspect (i.e., frequency stability). These help to prove the practicability and generality of proposed composite stability indices. The remaining part of this section focuses on introducing the theoretical bases and detailed computations of the proposed composite stability indices, namely the normalised Euclidean Distance for stability (NEDS) and the parallel circuit inspired composite stability index (PCICSI).

2.3.1 Normalised Euclidean Distance for Stability

Euclidean Distance (ED) measures the distance between points or manifolds in multi-dimensional spaces based on Pythagoras Theorem [119]. In the case of a three-dimensional space as illustrated in Fig. 2.3, the ED between point a and the origin (Fig. 2.3 (a)) and the ED between point a and point b (Fig. 2.3 (b)) can be derived as (2.36) and (2.37), respectively. In a more general situation, which is a n-dimensional space, the ED between two manifolds is calculated as (2.38), where a_i and b_i are variables of two manifolds.

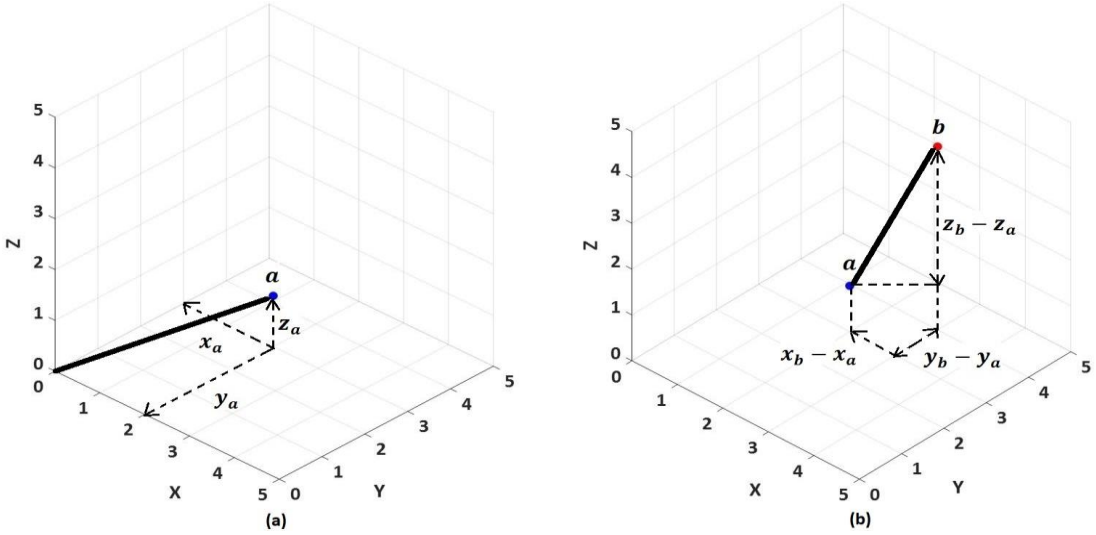

Figure 2.3 Euclidean Distance between point a and the origin (a) and Euclidean Distance between point a and point b (b)

$$ED_{ao} = \sqrt[2]{(x_a)^2 + (y_a)^2 + (z_a)^2} \tag{2.36}$$

$$ED_{ab} = \sqrt[2]{(x_b - x_a)^2 + (y_b - y_a)^2 + (z_b - z_a)^2} \quad (2.37)$$

$$ED = \sqrt[2]{\sum_{i=1}^{n} (a_i - b_i)^2} \quad (2.38)$$

Regarding power system stability assessment, each stability index considered in combined system stability can be modelled as a dimension in a multi-dimensional space. As four stability indices (i.e., σ, TSI, FN and RoCoF) are adopted in this thesis for combined system stability assessment, a four-dimensional space can be developed where each dimension is represented by a selected stability index. Therefore, the stable operating points of power systems should be located in the space with boundaries defined as σ = 0, TSI = 0, FN = 47 Hz (consider over-demand situations only and assume FN limit to be 47 Hz) and RoCoF = -1 Hz/s (consider over-demand situations only and assume RoCoF limit to be -1 Hz/s). When any of the above-mentioned boundaries (i.e., stability limits) are violated, the system is considered unstable.

By defining a system stable operational space in a four-dimensional space and stability limits associated with each dimension, the combined system stability performance of an operating point i can be evaluated by the distance to combined stability limit, as shown in (2.39), where σ_{lim}, TSI_{lim}, FN_{lim} and $RoCoF_{lim}$ are stability limits defined for σ, TSI, FN and RoCoF, respectively.

$$ED_i = \sqrt[2]{(\sigma_i - \sigma_{lim})^2 + (TSI_i - TSI_{lim})^2 + (FN_i - FN_{lim})^2 + (RoCoF_i - RoCoF_{lim})^2} \quad (2.39)$$

It can be recalled from Section 1.6.1 that the MCS-based probabilistic analysis method delivers a set of estimated outputs by sampling statistical inputs randomly and performs repeatable deterministic analysis for each set of sampled inputs, the results of the probabilistic combined system stability assessment are four sets of selected stability indices (i.e., σ, TSI, FN and RoCoF). The statistical values, such as the mean value and the most probable value of each set of stability indices, can be used to evaluate the overall performance of each stability aspect at a certain operating point. In this thesis, the mean values [120], given as (2.40), of selected stability indices are adopted to

evaluate the overall stability performance of each stability aspect based on MCS-based probabilistic stability assessments. In (2.40), x_i indicates the output of ith sampled inputs and n represents the total number of input samples. An example is given as follows to evaluate combined system stability performance using ED.

$$\bar{x} = \frac{1}{n}\sum_{i=1}^{n} x_i \tag{2.40}$$

Example 1: Ten values have been produced randomly for each individual stability index considered in this thesis regarding an operating point i with the consideration of operational uncertainties. Detailed values of all individual stability indices are:

$\sigma_i = [-0.30, -0.25, -0.33, -0.32, -0.27, -0.30, -0.27, -0.30, -0.29, -0.28]$

$TSI_i = [69.2, 60.0, 68.4, 66.3, 65.9, 67.5, 66.7, 67.1, 69.0, 71.2]$

$FN_i = [49.65, 49.82, 49.92, 49.81, 49.87, 49.79, 49.90, 49.89, 49.88, 49.90]$

$RoCoF_i = [-0.15, -0.20, -0.18, -0.19, -0.11, -0.09, -0.25, -0.17, -0.17, -0.19]$

The mean values of each set of stability index can be obtained as $\overline{\sigma_i}$ = -0.29 s^{-1}, $\overline{TSI_i}$ = 67.13, $\overline{FN_i}$ = 49.84 Hz and $\overline{RoCoF_i}$ = -0.17 Hz/s. By adopting stability limits as σ_{lim} = 0 s^{-1}, TSI_{lim} = 0, FN_{lim} = 47 Hz and $RoCoF_{lim}$ = -1 Hz/s, combined system performance can be quantified by ED as:

$$ED_i = \sqrt[2]{(-0.29-0)^2 + (67.13-0)^2 + (49.84-47)^2 + (-0.17+1)^2} = 67.2 \tag{2.41}$$

It can be seen from (2.41) that the ED value calculated regarding operating point i is very close to the TSI mean value ($\overline{TSI_i}$), indicating the combined system stability is dominated by the transient stability due to its larger indicator (i.e., TSI) values. However, this is not desired in combined system stability assessment because the critical stability aspect should not be defined based on the magnitude of corresponding indicators. In other words, the variations of individual stability indices and the contributions of each stability aspect need to be properly balanced in composite stability indices.

NEDS is thus proposed to balance the variations and contributions of individual stability distances (the distances between stability indices and corresponding stability limits) by normalising mean values (due to the implementation of MCS-based probabilistic stability assessments) of each set of stability distances from a particular operating point with respect to the corresponding most probable values obtained from all operating points, as shown in (2.42), where D_{np}, $\overline{D}$ and D_{mp} are normalised stability distance with respect to the most probable value, mean value of the stability distance result set and the most probable value of the same stability distance result set, respectively. The most probable value is adopted as the reference value in the NEDS because it is less affected by extreme events (i.e., high impact low probability (HILP) events) that result in extremely high (low) stability indices, and thus it is more 'stable' as a reference

$$D_{np} = \frac{\overline{D}}{D_{mp}} \tag{2.42}$$

The most probable value of a set of stability distances is indicated by the peak value (i.e., maximum value) of the corresponding probability density function (PDF) curve [121]. Adopting the damping results in Example 1 (i.e., σ_i = [-0.30, -0.25, -0.33, -0.32, -0.27, -0.30, -0.27, -0.30, -0.29, -0.28]) as an example, the PDF curve of the corresponding stability distance with σ_{lim} = 0 is shown as Fig. 2.4 and the peak value is reached at σ_i' = -0.29 where the prime (apostrophe) represents the stability distance to the limit; therefore, the most probable value of the damping results is σ_i' = -0.29. By normalising all stability distances adopted in this thesis, the NED-based composite stability index (i.e., NEDS) is computed as (2.43) where prime (apostrophe) and np subscript indicate the distance to the corresponding limit and normalised stability distance with respect to their most probable values, respectively.

$$NEDS = \frac{1}{2} \times \sqrt[2]{\left(\sigma_{np}'\right)^2 + \left(TSI_{np}'\right)^2 + \left(FN_{np}'\right)^2 + \left(RoCoF_{np}'\right)^2} \tag{2.43}$$

In (2.43), 1/2 is introduced such that NEDS is equal to one when all stability distances are at the corresponding most probable values. NEDS larger than one means the combined stability performance is better than the most probable situation, while the combined stability performance worse than the most probable situation is indicated by

NEDS smaller than one. To illustrate the practicability of NEDS, it is used in Example 2, shown as follows, for combined system stability assessment based on the same data given in Example 1.

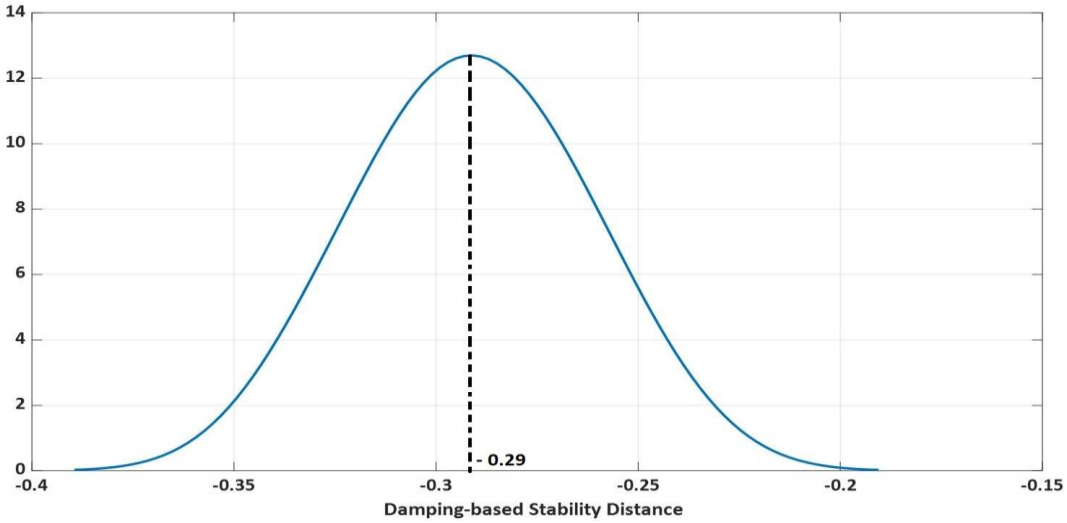

Figure 2.4 PDF curve of example damping results in Example 1 to identify the most probable value

Example 2: Based on the stability indices given in Example 1, the stability distances to the corresponding stability limits, assuming σ_{lim} = 0 s^{-1}, TSI_{lim} = 0, FN_{lim} = 47 Hz and $RoCoF_{lim}$ = -1 Hz/s, can be calculated as:

$$\sigma_i' = [-0.30, -0.25, -0.33, -0.32, -0.27, -0.30, -0.27, -0.30, -0.29, -0.28]$$

$$TSI_i' = [69.2, 60.0, 68.4, 66.3, 65.9, 67.5, 66.7, 67.1, 69.0, 71.2]$$

$$FN_i' = [2.65, 2.82, 2.92, 2.81, 2.87, 2.79, 2.90, 2.89, 2.88, 2.90]$$

$$RoCoF_i' = [0.85, 0.80, 0.82, 0.81, 0.89, 0.91, 0.75, 0.83, 0.83, 0.81]$$

The mean values for stability distances based on σ, TSI, FN and RoCoF are -0.29, 67.13, 2.84 and 0.83, respectively. The corresponding most probable values are -0.29, 67.39, 2.89 and 0.82. Hence, NEDS regarding operating point i is given as:

$$NEDS^i = \frac{1}{2} \times \sqrt[2]{\left(\frac{-0.29}{-0.29}\right)^2 + \left(\frac{67.13}{67.39}\right)^2 + \left(\frac{2.84}{2.89}\right)^2 + \left(\frac{0.83}{0.82}\right)^2} = 0.998 \qquad (2.44)$$

Based on (2.43) and (2.44), the proposed composite stability index (i.e., NEDS) balances

different magnitudes of individual stability distances and provides a comparison between the combined system stability performances of the current operating point under study and the most probable situation throughout, for instance, a day, a month, a year, etc. As for stable system operating points, deteriorated combined system stability performances compared with the most probable situation are represented by NEDS values smaller than one, which also indicate that stability enhancement measures are needed. NEDS values greater than one indicate the combined system stability performance of the current operating point is better than the most probable situation and the larger the NEDS is, the more stable the system is. Hence, NEDS can be considered as an efficient indicator to guide deployment of system stability enhancement measures (e.g., DSM) in stable operating points.

It can also be noted according to (2.43) and (2.44) that NEDS has limited ability to identify unstable operating points (when one or several stability indices violate corresponding stability limits) because all stability distances are squared during the calculation. An example (Example 3) is provided as follows:

Example 3: Substituting the FN results in Example 1 with FN_i = [44.35, 44.18, 44.08, 44.19, 44.13, 44.21, 44.1, 44.11, 44.12, 44.1] and adopting the results for all remaining stability indices in Example 1, the stability distances of the adopted stability indices, assuming σ_{lim} = 0 s^{-1}, TSI_{lim} = 0, FN_{lim} = 47 Hz and $RoCoF_{lim}$ = -1 Hz/s, can be calculated as:

$$\sigma_i' = [-0.30, -0.25, -0.33, -0.32, -0.27, -0.30, -0.27, -0.30, -0.29, -0.28]$$

$$TSI_i' = [69.2, 60.0, 68.4, 66.3, 65.9, 67.5, 66.7, 67.1, 69.0, 71.2]$$

$$FN_i' = [-2.65, -\ 2.82, -\ 2.92, -2.81, -2.87, -2.79, -2.90, -2.89, -2.88, -2.90]$$

$$RoCoF_i' = [0.85, 0.80, 0.82, 0.81, 0.89, 0.91, 0.75, 0.83, 0.83, 0.81]$$

The mean values of σ_i', TSI_i', FN_i' and $RoCoF_i'$ are -0.29, 67.13, -2.84 and 0.83, respectively, and the corresponding most probable values are -0.29, 67.39, -2.89 and 0.82. Therefore, the NEDS for this frequency unstable operating point is:

$$NEDS^i = \frac{1}{2} \times \sqrt[2]{\left(\frac{-0.29}{-0.29}\right)^2 + \left(\frac{67.13}{67.39}\right)^2 + \left(\frac{-2.84}{-2.89}\right)^2 + \left(\frac{0.83}{0.82}\right)^2} = 0.998 \qquad (2.45)$$

Because the same NEDS value has been obtained in Examples 2 and 3, NEDS does not identify the unstable operating point, which may lead to severe consequences in real power systems. Additionally, NEDS also requires regular updated reference values (i.e., the most probable values of each stability distance) such that the most probable operating situation is accurate and reliable for combined system stability assessments. However, by normalising individual stability distances with respect to corresponding most probable values, NEDS provides a comparison between the current combined system stability performance and the most probable situation. Hence, NEDS is expected to be able to guide deployments of stability enhancement solutions (e.g., DSM) when the power system is operated without a risk of losing stability, which is the most common situation in real systems. Due to the potential benefits of the NEDS, it is further validated in Chapter 6 of this thesis.

2.3.2 Parallel Circuit Inspired Composite Stability Index

Parallel circuit inspired composite stability index (PCICSI) also relies on the normalisation of distances between individual stability indices to corresponding stability limits in order to balance different magnitudes of stability distances. But in the case of PCICSI, the mean values (due to the implementation of MCS-based probabilistic stability assessments) of individual stability indices are normalised by the maximum stability distance, indicating the best stability performance, obtained from all operating points under study. Furthermore, the normalisation is only applied to stable stability indices, while stability indices indicating instability are issued a stability distance of zero.

The normalisations performed for σ, TSI, FN and RoCoF follow (2.46), (2.47), (2.48) and (2.49), respectively.

$$\sigma'_{nm} = \begin{cases} \dfrac{\sigma_{lim} - \bar{\sigma}}{\sigma_{Ref}}, & \bar{\sigma} < 0 \ \ 1/s \\ 0, & \bar{\sigma} \geq 0 \ \ 1/s \end{cases} \qquad (2.46)$$

$$TSI'_{nm} = \begin{cases} \dfrac{\overline{TSI} - TSI_{lim}}{TSI_{Ref}}, & \overline{TSI} > 0 \\ 0, & \overline{TSI} \leq 0 \end{cases} \quad (2.47)$$

$$FN'_{nm} = \begin{cases} \dfrac{\overline{FN} - FN_{lim}}{FN_{Ref}}, & \overline{FN} > 47 \ \ Hz \\ 0\ , & \overline{FN} \leq 47 \ \ Hz \end{cases} \quad (2.48)$$

$$RoCoF'_{nm} = \begin{cases} \dfrac{|RoCoF_{lim}\ | - |\overline{RoCoF}|}{\left|RoCoF_{Ref}\ \right|}\ , & |\overline{RoCoF}| < \ \ 1 \ \ Hz/s \\ 0\ , & |\overline{RoCoF}| \geq \ \ 1 \ \ Hz/s \end{cases} \quad (2.49)$$

Where prime (apostrophe) and nm subscript indicate the distance to corresponding stability limit (represented by lim subscript) and normalised stability distance with respect to their maximum values (represented by Ref subscript), respectively.

The composition of PCICSI, as shown in Fig. 2.5, is inspired by the parallel connected circuit where all impedances share the same voltage, and the current is divided based on the magnitude of the impedances. Similar to the equivalent impedance of parallel connected circuits, the PCICSI is calculated as (2.50) where normalised stability distances are obtained from (2.46) to (2.49) and 1/4 is introduced, as all stability distances (indices) are considered equally weighted. Equal weightings are used when all violations of particular stability limits are equally important, which may not be the case in different systems that may be more sensitive to a particular stability issue. The weightings can be adjusted to reflect the particular concerns of a system operator, and therefore are application specific. For general assessment in this thesis though, at least as a first approximation, equal weightings have been used.

$$\frac{1}{PCICSI} = \frac{1}{4} \times \left(\frac{1}{\sigma'_{nm}} + \frac{1}{TSI'_{nm}} + \frac{1}{FN'_{nm}} + \frac{1}{RoCoF'_{nm}} \right) \quad (2.50)$$

Based on (2.50), the PCICSI ranges from zero to one for a stable system and it is equal to zero when any stability index (aspect) violates its stability limit. The closer the PCICSI is to one, the more stable the system is. When all stability indices (aspects) show the largest distances to corresponding limits (i.e., the best stability performance), which may not be achievable in real power system operations but is theoretically possible, PCICSI is

equal to one. The features of PCICSI with corresponding features of parallel connected circuits are summarised in Table 2.2.

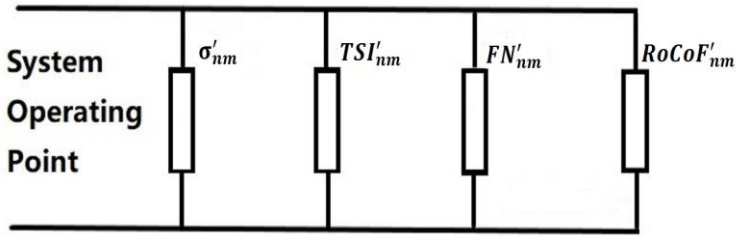

Figure 2.5 Graphical representation of the structure of PCICSI

Table 2.2 Features of parallel connected circuits and corresponding features of composite stability index (PCICSI)

Parallel Connected Circuits	PCICSI
All impedances share the same voltage values.	All stability distances are derived based on the same operating point.
Current is divided according to the impedance, larger current flows through the branch with smaller impedance.	The smaller stability distance, e.g., for one particular aspect of stability, indicates more critical condition and therefore, requires more attention.
The equivalent impedance of the circuit is zero if any individual impedance is zero, i.e., short circuit.	The PCICSI is zero if any normalised individual stability distance is zero, i.e., any aspect of stability is unstable.
The equivalent impedance can be calculated in the same way if more impedances are connected in parallel.	The PCICSI can be calculated in the same way if more stability indices (aspects) are considered in combined system stability.

Compared with NEDS, PCICSI provides a comparison between combined system stability performances of the operating point under study and the best performed operating point observed from, for instance, a day, a month, a year, etc. As the best performed operating point can be fixed for a long period while the most probable operating point changes regularly, the computation cost of PCICSI is smaller than that of NEDS. Moreover, as discussed in Table 2.2, PCICSI is capable of identifying system instability when any stability index violates the corresponding stability limit, which is the most important advantage of PCICSI compared with NEDS. However, by referring to the best performed operating point, which happens once during the entire period of study, PCICSI is not efficient at guiding the deployments of stability enhancement and improvement measures. The practicability of PCICSI to evaluate combined system stability performance and identify system instability is investigated by Example 4, as shown below:

Example 4: Adopting the same stability index results and stability limits (i.e., σ_{lim} = 0 s^{-1}, TSI_{lim} = 0, FN_{lim} = 47 Hz and $RoCoF_{lim}$ = -1 Hz/s) as shown in Example 1, the best performed stability indices are σ_i = -0.33 s^{-1}, TSI_i = 71.2, FN_i = 49.9 Hz and $RoCoF_i$ = -0.09 Hz/s. Consequently, the largest stability distances to the corresponding limits are 0.33, 71.2, 2.9 and 0.91 based on σ, TSI, FN and RoCoF, respectively. Given the mean values of the corresponding stability indices are $\overline{\sigma_i}$ = -0.29 s^{-1}, $\overline{TSI_i}$ = 67.13, $\overline{FN_i}$ = 49.84 Hz and $\overline{RoCoF_i}$ = -0.17 Hz/s, the normalised stability distances are:

$$\sigma'_{nm} = \frac{0-(-0.29)}{0.33} = 0.88 \tag{2.51}$$

$$TSI'_{nm} = \frac{67.13-0}{71.2} = 0.94 \tag{2.52}$$

$$FN'_{nm} = \frac{49.84-47}{2.9} = 0.98 \tag{2.53}$$

$$RoCoF'_{nm} = \frac{1-0.17}{0.91} = 0.91 \tag{2.54}$$

The combined system stability regarding operating point i evaluated using PCICSI is:

$$\frac{1}{PCICSI_i} = \frac{1}{4} \times \left(\frac{1}{0.88} + \frac{1}{0.94} + \frac{1}{0.98} + \frac{1}{0.91}\right) \tag{2.55}$$

Solving (2.55) leads to $PCICSI_i$ = 0.93, which sits between 0.88 (the worst performed stability index) and 0.98 (the best performed stability index). Thus, different stability performances have been properly balanced in PCICSI. If the FN results in Example 3 are used, where $\overline{FN_i}$ = 44.16 Hz, the new value of FN'_{nm} is zero according to (2.48). Therefore, the combined system stability for this unstable operating point evaluated using PCICSI is:

$$\frac{1}{PCICSI_i} = \frac{1}{4} \times \left(\frac{1}{0.88} + \frac{1}{0.94} + \frac{1}{0} + \frac{1}{0.91}\right) \tag{2.56}$$

And $PCICSI_i$ = 0. Based on Example 4, it is clear that PCICSI can be used to evaluate combined system stability and identify system instability.

2.4 Summary

This chapter first introduces widely adopted stability indices for small disturbance, transient stability and frequency stability assessments, and composite stability indices developed based on several individual stability indices to improve the accuracy and efficiency of system stability assessment of a particular stability aspect. In response to the need to develop an efficient tool for simultaneous assessment of multiple aspects of system stability, two composite stability indices, namely NEDS and PCICSI, are proposed to assess combined system stability with the consideration of the rotor angle (small disturbance and transient) stability and frequency stability. Both composite stability indices evaluate combined system stability by considering simultaneously the distances to the corresponding stability limits while relying on the calculation of widely adopted stability indices for different stability aspects. Although each proposed composite stability index has corresponding advantages and limitations, it has been found from several examples that NEDS cannot identify system instability, which significantly restricts its application. However, PCICSI can clearly evaluate combined system stability and identify system instability. The development of the composite stability indices for combined system stability assessments, which consider multiple aspects of power system stability simultaneously, is the first original contribution of this thesis.

3 Modelling of Test Power Systems

3.1 Introduction

The three power system models adopted in this thesis for studies with different purposes are introduced in this chapter, focusing on system topologies, and modelling of important system components (i.e., synchronous generators, RES-based generators and system demands).

3.2 Overview of Test Power Systems

MCS-based probabilistic stability assessments are applied based on three different power system models (i.e., modified IEEE 9-bus test system, modified IEEE 68-bus test system and 4 transmission network equivalent (4TNE) system) to investigate the performance of proposed composite stability indices and the impact of advanced DSM on combined system stability. The topologies of all system models under study are shown as a single line diagram in Fig. 3.1, Fig. 3.2 and Fig. 3.3 for the modified IEEE 9-bus test system, modified IEEE 68-bus test system and 4TNE system, respectively.

Modified IEEE 9-bus test system consists of 9 buses interconnected by 6 transmission lines, seven synchronous generators connected at Buses 1, 2 and 3, three loads connected at Buses 5, 7 and 9, and a wind farm modelled as an aggregation of full

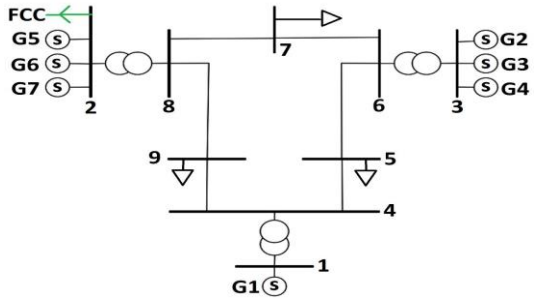

Figure 3.1Modified IEEE 9-bus test system with RES-based generation

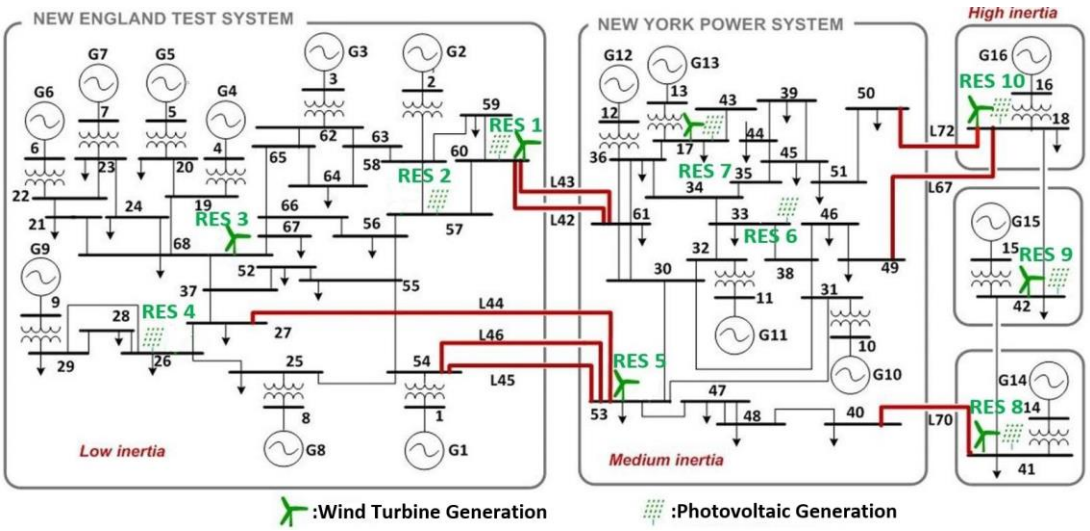

Figure 3.2 Modified IEEE 68-bus test system with RES-based generation

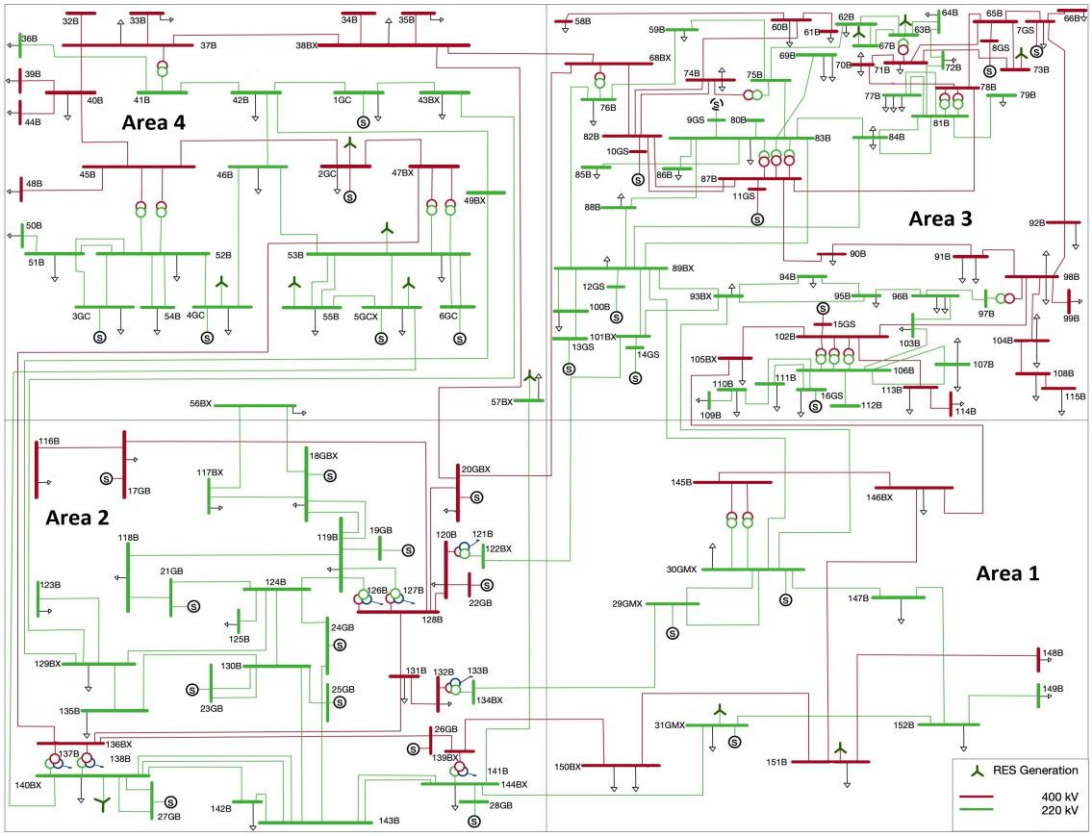

Figure 3.3 4TNE system with RES-based generation

converter connected (FCC) distributed generators and connected at Bus 2.

Modified IEEE 68-bus test system has 68 buses distributed in 5 interconnected areas. There are 72 transmission lines, 16 synchronous generators, 35 loads and 10 integration points (i.e., Buses 17, 18, 26, 33, 41, 42, 53, 57, 60 and 68) of RES-based generation, which have been modelled as aggregations of double fed induction generators (DFIGs) and FCC distributed generators.

The 4TNE system is an equivalent representation of four interconnected real-world transmission systems comprising 152 buses rated at either 400 kV or 220 kV, 42 synchronous generators, 142 loads (including 95 normal loads and 47 equivalent representations of cross-border power transfer) and 12 integration points of RES-based generation modelled as aggregations of DFIGs. It should be noted here that some components (e.g., synchronous generators and loads) connecting to the same bus have been merged and are represented by a single symbol in Fig. 3.3. The 4TNE system has been approved by four TSOs who provided network information as an appropriate model for generic steady state and dynamic studies of their interconnection.

The performances of proposed composite stability indices to assess combined system stability have been studied based on all system models introduced above, while the impacts of advanced DSM on individual stability aspects and combined system stability are investigated based on the modified IEEE 68-bus test system and 4TNE system because there are very few demands in the modified IEEE 9-bus test system to be manipulated.

3.3 Modelling of System Components

3.3.1 Modelling of Synchronous Generators

As one of the most important components in power systems, synchronous generators and corresponding modelling methodologies can affect system dynamic responses significantly. This sub-section thus focuses on introducing modelling of synchronous generators in all system models.

A standard 6th order dynamic model neglecting stator transient has been used to depict the dynamic behaviours of all synchronous generators in this research; the dynamic model adopted can be represented by six full differential equations, shown as (3.1) to (3.6).

$$e_{fd} = R_{fd}I_{fd} + \frac{1}{\omega_0}p\psi_{fd} \tag{3.1}$$

$$0 = R_{1d}I_{1d} + \frac{1}{\omega_0}p\psi_{1d} \tag{3.2}$$

$$0 = R_{1q}I_{1q} + \frac{1}{\omega_0}p\psi_{1q} \tag{3.3}$$

$$0 = R_{2q}I_{2q} + \frac{1}{\omega_0}p\psi_{2q} \tag{3.4}$$

$$p\omega = \frac{1}{2H}(T_m - T_e - K_D(\omega - 1)) \tag{3.5}$$

$$p\delta = \omega_0(\omega - 1) \tag{3.6}$$

In (3.1) to (3.6), variables of field winding are noted with fd subscript, variables of damper winding on the d-axis are noted with $1d$ subscript, variables of damper windings on the two q-axes are noted with $1q$ and $2q$ subscripts. e_{fd} is the field winding voltage, R_{fd} is the field winding resistance, R_{1d}, R_{1q} and R_{2q} are the damper winding resistances, I_{fd} is the field winding current, I_{1d}, I_{1q} and I_{2q} are the damper winding current, ψ_{fd} is the field winding magnetic flux, ψ_{1d}, ψ_{1q} and ψ_{2q} are the damper winding magnetic fluxes. ω and ω_0 are the rotating speed and synchronous (nominal) speed of rotor, respectively. δ is the rotor angle, T_m and T_e are the mechanical and electrical torque, respectively. H is the inertia time constant, K_D is the damping coefficient, and:

$$p = {}^{d}/_{dt} \tag{3.7}$$

$$\omega_0 = 2\pi f \tag{3.8}$$

It is worth noting here that all electrical and torque variables in (3.1) to (3.6) are in p.u.,

rotor angle in electrical radians and rotor speeds in rad/s.

In addition to the modelling of synchronous generators, associate components (e.g., governor) and controllers (e.g., AVR) also need to be modelled properly for system stability assessments as they affect the dynamic responses of synchronous generators.

In the modified IEEE 9-bus test system as shown in Fig. 3.1, G1 has a fast-acting static exciter (IEEE ST1A) [122], an IEEEG3 speed governor (hydro turbine) [123] and a power system stabiliser (PSS). All synchronous generators at Bus 3 (i.e., G2, G3 and G4) are equipped with slow direct current (DC) exciters (IEEE DC1A) [124] and IEEEG1 speed governors (steam turbines) [125]. Moreover, synchronous generators connecting to Bus 2 (i.e., G5, G6 and G7) have the same DC exciters (IEEE DC1A) as generators at Bus 3, and GAST speed governors (gas fire turbines) [126]. Lastly, AVRs have been installed in all synchronous generators in the modified IEEE 9-bus test system.

In the modified IEEE 68-bus test system, all synchronous generators, except G9 where a fast-acting static exciter (IEEE ST1A) has been installed, are equipped with slow DC exciters (IEEE DC1A). Regarding speed governors, steam turbine-based speed governors (IEEEG1) are installed at G3, G4, G6 to G8 and G10 to G16 (where G4, G6 and G12 are modelled as nuclear power plants and all remaining generators are modelled as conventional coal-fired power plants), gas fire turbine-based speed governors (GAST) are installed at G1 and G2, while G5 and G9 are equipped with hydro turbine-based speed governors (IEEEG3). All synchronous generators in the modified IEEE 68-bus test system have AVR installed and only G9 has a PSS.

In the 4TNE system, the parameters of synchronous generators and corresponding controllers are either provided by or adopted through consultations with corresponding TSOs. 11/42 synchronous generators are equipped with various types of hydro turbine-based speed governors, 3/42 synchronous generators are equipped with gas fired turbine-based speed governors (GAST) and all remaining synchronous generators have various types of steam turbine-based speed governors (e.g., IEEEG1 and WSIEG1) [127]. PSSs can be found in 16/42 synchronous generators and AVR compensating systems are installed at 13/42 synchronous generators. Like the modified IEEE 9-bus test system and modified IEEE 68-bus test system, all synchronous generators in the 4TNE system have

AVR.

Exciters, speed governors and controllers adopted in the IEEE test systems (i.e., the modified IEEE 9-bus test system and modified IEEE 68-bus test system) are summarised in Table 3.1 where the 4TNE system has been excluded for confidential reasons. Detailed modelling parameters of exciters, speed governors and synchronous generator controllers are given in Appendix-A for the modified IEEE 9-bus test system (Appendix-A.1) and modified IEEE 68-bus test system (Appendix-A.2).

Table 3.1 Exciters, speed governors and synchronous generator controllers installed in the IEEE test systems [122 - 126]

Modified IEEE 9-bus Test System				
Generator(s)	**Exciter**	**Speed Governor**	**AVR**	**PSS**
G1	IEEE ST1A (static exciter)	IEEEG3(hydro)	Yes	Yes
G2, G3, G4	IEEE DC1A (DC exciter)	IEEEG1(steam)	Yes	No
G5, G6, G7	IEEE DC1A (DC exciter)	GAST (gas fire)	Yes	No
Modified IEEE 68-bus Test System				
Generator(s)	**Exciter**	**Speed Governor**	**AVR**	**PSS**
G1, G2	IEEE DC1A (DC exciter)	GAST (gas fire)	Yes	No
G3, G4, G6 to G8 and G10 to G16	IEEE DC1A (DC exciter)	IEEEG1(steam)	Yes	No
G5	IEEE DC1A (DC exciter)	IEEEG3(hydro)	Yes	No
G9	IEEE ST1A (static exciter)	IEEEG3(hydro)	Yes	Yes

3.3.2 Modelling of Renewable Energy Sources

In all power systems under study, RES-based generation is considered and modelled to capture two of the most important features (i.e., high variability and uncertainty of power generation) of modern and future power systems. In this thesis, RES-based generators generate electricity by harvesting wind energy and solar irradiation. Consequently, RES-based generators are modelled as aggregations of wind turbines or PV arrays in this thesis.

Based on the different types of generators used in wind turbines, wind turbines can be divided into several categories, including, but are not limited to, squirrel-cage induction generator (SCIG), wound rotor generators and permanent magnet generators [128]. Among all these wind turbines, Type 3 (DFIG) and Type 4 (FCC) wind turbines are adopted

in this thesis due to their high operational flexibility and high popularity in modern power systems. Configurations of DFIG and FCC wind turbines are shown in the top subplot and bottom subplot of Fig. 3.4, respectively. It can be seen from Fig. 3.4 that DFIG wind turbines are partly decoupled from the main power system by providing rotor excitations from a rotor-side converter, which is connected to the system through a grid-side converter [128]. A connection between rotor and power system enables additional control of stator power by adjusting the power injected to the rotor; moreover, it also allows wind turbines to be operated in a much wider speed range. Regarding the FCC wind turbine, it can be seen from Fig. 3.4 that FCC wind turbines are completely decoupled from the power system by connecting the generator stator and power system through converters, which enables a wind turbine to be operated at its optimal aerodynamic speed [128]. However, because all power generated by wind turbines needs to flow through converters, the ratings of converters in FCC wind turbines are much higher than converters in DFIG wind turbines, which also leads to higher costs of FCC wind turbines.

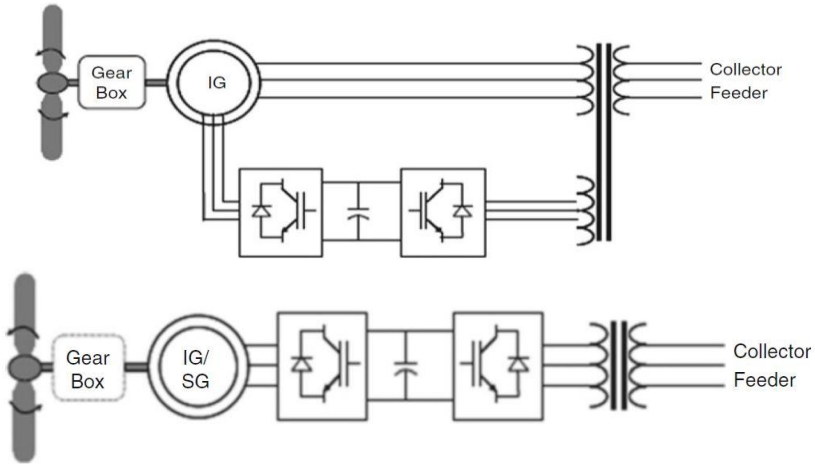

Figure 3.4 Configurations of Type 3 (DFIG) wind turbines (top subplot) and Type 4 (FCC) wind turbines (bottom subplot) (adopted from [128])

All DFIG- and FCC-based wind turbines in this thesis are modelled with structures suitable for system dynamic studies and similar to the models introduced by the Western Electricity Coordinating Council (WECC) in [129] and the International Electrotechnical Commission (IEC) in [130]. DFIG-based wind turbines have been modelled with essential aerodynamic controls (e.g., pitch control) and protections. All RES-based generation units are capable to provide reactive power compensations and they will remain

connected to the system during faults (i.e., all RES-based generation units have Fault Ride Through (FRT) ability).

In the modified IEEE 9-bus test system, a wind farm, modelled as an aggregation of Type 4 FCC wind turbines, is connected to Bus 2. The wind farm has the same installed capacity as the total installed capacity of all synchronous generators at bus 2 (i.e., G5 to G7). When the wind farm is disconnected from the system, all synchronous generators are operating to supply power and if the wind farm is delivering power to the system, G7 is decommissioned permanently to model the system inertia drop due to the integration of RES-based generation.

In the modified IEEE 68-bus test system, a wind farm modelled as an aggregation of Type 3 (DFIG) and Type 4 (FCC) wind turbines and a PV power plant modelled as an aggregation of FCC distributed generators are connected at each integration point of RES-based generation. It is assumed that all interconnected areas have identical installed capacity of RES-based generators (i.e., wind turbines and PV arrays). The proportions of wind farms and PV power plants and the proportions of DFIG and FCC generators at each integration point are summarised in Table 3.2.

In the 4TNE system, the installed capacities and locations of wind farms are provided by TSOs and all wind farms are modelled as aggregations of Type 3 (DFIG) wind turbines.

Table 3.2 Proportions (%) of wind farms and PV power plants and the proportions of DFIG and FCC generators at each integration point in the modified IEEE 68-bus test system

RES Integration	**Resources**		**Generator Type**	
Point	**Wind**	**Solar**	**DFIG**	**FCC**
RES1	65%	35%	50%	50%
RES2	0%	100%	0%	100%
RES3	100%	0%	50%	50%
RES4	0%	100%	0%	100%
RES5	100%	0%	50%	50%
RES6	0%	100%	0%	100%
RES7	65%	35%	50%	50%
RES8	50%	50%	35%	65%
RES9	35%	65%	35%	65%
RES10	65%	35%	50%	50%

All RES-based generators (i.e., individual wind turbines and PV arrays) are rated at 2 MW

in this thesis for the purpose of more convenient modelling and programming at transmission level. It is worth noting here that the PV converters have been modelled identical to the FCC-based wind turbines in this thesis [131]. Furthermore, in order to model the correlation between wind speeds and power outputs of wind turbines, the speed-power curve of Vestas-V80, a pitch controlled variable speed wind turbine rated at 2 MW [132], is adopted and shown in the subplot (a) of Fig. 3.5. Likewise, the daily power output curve of PV arrays (generation) is shown in the subplot (b) of Fig. 3.5 [133]. According to Fig. 3.5 (b), PV arrays generate electricity during the daytime (i.e., Hours 7 to 18) and wind turbines generate electricity when the wind speed is above 4 m/s and below 25 m/s.

In this thesis, RES penetration level is calculated as (3.9) where P_{RES} and P_G are used to indicate active powers generated by RES-based generators and all generators (including RES-based generators) in the system, respectively. RES penetration baseline refers to the RES penetration level when all RES-based generators operate at the rated output (i.e., 2 MW). The real RES penetration levels are usually lower than the baseline value because the power outputs of RES-based generators are constrained by wind speed and solar irradiation at corresponding operating points (Fig. 3.5). The RES penetration baselines are adjusted by changing the aggregation number of RES-based generators in wind farms and PV power plants.

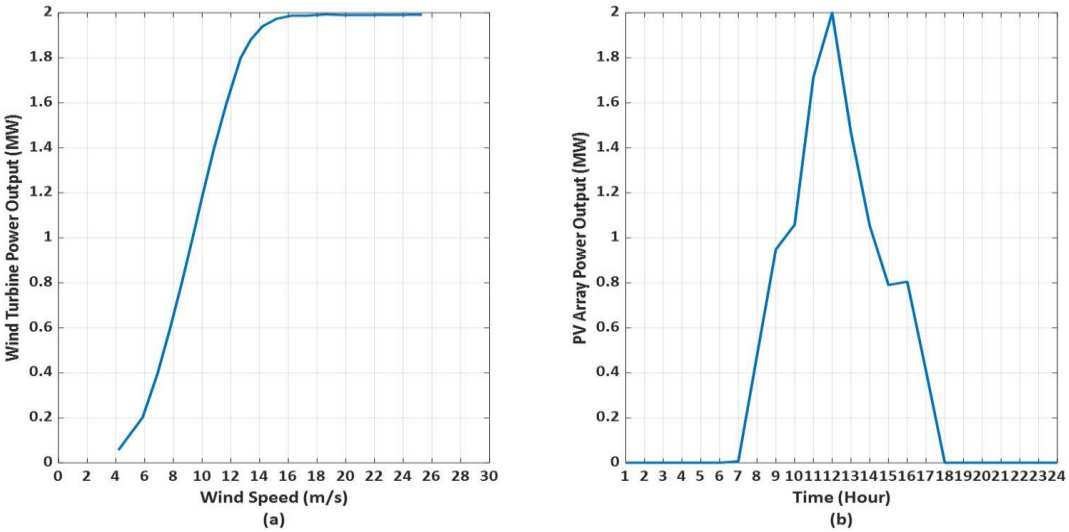

Figure 3.5 Speed-power curve of a Vestas-V80 wind turbine (a) and the daily power output curve of PV arrays (b) [132, 133]

$$RES\ \ Penetration\ \ Level = \frac{P_{RES}}{P_G}\ \times 100\% \tag{3.9}$$

3.3.3 Modelling of Load

Appropriate modelling of system demands (loads) is essential in power system stability assessment [134], especially in this thesis which focuses on assessing the impact of advanced DSM (i.e., load manipulations) on combined system stability. The terms 'demand' and 'load' are used interchangeably in this thesis. System demands are usually modelled differently based on their applicability in different power system studies (i.e., steady state and dynamic studies). Load models developed for steady state studies usually represent the load power behaviours (i.e., real and reactive power) as functions of the voltage and/or frequency only and they are categorised as static load models and described using algebraic equations. Typical static load models include exponential load, polynomial load, static IM load, etc. Regarding load models appropriate for dynamic studies, like dynamic exponential load model, dynamic IM load and composite load, the load power behaviours are modelled as functions of the voltage and/or frequency and time and described using a combination of algebraic and differential equations. It is worth noting here that the static load models can, and have quite frequently been used in system dynamic studies by assuming that the variations of voltage are too slow to affect the load behaviour during the transient period of interest [135].

3.3.3.1 Static Exponential Load

A static exponential load model, shown as (3.10) and (3.11), describes the load behaviours (i.e., consumptions of real power P and reactive power Q) as exponential functions of changes in voltage (U) and frequency (f). In (3.10) and (3.11), P_0 and Q_0 are real and reactive power consumptions when the load is supplied at nominal (i.e., rated) voltage (U_0) and nominal frequency (f_0). Exponential coefficients k_{pv}, k_{qv}, k_{pf} and k_{qf} represent the sensitivities of load demands (real and reactive powers) to variations of voltage and frequency.

$$P = P_0 \left(\frac{U}{U_0}\right)^{k_{pv}} \left(\frac{f}{f_0}\right)^{k_{pf}} \tag{3.10}$$

$$Q = Q_0 \left(\frac{U}{U_0}\right)^{k_{qv}} \left(\frac{f}{f_0}\right)^{k_{qf}} \tag{3.11}$$

Equations (3.10) and (3.11) can be simplified as (3.12) and (3.13), respectively, because voltage variations are much more frequent and larger than frequency variations in interconnected power systems [135]. All parameters in (3.12) and (3.13) have been defined as the same as (3.10) and (3.11), and when exponential coefficients (k_{pv} and k_{qv}) equal to 2, 1 and 0, (3.12) and (3.13) refer to constant impedance, constant current and constant power load models, respectively.

$$P = P_0 \left(\frac{U}{U_0}\right)^{k_{pv}} \tag{3.12}$$

$$Q = Q_0 \left(\frac{U}{U_0}\right)^{k_{qv}} \tag{3.13}$$

In this thesis, constant impedance (k_{pv}=k_{qv}=2) and constant power (k_{pv}=k_{qv}=0) load models are adopted to assess the impact of different load models on combined system stability and validate the accuracy and applicability of proposed composite stability indices (i.e., NEDS and PCICSI) in Chapter 6. A constant power load model is selected as it is still the most popular load model adopted for dynamic power system studies, especially in Europe and Africa, based on the international survey reported in [135], moreover, it is the model which is the least supportive to the system in case of voltage fluctuations. A constant impedance load model, however, is adopted because the system demand is the most sensitive to voltage variations when represented by this model, and such modelled demand is also the most supportive to the system when voltage changes.

3.3.3.2 Static Polynomial Load

A static polynomial load, also known as the ZIP load, can be defined as (3.14) and (3.15) with neglected dependency on frequency variations, and from where it can be seen that

static polynomial load is a combination of constant impedance (Z), constant current (I) and constant power (P) load models with corresponding weightings represented by p_Z and q_Z, p_I and q_I, and p_P and q_P, respectively. In the case of a constrained ZIP load model [136], participations of Z, I and P load models are required to range from zero to one and have a sum of one, as shown in (3.16) and (3.17). However, an accurate ZIP load model only requires the overall participation (i.e., sum) of Z, I and P load models to be one (i.e., equations (3.16) and (3.17)) [137]. All other parameters in (3.14) and (3.15) follow the same definitions as exponential load. The terms 'polynomial load' and 'ZIP load' are used interchangeably in this thesis.

$$P = P_0 \left[p_Z \left(\frac{U}{U_0} \right)^2 + p_I \left(\frac{U}{U_0} \right) + p_P \right] \tag{3.14}$$

$$Q = Q_0 \left[q_Z \left(\frac{U}{U_0} \right)^2 + q_I \left(\frac{U}{U_0} \right) + q_P \right] \tag{3.15}$$

$$p_Z + p_I + p_P = 1 \tag{3.16}$$

$$q_Z + q_I + q_P = 1 \tag{3.17}$$

As the ZIP load model exhibits Z, I and P characteristics simultaneously, it is considered to be more accurate than the exponential load model and used to model the static component of the composite load model [135].

3.3.3.3 Dynamic Induction Motor Load

Dynamic IM load model is used when the proportion of IM in the load mix is significant, a fifth order dynamic IM load can be depicted by the following equations [138]:

$$U_{ds} = R_s I_{ds} + \frac{d\psi_{ds}}{d\tau} - \omega_s \psi_{qs} \tag{3.18}$$

$$U_{qs} = R_s I_{qs} + \frac{d\psi_{qs}}{d\tau} + \omega_s \psi_{ds} \tag{3.19}$$

$$U_{dr} = R_r I_{dr} + \frac{d\psi_{dr}}{d\tau} - (\omega_s - \omega)\psi_{qr} \tag{3.20}$$

$$U_{qr} = R_r I_{qr} + \frac{d\psi_{qr}}{d\tau} + (\omega_s - \omega)\psi_{dr} \tag{3.21}$$

$$\frac{d\omega}{d\tau} = \frac{(M_e - M)}{\omega_b T_m} \tag{3.22}$$

$$\psi_{ds} = X_s I_{ds} + X_m I_{dr} \tag{3.23}$$

$$\psi_{qs} = X_s I_{qs} + X_m I_{qr} \tag{3.24}$$

$$\psi_{dr} = X_m I_{ds} + X_r I_{dr} \tag{3.25}$$

$$\psi_{qr} = X_m I_{qs} + X_r I_{qr} \tag{3.26}$$

where:

U_{ds}, U_{qs}: Stator voltage on d-axis and q-axis, respectively.

U_{dr}, U_{qr}: Rotor voltage on d-axis and q-axis, respectively.

I_{ds}, I_{qs}: Stator current on d-axis and q-axis, respectively.

I_{dr}, I_{qr}: Rotor current on d-axis and q-axis, respectively.

ψ_{ds}, ψ_{qs}: Stator flux linkages on d-axis and q-axis, respectively.

ψ_{dr}, ψ_{qr}: Rotor flux linkages on d-axis and q-axis, respectively.

ω, ω_s, ω_b: Rotor speed, synchronous speed and base speed, respectively.

R_s, R_r: Stator and rotor resistances, respectively.

X_s, X_r, X_m: Shunt reactance, rotor reactance and magnetising reactance.

M, M_e: Mechanical torque and electromagnetic torque, respectively.

τ, T_m: Normalised time and mechanical time constant of the motor, respectively.

Similar to the static exponential load, fifth order dynamic IM load models can be simplified to third order dynamic IM load models by neglecting stator transients (i.e.,

(3.18) and (3.19)). In this thesis, a fifth order dynamic IM load model is used to represent the dynamic component of the composite load mode.

3.3.3.4 Composite Load

In order to capture both the static and dynamic characteristics of loads in modern and future power systems, a composite load model, which is usually modelled as a parallel connection of a static load model and a dynamic IM load model, is introduced. The structure of a composite load model varies by adopting different static load models and dynamic IM models [139, 140]. In this thesis, the static part and the dynamic IM part of the composite load model are modelled as a static ZIP load and a fifth order dynamic IM load, respectively. The composite load model is depicted in Fig. 3.6. Due to the comprehensive modelling of system demands, the composite load model is considered to be the most appropriate load model available and the most accurate load model to simulate advanced DSM implementations (Chapter 7) [135].

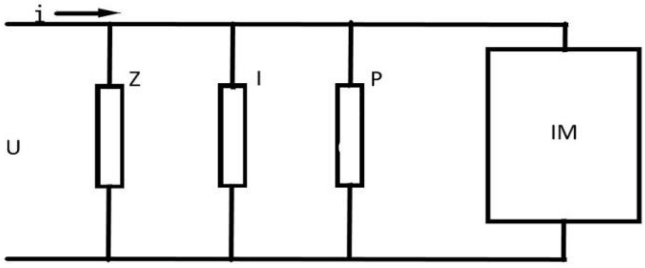

Figure 3.6 The composite load model adopted in this thesis

3.4 Summary

This chapter introduces three power system models utilised in this thesis focusing on the modelling of synchronous generators, RES-based generators and system demands. To capture the increased variability and uncertainty of power system operations, electronic interfaced wind turbines and PV arrays have been considered in this thesis. Regarding system demands, because the advanced DSM affects system operating performance by manipulating demand consumption patterns and load compositions, different load

models, namely constant impedance, constant power and composite load models, are adopted in this thesis.

4 Modelling of Load Composition and Advanced Demand Side Management

4.1 Introduction

The first part of this chapter focuses on discussing the modelling method of load compositions when the composite load model is adopted. The second part of this chapter discusses the modelling method of the advanced DSM adopted in this thesis, including the capacities of flexible demands, locations of flexible demands and demand payback effects.

4.2 Modelling of Load Composition

Load composition typically refers to different shares of components in the load model. By modelling the composite load model as a parallel connection of the static ZIP load and dynamic IM load, load composition covers the shares of the static ZIP load and dynamic IM load at a certain system bus, and the shares of Z, I and P loads in the static ZIP load. In the former case, load composition can be adjusted by changing the demands of the ZIP load and IM load unevenly, while in the latter case, load composition can be altered by changing the coefficients (i.e., p_Z, p_I, p_P, q_Z, q_I and q_P) in (3.14) and

(3.15).

Variations of load composition can be found in different load classes (e.g., residential, commercial and industrial), different operating points and systems before and after DSM implementations. Two different load categories, namely distribution networks (DNs) and large industrial customers (ICs), have been considered in this research and corresponding load compositions are performed separately. The load compositions of large IC load class are modelled based on [141] and [142], which shows that the proportions of constant impedance, constant current and IM loads vary between 10-12%, 7-8% and 70-80%, respectively, while the remaining part is modelled as constant power load. The load composition of a particular load at a particular operating point is modelled by random sampling of proportions of different load characteristics from the corresponding range.

In the case of DN load class, the load composition is determined utilising the CREST tool (an integrated demand model based on a bottom-up activity-based structure) [143] for different buses and operating points. Two examples of daily load composition are shown in the top subplot and bottom subplot of Fig. 4.1 for a large IC load bus and a DN bus, respectively [141 - 143].

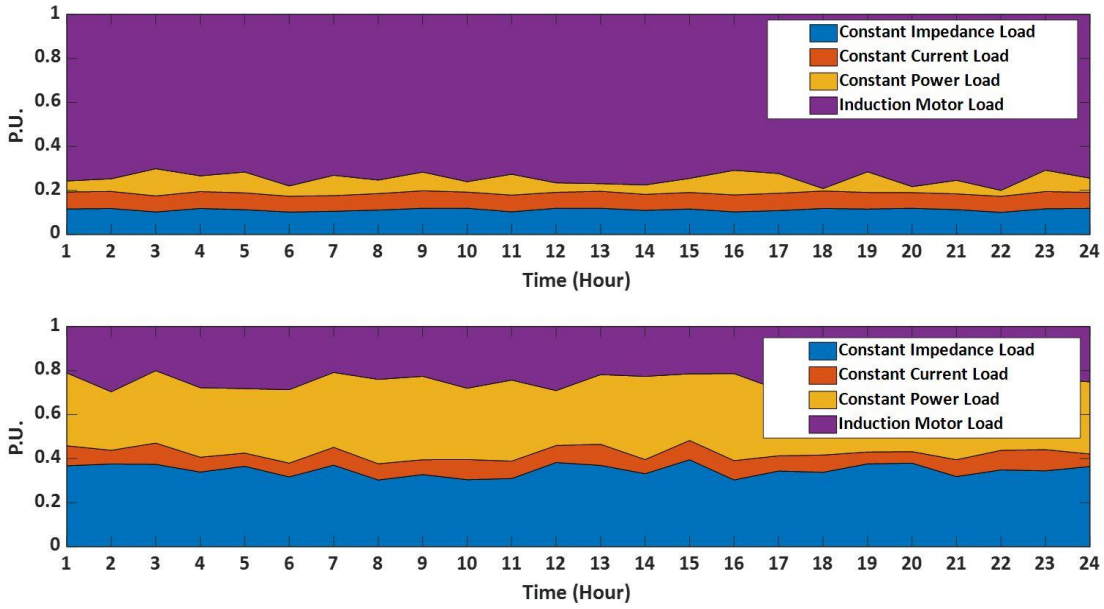

Figure 4.1 Examples of daily load composition variations of an industrial load bus (top subplot) and a distribution network load bus (bottom subplot) [141- 143]

4.3 Advanced Demand Side Management

As discussed in Section 3.2, the impact of advanced DSM on combined system stability is studied based on the modified IEEE 68-bus test system and 4TNE system because they have relatively more load and subsequently, more demand flexibility. The discussions regarding advanced DSM focus on the two above-mentioned system networks.

4.3.1 System Loading Curve

A system loading curve illustrates variations in system power consumption at different operating points throughout a period (e.g., a day, a month or a year). By indicating peak hours (hours with high power demands) and off-peak hours (hours with low power demands), a system loading curve can be used to develop and guide advanced DSM implementations.

4.3.1.1 Modified IEEE 68-bus Test System

As discussed previously, a transmission network usually delivers electrical power to DNs and large ICs that are connected at transmission level [15]; consequently, loads of the modified IEEE 68-bus test system are divided into two load categories, namely DN and large IC, based on their nominal real powers. More specifically, five loads (i.e., loads at Buses 52, 56, 59, 60 and 64) with the minimum nominal real powers are considered to be the large IC loads in the New England test system (NETS); similarly, another five loads (i.e., loads at Buses 33, 36, 40, 50, and 61) with the minimum nominal real powers are selected to be the large IC loads in the New York power system (NYPS). Regarding the high inertia areas represented by corresponding equivalent generators and equivalent loads as shown in Fig. 3.2, loads connected to Buses 41 and 42 are adopted to be the large IC loads due to their lower power consumptions. Nominal powers and detailed allocations of system load to different load categories can be found in Appendix-A.2.

A normalised daily DN loading curve and normalised daily large IC loading curve are

adopted from either real-world measurements [144] or open published reports [145], and shown as the blue solid line and red dashed line in Fig. 4.2. It should be noted here that all system loading curves in this thesis are normalised with respect to corresponding peak (maximum) values.

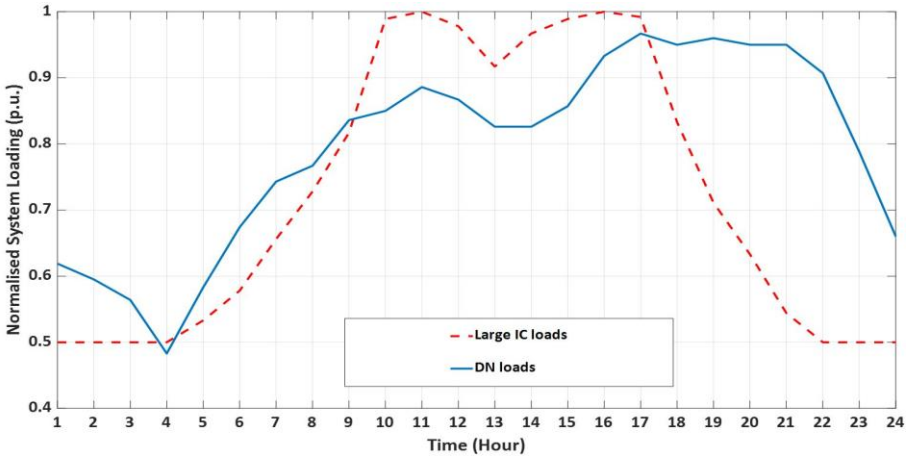

Figure 4.2 Normalised daily loading curve for DN and large IC loads [144 -145]

Considering all DN and large IC loads in the test system, the normalised daily system loading curve is shown as the blue solid line in Fig. 4.3 for the modified IEEE 68-bus test system.

4.3.1.2 The 4TNE System

In the case of the 4TNE system, because it is an equivalent representation of four interconnected transmission networks in the real world, system loading curves of individual areas are obtained from corresponding power consumption measurements published by European Network of Transmission System Operators for Electricity (ENTSO-E) [146]. The operating points, including the amounts of power consumption, are recorded on 10/01/2017 at 18:30 by corresponding TSOs; therefore, the system loading measurements of the same day (i.e., 10/01/2017) are adopted. Unfortunately, the 4TNE system model does not fully reflect the real system power consumptions; thus, scaling factors have been developed to scale down real measurements from ENTSO-E. Scaling factors for individual areas are developed following (4.1) and summarised in Table 4.1 where area numbers refer to Fig. 3.3. In (4.1), P_{TSO} and $P_{Measurement}$

represent system loading values from the TSO model and ENTSO-E measurement, respectively.

$$Scaling\ \ Factor\ \ = \frac{P_{TSO}}{P_{Measurement}} \tag{4.1}$$

The final daily loading curve adopted for the 4TNE system is the sum of the individual daily loading curves from ENTSO-E measurements multiplied by corresponding scaling factors as shown in Table 4.1. The normalised daily loading curve for the 4TEN system is shown as the red dashed line in Fig. 4.3.

Table 4.1 Measured and modelled power demand values on 10/01/2017 at 18:30 and scaling factors of each area in the 4TNE system [146]

Area (System)	Power Demand from Measurement (MW)	Power Demand from TSO Model (MW)	Scaling Factor
Area 1	653.57	480.37	0.74
Area 2	2237.40	1308.88	0.59
Area 3	7429.00	5958.06	0.80
Area 4	3079.00	1795.06	0.58

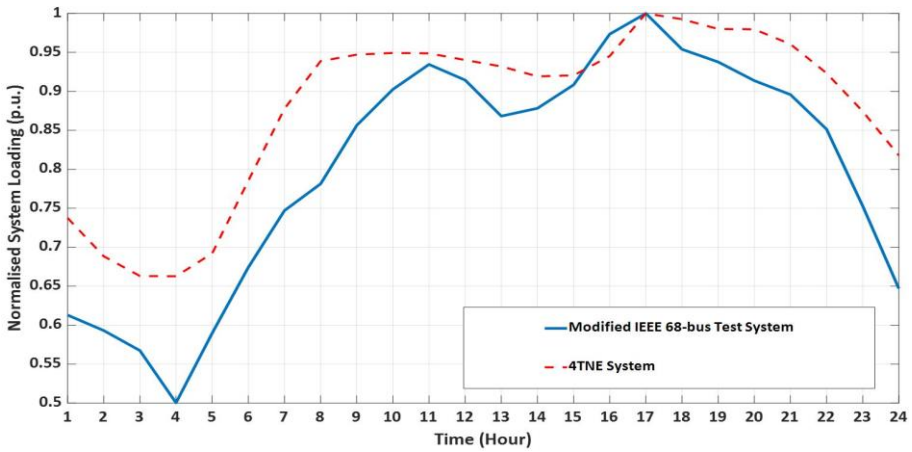

Figure 4.3 Normalised daily loading curve for the modified IEEE 68-bus test system and 4TNE system [146]

It can be seen from Fig. 4.3 that both systems (i.e., the modified IEEE 68-bus test system and 4TNE system) have their demand peaks at 17:00 and demand valleys at 04:00. Although the combined system loading curve for the modified IEEE 68-bus test system (the blue solid line in Fig. 4.3) has a more significant difference between the maximum and the minimum demands, its basic shape follows the loading curve from the ENTSO-E

measurements (the red dashed line in Fig. 4.3). Hence, the combined system loading curve for the modified IEEE 68-bus test system is verified and applicable for system studies.

4.3.2 Locations of Flexible Demands

4.3.2.1 Modified IEEE 68-bus Test System

By dividing all loads in the modified IEEE 68-bus test system into DN and large IC load categories, advanced DSM is expected to be provided through both DN and large IC buses. As 36 flexible demands (out of 95 normal system demands) connecting to 30 buses have been reported by TSOs based on near future system planning of the 4TNE system, 10 flexible demands (out of 35 normal system demands) connecting to 10 different buses have been modelled in the modified IEEE 68-bus test system such that the proportions (about 30%) of flexible buses in both systems are similar. Among these 10 flexible demands, 5 of them are selected from the DN load category and 5 of them are selected from the large IC category. The locations of these flexible demands are marked by red circles and red triangles in Fig. 4.4 for large IC and DN buses, respectively.

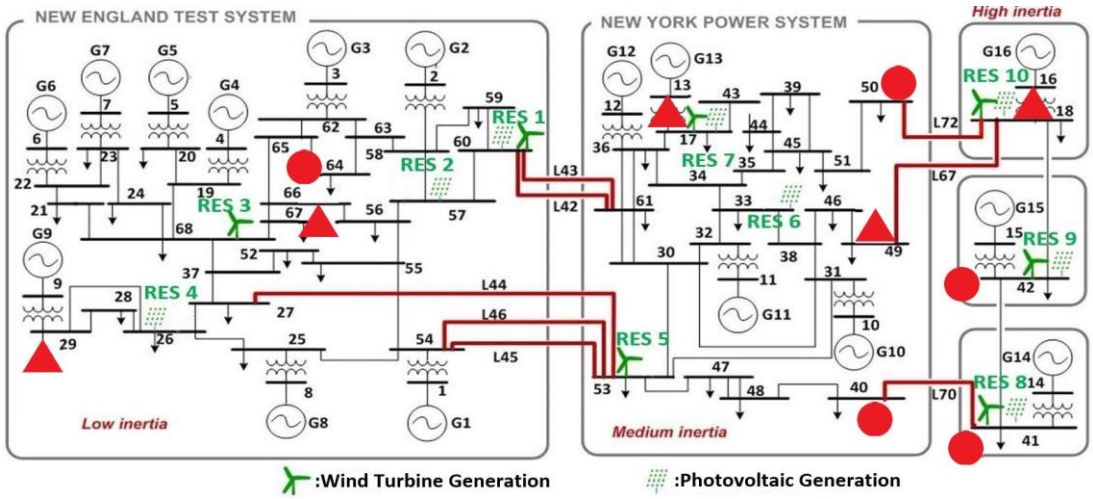

Figure 4.4 Modified IEEE 68-bus test system with emphasised locations of flexible DSM assets (red circles for large ICs and red triangles for DNs)

These locations are defined according to [96] which identified and ranked load buses based on the impact that the variation in their real power demand (a typical consequence of DSM) on system stability performance. More specifically, the five most

critical (variation in the real power demand leads to the most significant change of stability performance) IC buses (refer to Table A.13) and the five most critical DN buses (refer to Table A.13) have been selected as the locations of flexible demands based on the results reported in [96]. Load buses were ranked by adopting a Morris Screening method based on the IEEE 68-bus test system. Different selections of the locations of flexible demands can affect the impact of advanced DSM on combined system stability performance and these will be further studied and discussed in Chapter 7.

4.3.2.2 The 4TNE System

In the 4TNE system, the locations of flexible demand, marked by red circles and red triangles in Fig. 4.5 for large IC and DN buses, respectively, are provided by corresponding TSOs, and as mentioned previously, there are 36 flexible demands in the 4TNE system connecting to 30 buses.

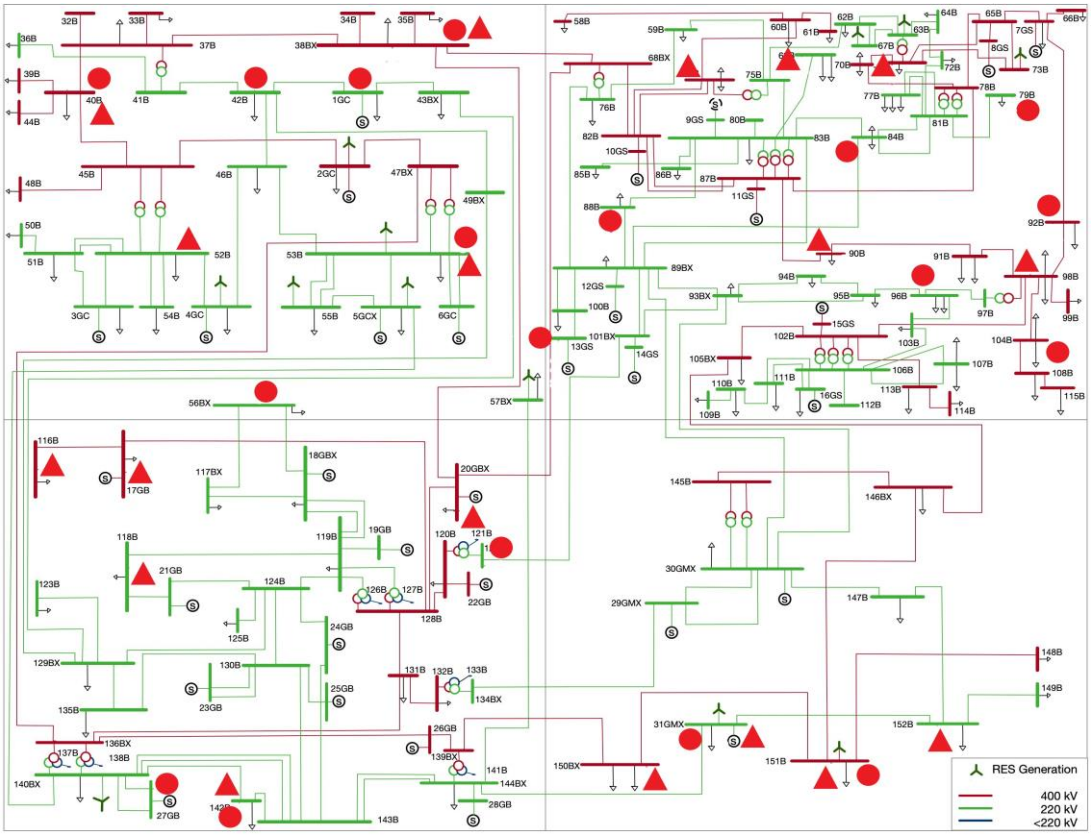

Figure 4.5 4TNE system with emphasised locations of flexible DSM assets (red circles for large ICs and red triangles for DNs)

4.3.3 Capacity and Modelling of Flexible Demands

In both the modified IEEE 68-bus test system and 4TNE system, due to the lack of information indicating the installed capacity of each flexible demand, 'flexible demands' refers to the controllable part of the flexible demands only in this thesis, although in many surveys and literature the stated value of flexible demand includes both, controllable and un-controllable parts. In other words, the capacity of flexible demand equals the amount of power curtailed or reconnected in response to advanced DSM signals in this study. Considering that flexible demands at transmission level may consist of multiple processes (i.e., actions or steps to achieve the desired objectives by consuming electricity), flexible demands are modelled based on flexible DSM processes exhibiting various load characteristics (e.g., constant power and IM) in this thesis.

4.3.3.1 Modified IEEE 68-bus Test System

Six industrial manufacturing processes and six residential and commercial processes are considered to be flexible and modelled by corresponding dominating load characteristics (i.e., the characteristics of loads that consumes the largest amount of electrical power) in the modified IEEE 68-bus test system; for instance, heating devices are modelled as constant impedance load and freezers are modelled as IM load [135, 147]. Furthermore, it is assumed that each large IC load bus consists of all six flexible industrial manufacturing processes and each DN load bus contains all six flexible residential and commercial processes to reflect complex load compositions at transmission level.

In order to obtain the total capacity of the advanced DSM, flexibilities of large IC and DN load buses are calculated based on the utilisation rate (in hours) and flexibility (%) of modelled DSM processes following (4.2) [148, 149]. Where D (%) is the flexibility, defined as the proportion of controllable demand with respect to the total demand, for either large IC load bus or DN load bus, n is the total number of DSM processes and it is equal to 6 in this case, U_i (h) is the utilisation rate representing how much time DSM process i is active throughout a year and F_i (%) is the flexibility of DSM process i which has been defined as identical to D. All DSM processes with corresponding

utilisation rates and flexibility values are summarised in Table 4.2.

$$D = \frac{\sum_{i=1}^{i=n}\left(\frac{U_i}{8760} \times F_i\right)}{n} \times 100\% \qquad (4.2)$$

Based on (4.2) and parameter values summarised in Table 4.2, the flexibilities calculated for large IC and DN load buses are about 55% and 20%, respectively. These flexibility values are multiplied by nominal powers (both real and reactive powers) of 10 selected locations (buses) of DSM and the final capacity of advanced DSM in the modified IEEE 68-bus test system is 3125.8 MW (1278.2 MW from large IC loads and 1847.6 MW from DN loads), which is about 18% in total of the system peak demand. Theoretically, this means in total that 3125.8 MW loads can be manipulated by advanced DSM simultaneously.

Table 4.2 Flexible DSM processes (large IC and DN) in the modified IEEE 68-bus test system with corresponding DSM capacity [148 - 149]

Flexible DSM Processes – Large IC				
DSM Process	**Capacity (MW)**	**Utilisation Rate U_i (h)**	**Flexibility F_i (%)**	**Load Characteristic**
Electrolytic Primary Aluminium	78.62	7065	25	Constant Impedance
Chloralkali Process (Amalgan)	229.63	7370	70	Constant Impedance
Chloralkali Process (Membrane)	196.82	7370	60	Constant Impedance
Electric Arc Furnace	292.43	6570	100	Constant Impedance
Wood Pulp Production	249.26	5600	100	Constant Impedance
Cement Mill	231.45	5200	100	IM
Flexible DSM Processes – DN				
DSM Process	**Capacity (MW)**	**Utilisation Rate U_i (h)**	**Flexibility F_i (%)**	**Load Characteristic**
Night Storage Heater	231.34	1200	100	Constant Impedance
Heat Pump	347.01	1800	100	Constant Impedance
Warm Water Heating	74.7	1550	25	Constant Impedance
Air Supply	424.12	4400	50	IM
Cold Storage	696.69	5090	71	IM
Air Conditioning	73.74	510	75	IM

The capacity for DSM process i is then obtained by multiplying corresponding weighting (w_i) calculated as (4.3), where all variables follow the same definition as (4.2), by total capacity of either large IC or DN flexible DSM processes.

$$w_i = \frac{\frac{U_i}{8760} \times F_i}{\sum_{i=1}^{i=n} \left(\frac{U_i}{8760} \times F_i\right)} \tag{4.3}$$

For instance, Table 4.2 shows that the electric arc furnace has a utilisation rate of 6570 h and a flexibility of 100%, hence, its weighting (w) is:

$$w = \frac{\frac{6570}{8760} \times 100\%}{3.28} = 0.2288 \tag{4.4}$$

where 3.28 is the sum of all 6 large IC flexible DSM processes and it is obtained from (4.5):

$$\frac{7065 \times 25\% + 7370 \times 70\% + 7370 \times 60\% + 6570 + 5600 + 5200}{8760} = 3.28 \tag{4.5}$$

And the capacity of electric arc furnace is:

$$c = 0.2288 \times 1278.2 = 292.43 \ \ MW \tag{4.6}$$

The capacities and dominating load characteristics (i.e., the characteristics of loads that consumes the largest amount of electrical power) of individual DSM processes are summarised in Table 4.2. It is worth noting here that DSM processes are modelled as the corresponding dominating load characteristic only if the composite load model is used to model system demands (all 35 loads in the modified IEEE 68-bus test system), in which case DSM manipulates not only load consumption patterns, but also load compositions.

The practicability of advanced DSM to change load consumption patterns and load compositions is investigated by Example 5, as shown below:

Example 5: Assume a load bus has a nominal real power demand of 1000 MW, where 500 MW demand is modelled as the dynamic IM, 200 MW demand is modelled as the constant impedance load, 200 MW demand is modelled as the constant current load and 100 MW demand is modelled as the constant power load. It has been reported that there are 100 MW flexible dynamic IM loads and 100 MW flexible constant impedance loads at this bus. Therefore, the real power consumption of the static part of the load before the implementation of DSM can be represented by (4.7).

$$P = 500\left[\frac{200}{500}\times\left(\frac{U}{U_0}\right)^2 + \frac{200}{500}\times\left(\frac{U}{U_0}\right) + \frac{100}{500}\right] \quad (4.7)$$

Which can be further simplified as (4.8):

$$P = 500\left[0.4\left(\frac{U}{U_0}\right)^2 + 0.4\left(\frac{U}{U_0}\right) + 0.2\right] \quad (4.8)$$

If all flexible demands are curtailed in a DSM program, the remaining dynamic IM load is 400 MW (500-100=400), and the real power consumption of the remaining ZIP load can be represented by (4.9):

$$P = 400\left[\frac{100}{400}\times\left(\frac{U}{U_0}\right)^2 + \frac{200}{400}\times\left(\frac{U}{U_0}\right) + \frac{100}{400}\right] \quad (4.9)$$

Which can be further simplified as (4.10):

$$P = 400\left[0.25\left(\frac{U}{U_0}\right)^2 + 0.5\times\left(\frac{U}{U_0}\right) + 0.25\right] \quad (4.10)$$

It can be noted from (4.8) and (4.10) that the DSM program changes not only load consumption patterns (from 1000 MW in total to 800 MW in total), but also load compositions (i.e., altered coefficients for constant impedance, constant current and constant power loads).

4.3.3.2 The 4TNE System

Like the modified IEEE 68-bus test system, advanced DSM in the 4TNE system is also modelled based on individual DSM processes. However, the capacities (i.e., amounts of power that can be manipulated by advanced DSM) and locations of individual industrial DSM process are identified and provided by TSOs, therefore, this subsection focuses on estimating the flexibility of DN loads and capacity of DN flexible processes.

Firstly, DN loads in the 4TNE system are divided into four load classes, namely residential (33%), commercial (26%), small industrial (21%) and other (20%), with corresponding proportion given in the brackets [150]. Because DSM from industrial load classes has

been represented by large IC DSM processes, the flexibility of small industrial load class has been neglected due to its relatively lower flexibility and it is considered in this thesis that only residential and commercial load classes are flexible in DN loads.

Based on the survey reported in [151], residential electricity consumption includes space heating (21%), water heating (7%) and lighting and appliances (72%), which can be further divided into electronics (29%), wet appliances (25%), cold appliances (11%), lighting (14%), cooking (16%) and computing (5%) [152]. Among all load components, water heating, space heating and wet and cold appliances are adopted as flexible DSM processes [153]. Likewise, the commercial load class is further divided into 12 load components shown in Fig. 4.6 with corresponding proportions [154]. Commercial refrigeration, ventilation and space and water heating processes are considered to be flexible [153].

Then, the flexibility of DN loads is computed as about 28.3% by adding all shares of flexible DSM process, and the capacity of DSM from DN load category is 940 MW, which is about 8.87% of the system peak demand. Finally, the capacities of individual DSM processes are again obtained by multiplying the corresponding weightings by the total capacity of DN flexible processes (i.e., 940 MW).

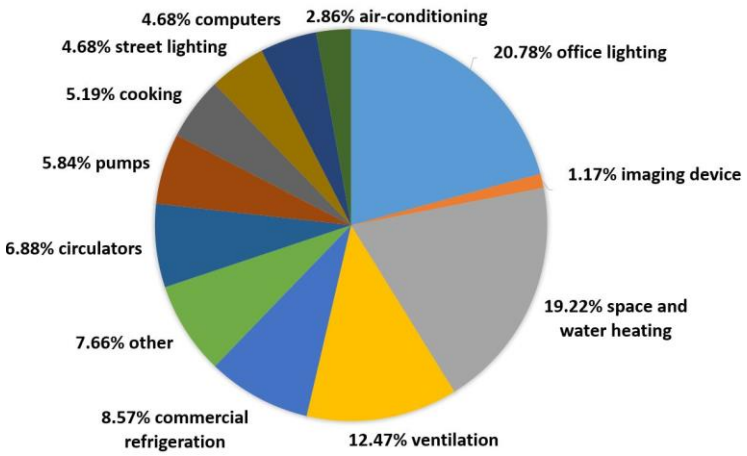

Figure 4.6 Proportions of electricity consumption in the commercial load class [154]

For instance, the weighting of residential wet appliances is calculated as (4.11) where 0.33 is the proportion of residential load with respect to the total demand, 0.72 is the proportion of lighting and appliances with respect to residential demand, 0.25 is the proportion of wet appliances with respect to residential lighting and appliances and

0.283 is the total flexibility of DN loads (i.e., 28.3%). The total capacity of residential wet appliances is 0.2×940 = 188 MW.

$$w = \frac{0.33 \times 0.72 \times 0.25}{0.283} = 0.2 \tag{4.11}$$

All DSM processes (including large IC and DN load categories) and corresponding capacities adopted in the 4TNE system are summarised in Table 4.3. The total capacity of flexible DSM processes (including both large IC and DN processes) in the 4TNE system is 1647.4 MW (707.4 MW from large IC processes, which is about 6.63% of the system peak demand and 940 MW from DN processes, which is about 8.87% of the system peak demand), which is about 15.5% of the system peak demand. As no case studies have been developed based on the 4TNE system with the composite load model, the dominating load characteristics are not discussed in this subsection. Moreover, each DN flexible demand is assumed to contain all six DN DSM processes, while each large IC flexible demand represents a particular DSM process.

Table 4.3 Flexible DSM processes (large IC and DN) in the 4TNE system with corresponding DSM capacity

Flexible DSM Processes – Large IC			**Flexible DSM Processes – DN**		
DSM Process	**Capacity (MW)**	**Flexibility (%)**	**DSM Process**	**Capacity (MW)**	**Flexibility (%)**
Chemical	18.06	100	Residential Space/Water Heating	310.2	100
Steel Manufacturing	72.38	100	Wet Appliance	188	100
Cement Manufacturing	30	100	Cold Appliance	94	100
Coal Mining	37	100	Ventilation	103.4	100
Paper Mill	9	100	Refrigeration	75.2	100
Aluminium Manufacturing	16.91	100	Commercial Space/Water Heating	169.2	100
Hydro Pump Storage	524	100			

4.3.4 Demand Payback Effect

Power system customers who provided DSM services by curtailing their power

consumptions may require power compensations, which are also referred to as demand payback effects, before or after the curtailment to obtain the same or a similar level of convenience and comfortability. Demand payback effect is one of the most important components in system financial and operational analyses [155, 156]. Implementation of DSM with the consideration of demand payback effect is generally modelled as load shifting (i.e., removing electricity demand from one period to another period), while DSM programs without requiring demand payback can be modelled as load curtailments.

Although demand payback effect plays an essential role in DSM planning and implementation, it is complex and difficult to be modelled and forecasted as customers may exhibit different requirements for demand payback. The characteristics of demand payback are usually modelled based on five parameters (i.e., T, t_{flex}, t_{pb}, $flex_{\%}$ and $pb_{\%}$), whose definitions are summarised in Table 4.4 [156]. As discussed previously, by assuming that all DSM processes are fully controllable, parameter $flex_{\%}$ is 100% for all processes. Furthermore, it is assumed that the percentage of payback ($pb_{\%}$) is also equal to 100%, such that all curtailed energy is compensated for customers. Therefore, modelling of demand payback effect is based on maximum times of response (T), flexibility hour (t_{flex}) and payback hour (t_{pb}) in this thesis.

Table 4.4 Definitions of demand payback modelling parameters [156]

Parameters	Definitions
Maximum Times of Response ($\boldsymbol{T}$)	Maximum times that the DSM service can be called per day.
Flexibility Hour ($\boldsymbol{t_{flex}}$)	Time interval when the flexible demand is providing DSM.
Payback Hour ($\boldsymbol{t_{pb}}$)	Time interval when the system operators must provide power consumptions to customers who curtailed their demand.
Flexibility ($\boldsymbol{flex_{\%}}$)	Percentage of load that can be manipulated by DSM.
Percentage of payback ($\boldsymbol{pb_{\%}}$)	Percentage of curtailed load that needs to be compensated.

The DSM programs and modelling parameters of demand payback effect are summarised in Table 4.5 and Table 4.6 for flexible DSM processes in the modified IEEE 68-bus test system and 4TNE system, respectively. It is worth noting here that some DN DSM processes (e.g., night storage heater) that last for very long periods (e.g., 12 hours)

in [153] have been divided into more segments (i.e., maximum times of response per day) with reduced flexibility hour for each segment in order to represent more realistic behaviours of flexible demands.

Table 4.5 DSM programs and modelling parameters of demand payback effect in the modified IEEE 68-bus test system [153]

DSM Process	DSM Program	Maximum Times of Response per Day	Flexibility Hour t_{flex} (h)	Payback Hour t_{pb} (h)
Electrolytic Primary Aluminium	Load Curtailment	1	4	N/A
Chloralkali Process (Amalgan)	Load Curtailment	1	4	N/A
Chloralkali Process (Membrane)	Load Curtailment	1	4	N/A
Electric Arc Furnace	Load Curtailment	1	4	N/A
Wood Pulp Production	Load Shifting	1	3	24
Cement Mill	Load Shifting	1	3	24
Night Storage Heater	Load Shifting	3	4	4
Heat Pump	Load Shifting	3	2	2
Warm Water Heating	Load Shifting	3	4	4
Air Supply	Load Shifting	3	1	2
Cold Storage	Load Shifting	3	2	2
Air Conditioning	Load Shifting	3	1	2

Table 4.6 DSM programs and modelling parameters of demand payback effect in the 4TNE system [153]

DSM Process	DSM Program	Maximum Times of Response per Day	Flexibility Hour t_{flex} (h)	Payback Hour t_{pb} (h)
Chemical	Load Curtailment	1	4	N/A
Steel Manufacturing	Load Curtailment	1	4	N/A
Cement Manufacturing	Load Shifting	1	3	24
Coal Mining	Load Shifting	1	3	24
Paper Mill	Load Shifting	1	3	24
Aluminium Manufacturing	Load Curtailment	1	4	N/A
Hydro Pump Storage	Load Shifting	1	24	24
Residential Space/Water Heating	Load Shifting	3	4	4
Wet Appliance	Load Shifting	3	6	24
Cold Appliance	Load Shifting	3	1	2
Ventilation	Load Shifting	3	1	2
Refrigeration	Load Shifting	3	2	2
Commercial Space/Water Heating	Load Shifting	3	4	4

4.3.5 Implementations of Advanced Demand Side Management

Implementations of advanced DSM in the modified IEEE 68-bus test system and 4TNE system follow the DSM capacities defined in Table 4.2 and Table 4.3, respectively, and the demand payback effects constrained by the parameters in Table 4.5 and Table 4.6, respectively. The aim of the advanced DSM is to obtain a flatter daily loading curve without creating a new demand peak and demand valley. Moreover, it is worth mentioning here that this research focuses on investigating the overall impact of advanced DSM on combined system stability performance; how to motivate customers to provide DSM is beyond the scope of this thesis. DSM implementations are illustrated in Fig. 4.7 and Fig. 4.8 for the modified IEEE 68-bus test system and 4TNE system, respectively. Load curtailments are represented by green blocks and load reconnections, caused by demand payback effects, are represented by red shadowed blocks.

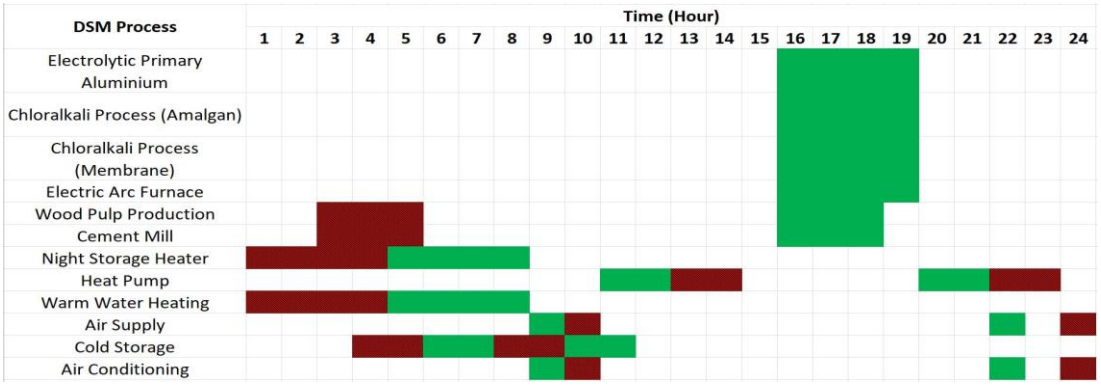

Figure 4.7 Implementations of DSM processes in the IEEE 68-bus test system

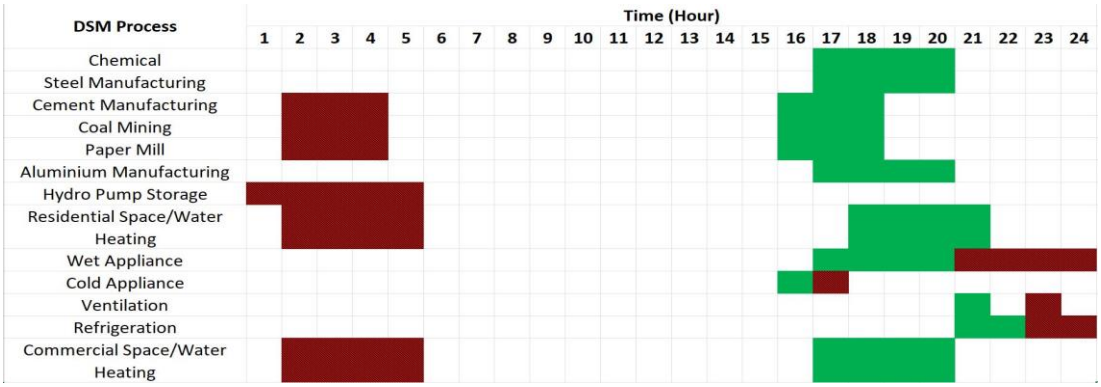

Figure 4.8 Implementations of DSM processes in the 4TNE system

It can be seen from Fig. 4.7 and Fig. 4.8 that system loads have been manipulated at 23/24 hours and 14/24 hours throughout the day in the modified IEEE 68-bus test system and 4TNE system, respectively. The daily loading curves of the system before and after advanced DSM implementations are illustrated as the blue solid line and the red dotted line, respectively, in the subplot (a) of Fig. 4.9 for the modified IEEE 68-bus test system and subplot (b) of Fig. 4.9 for the 4TNE system. Furthermore, the distributions of system loading before and after the advanced DSM implementation are illustrated as load duration curves in subplots (a) and (b) of Fig. 4.10 for the modified IEEE 68-bus test system and 4TNE system, respectively.

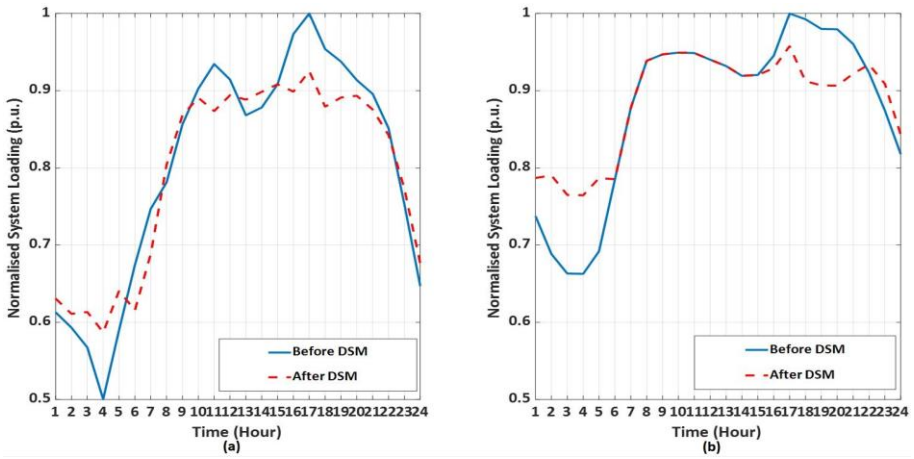

Figure 4.9 Normalised daily loading curve for the modified IEEE 68-bus test system (a) and the 4TNE system (b) before and after advanced DSM implementation

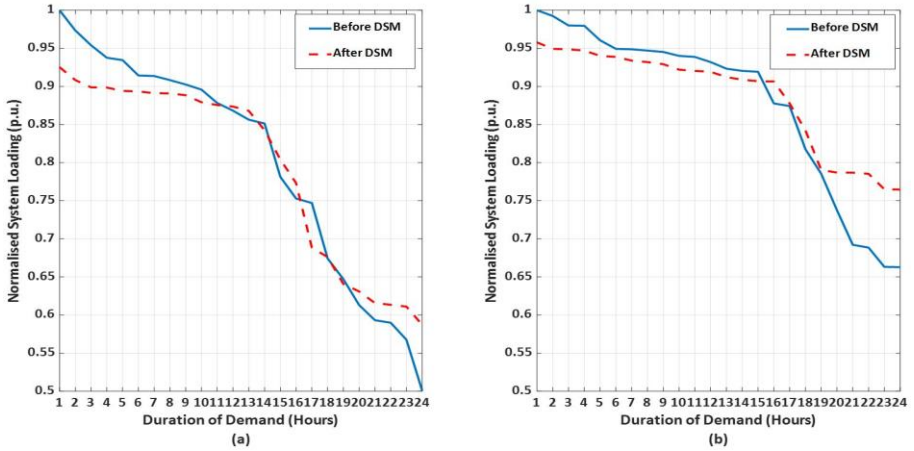

Figure 4.10 Normalised load duration curves for the modified IEEE 68-bus test system (a) and the 4TNE system (b) before and after advanced DSM implementation

According to Fig. 4.9 and Fig. 4.10, implementations of advanced DSM narrow the distributions of normalised system loading in both cases. Focusing on the subplot (a) of

Fig. 4.10, advanced DSM increases the minimum system loading value and decreases the maximum system loading value in the modified IEEE 68-bus test system. In the case of the 4TNE system (subplot (b) of Fig. 4.10), advanced DSM also reduces the maximum system loading value. The minimum system loading value has been increased significantly by advanced DSM.

4.4 Summary

The modelling of load compositions for different load categories (i.e., large IC and DN) has been discussed based on the composite load model (i.e., a parallel connection of the static ZIP load and dynamic IM) adopted in this thesis. The modelling of advanced DSM has also been introduced and discussed in this chapter. As the availability of DSM services and the flexibility of system demands may change significantly in different power systems, two advanced DSM scenarios have been developed based on the modified IEEE 68-bus test system and 4TNE system. In both advanced DSM scenarios, implementations of advanced DSM are developed based on several flexible DSM processes from large IC and DN load categories. Flexibility, location and demand payback effect of each DSM process are adopted and modelled according to either open published research or real-world information provided by TSOs. Considering that advanced DSM can change load consumption patterns and load composition simultaneously, DSM processes are modelled using the corresponding dominating load characteristics in the case of the modified IEEE 68-bus test system when the composite load model is adopted. The proposed advanced DSM scenarios are proved to be able to narrow the distributions of system loading and lead to flatter loading curves without creating a new demand peak and demand valley.

Even though the advanced DSM is modelled comprehensively in this thesis to assess the impact of advanced DSM on combined system angular and frequency stability, it is suitable for other large-scale power system studies, such as assessing the impacts of DSM on steady state system congestions and assessing the impact of DSM on operations of electricity market. The comprehensive modelling of DSM for the purpose of system dynamic studies is the second original contributions of this thesis.

5 Probabilistic Assessment of Power System Stability

5.1 Introduction

MCS-based probabilistic analysis method is adopted in this research to assess system stability performances at each operating point. This chapter first introduces system operational uncertainties, which are considered as input variables for MCS-based probabilistic stability assessments. It is followed by the introduction and discussion of the Monte Carlo stopping rule to determine the number of repeatable simulations (i.e., iterations) performed to guarantee the accuracy of the results. Finally, the MCS-based probabilistic stability assessments and all steps involved are discussed in this chapter.

5.2 System Operational Uncertainties

Due to the stochastic and intermittent natures of renewable primary energy source (e.g., wind and solar irradiation), RES-based generation is one of the main sources of high variability and uncertainty in modern and future power systems. As only wind turbines and PV arrays are modelled in system models under study, corresponding power outputs modelled by widely adopted probability distributions are sampled randomly for MCS-based probabilistic stability assessments.

Although a lot of probability distributions, for instance, generalised extreme value (GEV)-Lognormal [157], Extended Generalised Lindley [158] and Multi-Peak Gaussian [159] have been adopted and recommended to capture and model the uncertainties of wind speed, Weibull distribution [160], whose probability density function (PDF) is given as (5.1), is adopted in this research as it is probably the widest adopted probability distribution to capture uncertain variations of wind speed [161 - 163]. As can be seen from (5.1), Weibull distribution is a continuous probability distribution of variable x characterised by two parameters, shape parameter k and scale parameter α.

$$f_w = f(x) = \begin{cases} \frac{k}{\alpha}\left(\frac{x}{\alpha}\right)^{k-1} e^{-\left(\frac{x}{\alpha}\right)^k}, & x \geq 0 \\ 0, & x < 0 \end{cases} \tag{5.1}$$

Furthermore, the short-term (i.e., from a few minutes to several hours) forecast error of wind speed is considered and modelled following a normal distribution (also known as Gaussian distribution) whose PDF is shown as (5.2) [164 - 166]. A variable x is following a normal distribution if its mean value μ and standard deviation σ satisfy (5.2). In this thesis, wind speed is firstly sampled following a Weibull distribution, then, normal distributions are introduced for each sampled wind speed to evaluate the forecast error. Finally, forecasted wind speeds are transferred to wind turbine power outputs according to the speed-power curve of Vestas-V80 as shown in Fig. 3.5 (a).

$$f_n = \ f(x) = \frac{1}{\sigma\sqrt{2\pi}} e^{-\frac{(x-\mu)^2}{2\sigma^2}} \tag{5.2}$$

Similarly, multiple probability distributions, such as normal distribution [167] and Beta distribution [168], have been utilised to model uncertain solar irradiation (power output of PV array). Solar irradiation and subsequently, normalised power output of PV array are assumed to follow a Beta distribution with PDF defined as (5.3) in this thesis. In (5.3), x is the normalised PV output value with respect to the maximum output value, $\Gamma(\cdot)$ is the gamma function as defined in (5.4), α and β are shape parameters. By assuming $B(\alpha, \beta) = \frac{\Gamma(\alpha)\Gamma(\beta)}{\Gamma(\alpha+\beta)}$, equation (5.3) can be simplified as (5.5).

$$f_b = \ f(x) = \frac{\Gamma(\alpha)\Gamma(\beta)}{\Gamma(\alpha+\beta)} (x)^{\alpha-1}(1-x)^{\beta-1} \tag{5.3}$$

$$\Gamma(\alpha) = \int_0^\infty u^{\alpha-1} e^{-u} du \tag{5.4}$$

$$f_b = \ f(x) = B(\alpha, \beta)(x)^{\alpha-1}(1-x)^{\beta-1} \tag{5.5}$$

Normalised power output of PV array, which follows the Beta distribution, is considered as a scaling factor, and multiplied by the maximum power output of different operating points (as shown in Fig. 3.5 (b)) to derive the actual power output of PV arrays.

In addition to the variability and uncertainty contributed by RES-based generation, uncertainty of system loading also leads to significant impacts on system generation adequacy and subsequently, system dynamic response [169]. As many existing studies [169 - 171] adopted the normal distribution to model uncertainty of system loading, in this thesis, system loadings at a particular operating point are defined to follow a normal distribution with a specified standard deviation and mean values derived from system loading curves as shown in Fig. 4.3. Modelling of system loading uncertainty generates extra scaling factors, which are multiplied by the normalised system loading value (Fig. 4.3) to obtain the final scaling factors of system loading at a particular operating point. The real power consumption of each demand is equal to the product of the final scaling factor and the nominal demand value.

Power transmission and distribution systems, which connect power generation and demand, may also exhibit operational variability and uncertainty. For instance, variations of wind speed and ambient temperature affect the ratings of transmission lines, which further affects system stability and reliability performances [172]. Modelling of operational uncertainty in the power transmission sector focuses on fault characteristics (e.g., fault duration) in this thesis. More specifically, assuming faults (three phase faults only as they typically lead to the most challenging stability issues) can only happen on transmission lines (disconnections of synchronous generators are considered in frequency stability assessments), faulted lines (i.e., the transmission line where the fault occurred) are selected randomly following a uniform distribution, whose PDF is given as (5.6) [173]. A uniform distribution is used to model the fault location, which means that the fault may happen with equal probability at any line of the test system and at any point along the line. In real systems though the probability of more faults happening

along longer transmission lines could be higher, the probability of faults may also depend on the geographical location of the line which was not available for the test system considered [174]. Finally, a normal distribution with a mean value of 5 cycles (100 ms for power systems rated at 50 Hz) and a standard deviation of 0.67 cycles is introduced to model the uncertainty of fault duration (i.e., the time period between fault occurrence and fault clearance) [175].

$$f_u = f(x) = \begin{cases} \dfrac{1}{b-a}, & a \le x \le b \\ 0, & x < a \ \ or \ \ x > b \end{cases} \tag{5.6}$$

All system operational uncertainties considered in this thesis with corresponding probability distributions and modelling parameters are summarised in Table 5.1.

Table 5.1 System operational uncertainties with corresponding probability distribution and modelling parameters

Operational Uncertainty	**Probability Distribution**	**Modelling Parameter**	**Reference**
Wind Speed	Weibull Distribution	k=2.2, α=11.1	[176]
Short-term Wind Speed Error	Normal Distribution	σ=3.33% (3σ=10% of μ)	N/A
Solar Irradiation (normalised PV array output)	Beta Distribution	α=13.7, β=1.3	[177]
Demand Loading	Normal Distribution	σ=3.33% (3σ=10% of μ)	[174]
Faulted Line	Uniform Distribution	a=0, b=Number of Lines	[174]
Fault Location	Uniform Distribution	a=0, b=100%	[174]
Fault Duration	Normal Distribution	μ=5 cycles, σ=0.67 cycles	[175]

5.3 Monte Carlo Stopping Rule

By performing repeatable deterministic analyses based on random sampled input variables, the accuracy and computational cost of MCS-based probabilistic stability assessments rise with the increase in the number of repeatable deterministic analyses (i.e., iterations). In order to properly balance the accuracy of the results and the computational cost, the number of iterations for MCS is usually determined by the Monte Carlo stopping rule [78, 178, 179] as given in (5.7), where E is the sample mean error, δ is the desired confidence level, Φ^{-1}, $\sigma^2(X)$ and $\bar{X}$ represent an inverse

Gaussian conditional probability distribution, variance and mean value of the input sample X with a size of N. According to (5.7), the Monte Carlo stopping rule calculates the mean error of each result sample and compares it with the desired error [178]; the MCS can be stopped when the error E is lower than the desired error.

$$E = \left[\left\{\Phi^{-1}\left(1 - {}^{\delta}/_{2}\right) \times \sqrt{{}^{\sigma^2(X)}/_{N}}/\bar{X}\right\}\right] \tag{5.7}$$

As the Monte Carlo stopping rule concentrates on a particular result sample, different numbers of iterations are required for MCS-based probabilistic stability assessments performed for different system models, different operating points and different aspects of power system stability. Based on the previous research on the modified IEEE 68-bus test system discussed in [78] and [180], transient stability assessment evaluated by the TSI usually requires many more iterations to achieve the same confidence level than all other stability indices considered in this thesis (i.e., damping of the most critical electromechanical mode, frequency nadir and RoCoF) due to the large magnitude and large variation range of TSI. Therefore, the numbers of iterations for all system models under study are determined based on the transient stability assessments (i.e., TSI) performed at both demand valley (i.e., Hour 4) and demand peak (i.e., Hour 17). The relationship between mean error E and number of iterations N are illustrated in Fig. 5.1 to Fig. 5.3 for the modified IEEE 9-bus test system, modified IEEE 68-bus test system and 4TNE system, respectively. Two confidence levels (99% confidence level illustrated as blue solid lines in Fig. 5.1 to Fig. 5.3 and 95% confidence level illustrated as red dashed lines in Fig. 5.1 to Fig. 5.3) and a sample mean error of 1% (E=0.01) have been adopted in this thesis to determine iteration numbers of MCS-based probabilistic stability assessments.

According to Fig. 5.1, the number of iterations based on the modified IEEE 9-bus test system is set to be 200 because sample mean errors of both demand valley (subplot (a) of Fig. 5.1) and demand peak (subplot (b) of Fig. 5.1) drop below 0.01 before 200 iterations. Likewise, the numbers of iterations are defined to be 500 and 200 for the modified IEEE 68-bus test system and 4TNE system, respectively.

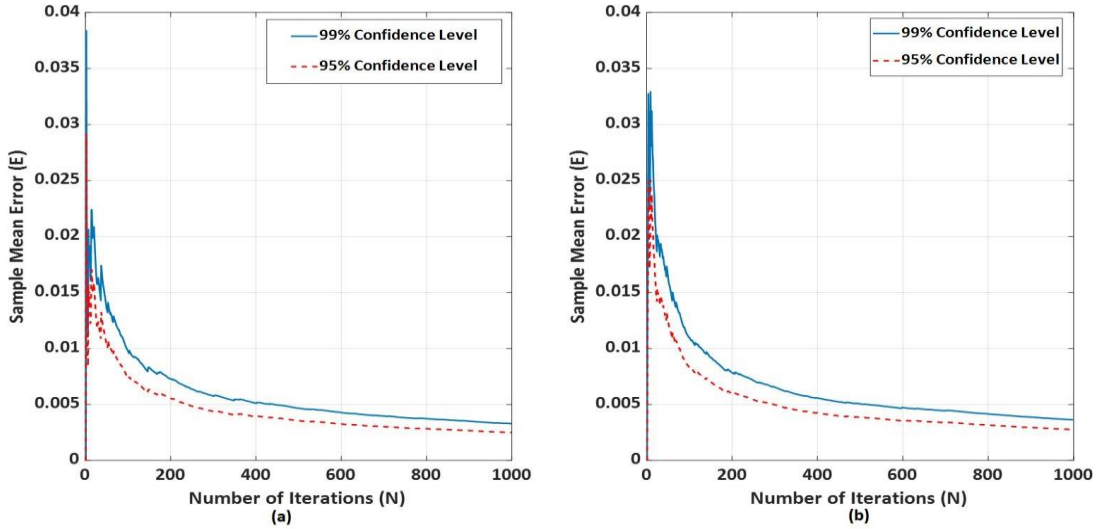

Figure 5.1 Error-vs-number of iteration curves of TSI at demand valley (a) and demand peak (b) of the IEEE 9-bus test system

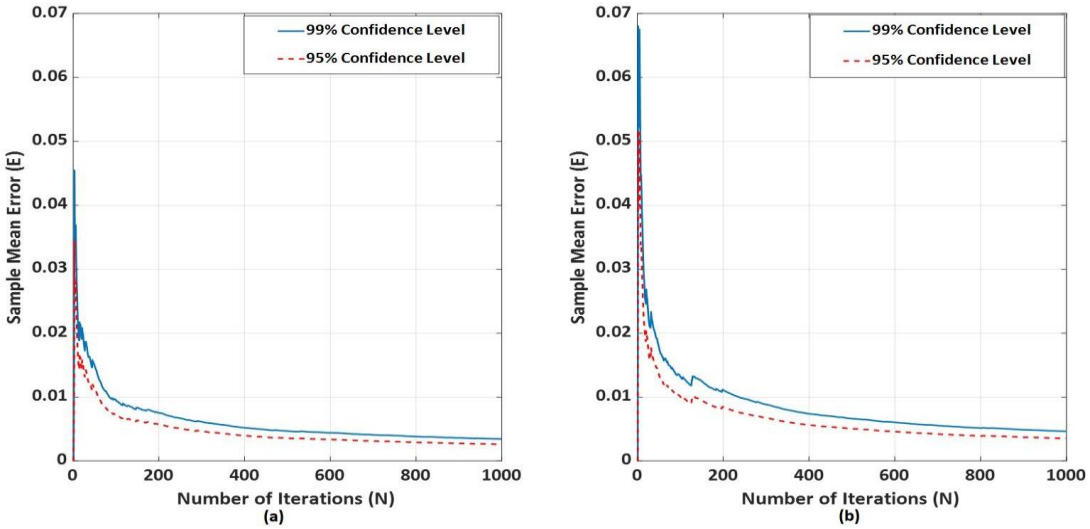

Figure 5.2 Error-vs-number of iteration curves of TSI at demand valley (a) and demand peak (b) of the IEEE 68-bus test system

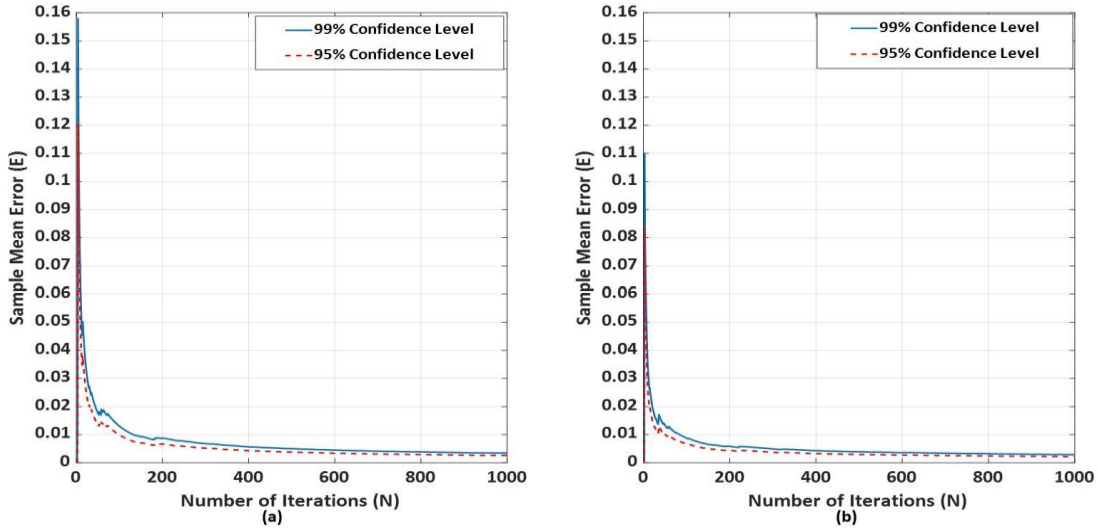

Figure 5.3 Error-vs-number of iteration curves of TSI at demand valley (a) and demand peak (b) of the 4TNE system

5.4 Monte Carlo Simulation based Probabilistic System Stability Assessment

An overview of the MCS-based probabilistic stability assessment with N iterations and O operating points adopted in this thesis is shown as a flow chart in Fig. 5.4. Step numbers are given at the right bottom corner of each block, and all steps are discussed in detail as follows:

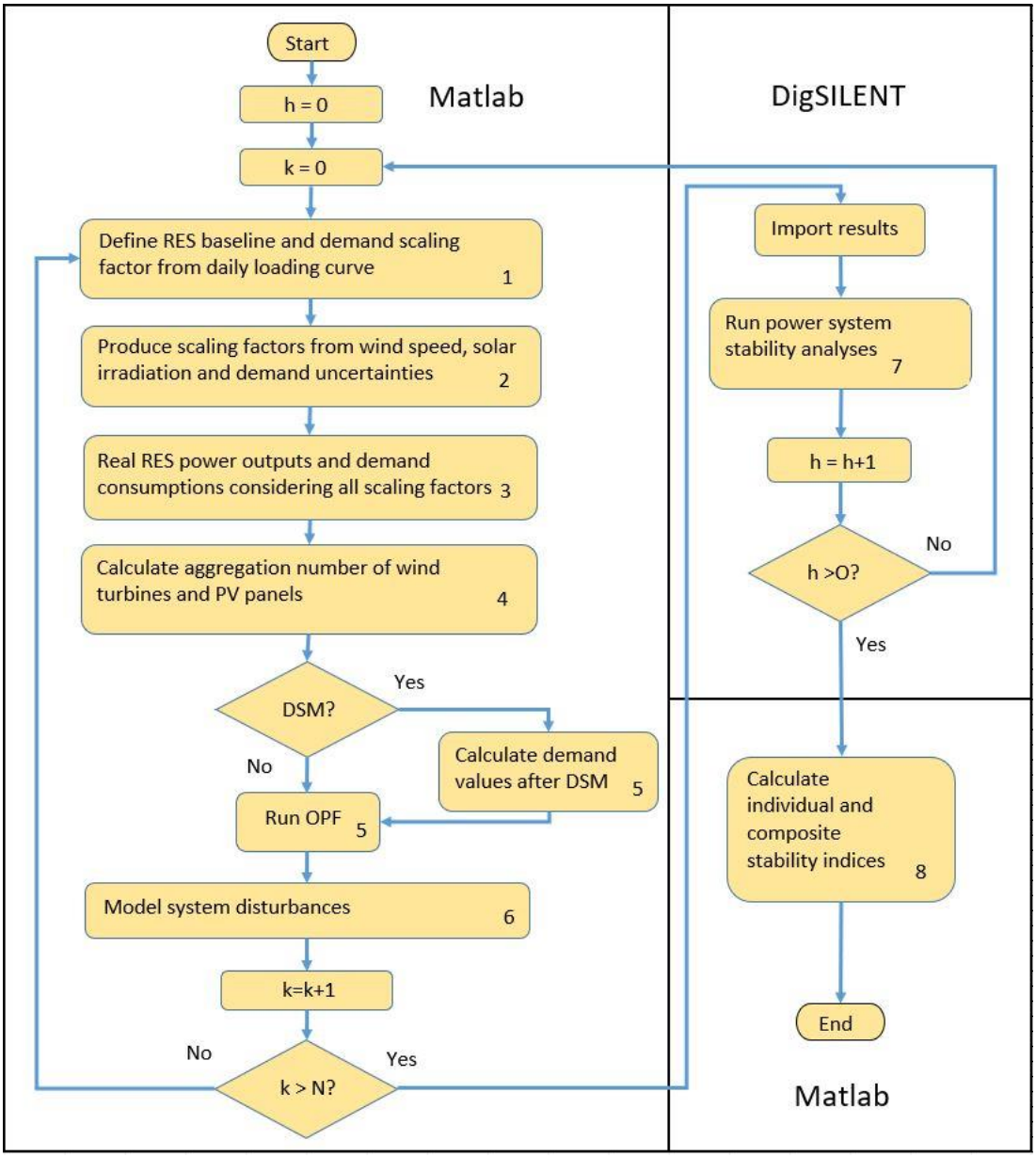

Figure 5.4 Flow chart of MCS-based probabilistic stability assessments

Step 1: In the first step of the MCS-based probabilistic stability assessment, nominal power output of RES-based generation is determined based on the pre-defined RES baseline calculated following (3.9). In the meantime, a demand scaling factor is derived from corresponding normalised system loading curve (Fig. 4.3) for the given operating point. The nominal RES-based power generation and demand scaling factors from the normalised system loading curve are fixed for all iterations of hth operating point.

Step 2: Uncertainties of RES-based generation and system demand are modelled in this step by producing extra scaling factors following corresponding probability distributions as introduced in Section 4.2. More specifically, Beta distributions and normal distributions are used to model uncertain solar irradiation and system demand, respectively, in different iterations of a given operating point (e.g., hth operating point). It should be noted here that each PV power plant and each load are sampled separately. Furthermore, the mean value of the normal distribution for system demand is adopted as the scaling factor from Step 1. Therefore, $N_P \times O$ (N_P is the total number of PV power plants and O is the total number of operating points) different Beta distributions and $N_L \times O$ (N_L is the total number of system loads) different normal distributions are produced, and each probability distribution will be sampled N (i.e., the total number of iterations) times in the MCS-based probabilistic stability assessment. Regarding wind speeds, a Weibull distribution is introduced to model uncertain wind speeds of a particular wind farm and a particular operating point. For a given operating point and a given wind farm, a normal distribution, whose mean value is the wind speed sampled from the Weibull distribution, is adopted to model short-term forecast errors. In summary, $N_W \times O$ (N_W is the total number of wind farms) different Weibull distributions and $N_W \times O$ different normal distributions are produced to model uncertainties of wind speed in the MCS-based probabilistic assessments. It can be noted from the above discussions that the performances of PV generation and system demand are sequential at different operating points throughout the day, while the performances of wind generation are dispersive due to the lack of daily wind profiles. These assumptions have been adopted in this thesis because the impacts on system stability performance are mainly analysed based on individual operating points. The correlations between different operating points have been neglected in this thesis primarily due to

the lack of real test system operational data. The assumption of non-consecutive wind speeds has resulted in more diverse operating points (hence wider exploration of system stability space) of the system than it would be encountered in realistic systems.

Step 3: In this step, power generation of PV array and system demand at kth iteration and hth operating point are computed by multiplying nominal generation (demand) by all related scaling factors sampled based on corresponding probability distributions. It should be pointed out here that the nominal power of PV array changes following a profile as shown in the subplot (b) of Fig. 3.5 throughout a day. Sampled wind speed at kth iteration and hth operating point is transferred into output power of a wind turbine following the speed-power curve as shown in the subplot (a) of Fig. 3.5. As solar irradiations and wind speeds are sampled separately, different PV power plants and wind farms have different power outputs at a certain iteration and a certain operating point.

Step 4: Wind farms and PV power plants are modelled as aggregations of unit wind turbines and PV arrays rated at 2 MW in this thesis. Hence, corresponding power outputs can be adjusted by changing the aggregation number of wind turbines and PV arrays, which are determined according to the RES-based generation from Step 3 and assuming all RES units operate at rated power. Aggregation numbers are exported directly for further power system stability assessments.

Step 5: Optimal power flow (OPF) aims to provide a conventional power flow solution such that the objective function (e.g., minimising the operating cost of the system or minimising power losses of the system) can be satisfied [181] with the consideration of various constraints (e.g., thermal limit of transmission lines and voltage limit of buses). In the MCS-based probabilistic stability assessment as shown in Fig. 5.4, OPF, with the objective function of minimising the operating cost of the system, is introduced to determine the dispatch (derating) of synchronous generators at a particular operating condition (i.e., kth iteration of hth operating point). More specifically, all synchronous generators are assumed to have four identical generation units, a synchronous generator is derated (by closing one or multiple generation units) when its power output determined by the OPF is lower than 3/4 (in case of disconnection of a single unit) of the rated power taking into account a rated power factor of 0.85 and a 15% spare capacity

per generating unit. The deratings of synchronous generators are modelled by reducing apparent power (S).

The operating cost of ith synchronous generator (C_i) is calculated following a quadratic equation as shown in (5.8) where P_G^i represents the power output of ith synchronous generator, c_2, c_1 and c_0 are cost coefficients. In this thesis, OPF is performed in the environment of Matpower [182] and OPF results are exported for power system stability assessments in DigSILENT PowerFactory. Cost coefficients for all synchronous generators in the modified IEEE 9-bus test system, modified IEEE 68-bus test system and 4TNE system can be found in Appendix-A.1, Appendix-A.2 and Appendix-A.3, respectively.

$$C_i = c_2 {P_G^i}^2 + c_1 P_G^i + c_0 \tag{5.8}$$

Finally, in the case of studies after the implementation of advanced DSM, system demands are increased or decreased according to DSM programs and DSM capacities defined in Tables 4.2 to 4.6; and OPF are performed accordingly. When system demands are modelled as composite loads, number of IMs and power coefficients (refer to (3.14) and (3.15)) are updated after the implementations of advanced DSM.

Step 6: This step focuses on producing system disturbances for system transient and frequency stability assessments. For transient stability assessments, self-clearing three-phase short circuit faults on transmission lines with zero fault impedance are adopted as system disturbances due to more severe consequences. The line fault of kth iteration and hth operating point is characterised by a faulted line, fault location and fault duration sampled based on corresponding probability distributions as discussed in Section 5.2. In the case of frequency stability assessments, system disturbances are selected based on different system models and purposes of study. In the case of the IEEE 9-bus test system, a demand of 15 MW (about 4.8% of the system peak demand) is connected to the Bus 5 (Fig. 3.1) to introduce an imbalance between power generation and demand. As for the IEEE 68-bus test system and 4TNE system, the largest synchronous generator (about 6.8% of the system peak demand in the IEEE 68-bus test system and 9.4% of the system peak demand in the 4TNE system) is disconnected from the system to investigate the impact of RES-based generation and load models on

combined system stability performance evaluated by proposed composite stability indices (Chapter 6). In order to study the overall impact of the advanced DSM on combined system stability, disturbances adopted for frequency stability assessment are reconnections of all available DSM assets at a certain operating point depending on the available demand flexibility at the time (Chapter 7).

It can be seen from the above discussions that different disturbances have been adopted for small disturbance, transient and frequency stability assessments even though they are performed based on the same operating points. Consequently, all adopted stability indices (and corresponding distances to respective stability limit), except FN and RoCoF, are independent. The aim of different modelling of disturbances is to cover as many realistic situations as possible. Step 1 to Step 7 repeat N times until all iterations have been covered.

Step 7: Power system stability assessments for small disturbance, large disturbance and frequency stability are performed in this step focusing on a particular operating condition (i.e., kth iteration and hth operating point) in the environment of DigSILENT PowerFactory. Small disturbance stability is studied by modal analysis, while large disturbance and frequency stability are studied by root mean squared (RMS) simulations lasting for 15 seconds. During these 15 second simulation periods, system stability performance alters only as the result of introduced disturbance; in other words, system operational uncertainties, such as wind speed and system demand, are kept fixed during RMS simulations. Step 1 to Step 8 repeat O times until all operating points have been covered.

Step 8: Statistical values of Individual stability indices and composite stability indices are calculated in this step in the environment of Matlab to evaluate individual stability aspects and combined system stability performance of a certain operating point (condition).

It can be noted from the above discussions that MCS-based probabilistic stability assessments do not necessarily need to be sequential. In other words, the results of MCS-based probabilistic stability assessments are independent of the order of operating points under study, as long as all operating points are covered. These are because all

results (power system stability performances) are compared and analysed based on either individual operating points or overall performance of the system considering all operating points throughout the day. This thesis selects operating points under study sequentially (e.g., hour after hour) only for the conveniences of programming and simulations.

5.5 Summary

In order to assess individual aspects of system stability and combined system stability performance with the consideration of high variability and uncertainty of power system operations, an MCS-based probabilistic stability assessment is adopted in this thesis. The adopted research method samples several operational uncertainties from power generation (e.g., wind speeds and solar irradiations), transmission (e.g., fault location) and demand (e.g., demand loading) sectors randomly following corresponding widely adopted probability distributions and performs repeatable deterministic analysis for each set of sampled input variables. The total number of repeatable deterministic analyses is determined by balancing the accuracy of results and computational cost according to a Monte Carlo stopping rule. Different numbers of repeatable deterministic analyses and subsequently, different computational costs, have been obtained from different test systems under study. The MCS-based probabilistic stability assessments, which have been discussed based on a flow chart, are performed in a mixed environment of DigSILENT PowerFactory and Matlab, and they are adopted to validate the accuracy and applicability of the proposed composite stability indices in Chapter 6 and assess the impacts of advanced DSM on combined system stability performance in Chapter 7.

The probabilistic framework discussed in this chapter mainly aims to assess the impact of advanced DSM, which has been modelled with the consideration of dominant load characteristics and demand payback effects, on power system stability performance. It can be equally used in other power system studies to cover high variability and uncertainty of operation of modern and future power systems. Hence, the probabilistic framework developed with the consideration of system operational uncertainties is the third original contribution of this thesis.

6 Assessment of Power System Stability using Proposed Composite Stability Indices

6.1 Introduction

This chapter first investigates the impacts of RES-based generation and different load models on individual stability aspects (i.e., small disturbance stability, transient stability and frequency stability) using corresponding stability indices based on three test power systems as introduced in Chapter 3 and the MCS-based probabilistic stability assessments as discussed in Chapter 5. Then, the proposed stability indices (i.e., NEDS and PCICSI) are adopted to assess the impacts of RES-based generation and different load models on multiple aspects of system stability simultaneously. The accuracy and applicability of the proposed composite stability indices are verified by comparing the performance of the most affected stability aspect based on individual stability distances and the combined system stability performance based on proposed composite stability indices. Finally, the advantages and disadvantages of proposed composite stability indices are discussed, and their efficiency and accuracy are compared. The superior index for combined stability assessments is identified and it will be used in subsequent chapters to assess the overall impact of the advanced DSM on combined system stability performance.

6.2 Effect of Renewable Energy Source-Based Power Generation on Power System Stability

In this section, the impacts of RES-based generation on combined system stability are quantified by NEDS and PCICSI based on all system models under study (i.e., the modified IEEE 9-bus test system, modified IEEE 68-bus test system and 4TNE system). Because of the small size and simple topology of the modified IEEE 9-bus test system, the computation cost of MCS-based probabilistic stability assessments is low and they are performed every half hour to extend the result set for validations of proposed composite stability indices. For the remaining system models, MCS-based probabilistic stability assessments are carried out hourly throughout the day to balance the accuracy of results (depends on the size of result set) and computational cost. In other words, a total of 48 operating points has been studied in the case of the modified IEEE 9-bus test system, while 24 operating points have been studied for the modified IEEE 68-bus test system and 4TNE system. All system demands are modelled as constant power load in this section due to its high popularity in power system dynamic studies [135].

As discussed in Section 5.4, since advanced DSM will not be covered in this chapter, the system disturbances adopted for frequency stability assessments are the connection of additional loads in the modified IEEE 9-bus test system, and the disconnection of the largest generator in the modified IEEE 68-bus test system and 4TNE system. The size of these disturbances, which may change at different operating points due to different system power demands, is around 4.8%, 6.8% and 9.4% of the corresponding peak demand in the modified IEEE 9-bus test system, modified IEEE 68-bus test system and 4TNE system, respectively.

Moreover, RES-based generators, with an installed capacity of 43% (modified IEEE 9-bus test system), 60% (modified IEEE 68-bus test system) and 8% (4TNE system) of the corresponding peak demand, have been modelled in corresponding system models to investigate the impact of RES-based generation on both, the individual aspects and on the combined system stability. It should be pointed out though that actual RES penetration levels at each operating point are usually lower than the installed capacities

(i.e., RES baseline) because of the uncertain wind speed and turbine generation profile (Fig. 3.5 (a)).

All adopted individual stability indices and corresponding stability limits can be found in Table 2.1 in Section 2.3.

6.2.1 Modified IEEE 9-bus Test System

6.2.1.1 Power System Stability Assessed by Individual Stability Indices

Before assessing the combined system stability performance by composite stability indices, daily variations of mean values (due to the MCS-based probabilistic stability assessments) of individual stability indices (i.e., σ, TSI, FN and RoCoF) before and after the integration of RES-based generation are illustrated as blue solid lines and red dashed lines, respectively, in Fig. 6.1 for the modified IEEE 9-bus test system.

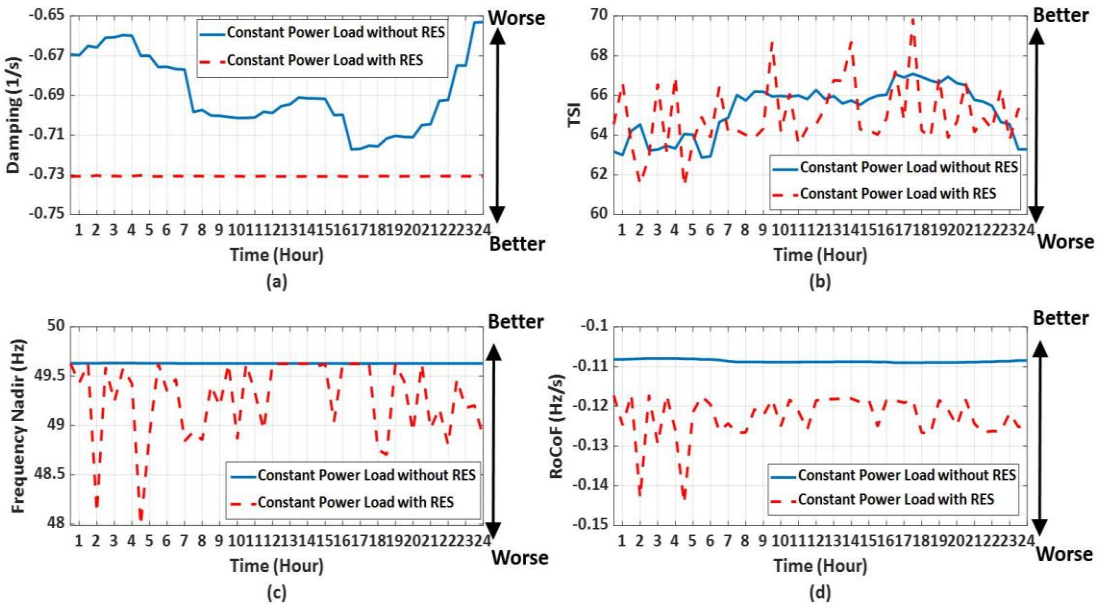

Figure 6.1 Variations of damping (a), TSI (b), FN (c) and RoCoF (d) of the modified IEEE 9-bus test system without/with RES-based generation throughout the day

It can be seen from Fig. 6.1 that when the test system is operated without RES-based generation (blue solid lines), small disturbance (subplot (a) of Fig. 6.1) and large disturbance (subplot (b) of Fig. 6.1) stability are better during peak hours (i.e., system operating points with high power demand) and worse during off-peak hours (i.e., system

operating points with low power demand). System frequency stability indices (i.e., FN and RoCoF) also change at different operating points, though their variations are minor. When the test system is operated with RES-based generation (red dashed lines), damping of the most critical electromechanical mode remains almost constant during the day at around -0.73 s^{-1}. On the other hand, significant variations of TSI and frequency stability indices can be observed during the day.

By comparing stability indices before and after the integration of RES-based generation, it can be seen that small-disturbance stability is improved by increasing the damping of the most critical electromechanical mode and decreasing the variation of damping throughout the day. Both frequency stability indices (i.e., FN and RoCoF), however, indicate that system frequency stability is weakened by the RES-based generation, especially during the off-peak hours (e.g., Hour 2 and Hour 4). During these hours, the system may suffer from significantly reduced FN and increased RoCoF. As far as transient stability is concerned, RES-based generation could either improve or weaken system transient stability at different operating points throughout the day. There is also an increase in the variation of TSI throughout the day, indicating that the system operation is more varied. The consistently opposite impact (i.e., beneficial and detrimental) of RES-based generation on small disturbance and frequency stability emphasises the importance of simultaneous assessment of multiple stability aspects by a composite stability index so that different and even opposite impacts can be properly balanced and prioritised.

In order to quantify the variations of each stability index, the percentage change, as defined in (6.1), has been derived based on the distance of the individual stability index to the corresponding stability limit. The introduced percentage change of stability distance at operating point i, Δx_i, measures the difference between mean values of stability distances (i.e., the distance between a particular stability index and corresponding limit) before (x_i^b) and after (x_i^a) the integration of RES-based generation. Based on (6.1), a positive change means that the corresponding stability aspect has been improved, while a negative change indicates a weakened stability performance. The largest percentage changes at each operating point are summarised in Table 6.1 for the modified IEEE 9-bus test system. The weakened system performance is indicated by grey

shaded cells.

$$\Delta x_i = \frac{x_i^a - x_i^b}{x_i^b} \times 100\% \tag{6.1}$$

It can be seen in Table 6.1 that the most significant changes of stability distance are negative at about half (25/48) of the operating points, indicating that the prevailing impact on individual aspects of system stability is detrimental at these operating points. Assuming that all stability indices are equally weighted, the impact of RES-based generation on combined system stability should be detrimental due to the dominating negative impact. Similarly, the impacts of RES-based generation are beneficial at the remaining 23/48 operating points where the dominating impacts are positive.

Table 6.1 The most significant percentage change of all stability distances due to the integration of RES-based generation based on the modified IEEE 9-bus test system

Operating Point	Stability Aspect	Percentage Change	Operating Point	Stability Aspect	Percentage Change
1	DA	9.19%	25	DA	5.08%
2	DA	9.1%	26	DA	5.23%
3	DA	9.89%	27	DA	5.75%
4	FN	-57.64%	28	DA	5.69%
5	DA	10.58%	29	DA	5.67%
6	FN	-14.75%	30	DA	5.64%
7	DA	10.8%	31	FN	-22.52%
8	DA	10.72%	32	DA	4.44%
9	FN	-62.57%	33	DA	1.9%
10	FN	-27.59%	34	TSI	-3.2%
11	DA	8.16%	35	TSI	4.14%
12	FN	-10.63%	36	FN	-33.11%
13	DA	7.96%	37	FN	-35.23%
14	FN	-29.92%	38	DA	2.88%
15	FN	-26.32%	39	TSI	-4.61%
16	FN	-29.54%	40	FN	-26.4%
17	FN	-8.43%	41	DA	3.67%
18	FN	-16.51%	42	FN	-25.08%
19	DA	4.27%	43	FN	-17.33%
20	FN	-29.14%	44	FN	-31.51%
21	DA	4.2%	45	DA	8.24%
22	FN	-11.07%	46	FN	-17.09%
23	FN	-25.67%	47	FN	-16.19%
24	DA	4.57%	48	FN	-28.48%

DA = Damping of the Most Critical Electromechanical Mode
TSI = Transient Stability Index
FN = Frequency Nadir

As all individual stability indices have been considered equally important in this thesis, the proposed composite stability indices are expected to reflect (be influenced by) the most affected stability aspect, indicated by the largest percentage change of individual stability distances, at each operating point.

6.2.1.2 Combined System Stability Assessed by Composite Stability Indices

The combined system stability performance quantified by NEDS and PCICSI, based on the mean values of individual stability distances obtained at each operating point, is illustrated in the subplot (a) and subplot (b) of Fig. 6.2, respectively. In Fig. 6.2, combined system stability performances before and after the integration of RES-based generation are illustrated by blue solid lines and red dashed lines, respectively. The most probable stability performance is represented by the black dotted line.

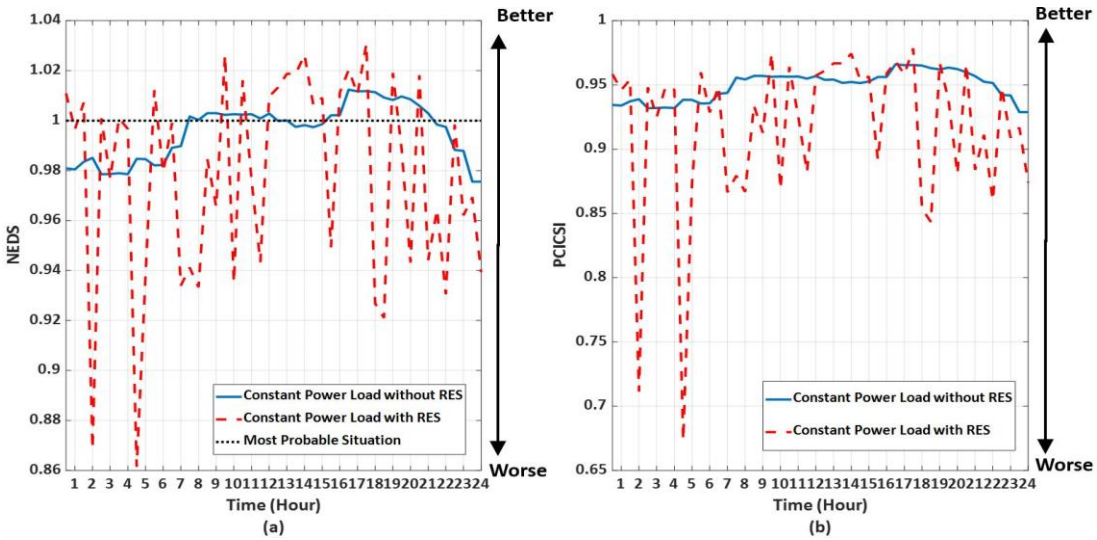

Figure 6.2 Combined system stability performance assessed by NEDS (a) and PCICSI (b) before and after the integration of RES-based generation in the modified IEEE 9-bus test system

Focusing on the blue solid line in the subplot (a) of Fig. 6.2, the combined system stability without RES-based generation is better than the most probable situation during peak hours due to improved small disturbance and transient stability (as shown in Fig. 6.1), and worse than the most probable situation during off-peak hours as the result of relatively low TSI and damping values. Moreover, there are 25/48 operating points

showing NEDS smaller than 1, indicating that the corresponding combined system stability performance is worse than the most probable situation. This number increases to 28/48 in the case of operating points with RES-based generation (i.e., red dashed line). If the system stability improvement measures are to be implemented when the combined system stability is worse than the most probable situation, the system with RES-based generation requires more stability support than that without RES-based generation, as can be seen from the subplot (a) of Fig. 6.2.

Regarding the accuracy of NEDS, which is considered as the ability of proposed composite stability indices to evaluate variations of combined system stability performances according to the most affected stability aspect (index), it can be seen from Fig. 6.2 and Table 6.1 that the impact of RES-based generation on combined system stability is dominated by the most affected stability distance (aspect). More specifically, the red dashed line is lower than the blue solid line, indicating weakened combined system stability performance, at operating points where the dominating impacts of RES-based generation on individual stability aspects are negative (Table 6.1). Conversely, at operating points where the dominating impacts on individual stability aspects are positive, the red dashed line is higher than the blue solid line representing improved combined system stability.

In terms of PCICSI (subplot (b) of Fig. 6.2), the shapes of both lines are similar to the NEDS (subplot (a) of Fig. 6.2), which means PCICSI may also capture variations of combined system stability and identify the impact of the RES-based generation. Referring to Table 6.1, the impact on combined system stability quantified by PCICSI is also dominated by the most affected stability distance (aspect). For instance, combined system stability has weakened significantly at 2:00 (operating point 4) and 4:30 (operating point 9) due to the significantly reduced stability distances of FN (-57.64% at operating point 4 and -62.57% at operating point 9). Therefore, the accuracy of PCICSI is identical to that of the NEDS. Considering that all stability indices included in PCICSI are normalised with respect to the corresponding best-case scenario, which appears as the extreme case, PCICSI is not suitable for guiding the implementations of stability enhancement solutions due to the lack of an appropriate reference.

6.2.2 Modified IEEE 68-bus Test System

6.2.2.1 Power System Stability Assessed by Individual Stability Indices

Mean values of individual stability indices before and after the integration of RES-based generation throughout the day are illustrated in Fig. 6.3 as blue solid lines and red dashed lines, respectively. It can be seen that all aspects of power system stability can either be improved or weakened by RES-based generation. The subplot (a) of Fig. 6.3 illustrates that small disturbance stability is more likely to be improved (at 17/24 operating points) by RES-based generation and such improvements are more significant during off-peak hours. Although the transient stability (subplot (b) of Fig. 6.3) can be either improved or weakened during the daytime, it is usually weakened by the RES-based generation during off-peak hours, except the demand valley (i.e., Hour 4), when all aspects of system stability have improved. Meanwhile, according to subplots (c) and (d) of Fig. 6.3, the impact of RES-based generation on frequency stability is usually beneficial during daytime and either beneficial or detrimental during late evening and early morning. Similar to the modified IEEE 9-bus test system, the integration of RES-based generation leads to opposite impacts (i.e., beneficial and detrimental) on small disturbance and remaining aspects of system stability at, for instance, Hours 1, 2 and 23.

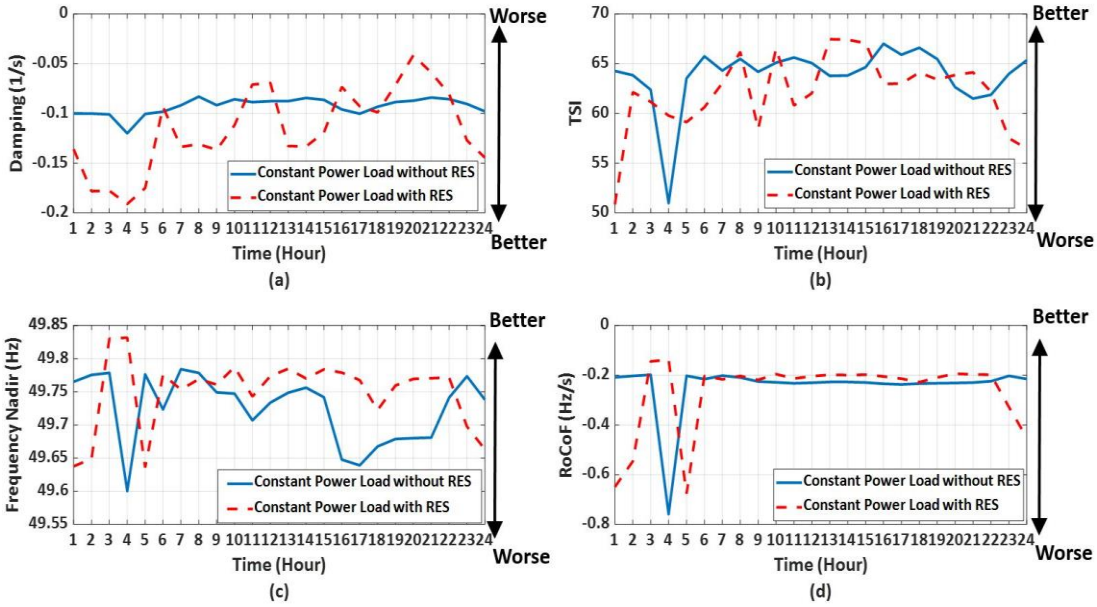

Figure 6.3 Variations of damping (a), TSI (b), FN (c) and RoCoF (d) of the modified IEEE 68-bus test system without/with RES-based generation throughout the day

The significant weakened frequency stability performances at demand valley (subplots (c) and (d)) are caused by the much larger size of the disturbance (16% of the total demand at Hour 4 compared with a daily average value of 9.5%) modelled as the disconnection of the largest generator in the system.

For all operating points under study, the most affected stability distances and corresponding percentage changes are summarised in Table 6.2 for the modified IEEE 68-bus test system. Decreased stability distances have been marked with grey backgrounds. Based on Table 6.2, small disturbance stability can be considered as the most critical stability aspect, as the distance of damping to corresponding limit shows the largest variation at 21/24 operating points. Furthermore, assuming all stability indices are equally weighted, the dominating impact of RES-based generation on individual stability aspects is beneficial at 14/24 operating points and detrimental at 10/24 operating points. Comparing Table 6.1 and Table 6.2, the average value of percentage changes of the most affected stability distance alters from 6.43% (modified IEEE 9-bus test system) to 64.99% (modified IEEE 68-bus test system) and -24.26% (modified IEEE 9-bus test system) to -24.33% (modified IEEE 68-bus test system) for increased stability distance and decreased stability distance, respectively, which indicate that the beneficial impacts of RES-based generation is more significant in power systems with relatively high RES penetration levels (60% baseline in the modified IEEE 68-bus test system), while the detrimental impacts of RES-based generation on the most affected stability aspect are relatively more stable.

6.2.2.2 Combined System Stability Assessed by Composite Stability Indices

Subplots (a) and (b) of Fig. 6.4 illustrate the combined system stability performance before (blue solid lines) and after (red dashed lines) the integration of RES-based generation based on the mean values of individual stability distances and quantified by NEDS and PCICSI, respectively. When the NEDS is used to assess combined system stability performance, it can be seen from the blue solid line in the subplot (a) that there are 12 operating points with NEDS smaller than 1 and 12 operating points with NEDS

larger than 1, indicating that the system has the same possibility of exhibiting improved or weakened combined system stability performance compared with the most probable situation. When the system is operated with RES-based generation (red dashed line), the number of operating points exhibiting better stability performance than the most probable situation increases from 12/24 to 14/24. Additionally, the NEDS is increased significantly around Hours 4, 8 and 14.

Table 6.2 The most significant percentage change of all stability distances due to the integration of RES-based generation based on the modified IEEE 68-bus test system

Operating Point	Stability Aspect	Percentage Change	Operating Point	Stability Aspect	Percentage Change
1	RoCoF	-55.71%	13	DA	51.52%
2	DA	78.05%	14	DA	57.85%
3	DA	76.12%	15	DA	38%
4	RoCoF	257.68%	16	DA	-23.62%
5	DA	74.19%	17	DA	-7.45%
6	TSI	-7.8%	18	DA	6.05%
7	DA	45.47%	19	DA	-19.35%
8	DA	57.67%	20	DA	-52.39%
9	DA	48.99%	21	DA	-29.95%
10	DA	30.31%	22	DA	-6.05%
11	DA	-19.98%	23	DA	40.56%
12	DA	-21.01%	24	DA	47.44%

DA = Damping of the Most Critical Electromechanical Mode
TSI = Transient Stability Index
RoCoF = Rate of Change of Frequency

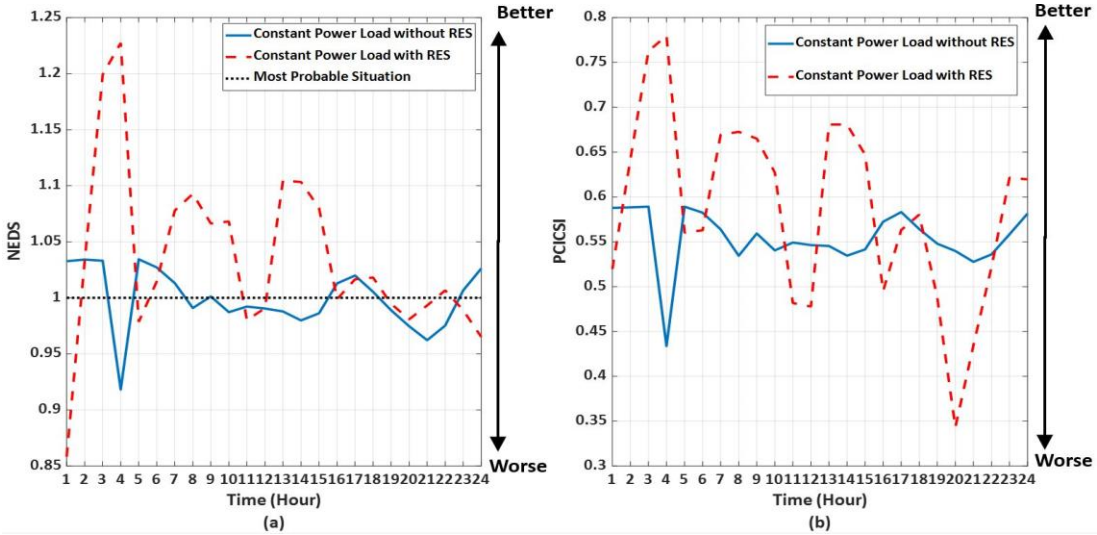

Figure 6.4 Combined system stability performance assessed by NEDS (a) and PCICSI (b) before and after the integration of RES-based generation in the modified IEEE 68-bus test system

As discussed previously, the impact of RES-based generation on combined system

stability is expected to be dominated by the most affected stability distance (aspect). However, it can be noted from Fig. 6.4 and Table 6.2 that the impact of RES-based generation on combined system stability is not dominated by the most affected stability aspect at 7/24 operating points. For instance, the NEDS indicates that the combined system stability improves from Hours 19 to 22 as the red dashed line is above the blue solid line, while the dominating impacts of RES-based generation on individual stability distance are negative at Hours 19 to 22 as summarised in Table 6.2. The opposite impacts of RES-based generation on combined system stability, identified by the NEDS, and their influence on the most affected stability distance are caused by the change of the most probable situation. More specifically, system stability performances of the most probable situation improve due to the integration of RES-based generation; hence, a detrimental impact on the combined system stability can be indicated by NEDS even though the most affected stability aspect improves. Therefore, although NEDS may clearly indicate variations in combined system stability around the most probable situation, the accuracy of the NEDS to assess the impact of new technologies and new devices decreases with the increase in variation of the most probable situation.

The accuracy of PCICSI, is much better than that of NEDS. Based on Table 6.2 and the subplot (b) of Fig. 6.4, the opposite impact can only be found at Hour 5 where the PCICSI indicates a detrimental impact on combined system stability, while the most affected stability distance (i.e., damping of the most critical electromechanical mode) actually improves. The reason for this opposite impact is that, although all other stability distances have reduced, the magnitudes of those reductions are smaller than the increase (74.19%) in damping of the most critical electromechanical mode. Therefore, the final impact on the combined system stability is no longer dominated by the most affected stability aspect and it becomes negative overall.

6.2.3 The 4TNE System

6.2.3.1 Power System Stability Assessed by Individual Stability Indices

Variations in mean values of individual stability indices caused by different operating points and RES-based generation based on the 4TNE system are illustrated in Fig. 6.5,

where stability performances before and after the integration of RES-based generation are illustrated by blue solid lines and red dashed lines, respectively.

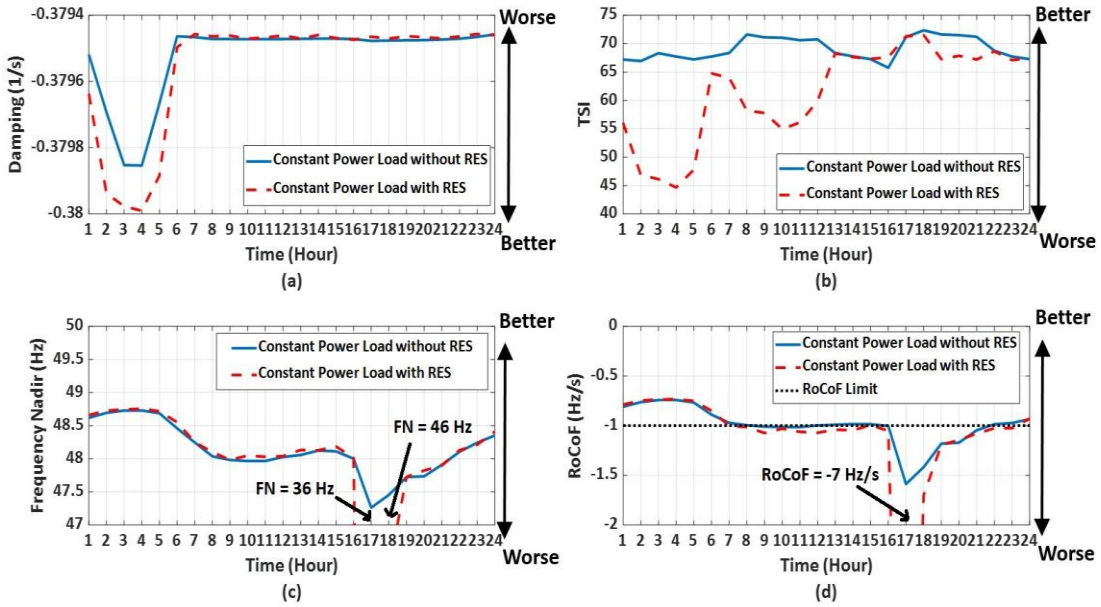

Figure 6.5 Variations of damping (a), TSI (b), FN (c) and RoCoF (d) of the 4TNE system without/with RES-based generation throughout the day

It can be seen from subplots (a), (c) and (d) that small disturbance and frequency stability are better (large stability distances to corresponding stability limits) during off-peak hours and worse (smaller stability distances to corresponding stability limits) during peak hours. Focusing on the frequency stability (subplots (c) and (d) of Fig 6.5), when the system is operated without RES-based generation (blue solid lines), RoCoF exceeds its stability limit at 9/24 operating points due to the relatively larger size of disturbance (9.4%). Consequently, the power system loses stability at these operating points. In the case of system operations with RES-based generation, FN and RoCoF exceed the corresponding stability limits (FN=47 Hz and RoCoF=-1 Hz/s) at 2/24 and 16/24 operating points, respectively, throughout the day. Extremely low FN values and high RoCoF values are shown in Fig. 6.5 to indicate system instability and they are obtained due to the insufficient and incomprehensive modelling of frequency controls (e.g., UFLS) and system protection devices (e.g., disconnection of tripped generators) in the test system. Furthermore, increased system loading at the demand peak also reduces system reserve capacities. RES-based generation increases not only the number of unstable operating points, but also the magnitude of the critical RoCoF (-1.6 Hz/s to -7 Hz/s). Likewise,

transient stability is weakened at 19/24 operating points by the RES-based generation, and significant detrimental impacts are noted before midday (i.e., Hour 12). However, small disturbance stability improves slightly around demand valley (i.e., Hour 4) due to the RES-based generation.

Table 6.3, where negative percentage changes (detrimental impacts on the most affected stability aspect) are marked by grey backgrounds, summarises the most affected stability distance (aspect) and corresponding percentage change at each operating point for the 4TNE system. As the result of significant detrimental impacts of RES-based generation on frequency stability, the most affected stability aspect is frequency stability at 19/24 operating points. Considering further the weakened transient stability during low demand hours, the most affected stability aspects, either transient stability or frequency stability, deteriorate at 21/24 operating points throughout the day, indicating that the overall impact of RES-based generation on system stability is detrimental.

Table 6.3 The most significant percentage change of all stability distances due to the integration of RES-based generation based on the 4TNE system

Operating Point	Stability Aspect	Percentage Change	Operating Point	Stability Aspect	Percentage Change
1	TSI	-16.59%	13	RoCoF	-534.19%
2	TSI	-30%	14	RoCoF	-381.45%
3	TSI	-32.48%	15	RoCoF	-62.51%
4	TSI	-34.07%	16	RoCoF	-1469.9%
5	TSI	-28.88%	17	FN	-6588.89%
6	RoCoF	35.28%	18	FN	-247.32%
7	RoCoF	-105.51%	19	RoCoF	-7.2%
8	RoCoF	-437.45%	20	RoCoF	15.6%
9	RoCoF	-666.99%	21	RoCoF	-73.05%
10	RoCoF	-119.78%	22	RoCoF	-278.07%
11	RoCoF	-361.08%	23	RoCoF	-193.65%
12	RoCoF	-3156.22%	24	RoCoF	8.49%

TSI = Transient Stability Index
FN = Frequency Nadir
RoCoF = Rate of Change of Frequency

6.2.3.2 Combined System Stability Assessed by Composite Stability Indices

In order to study the accuracy and applicability of the proposed composite stability

indices, combined system stability performances quantified by NEDS and PCICSI have been illustrated in subplots (a) and (b) of Fig. 6.6, respectively, for the 4TNE system. In Fig. 6.6, combined system stability before and after the integration of RES-based generation are illustrated by blue solid lines and red dashed lines, respectively, and the most probable stability performance is represented by the black dotted line in the case of NEDS.

When the NEDS is used to quantify combined system stability (subplot (a) of Fig. 6.6), high NEDS values, which indicate better combined system stability performances, can be found around demand valley (i.e., Hour 4) and demand peak (i.e., Hour 17). Recalling from Fig. 6.5 that the system loses stability due to high RoCoF values around demand peak regardless of the integration of RES-based generation, NEDS does not identify unstable system operating points and results in misunderstandings of the impact of RES-based generation.

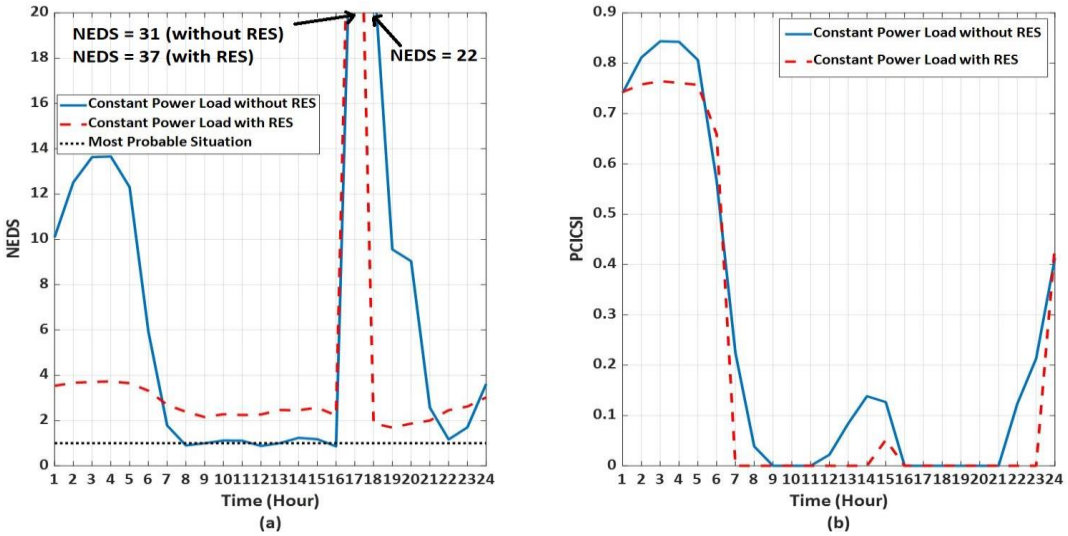

Figure 6.6 Combined system stability performance assessed by NEDS (a) and PCICSI (b) before and after the integration of RES-based generation in the 4TNE system

According to the definition of NEDS as given in (6.2), where σ'_{np}, TSI'_{np}, FN'_{np} and $RoCoF'_{np}$ represent normalised stability distances (with respect to the most probable value) of damping of the most critical electromechanical mode, TSI, FN and RoCoF, respectively, NEDS is determined based on the magnitude of distances of individual stability indices to corresponding stability limits. By neglecting the sign (i.e., positive when the corresponding stability aspect is stable or negative when the corresponding

stability aspect is unstable) of individual stability distance, NEDS can show similar, if not identical, results for stable and unstable operating points and, consequently, lose the ability to identify unstable operating points. For instance, the normalised stability distance of FN (FN'_{np}) equals 0.25 at Hour (operating point) 17 when the system operates without RES-based generation, while it (FN'_{np}) decreases to -70.89 due to the significantly reduced FN value caused by RES-based generation. However, decreased FN'_{np} (from 0.25 to -70.89) finally leads to similar NEDS values (NEDS=31 based on FN'_{np}=0.25 and NEDS=37 based on FN'_{np}=-70.89, as shown in the subplot (a) of Fig. 6.6) and, subsequently, the misjudged impact of RES-based generation.

$$NEDS = \frac{1}{2} \times \sqrt[2]{\left(\sigma'_{np}\right)^2 + \left(TSI'_{np}\right)^2 + \left(FN'_{np}\right)^2 + \left(RoCoF'_{np}\right)^2} \qquad (6.2)$$

PCICSI, on the other hand, clearly identifies 9/24 and 16/24 unstable operating points by exhibiting zero values in the case of system without and with RES-based generation, respectively. Additionally, weakened combined system stability performances caused by reduced TSI values have been captured and illustrated by PCICSI at Hours 4, 14 and 22. Therefore, the accuracy and applicability of PCICSI are much higher than those of the NEDS when the system is likely to lose stability.

6.3 Effect of Load Model on Combined System Stability

In this section, the proposed composite stability indices (i.e., NEDS and PCICSI) are used to assess the impact of different load models on combined system stability performance. Because the advanced DSM is not discussed in this chapter, only constant power and constant impedance load models are adopted and discussed. Moreover, all results illustrated in this section are obtained based on the same installed capacities of RES-based generation (i.e., 43% for the modified IEEE 9-bus test system, 60% for the modified IEEE 68-bus test system and 8% for the 4TNE system with respect to corresponding peak demands) as in Section 6.2. All remaining configurations of MCS-based probabilistic stability assessment, including but not limited to, fault types and system loading levels, are also identical to those discussed in Section 6.2.

6.3.1 Modified IEEE 9-bus Test System

6.3.1.1 Power System Stability Assessed by Individual Stability Indices

The mean values of individual stability indices based on the modified IEEE 9-bus test system are illustrated as blue solid lines and red dashed lines in Fig. 6.7 for constant power and constant impedance load models, respectively. It can be seen from Fig. 6.7 that the system exhibits better frequency stability performance and worse transient stability performance throughout the day when the constant impedance load model is adopted. There is clearly a need to introduce composite stability indices to balance the opposite impacts of constant impedance load model on frequency and transient stability. Regarding system small disturbance stability, constant power and constant impedance load models show similar damping values except at Hour 2:30 (operating point 5) and Hour 3:30 (operating point 7).

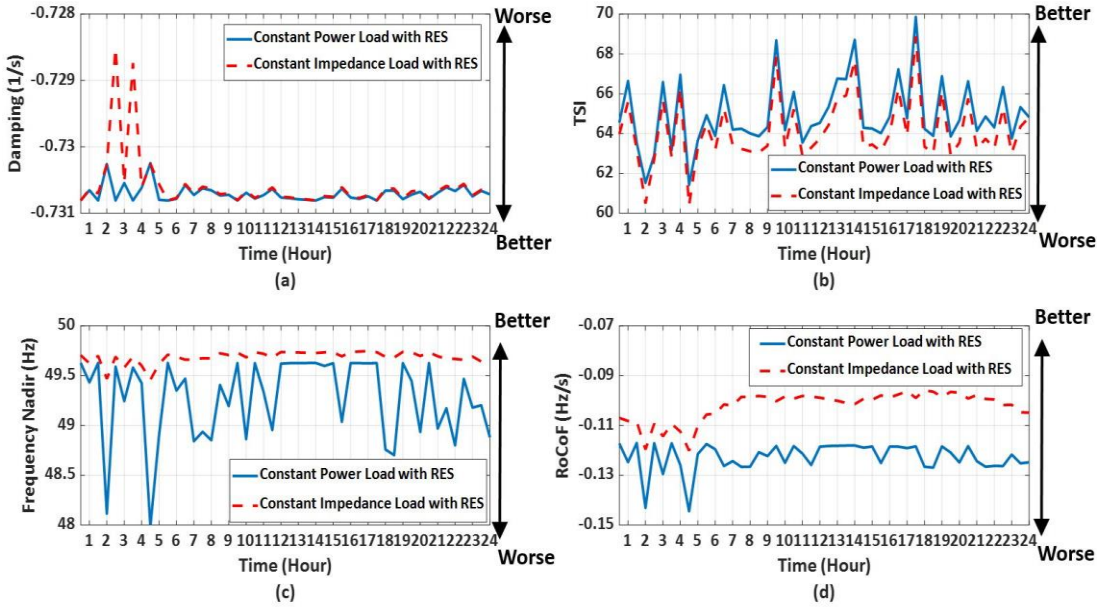

Figure 6.7 Variations of damping (a), TSI (b), FN (c) and RoCoF (d) of the modified IEEE 9-bus test system with constant power and constant impedance load models throughout the day

When system demands are modelled as constant impedance loads, the stability distances of small disturbance stability (subplot (a) of Fig. 6.7) decrease by 0.31% and 0.28% compared with constant power load at Hour 2:30 and Hour 3:30, respectively, while stability distances of FN (subplot (c) of Fig. 6.7) increase by 121% and 15%

compared with constant power load at Hour 2:30 and Hour 3:30, respectively. The beneficial impact on frequency stability is much greater than the detrimental impact on small disturbance stability. Additionally, two frequency stability indices (i.e., FN and RoCoF) indicate better system stability in the case of the constant impedance load, and only TSI indicates noticeable detrimental impacts on transient stability caused by constant impedance load throughout the day (except Hour 2:30 and Hour 3:30 which have been discussed above). Therefore, the combined system stability with the constant impedance load should be better than the constant power load if all stability indices are equally weighted.

6.3.1.2 Combined System Stability Assessed by Composite Stability Indices

Based on the performances of the mean values of individual stability indices illustrated in Fig. 6.7, combined system stability of the modified IEEE 9-bus test system with constant power (blue solid lines) and constant impedance (red dashed lines) load models are quantified by NEDS and PCICSI and illustrated in subplots (a) and (b) of Fig. 6.8 for NEDS and PCICSI, respectively.

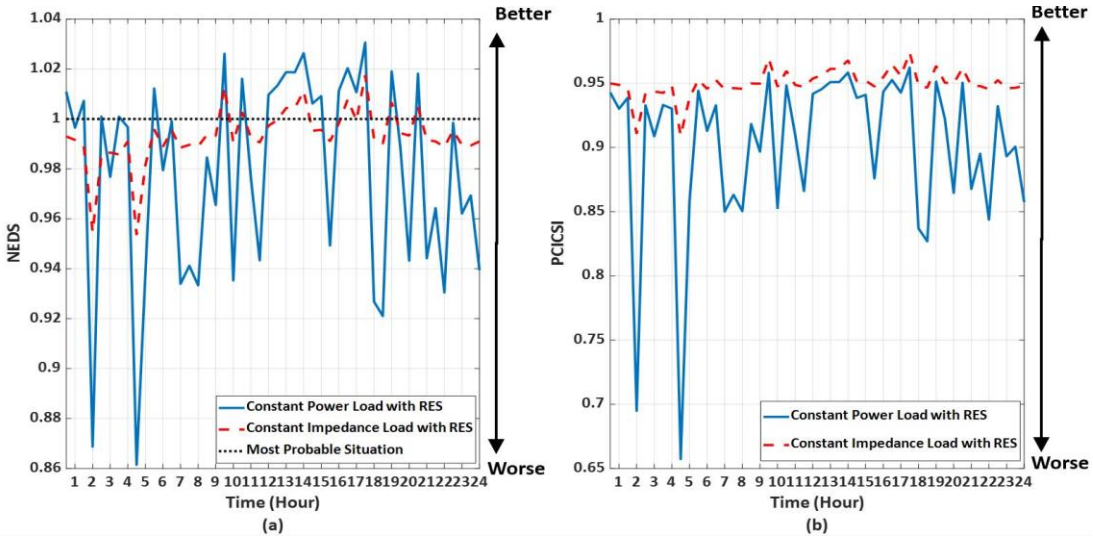

Figure 6.8 Combined system stability performance assessed by NEDS (a) and PCICSI (b) with constant power and constant impedance load models in the modified IEEE 9-bus test system

Focusing on the subplot (a) of Fig. 6.8, the distribution of NEDS values in the case of

constant impedance load (red dashed line) is more concentrated around the most probable situation than the constant power load (blue solid line) and thus the system exhibits better combined system stability performance when all demands are modelled as constant impedance loads. Likewise, PCICSI also indicates better combined system stability performances in the case of constant impedance load because the red dashed line is always higher than the blue solid line. The conclusions derived from composite stability indices agree with the findings from individual stability indices.

6.3.2 Modified IEEE 68-bus Test System

6.3.2.1 Power System Stability Assessed by Individual Stability Indices

Regarding the modified IEEE 68-bus test system, daily variations of individual stability indices are illustrated as blue solid lines and red dashed lines for constant power and constant impedance load models, respectively, in Fig. 6.9. Here, it can be noted that better stability performance can be found in the case of either constant power or constant impedance load models.

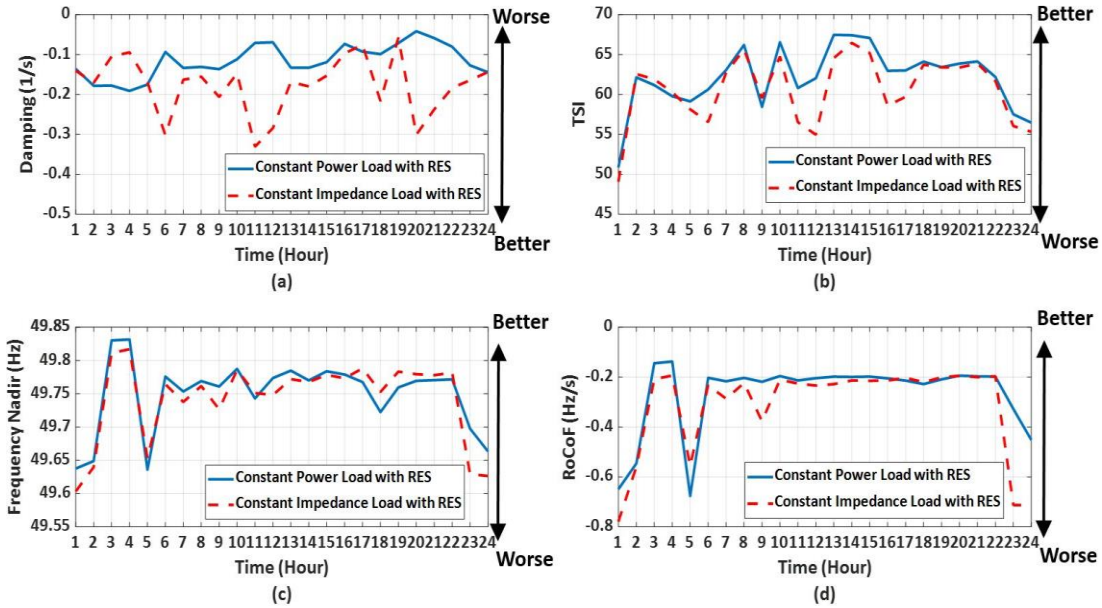

Figure 6.9 Variations of damping (a), TSI (b), FN (c) and RoCoF (d) of the modified IEEE 68-bus test system with constant power and constant impedance load models throughout the day

By summarising the most affected stability distance (aspect) and corresponding

percentage change of each operating point in Table 6.4, where percentage changes of stability distance at operating point i (Δx_i) are calculated using (6.3) and all decreased stability distances (i.e., detrimental impacts) are emphasised by the grey background, it can be found that small disturbance stability is the most affected stability aspect at 20/24 operating points, and thus variations of combined system stability due to different load models should be dominated by small disturbance stability. In (6.3), the mean values of stability distances at operating point i in the case of constant power and constant impedance load models are represented by x_i^{cp} and x_i^{cz}, respectively.

$$\Delta x_i = \frac{x_i^{cz} - x_i^{cp}}{x_i^{cp}} \times 100\% \tag{6.3}$$

Table 6.4 The most significant percentage change of all stability distances due to different load models based on the modified IEEE 68-bus test system

Operating Point	Stability Aspect	Percentage Change	Operating Point	Stability Aspect	Percentage Change
1	RoCoF	-37.03%	13	DA	27.04%
2	DA	-4.15%	14	DA	34.94%
3	DA	-40.92%	15	DA	28.48%
4	DA	-50.57%	16	DA	32.23%
5	RoCoF	37.22%	17	DA	-18.74%
6	DA	223.6%	18	DA	119.25%
7	DA	22.06%	19	DA	-19.35%
8	DA	18.63%	20	DA	625.02%
9	DA	51.04%	21	DA	303.62%
10	DA	31.67%	22	DA	128.26%
11	DA	366.76%	23	RoCoF	-57.26%
12	DA	310.64%	24	RoCoF	-47.75%

DA = Damping of the Most Critical Electromechanical Mode
RoCoF = Rate of Change of Frequency

6.3.2.2 Combined System Stability Assessed by Composite Stability Indices

Combined system stability performances based on mean values of individual stability distances and assessed by NEDS and PCICSI are illustrated in subplots (a) and (b) of Fig. 6.10, respectively. In Fig. 6.10, the stability performances of constant power and constant impedance load models are depicted by blue solid lines and red dashed lines,

respectively. As in Section 6.2.2.2, a significant change in the most probable situation can lead to misunderstandings with regard to combined system stability performance. For instance, the combined system stability performance at Hour 5 is slightly worse than the most probable situation (NEDS = 0.98) when the constant power load model is adopted (i.e., the blue solid line). However, when the constant impedance load model is adopted (i.e., the red dashed line), the combined system stability performance quantified by NEDS reduces to 0.88 due to the improved most probable situation. Consequently, NEDS indicates a weakened stability performance at Hour 5 when constant impedance load is adopted, even though the most affected stability distance (i.e., RoCoF) increased by 37.22%.

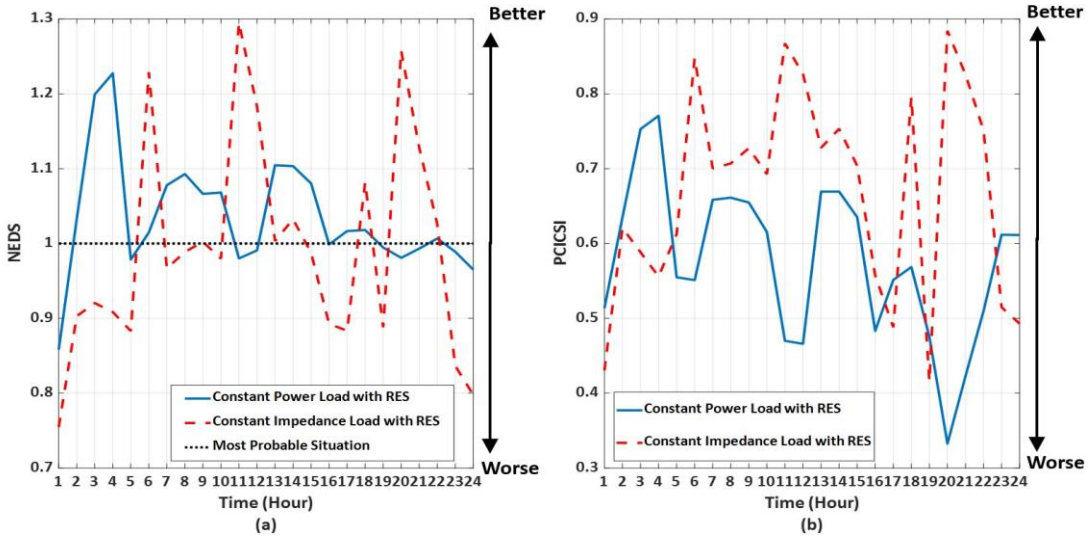

Figure 6.10 Combined system stability performance assessed by NEDS (a) and PCICSI (b) with constant power and constant impedance load models in the modified IEEE 68-bus test system

According to the subplot (b) of Fig. 6.10, PCICSI clearly captures variations in the most affected stability distance at all operating points. More specifically, the red dashed line is below the blue solid line, indicating that the combined system stability with constant impedance load model is worse than the constant power load model, at only 8 operating points (Hours 1 to 4, 17, 19, 23 and 24). These operating points have also been identified in Table 6.4 because the most affected stability distance shows weakened stability performance when system demands are modelled as constant impedance loads. Consequently, PCICSI is considered to be more accurate than NEDS to assess the impact of different load models on combined system stability, based on the modified IEEE 68-bus test system.

6.3.3 The 4TNE System

6.3.3.1 Power System Stability Assessed by Individual Stability Indices

Although the 4TNE system has the lowest installed capacity of the RES-based generation (8% of the system peak demand), it has the largest number of loads (142) among all system models under study. The impact of different load models on system stability performances can be more significant in the case of the 4TNE system. Daily variations of mean values of individual stability indices are illustrated by blue solid lines and red dashed lines for the 4TNE system with constant power and constant impedance load models, respectively, in Fig. 6.11.

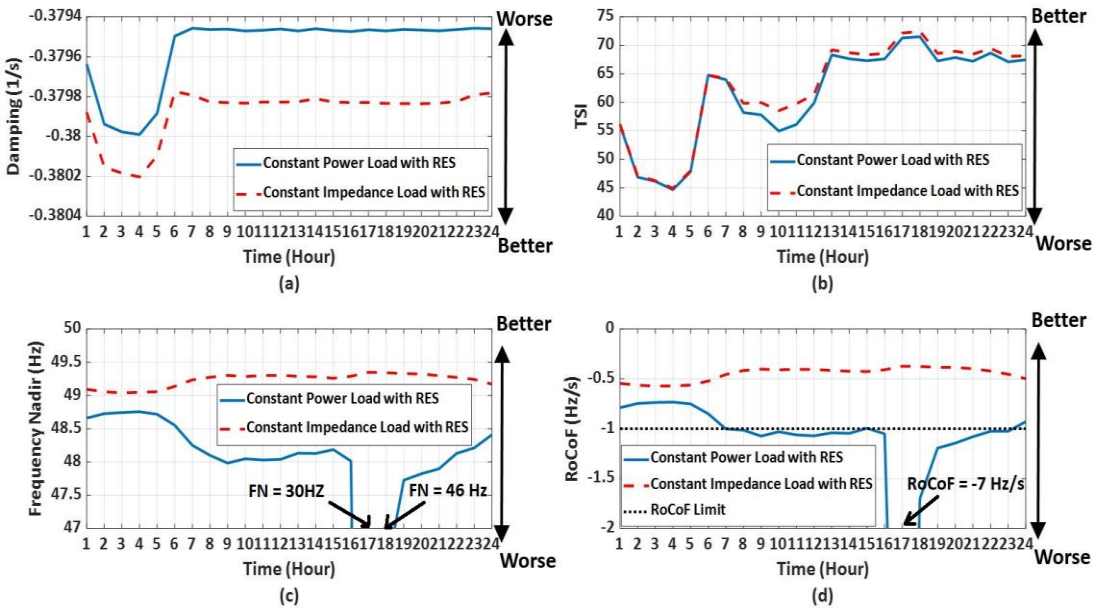

Figure 6.11 Variations of damping (a), TSI (b), FN (c) and RoCoF (d) of the 4TNE system with constant power and constant impedance load models throughout the day

It can be seen in Fig. 6.11 that all stability indices indicate better stability performance in the case of the constant impedance load model (red dashed lines) and, more importantly, the system can be stabilised during the daytime when the constant power load model is adopted. Therefore, accurate and realistic load models are essential in power system stability assessments. Similar to Section 6.2.3.1, extremely low FN and high RoCoF values around demand peak are shown to indicate system instability, even though they cannot be seen in real systems. They are caused by not including the

frequency controls and protection algorithms in the model, which are designed and applied in real systems to restore system frequency and prevent further drops of frequency when it violates stability limit. The observed extreme values though serve the purpose of demonstrating the ability of PCICSI to identify the critical cases, i.e., system instability, which NEDS fails to identify.

6.3.3.2 Combined System Stability Assessed by Composite Stability Indices

Regarding proposed composite stability indices, combined system stability performances are illustrated in subplots (a) and (b) of Fig. 6.12 for NEDS and PCICSI, respectively. In Fig. 6.12, stability performances with constant power and constant impedance load models are depicted by blue solid lines and red dashed lines, respectively.

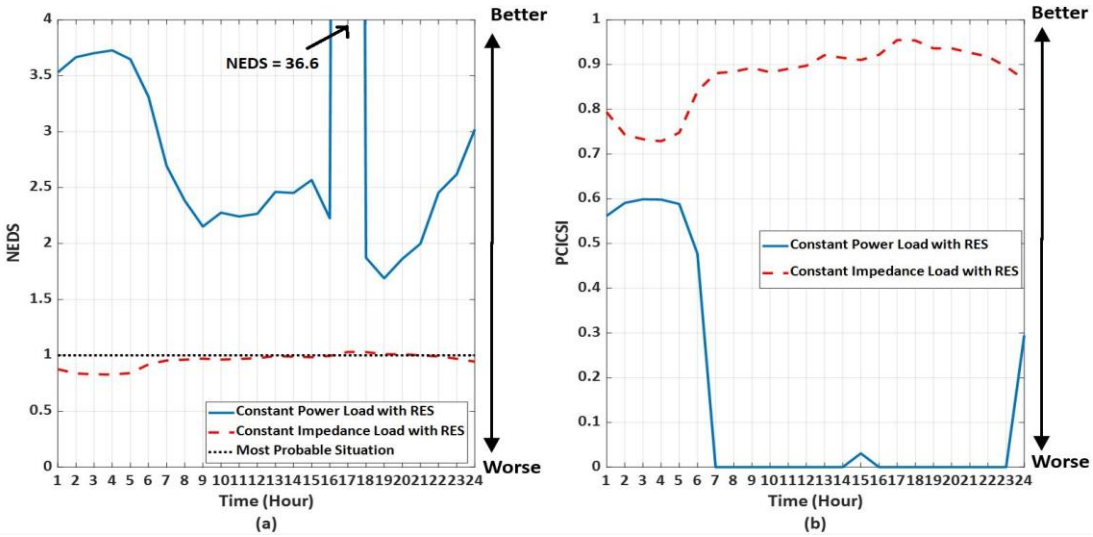

Figure 6.12 Combined system stability performance assessed by NEDS (a) and PCICSI (b) with constant power and constant impedance load models in the 4TNE system

As discussed in Section 6.2.3.2, NEDS cannot identify system instability and thus the combined system stability quantified by NEDS for the constant power load model (the blue solid line in the subplot (a) of Fig. 6.12) is misleading. When the system regains stability by modelling demand with the constant impedance load model, NEDS shows better combined system stability performance during peak hours and worse stability performance during off-peak hours, which agrees with the behaviours of all individual

stability indices as illustrated in Fig. 6.11. Focusing on the subplot (b) of Fig. 6.12, the beneficial impacts of the constant impedance load model on combined system stability have been illustrated by increased PCICSI values at all operating points. By identifying unstable operating points in the case of constant power load model, PCICSI emphasises operating points where system stability can be regained with the constant impedance load model. Moreover, similar to NEDS, PCICSI indicates better stability performance during peak hours and worse stability performance during off-peak hours. Considering that the system exhibits better stability performance during off-peak hours and loses stability during peak hours in the case of the constant power load model, the importance of accurate and realistic load models is emphasised again.

6.4 Comparison Between Proposed Composite Stability Indices

Both proposed stability indices (i.e., NEDS and PCICSI) assess combined system stability by considering the distances to corresponding stability limits while simultaneously relying on the calculation of widely adopted stability indices for different stability aspects. Better performances of combined system stability are expected to be represented by larger values of proposed composite stability indices while worse stability performances are expected to be represented by smaller values of composite stability indices.

When the system is operated without risk of losing stability, both NEDS and PCICSI can illustrate variations in combined system stability in such a way that better stability performances are represented by larger index values. As all stability distances are normalised with respect to the corresponding most probable value in the case of NEDS, the relationship between the current operating point and the most probable situation can also be identified by NEDS. The most probable value is adopted as the reference because it represents the most common stability performance, and it will not be affected by extreme cases. Therefore, NEDS can be used to guide the implementations of stability enhancement measures, for instance, implementing stability enhancement and improvement measures when the combined system performance is worse than the most

probable (common) situation. Regarding PCICSI, since all stability distances are normalised with respect to the corresponding maximum value (i.e., the best performed case), which is usually an extreme case, the reference case guiding the implementations of stability enhancement and improvement measures cannot be defined based on PCICSI.

When the system is operated with a risk of losing stability, the accuracy of NEDS decreases significantly due to the lack of ability to identify system instability. According to the definition of NEDS, the value of NEDS is determined based on the magnitude of individual stability distance. A positive NEDS can be obtained even when individual stability distances show negative values, which indicate system instability. PCICSI, however, can clearly identify system instability by exhibiting zero values. This is one of the major advantages of PCICSI over NEDS.

The ability of NEDS and PCICSI to assess the impact of new technologies and devices on combined system stability also varies significantly. More specifically, when the most probable situation has not been affected significantly by the introduction of new technologies and devices, NEDS and PCICSI can assess the impact on combined system stability by comparing index values before and after implementation of new technologies and devices. The direction of such impact (i.e., beneficial or detrimental) is determined based on the most affected stability distance (aspect) if all stability indices are considered equally weighted. However, if the most probable situation changes significantly after the implementation of new technologies and devices, the accuracy of NEDS decreases, leading to misunderstandings and misjudgements about the impact on combined system stability. Fortunately, the accuracy of PCICSI will not be affected because all stability distances (before and after the implementation of new technologies and devices) are normalised to the same reference (i.e., the maximum stability distance).

It can be noted from the above discussions that the accuracy of the proposed stability indices depends strongly on the reference values adopted. Accurate reference values are usually obtained from a large historical data base. In the case of NEDS, the larger the historical data base, the better (more reliable and accurate) reference values can be obtained. Even though the most probable value is not affected by extreme cases, it requires regular updates to guarantee its accuracy and reliability. In terms of PCICSI,

because the reference value adopted is based on an extreme case, it only needs to be updated when another extreme case indicating better stability performance appears. The reference case for PCICSI can also be updated regularly. The 'initial' best stability performance can be obtained from measurements during a day and then updated regularly (e.g., monthly, quarterly, annually, etc.), as the new measurements become available.

Due to the higher accuracy and applicability of PCICSI, especially in the case of the modified IEEE 68-bus test system and 4TNE system which will be used to investigate the overall impact of the advanced DSM on combined system stability, only PCICSI is adopted to assess combined system stability performance in the remaining part of this thesis.

6.5 Summary

In response to the need to assess multiple aspects of power system stability simultaneously, two composite stability indices (i.e., NEDS and PCICSI) have been introduced for the assessment of combined system stability by considering the distances to corresponding stability limits while simultaneously relying on the calculation of widely adopted stability indices for different stability aspects. Performances of the proposed composite stability indices are assessed by the MCS-based probabilistic stability assessment in three system models with various penetration levels of RES-based generation and different load models (i.e., constant power and constant impedance load models) in this chapter.

When the proposed composite stability indices are used to assess combined system stability performance, it has been found that NEDS and PCICSI can clearly evaluate combined system stability by indicating the distance of system operating points from the stability limits for a stable power system. Additionally, NEDS provides comparisons between the current operating point and the most probable situation, which makes it suitable for guiding the implementations of stability enhancement and improvement measures. However, when the system has unstable operating points, only PCICSI can clearly identify system instability and thus the applicability of PCICSI is higher than that

of NEDS.

When the proposed composite stability indices are adopted to assess the impacts of new technologies and devices (i.e., integration of RES-based generation and different load models in this chapter), the accuracy of NEDS decreases if the most probable situation changes significantly after the implementation of new technologies and devices. However, the direction of impact (i.e., beneficial or detrimental) on combined system stability is usually dominated by the most affected stability distance (aspect) in the case of PCICSI. Therefore, the overall accuracy and applicability of PCICSI is higher than that of NEDS.

Because the impact of the advanced DSM on combined system stability will be investigated based on the modified IEEE 68-bus test system and 4TNE system, and PCICSI has been proved to be more accurate and efficient than the NEDS, especially in the above-mentioned system models, the remaining part of the thesis will use PCICSI to evaluate combined system stability performance. The simultaneous assessment of rotor angle and frequency stability of a power system using composite stability indices is the fourth original contribution of this thesis.

7 The Impacts of Advanced Demand Side Management on Angular and Frequency Stability

7.1 Introduction

In Chapter 6, the PCICSI was proved to be more efficient and accurate than the NEDS, especially when power systems face the risk of instability. The PCICSI is thus adopted to assess the impacts of advanced DSM on combined system stability in this chapter. Moreover, the overall impacts of advanced DSM on the combined system stability performance under different operating and modelling conditions (e.g., RES baselines and the modelling of loads) are estimated on a daily basis, and a range of case studies have been developed to identify the critical factors (e.g., the modelling method of loads) that affect the impact of advanced DSM on combined system stability. All results illustrated to assess the impact of advanced DSM on combined system stability performances were obtained from MCS-based probabilistic stability assessments based on the modified IEEE 68-bus test system and 4TNE system discussed in Chapter 3. Finally, this chapter assesses and discusses system dynamic responses when the system transfers from pre-DSM to post-DSM operating points, which are usually neglected in DSM planning and implementing processes. The results of DSM activation transient period were obtained from either the MCS-based probabilistic stability assessments discussed in Section 5.4 or a random deterministic stability assessment selected from the MSC-based probabilistic stability assessments.

7.2 Case Studies

Seven case studies have been developed under different operating conditions to assess the effects of various factors (e.g., the location and capacity of advanced DSM) on the impact of advanced DSM on combined system stability so that the critical factors can be identified. All case studies and their corresponding important operating conditions are summarised in Table 7.1.

Table 7.1 Case studies

Case Studies	RES Baseline	DSM Capacity	Test System	Load Model (All Load Buses)	Note
Case 1	0%	18%	Modified IEEE-68	Constant Power	N/A
Case 2	30%	18%	Modified IEEE-68	Constant Power	N/A
Case 3	60%	18%	Modified IEEE-68	Constant Power	N/A
Case 4	60%	5%	Modified IEEE-68	Constant Power	Changed DSM Locations
Case 5	60%	21.6%	Modified IEEE-68	Constant Power	Increased DSM Capacity (1.2×)
Case 6	60%	18%	Modified IEEE-68	Composite	N/A
Case 7	8%	15.5%	4TNE	Constant Power	N/A

It can be noted from Table 7.1 that Cases 1, 2 and 3 are developed to investigate the impact of advanced DSM with different installed capacities of RES-based generation (RES penetration levels). All RES baselines in Table 7.1 are computed following (3.9), assuming that all RES-based generation units operate at the rated power (i.e., 2 MW). The real RES penetration level, however, can be lower than the baseline due to reduced wind speed. By sharing an identical RES baseline, Cases 3, 4, 5 and 6 focus on the impact of different modelling of the advanced DSM. More specifically, Cases 3 and 4 investigate the impact of different locations of flexible DSM assets on combined stability performance. It is worth noting here that the DSM capacity of Case 4 decreases to 5% (820 MW) of system peak demand due to the variation in locations of flexible DSM assets. The locations of flexible DSM assets in Case 4 are marked by blue circles and blue triangles in Fig. 7.1 for large IC and DN buses, respectively. The locations of flexible DSM assets in Case 3 (and all other remaining case studies developed based on the modified IEEE 68-bus test system) are represented by red circles and red triangles in Fig. 7.1 for large IC and DN

buses, respectively. The altered locations of flexible DSM assets are also determined based on [96], which identified and ranked load buses based on the impact of the variation in their real power demand on system stability performance.

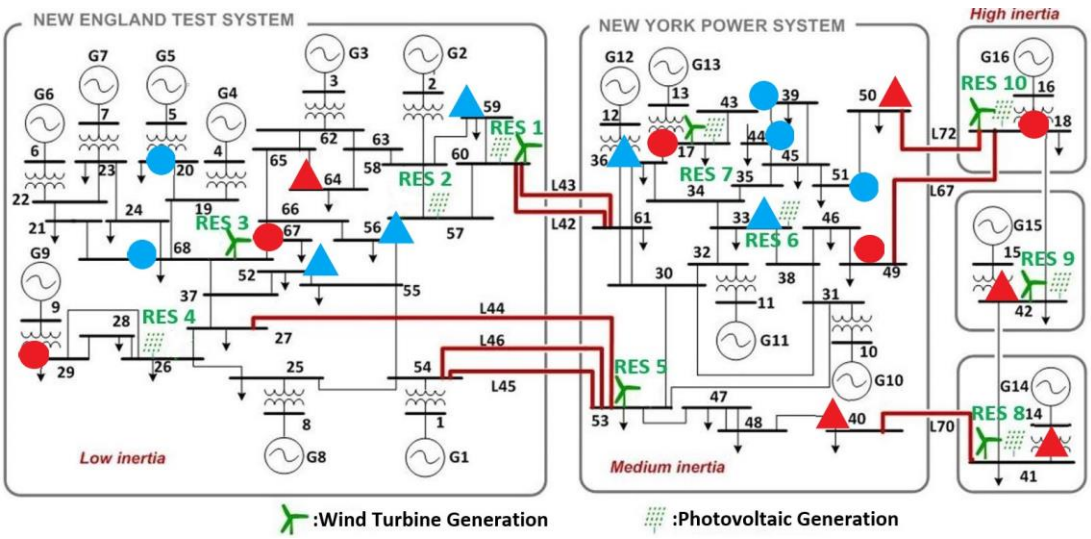

Figure 7.1 The modified IEEE 68-bus test system with the emphasised locations of flexible DSM assets (circles for large ICs and triangles for DNs)

Moreover, the total DSM capacity is increased by 20%, which results in a total DSM capacity of 21.6% (3751 MW) of system peak demand, in Case 5 to study the impact of increased DSM capacity.

In Case 6, which aims to assess and emphasise the importance of accurate and realistic load modelling, all flexible DSM processes and all system loads are modelled by a composite load model (i.e., a parallel connection of the static ZIP load and dynamic IM load). The proportions of the static ZIP load and dynamic IM load are determined according to Step 7 in Section 5.4, different load compositions can be observed from different locations (i.e., load buses), different operating points and implementations of DSM programs.

Finally, Case 7 focuses on more realistic situations in which system models and DSM implementations are either provided by or adopted through consultations with corresponding TSOs. It can be noted from Table 6.1 that most case studies (except Case 6) adopt a constant power load model because it is still the most widely adopted load model for system dynamic studies and it typically leads to the most conservative results.

[135].

7.3 Impacts of Advanced Demand Side Management on Individual Stability Aspects

Before assessing the impact of advanced DSM on the combined stability performance using the PCICSI, this section discusses and evaluates the impact of advanced DSM on individual stability aspects using the variations of the corresponding stability indices adopted in this thesis. More specifically, the percentage change of stability distance at the operating point i (Δx_i) has been calculated by (7.1), where x_i^d and x_i^w indicate stability distances after and before the implementation of advanced DSM, respectively.

$$\Delta x_i = \frac{x_i^d - x_i^w}{x_i^w} \times 100\% \tag{7.1}$$

Based on (7.1), a positive percentage change of stability distance (Δx_i) indicates that the stability distance has been increased, and thus the corresponding stability aspect has been improved by advanced DSM at the operating point i. By contrast, decreased stability distance and subsequently, deteriorated stability performance, are represented by a negative Δx_i.

7.3.1 Impacts of Advanced Demand Side Management on Small Disturbance Stability

It can be recalled from Section 2.2.1 of this thesis that small disturbance stability is assessed by damping of the most critical electromechanical mode. Hence, the impact of advanced DSM on small disturbance stability can be assessed by the percentage change of the damping-based stability distance at each operating point throughout the day.

Focusing on the modified IEEE 68-bus test system, the percentage changes of the damping-based stability distance are illustrated by the red dashed line, black dotted line and blue solid line for Cases 1, 2 and 3, respectively, in subplot (a) of Fig. 7.2. Similarly,

the percentage changes of the damping-based stability distance in Cases 3, 4, and 5 are illustrated by the blue solid line, red dashed line and black dotted line, respectively, in the subplot (b) of Fig. 7.2. Finally, the blue solid line and red dashed line in the subplot (c) of Fig. 7.2 represent the percentage changes of the damping-based stability distance in Case 3 and Case 6, respectively. Regarding the 4TNE system, the percentage changes of the damping-based stability distance of Case 7 are illustrated by the blue solid line in the subplot (d) of Fig. 7.2.

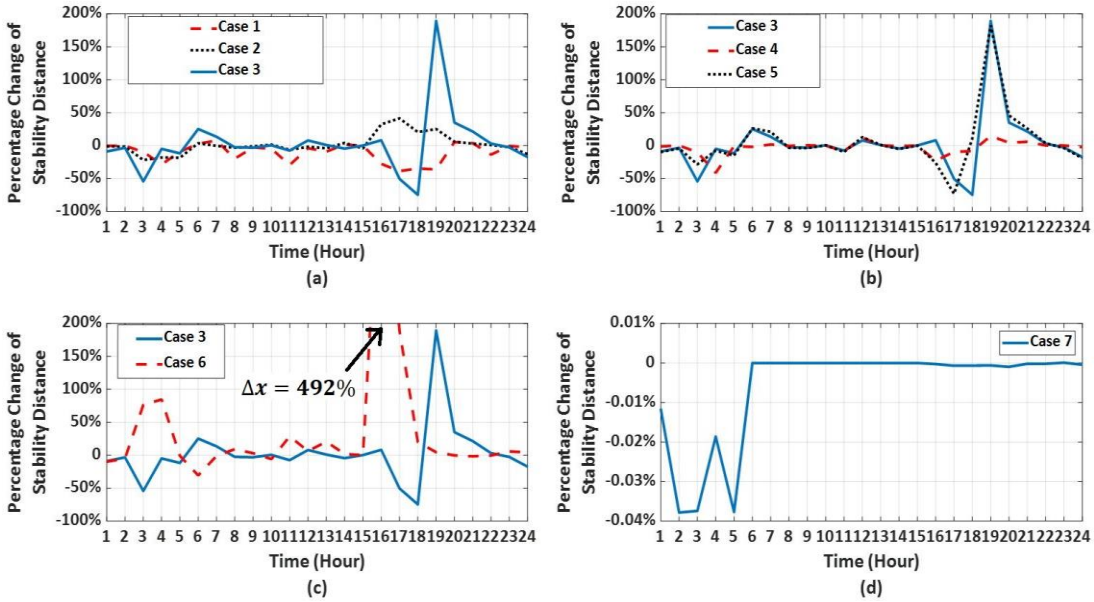

Figure 7.2 The percentage changes of the damping-based stability distance in Cases 1 to 3 (a), Cases 3 to 5 (b), Cases 3 and 6 (c) and Case 7 (d) at different operating points throughout the day

When the advanced DSM is implemented in power systems with different RES baselines, it can be noted from the subplot (a) of Fig. 7.2 that different RES baselines can lead to both quantitative (e.g., Hours 3 and 4) and qualitative (e.g., Hours 17 and 18) changes in the impact of advanced DSM. Similarly, quantitative (e.g., Hours 15 and 16) and qualitative (e.g., Hours 3 and 17) variations of the impact of advanced DSM are also noted when different load models are adopted (subplot (c) of Fig. 7.2). Moreover, focusing on the subplot (b) of Fig. 7.2, it can be noted from the blue solid line (Case 3) and black dotted line (Case 5) that increased DSM capacity are more likely to result in quantitative changes in the impact of advanced DSM. Meanwhile, the impact of advanced DSM on small disturbance stability is reduced in Case 4 due to the altered location of flexible DSM assets, and subsequently, reduced DSM capacity. Finally, in the

case of the 4TNE system (Case 7), small disturbance stability is more sensitive to demand payback effects (i.e., load reconnections) during off-peak hours. However, the impact of advanced DSM is minor compared with the case studies developed based on the modified IEEE 68-bus test system (subplots (a) to (c)).

In order to assess the distribution of the impact of advanced DSM on small disturbance stability, boxplots, which display data distribution based on five statistical values (i.e., minimum (Min), 25th percentile (Q1), median, 75th percentile (Q3) and maximum (Max) values) and outliers, are adopted in this thesis. An example of a boxplot is given in Fig. 7.3, and based on Fig. 7.3, the above-mentioned statistical values can be defined as follows:

- **Median value:** By sorting the data sample in ascending order, the median value is in the middle of the data sample.
- **25th percentile value (Q1):** By sorting the data sample in ascending order, the 25th percentile value is in the middle of the smallest value and the median value.
- **75th percentile value (Q3):** By sorting the data sample in ascending order, the 75th percentile value is in the middle of the median value and the largest value.
- **Minimum value (Min):** By calculating the difference between the 25th and 75th percentile values and defining it as an interquartile range (IQR), the minimum value is the smallest value between Q1-1.5×IQR and Q3+1.5×IQR.
- **Maximum value (Max):** The maximum value is the largest value between Q1-1.5×IQR and Q3+1.5×IQR.
- **Outliers:** Outliers are data points smaller than the minimum value or larger than the maximum value.

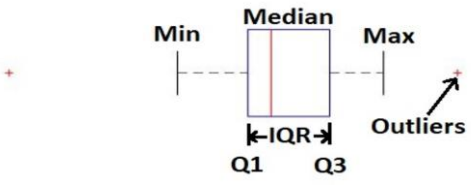

Figure 7.3 An example of a boxplot and the definitions of statistical values

The distributions of the percentage change of the damping-based stability distance in all case studies are illustrated in Fig. 7.4 as boxplots. It can be noted that small disturbance stability is more likely to deteriorate without RES-based generation (Case 1), and more beneficial effects of advanced DSM can be observed when the RES baseline increases (Cases 2 and 3). Furthermore, the impact of advanced DSM on small disturbance stability rises with the increase of the RES baseline, as the IQR of Case 3 is larger than the IQR of Case 2.

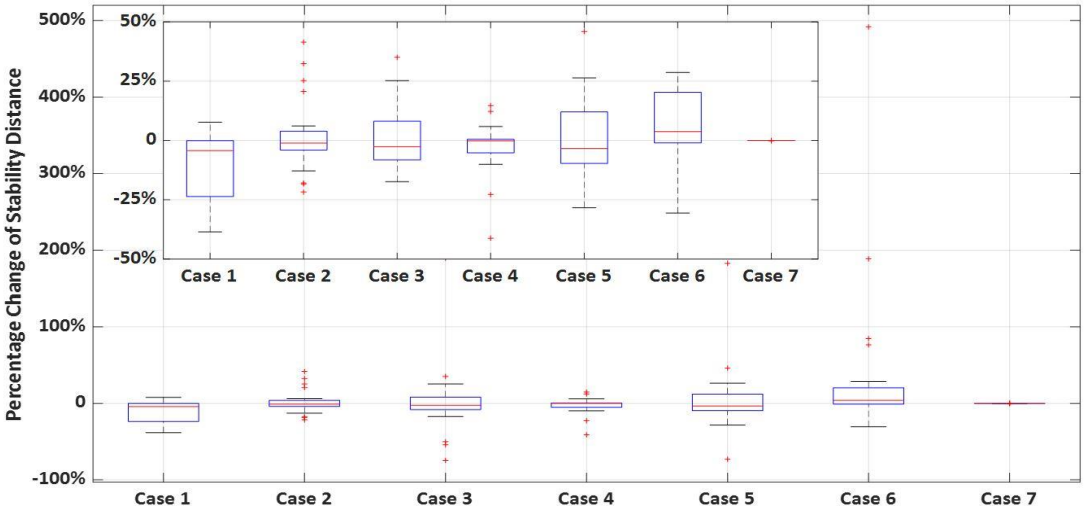

Figure 7.4 Boxplots of the percentage changes of the damping-based stability distance in all case studies

Moreover, it can be noted from Cases 3, 4 and 5 that altered locations of flexible DSM assets and reduced DSM capacity (Case 4) lead to decreased effects on small disturbance stability, while increased DSM capacity (Case 5) can heighten the impact of advanced DSM on small disturbance stability, as the IQR has been increased in Case 5. Regarding different load models, the median value of Case 6 (composite load model) is above zero, which indicates an improved stability performance. The median value of Case 3 (constant power load model) is below zero, indicating a deteriorated stability performance. Therefore, an accurate and realistic load model is one of the most important factors when assessing the impact of advanced DSM on small disturbance stability. As discussed previously, advanced DSM has very limited impact on small disturbance stability in the case of the 4TNE system (Case 7). Hence, the boxplot developed for Case 7 is much smaller compared with other case studies.

7.3.2 Impacts of Advanced Demand Side Management on Transient Stability

It can be recalled from Section 2.2.2 of this thesis that system transient stability is assessed by the transient stability index (TSI). Therefore, the impact of advanced DSM on transient stability can be assessed by the percentage change of the TSI-based stability distance at each operating point throughout the day.

In order to assess the impact of advanced DSM on transient stability with different RES baselines, the percentage changes of the TSI-based stability distance in Cases 1, 2 and 3 are illustrated as the red dashed line, black dotted line and blue solid line, respectively, in the subplot (a) of Fig. 7.5. In the subplot (b) of Fig. 7.5, the percentage changes of the TSI-based stability distance in Cases 3, 4 and 5 are illustrated as the blue solid line, red dashed line and black dotted line, respectively, to investigate the impact of advanced DSM with different locations and capacities. The subplot (c) of Fig. 7.5 focuses on studying the impact of load models by comparing transient stability variations in Case 3 (blue solid line) with Case 6 (red dashed line), and the subplot (d) of Fig. 7.5 concentrates on the impact of advanced DSM in a more realistic power system model (Case 7).

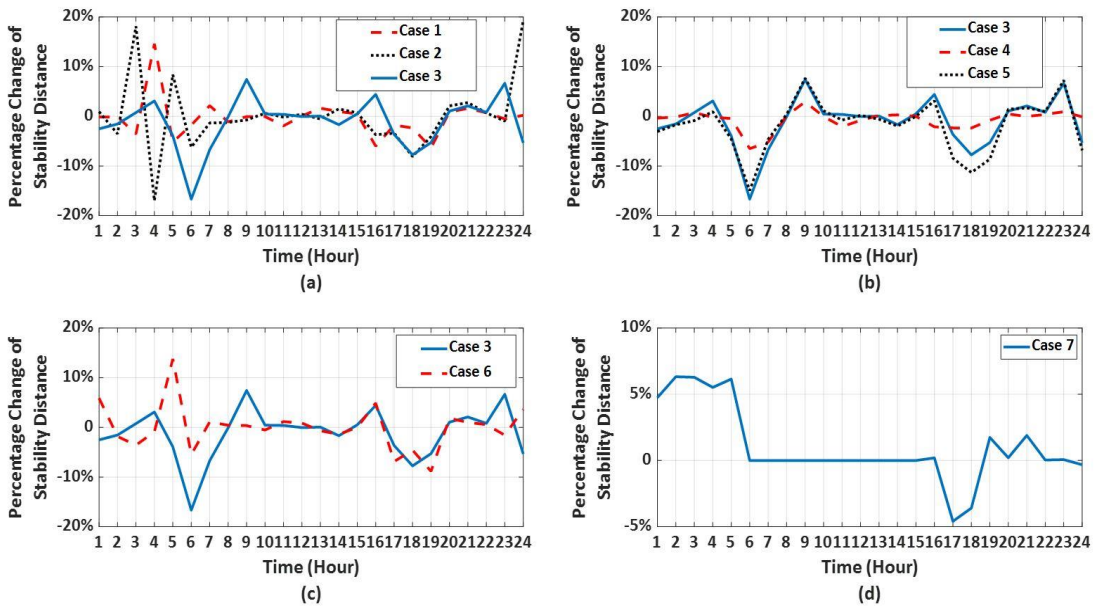

Figure 7.5 The percentage changes of the TSI-based stability distance in Cases 1 to 3 (a), Cases 3 to 5 (b), Cases 3 and 6 (c) and Case 7 (d) at different operating points throughout the day

Similar to the findings obtained from small disturbance stability, different RES baselines can lead to both quantitative (e.g., Hours 6 and 21) and qualitative (e.g., Hours 4 and 5) changes in the impact of advanced DSM on transient stability. According to the subplot (b) of Fig. 7.5, the back dotted line (Case 5) basically follows the blue solid line (Case 3), which means that increased DSM capacity leads to only quantitative variations of the effects of advanced DSM. It can also be noted from the subplot (b) of Fig. 7.5 that the impact of advanced DSM on transient stability has been decreased by altering the locations of flexible DSM assets (red dashed line), which further leads to decreased DSM capacity. Additionally, opposite impacts of advanced DSM caused by different load models can be observed at most off-peak hours. For instance, system transient stability deteriorates at Hour 5 because of the demand payback effect when a constant power load model is adopted (Case 3), while the red dashed line indicates an improved transient stability performance at Hour 5 in the case of the composite load model. Regarding peak hours, different load models lead to quantitative changes of the impact of advanced DSM on transient stability. In Case 7, system transient stability can be improved during off-peak hours because of the demand payback effect, but either improved or deteriorated during peak hours as a result of load curtailment.

The distributions of the percentage change of the TSI-based stability distance are illustrated as boxplots in Fig. 7.6 for all case studies.

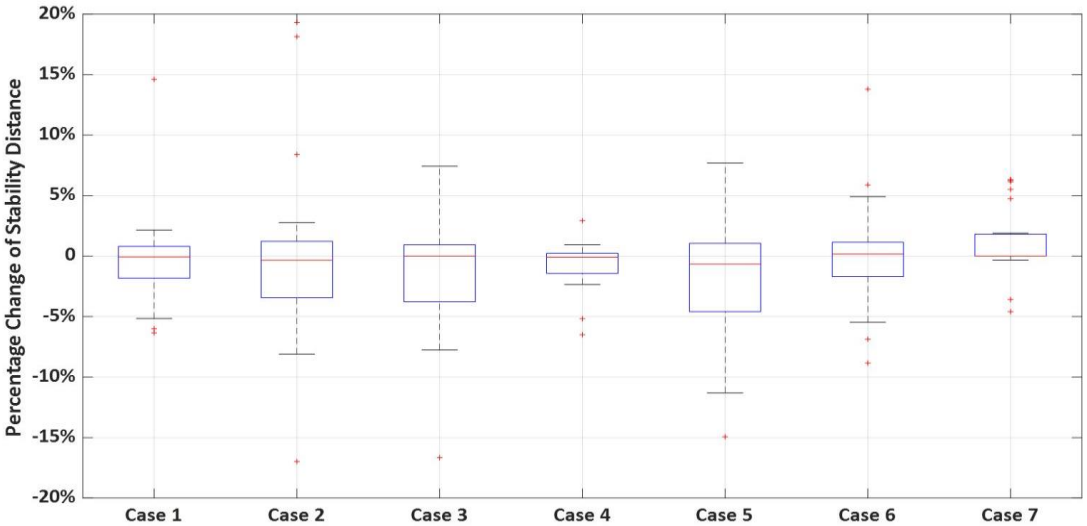

Figure 7.6 Boxplots of the percentage changes of the TSI-based stability distance in all case studies

Based on Fig. 7.6, system transient stability is more sensitive to advanced DSM when the system is operated with RES-based generation as Cases 2 and 3 exhibit larger IQRs. Focusing on Case 3, it can be noted that the median value (represented by the red lines in boxplots) is around zero, while the magnitude of the 25^{th} percentile value (Q1) is much larger than the magnitude of the 75^{th} percentile value (Q3). These phenomena indicate that system transient stability has roughly the same possibility of improving or deteriorating, and the detrimental impact on transient stability is more significant than the beneficial one when the system is operated with a high RES baseline. With the increase in DSM capacity (Case 5), the median value drops below zero, which means that the system is more likely to deteriorate in this case. Moreover, increased DSM capacity also results in a larger IQR compared with Case 3; hence, the impact of advanced DSM on transient stability can be heightened by increased DSM capacity. By contrast, reduced DSM capacity caused by variations in the location of flexible DSM assets leads to a significantly reduced impact on transient stability in Case 4. Similarly, the impact of advanced DSM on transient stability can also be reduced by the adoption of a composite load model (Case 6) as the inflexible load model (i.e., constant power load) has been substituted by a more flexible load model (i.e., composite load). Finally, the beneficial impacts of advanced DSM are more significant than the detrimental impacts, based on a more realistic system model (i.e., the 4TNE system).

7.3.3 Impacts of Advanced Demand Side Management on Frequency Stability

It can be recalled from Section 2.2.3 of this thesis that system frequency stability is assessed by the frequency nadir (FN) and the rate of change of frequency (RoCoF). The impact of advanced DSM on frequency stability can thus be assessed by the percentage changes of both the FN-based stability distance and the RoCoF-based stability distance at each operating point throughout the day.

The percentage changes of the FN-based stability distance and the RoCoF-based stability distance are illustrated in Fig. 7.7 and Fig. 7.8, respectively. The percentage changes of

Cases 1, 2 and 3 are illustrated as red dashed lines, black dotted lines and blue solid lines, respectively, in subplots (a) of Fig. 7.7 and Fig. 7.8, while the percentage changes of Cases 3, 4 and 5 are illustrated as blue solid lines, red dashed lines and black dotted lines, respectively, in subplots (b) of Fig. 7.7 and Fig. 7.8. In subplots (c) of Fig. 7.7 and Fig. 7.8, the percentage changes of Cases 3 and 6 are represented by blue solid lines and red dashed lines, respectively. The impact of advanced DSM on frequency stability based on the 4TNE system is illustrated in subplots (d) of Fig. 7.7 and Fig. 7.8.

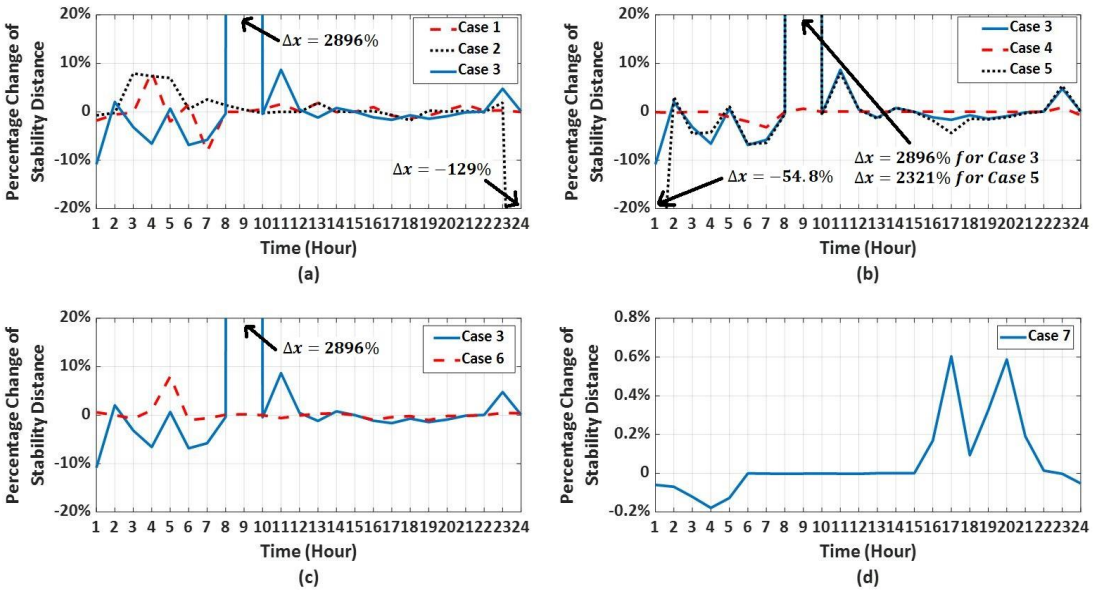

Figure 7.7 The percentage changes of the FN-based stability distance in Cases 1 to 3 (a), Cases 3 to 5 (b), Cases 3 and 6 (c) and Case 7 (d) at different operating points throughout the day

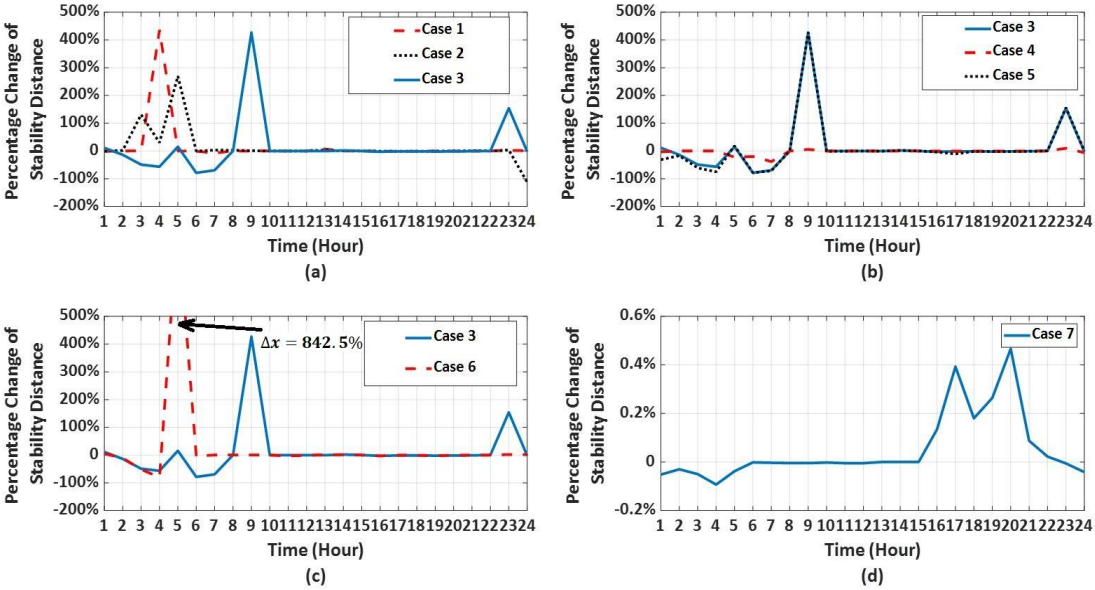

Figure 7.8 The percentage changes of the RoCoF-based stability distance in Cases 1 to 3 (a), Cases 3 to 5 (b), Cases 3 and 6 (c) and Case 7 (d) at different operating points throughout the day

It can be noted from subplots (a) of Fig. 7.7 and Fig. 7.8 that different RES baselines affect not only the magnitudes of the impact of advanced DSM on frequency stability, but also the directions (i.e., beneficial and detrimental) of the impact of advanced DSM. For instance, system frequency stability, assessed by both FN and RoCoF, is more likely to be improved by demand payback effects around off-peak hours when the RES baseline is relatively low (Cases 1 and 2). However, when the RES baseline increases to 60% (Case 3), both FN and RoCoF indicate that system frequency stability is more likely to deteriorate around off-peak hours due to demand payback effects. This is caused by the low system inertia during off-peak hours as a result of low capacity of synchronous generation and high capacity of RES-based generation. It should be noted here that advanced DSM contributes positively to system frequency stability at Hour 9. Note: An extremely high percentage change of stability distance can be observed at Hour 9 because the stability distance before the DSM (x_i^w in (7.1)) is very low.

Regarding the location and capacity of flexible DSM assets, it can be noted from subplots (b) of Fig. 7.7 and Fig. 7.8 that the impacts of advanced DSM on frequency stability without and with increased capacity are very similar except for Hour 1, in which increased DSM capacity can endanger system frequency stability. When the locations of flexible DSM assets are altered, both the DSM capacity and locations of system disturbances (modelled as the reconnection of DSM assets) are affected. Consequently, the system remains stable throughout the day, and the impact of advanced DSM on frequency stability is smaller as a result of reduced DSM capacity. Moreover, the use of a composite load model (Case 6) can also help the system to remain stable due to its more flexible load characteristics, and lead to both quantitative and qualitative variations in the impact of advanced DSM on frequency stability compared with a constant power load model (Case 3).

Focusing on the 4TNE system (Case 7), frequency stability can deteriorate during off-peak hours by demand payback effects and improve during peak hours as a result of load curtailments. Comparing the impact of advanced DSM based on the modified IEEE 68-bus test system (Cases 1 to 6) with the 4 TNE system (Case 7), it can be noted that system frequency stability is more vulnerable to DSM implementations during off-peak hours in the case of the modified IEEE 68-bus test system, while the impact of advanced DSM on

frequency stability is more significant during peak hours based on the 4TNE system.

The distributions of the percentage change of FN-based and RoCoF-based stability distances are illustrated as boxplots in Fig. 7.9 and Fig. 7.10, respectively, for all case studies.

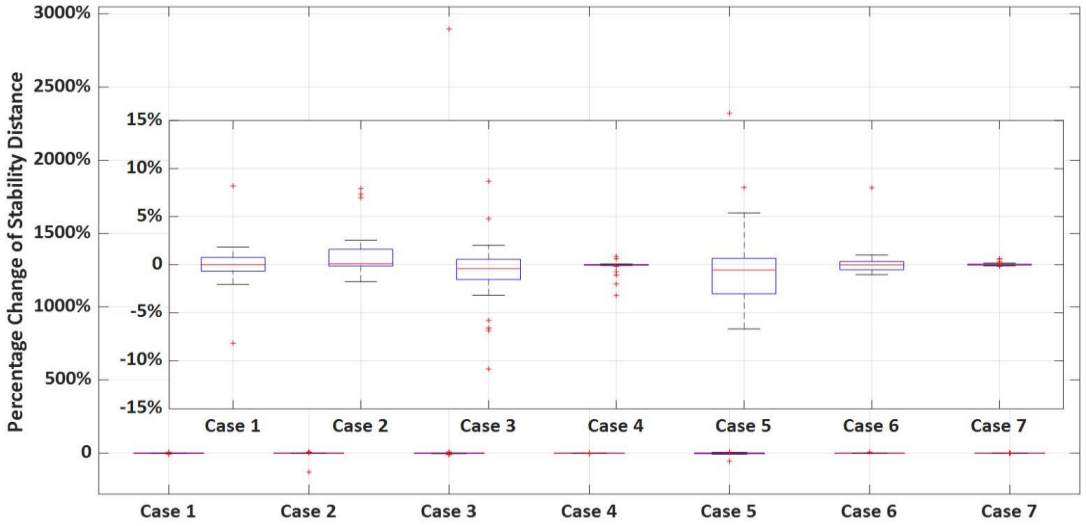

Figure 7.9 Boxplots of the percentage changes of the FN-based stability distance in all case studies

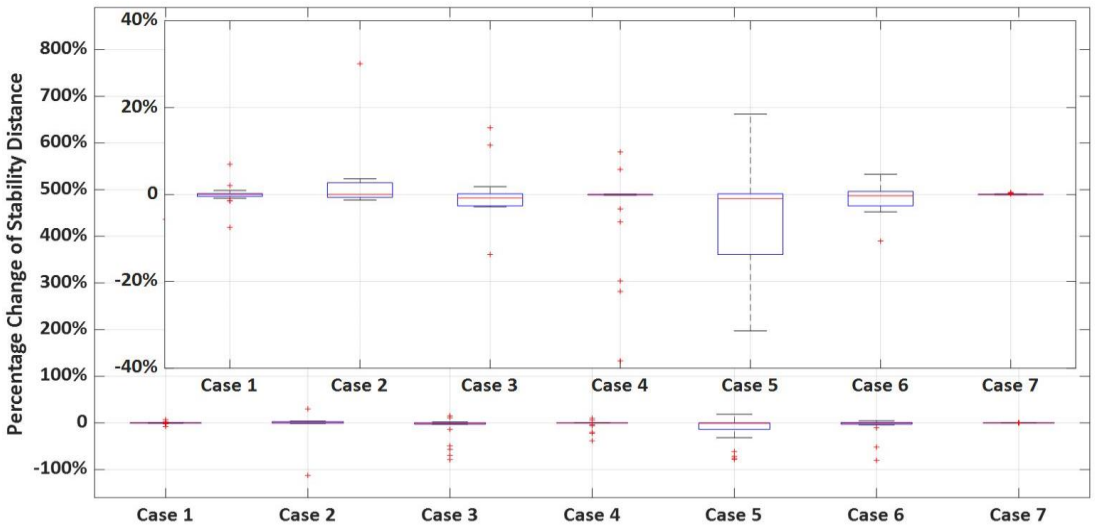

Figure 7.10 Boxplots of percentage changes of the RoCoF-based stability distance in all case studies

According to Fig. 7.9 and Fig. 7.10, the beneficial impact of advanced DSM is more significant than the detrimental impact when the system RES baseline is 30% (Case 2). However, when the RES baseline increases to 60% (Case 3), system frequency stability is more likely to deteriorate due to advanced DSM because the median value drops below

zero. Furthermore, the impact of advanced DSM on frequency stability can be further heightened by increasing DSM capacity (Case 5); and reduced by altering the location of flexible DSM assets (Case 4) and adopting composite load model (Case 6). The impact of advanced DSM is also minor for the 4TNE system (Case 7) compared with the modified IEEE 68-bus test system (Cases 1 to 6). Finally, the percentage changes of stability distance can be extremely high if the power system is very close to the stability limit before the DSM. These situations are considered as the extreme cases and illustrated by the outliers in Figs. 7.9 and 7.10.

In summary, this section assesses the impact of advanced DSM and several important factors (e.g., RES baselines and the modelling of loads) on small disturbance, transient and frequency stability by studying the variation and distribution of the percentage changes of individual stability distances. Based on Figs. 7.2 to 7.10, some important conclusions can be obtained:

- The advanced DSM (i.e., load shifting) adopted in this thesis can either improve or deteriorate individual stability aspects at different operating points. Furthermore, the effects of advanced DSM tend to be greater during demand payback hours (i.e., off-peak hours). In certain circumstances, appropriate DSM implementation can stabilise the power system. On the other hand, inappropriate DSM implementation can lead to system instability.

- Different RES baselines and different load models can result in both quantitative and qualitative changes in the impact of advanced DSM on individual stability aspects. The greater impact of advanced DSM is usually obtained when the system operates with a higher RES baseline.

- Variations of DSM capacity usually lead to quantitative changes of the impact of advanced DSM. The locations of flexible DSM assets can affect the impact of advanced DSM by changing the DSM capacity and, they may also stabilise the system by altering the locations of system disturbances (i.e., load reconnection). The greater impact of advanced DSM is usually caused by the larger DSM capacity.

- The impact of advanced DSM is more significant based on the IEEE test system

probably due to the larger DSM capacity (18% of peak demand for the modified IEEE 68-bus test system compared with 15.5% of peak demand for the 4TNE system), wider application (23/24 hours for the modified IEEE 68-bus test system compared with 14/24 hours for the 4TNE system) and higher penetration of RES-based generation (30% or 60% in the modified IEEE 68-bus test system compared with 8% in the 4TNE system).

7.4 Impacts of Advanced Demand Side Management on Combined System Stability

This section adopts the proposed PCICSI, which has been discussed in Section 2.3.2 and verified in Chapter 6, to assess the impact of advanced DSM on combined system stability by considering small disturbance, transient and frequency stability simultaneously. The first part of this section focuses on illustrating the combined system stability performance using the PCICSI, while the second part of this section assesses the impact of advanced DSM on combined system stability at different operating points in different case studies. The third part of this section quantifies the overall impact of advanced DSM on a daily basis to identify critical factors (case studies).

7.4.1 Illustration of Combined System Stability Using Composite Stability Index

By adopting and performing MCS-based probabilistic stability assessments discretely (i.e., hourly) throughout the day, the combined system stability performance is assessed by the PCICSI at each hour. Due to the lack of operational information on both test and equivalent systems at shorter time intervals (to an extent) and the high computational cost (mostly) associated with performing MCS-based probabilistic stability assessments, the stability assessment is performed and illustrated for discrete hours. The hourly variation of the PCICSI in Fig. 7.11 is presented by a continuous curve (instead of bar charts for example) to improve the clarity of the presentation. In doing so, an assumption

has been made that the combined system stability performance changes linearly from one operating point to the next. The accuracy of the illustration of the results can be easily improved, albeit at a high computational cost, by performing dynamic simulations at reduced timescales (e.g., every 15 minutes or every 5 minutes) with more detailed and accurate modelling of operational uncertainties (e.g., wind speed). Even though the accuracy of the illustration and the calculation of the effect of DSM would improve, the trend and indication of the size of the effect can still be captured by hourly assessment and the adopted continuous line representation.

The daily combined system stability performance for different case studies is illustrated in the different subplots of Fig. 7.11.

It can be noted from blue solid lines (combined system performance at pre-DSM operating points) in subplots (a) to (c) of Fig. 7.11 that the integration of RES-based generation leads to either improved (larger PCICSI values) or deteriorated (smaller PCICSI values) combined system stability performance. With a high RES baseline (Case 3), the system can be unstable at a certain operating point (i.e., Hour 9 in the subplot (c)). The combined system stability performance is also affected by the load models adopted. When the system loads are modelled as a composite model (blue solid line in the subplot (f) of Fig. 7.11), combined system stability is usually better than that in the case of a constant power load model (blue solid line in the subplot (c) of Fig. 7.11) due to increased proportions of more flexible load characteristics (e.g., constant impedance load and dynamic IM). Especially at Hour 9, unstable operating point observed in the case of a constant power load model has been stabilised by adopting a composite load model.

Additionally, it can be noted from the subplot (g) of Fig. 7.11 that the combined system stability performance of the 4TNE system is more stable throughout the day. The smaller variation of combined system stability performance (PCICSI) can be explained by the much smaller penetration of RES-based generation (8% in the 4TNE system compared with 30% and 60% in the modified IEEE 68-bus test system) and the smaller difference between power demand values of demand valley and demand peak (0.34 p.u. in the 4TNE system compared with 0.5 p.u. in the modified IEEE 68-bus test system). Moreover,

the reduced size of disturbances adopted for the frequency assessments may also lead to insignificant variations in the combined system stability performance. More specifically, the average size of disturbances adopted for frequency stability assessment is 9.5% (with a maximum value of 16%) of the total demand at the corresponding operating point in the modified IEEE 68-bus test system. In the case of the 4TNE system, the average size of disturbances adopted for frequency stability assessment is 6% (with a maximum value of 9%) of the total demand at the corresponding operating point.

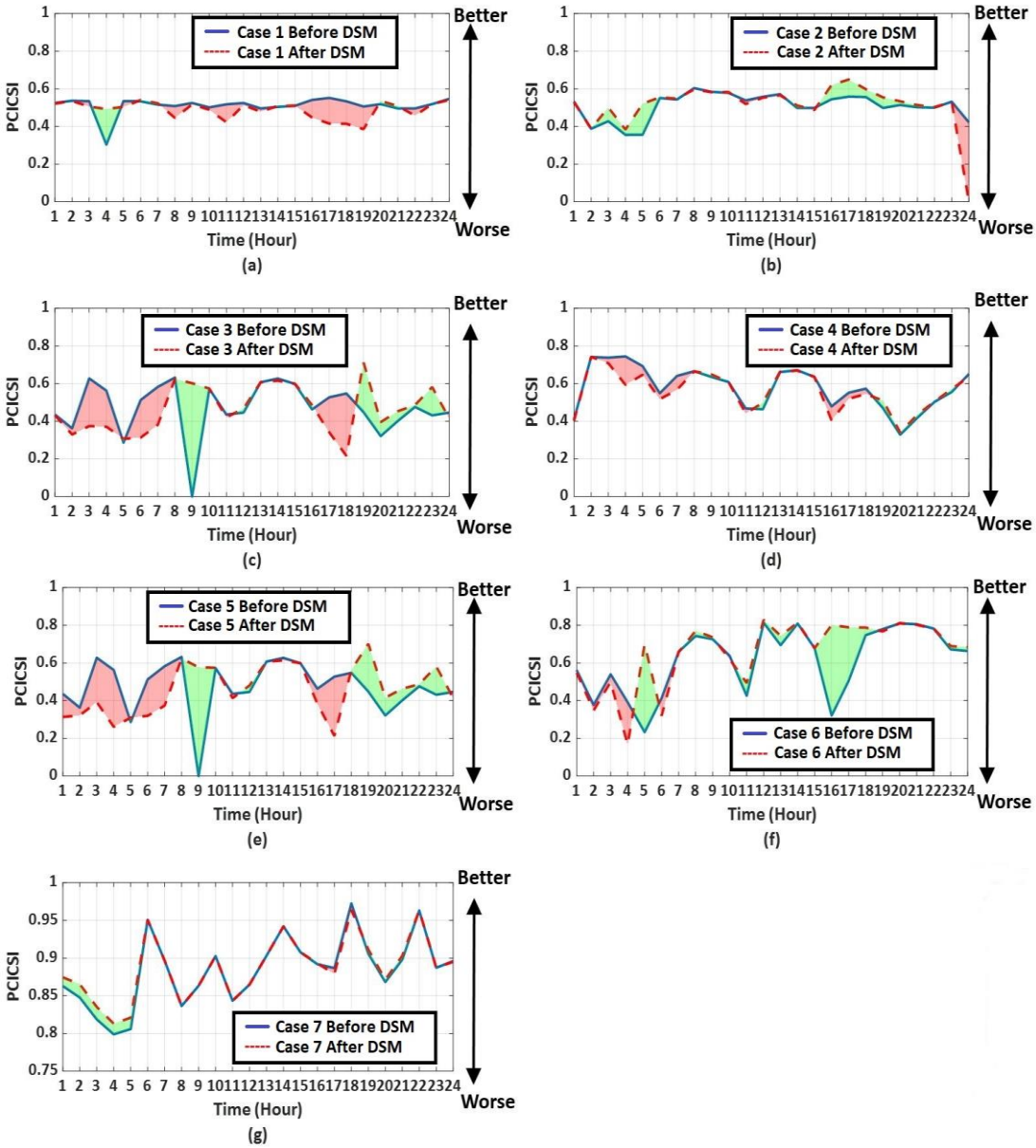

Figure 7.11 Combined system stability performance illustrated by PCICSI curves for Case 1 (a), Case 2 (b), Case 3 (c), Case 4 (d), Case 5 (e), Case 6 (f) and Case 7 (g)

7.4.2 Assessment of the Impact of Advanced Demand Side Management on Combined System Stability

By representing the daily combined system stability performances as daily PCICSI curves before/after DSM deployment, the impact of advanced DSM on combined system stability can be illustrated by the areas between the PCICSI curves of pre-DSM (before the implementations of advanced DSM) and post-DSM (after the implementations of advanced DMS) operating points. When the PCICSI curve with advanced DSM is higher than (above) the curve without advanced DSM, combined system stability improves, and such areas are marked by green backgrounds in Fig. 7.11 for all case studies. On the other hand, when the PCICSI curve with advanced DSM is lower than (below) the curve without advanced DSM, combined system stability deteriorates, and such areas are marked by red backgrounds in Fig. 7.11 for all case studies.

Based on subplots (a) to (c) of Fig. 7.11, it can be noted that advanced DSM mainly leads to improved stability performance around off-peak hours in Case 1 (subplot (a) of Fig. 7.11) for the test system without RES-based generation. When the test system is operated with a 30% RES baseline (Case 2), advanced DSM usually improves the combined system stability even during peak hours. However, the demand payback effect leads to system instability at Hour 24 in this case. In Case 3 (subplot (c) of Fig. 7.11), implementations of advanced DSM could either improve or deteriorate combined system stability performance and stabilise an unstable operating point (Hour 9).

The impacts of advanced DSM in Cases 4 (subplot (d) of Fig. 7.11) and 5 (subplot (e) of Fig. 7.11) are similar to Case 3, except the unstable operating point has been removed in Case 4 and consequently, advanced DSM no longer stabilises unstable operating points. Comparing Cases 3 (subplot (c) of Fig. 7.11) and 6 (subplot (f) of Fig. 7.11), combined system stability is more likely to be improved by adopting composite load models. Finally, it can be noted from the subplot (g) of Fig. 7.11 that the beneficial impact of advanced DSM is more significant during off-peak hours based on the 4TNE system. Although combined system stability can either improve or deteriorate during peak hours, the impact of advanced DSM is minor compared with off-peak hours.

Recalling from Section 7.3, the impacts of advanced DSM and different operational and modelling factors on individual stability aspects are assessed by the percentage change of the stability distance at each operating point. Similarly, the impact of advanced DSM on combined system stability can be quantified by percentage changes of the PCICSI at different operating points. The percentage change of the PCICSI regarding the operating point i (ΔX_i) is calculated as (7.2), where X_i^d and X_i^w are the PCICSI values after and before DSM implementation, respectively.

$$\Delta X_i = \frac{X_i^d - X_i^w}{X_i^w} \times 100\% \tag{7.2}$$

According to (7.2), improved combined system stability exhibits a larger PCICSI value after the DSM implementation and subsequently, positive percentage change values. In contrast, a negative value of the percentage change indicates a decreased PCICSI value and deteriorated combined system stability due to advanced DSM. In this thesis, PCICSI combines and balances the impacts of advanced DSM on different stability aspects (indices) assuming all stability aspects (indices) are equally important. Consequently, some small detrimental impacts of advanced DSM will be hided in PCICSI if other stability aspects have been improved significantly. Different weighting factors can be developed and introduced to represent different importance of individual stability aspects (indices) and avoid unreasonable assessments of combined system stability performance. Developing accurate weighting factors for PCICSI is considered as one of the most important future areas of research to extend the work discussed in this thesis.

The impacts of advanced DSM on combined system stability with different RES baselines are illustrated in the subplot (a) of Fig. 7.12, in which Cases 1 to 3 are represented by the red dashed line, black dotted line and blue sold line, respectively. In the subplot (b) of Fig. 7.12, the blue solid line, red dashed line and black dotted line are used to illustrate the impact of advanced DSM on combined system stability for Cases 3, 4 and 5, respectively. The subplot (c) of Fig. 7.12 focuses on illustrating the impacts of different load models (the blue solid line for the constant power load model and the red dashed line for the composite load model) and the subplot (d) illustrates the impact of advanced DSM based on the 4TNE system (Case 7).

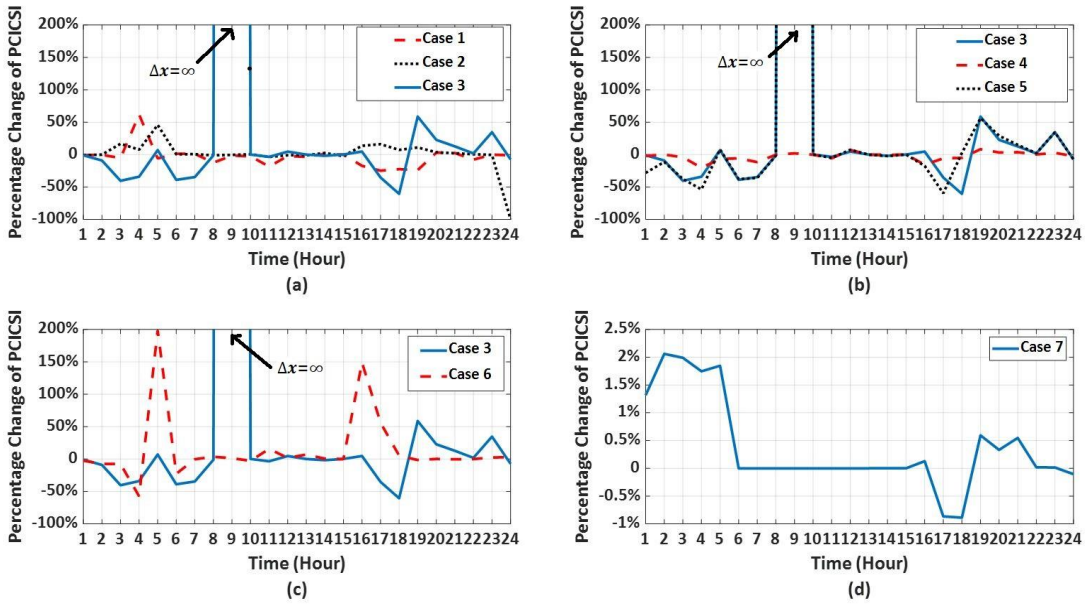

Figure 7.12 The percentage changes of the PCICSI in Cases 1 to 3 (a), Cases 3 to 5 (b), Cases 3 and 6 (c) and Case 7 (d) at different operating points throughout the day

It can be noted from the subplot (a) of Fig. 7.12 that RES baselines can affect both the magnitude and direction (beneficial or detrimental) of the impact of advanced DSM on combined system stability. More specifically, demand payback effects usually lead to improved combined system stability with relatively low RES baselines (0% in Case 1 and 30% in Case 2) and deteriorated combined system stability with a relatively high RES baseline (60% in Case 3). Moreover, qualitative changes of the impact of advanced DSM on combined system stability can be also observed around peak demand (i.e., Hour 17) as a consequence of different RES baselines.

Likewise, different load models adopted to model DSM implementations and system loads also lead to significantly varied impacts of advanced DSM. At Hour 5 and Hour 16, composite load model (Case 6) exhibits a much larger beneficial impact on combined system stability. At Hour 17, combined system stability can improve and deteriorate in the case of the composite load model (Case 6) and the constant power load model (Case 3), respectively. Therefore, the system RES baseline and the modelling of demand are critical for assessing the impact of advanced DSM, as they both result in not only quantitative, but also qualitative changes of the result, which may further affect the planning and implementation of DSM programs.

Regarding the impact of DSM capacity and locations of flexible DSM assets, it can be

noted from the subplot (b) of Fig. 7.12 that the black dotted line (Case 5) basically follows the blue solid line (Case 3), indicating that DSM capacity mostly results in only quantitative variations in the DSM impact. Before analysing the impact of the DSM location, it is worth noting here that the percentage change of the PCICSI is infinite at Hour 9 in Case 3 because the system loses stability before the implementation of DSM (i.e., X_i^w=0). By altering the locations of flexible DSM assets, DSM capacity and the potential locations of system disturbance, which has been modelled as reconnections of flexible DSM assets, are changed. Consequently, the combined system stability performance in pre-DSM operating points and the impact of advanced DSM can both be affected by the locations of flexible DSM assets.

Finally, combined system stability based on the 4TNE system can be improved using load reconnections during off-peak hours, but it can either improve or deteriorate due to load curtailments during peak hours. Comparing the impact of advanced DSM on individual stability aspects (subplots (d) of Figs. 7.2, 7.5, 7.7 and 7.8) with combined system stability (subplot (d) of Fig. 7.12), it can be found that combined system stability is dominated by transient stability because it is the most sensitive stability aspect and exhibits much larger percentage changes due to the implementation of advanced DSM.

In order to study the distribution of the impact of advanced DSM on combined system stability, boxplots, as shown in Fig. 7.13, are produced to cover all the percentage changes of the PCICSI illustrated in Fig. 7.12.

Focusing on Cases 1 to 2, it can be noted from Fig. 7.13 that an increased RES baseline (Case 2) leads to a decreased DSM impact on combined system stability, as the IQR has been reduced in Case 2. Moreover, because the median value (red line) and 25th percentile value (lower edge of the blue box) almost overlapped in Case 2, the beneficial impact of advanced DSM is more significant than the detrimental impact. However, when the RES baseline further increases to 60% (Case 3), the IQR has been significantly increased, which indicates that the system combined stability performance is more sensitive to advanced DSM with high RES baselines. Additionally, the 25th percentile value is significantly reduced in Case 3 and the median value is closer to the 75th percentile value. These phenomena indicate that the detrimental impact of advanced

DSM on combined system stability is more significant than the beneficial impact in this case.

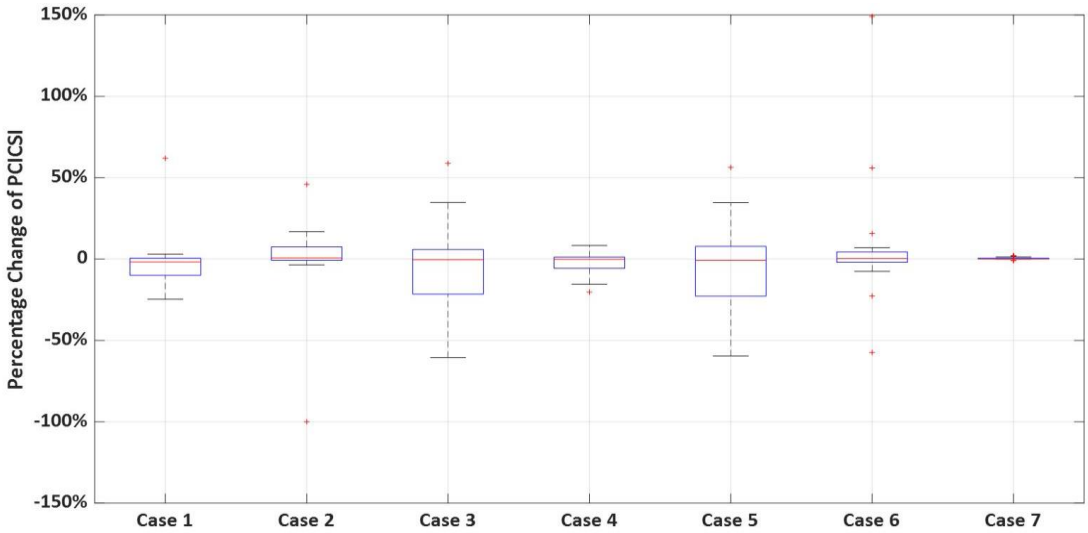

Figure 7.13 Boxplots of the percentage changes of the PCICSI in all case studies

The similar boxplots in Cases 3 and 5 prove that DSM capacity mostly leads to only quantitative changes in the DSM impact. The impact of advanced DSM can be significantly reduced due to the altered location of flexible DSM assets and reduced DSM capacity (Case 4). Comparing Case 3 with Case 6, it can be noted that the distribution of percentage changes of the PCICSI is more concentrated in Case 6, although significantly affected combined system stability performances are indicated by outliers. As discussed previously, the impact of advanced DSM based on the 4TNE system is minor compared with other case studies based on the modified IEEE 68-bus test system.

7.4.3 Quantification of the Overall Impact of Advanced Demand Side Management on Combined System Stability

In subsection 7.4.2, the impact of advanced DSM on combined system stability has been quantified by the percentage change of the PCICSI at each operating point. This subsection, however, focuses on the daily overall impact of advanced DSM on combined system stability.

As the beneficial and detrimental impacts of advanced DSM have been represented by the green and the red areas illustrated in Fig. 7.11, the overall impact of advanced DSM on combined system stability throughout the day can be quantified as the difference between the sum of green areas and the sum of red areas. A negative result indicates a detrimental overall impact of advanced DSM on combined system stability while a positive result represents an overall beneficial impact of advanced DSM. The quantified overall impact of advanced DSM on combined system stability is summarised in Table 7.2 for all case studies. As discussed earlier, the accuracy of this assessment can be improved by using smaller time steps (e.g., every 15 minutes) to assess the composite stability index.

Table 7.2 The quantified overall impact of advanced DSM on combined system stability

Case Study	Quantified Overall Impact	Case Study	Quantified Overall Impact
Case 1	-0.54	Case 5	-0.28
Case 2	+0.32	Case 6	+1.03
Case 3	-0.24	Case 7	+0.07
Case 4	-0.37		

It can be noted from Table 7.2 that the most detrimental impact of DSM is found in Case 1 when the system is free of RES-based generation. When the system RES baseline increases to 30% (Case 2), the overall impact of advanced DSM becomes positive (i.e., beneficial); however, advanced DSM causes combined system stability to deteriorate again as the RES baseline further increases to 60% (Case 3). Furthermore, the detrimental impact of advanced DSM in the case of high RES baselines (Case 3) is slightly heightened by increased DSM capacity (Case 5). Regarding Case 4, Table 7.2 indicates a more significant detrimental impact with altered locations of flexible DSM assets, even though the impact of advanced DSM on combined system stability has been reduced due to decreased DSM capacity (from 3125.8 MW in Case 3 to 820 MW in Case 4). The reason for this conflict is that the unstable pre-DSM operating point has been removed in Case 4 because of the altered locations of disturbance. Hence, the significant beneficial impact, which compensates for the overall detrimental impact of advanced DSM in Case 3, is missing in Case 4. Finally, a more significant overall impact of advanced DSM is obtained in Case 4.

In Case 6, advanced DSM significantly improves the combined system stability

performance throughout the day. The beneficial impact of advanced DSM in the case of the composite load model is more significant than all other detrimental impacts observed in other case studies. The significant quantitative differences in the impacts of advanced DSM in Cases 3 and 6 emphasise the importance of the accurate modelling of demand when studying the impact of DSM on system stability performance. Focusing on the 4TNE system (Case 7), the impact of advanced DSM on combined system stability is found to be minor due to the limited DSM implementation (14/24 hours rather than 23/24 hours in the case of the modified IEEE 68-bus test system) dictated by the size, availability and flexibility of the real-world DSM assets, relatively smaller sizes of actual system disturbances and the much lower penetration of RES-based generation that impacts the overall system dynamic response.

In summary, by assessing the impact of advanced DSM on combined system stability using the proposed composite stability index (i.e., PCICSI) and investigating the impact of advanced DSM in case studies with different RES baselines, locations of flexible DSM assets, DSM capacities and load models, the following conclusions can be obtained:

- The combined system stability, which considers small disturbance, transient and frequency stability simultaneously, can either improve or deteriorate due to the advanced DSM adopted in this thesis. Inappropriate implementations of advanced DSM can lead to system instability, while unstable system operating points can be stabilised by appropriate implementations of advanced DSM. The actual effect of the advanced DSM depends on the capacity and location of the flexible DSM assets, RES-based generation baselines and modelling of loads.

- Among all operational and modelling factors considered in this thesis, the RES baseline and modelling of demand are critical for assessing the DSM impact, as they both result in qualitative changes in the result. They should be defined as realistically as possible in real-world planning and implementation of DSM programs.

- Locations of flexible DSM assets and DSM capacity mostly affect the magnitude of the impact of advanced DSM, while the direction of the impact (beneficial or detrimental) remains the same.

- The impact of advanced DSM on the combined system stability of a system with a low penetration of RES-based generation, small capacity of flexible DSM assets and limited DSM implementation is modest.

Comparing the conclusions obtained in Section 7.3 and Section 7.4, the impact of advanced DSM on individual stability aspects quantified by corresponding stability indices and the impact of advanced DSM on combined system stability quantified by the PCICSI are identical. Therefore, the proposed composite stability index facilitates an efficient and accurate assessment of the combined system stability performance to estimate the impact of advanced DSM and identify critical factors that affect the impact of advanced DSM on combined system stability.

7.5 Impacts of the Activation of Advanced Demand Side Management on System Angular and Frequency Stability

By manipulating demand consumption patterns and load compositions, advanced DSM itself can be considered as a disturbance for pre-DSM operating points. Consequently, the activation of advanced DSM (reconnection and disconnection of system demands) can affect and even endanger system stability performance.

Previous assessments of the impact of advanced DSM on system stability are performed by comparing the system stability performances of pre-DSM and post-DSM operating points. In this section, the assessments of the impact of advanced DSM focus on the transient period between pre-DSM and post-DSM operating points. Based on the conclusion obtained in Section 7.3 and Section 7.4 (i.e., the RES baseline and modelling of demand are critical for assessing the DSM impact), a composite load model and a high RES baseline (60%) have been adopted, based on the modified IEEE 68-bus test system.

The implementation of advanced DSM (i.e., disturbances) is illustrated again in Fig. 7.14, in which green blocks are used to represent load curtailments and red shadowed blocks

are adopted to indicate demand payback effects (i.e., load reconnections). Instead of emphasising the name of each flexible DSM process, the capacity and dominating load characteristic are emphasised in Fig. 7.14.

All RMS simulations performed in this section to assess system transient and frequency stability last for 60 seconds, so that appropriate time delays could be introduced between DSM processes to improve stability performance during DSM activation transient periods.

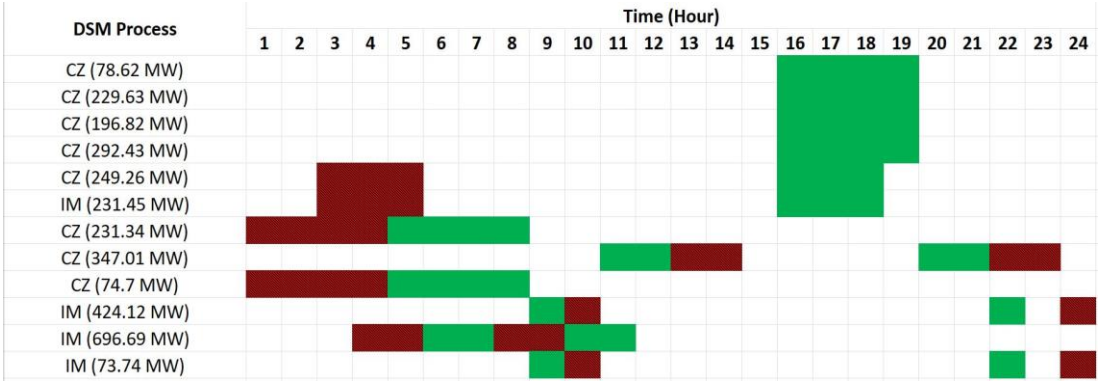

CZ = Constant Impedance
IM = Induction Motor

Figure 7.14 The Implementations of the DSM process in the modified IEEE 68-bus test system with emphasised DSM capacity and the dominating load characteristic

7.5.1 Power System Stability Performance of the Demand Side Management Activation Transient Period

By performing MCS-based probabilistic stability assessments, the system transient and frequency stability performances at each operating point are assessed by the mean values of adopted stability indices. In addition to the previous individual stability indices (i.e., TSI, FN and RoCoF) adopted to assess the impact of advanced DSM on system transient and frequency stabilit, the frequency zenith (FZ), the rate of change of the generator output current (RoCoC) and the rate of change of the rotor speed (RoCoS) have also been used to assess transient and frequency stability.

RoCoC (in pu/s) and RoCoS (in pu/s) are defined as (7.3) and (7.4), respectively, where

$I_{t+\Delta t}$ and $\omega_{t+\Delta t}$ are the output current and the rotor speed of the synchronous generator in p.u. at time instance $t + \Delta t$, respectively. Similarly, the output current and the rotor speed of the generator in p.u. at time instance t are represented by I_t and ω_t, respectively. Δt is the size of the measurement window and it equals 100 ms.

$$RoCoC = \frac{I_{t+\Delta t} - I_t}{\Delta t} \tag{7.3}$$

$$RoCoS = \frac{\omega_{t+\Delta t} - \omega_t}{\Delta t} \tag{7.4}$$

The mean values of TSI, and maximum mean values of FN/FZ, RoCoF, RoCoC and RoCoS observed from all buses or generators are summarised in Table 7.3 for each operating point.

Table 7.3 Mean values and the maximum mean values of transient and frequency stability indices at each operating point

Operating Point	FN/FZ (Hz)	$\lvert RoCoF \rvert$ (Hz/s)	TSI	$\lvert RoCoC \rvert$ (pu/s)	$\lvert RoCoS \rvert$ (pu/s)
Hour 1	49.70	1.52	53.60	0.50	0.07
Hour 2	49.85	0.74	65.91	0.08	0.02
Hour 3	49.50	1.61	56.08	0.24	0.05
Hour 4	0.00	269.24	15.56	11.13	0.15
Hour 5	49.19	4.86	49.45	0.72	0.09
Hour 6	50.29	0.90	54.27	0.19	0.01
Hour 7	50.26	4.15	58.71	0.20	0.02
Hour 8	49.42	2.19	68.03	0.17	0.01
Hour 9	49.82	0.25	68.06	0.07	0.00
Hour 10	50.05	0.20	69.81	0.06	0.00
Hour 11	50.41	4.64	49.33	0.25	0.01
Hour 12	50.08	0.13	66.57	0.04	0.00
Hour 13	49.92	0.11	71.96	0.01	0.00
Hour 14	49.92	0.11	72.78	0.01	0.00
Hour 15	N/A	N/A	N/A	N/A	N/A
Hour 16	50.21	0.36	61.81	0.07	0.01
Hour 17	50.21	0.47	63.71	0.09	0.01
Hour 18	50.21	0.44	63.13	0.09	0.01
Hour 19	50.20	0.36	64.41	0.07	0.01
Hour 20	50.07	0.09	70.03	0.04	0.00
Hour 21	50.07	0.09	69.87	0.04	0.00
Hour 22	49.53	0.56	61.40	0.16	0.01
Hour 23	49.91	0.13	71.55	0.02	0.00
Hour 24	49.50	1.13	61.64	0.20	0.01

It can be noted from Table 7.3 that the maximum magnitude of RoCoF exceeds the

stability limit (i.e., $|RoCoF|$ =1Hz/s) at 8/24 operating points, which have been emphasised by the grey background. Focusing on the demand valley (Hour 4), all stability indices indicate a significantly deteriorated power system stability performance due to the activation of advanced DSM. In other words, the power system loses stability when it transfers from pre-DSM to post-DSM operating points. These operating points with endangered stability performances emphasise the importance of the DSM activation transient period in the planning and implementation of DSM programs.

7.5.2 Critical Synchronous Generators and Corresponding Locations

As RoCoC and RoCoS can be obtained for each synchronous generator, they can be adopted to rank all synchronous generators and identify the critical generator based on the corresponding stability performances during the DSM activation transient period. Considering that the critical generator is the most sensitive generator to DSM activation and exhibits the largest RoCoC and RoCoS values, the critical generators identified based on RoCoC and RoCoS are summarised in Table 7.4 for all operating points.

Table 7.4 The Critical generator for each operating point identified by RoCoC and RoCoS

Operating Point	Critical Generator (Largest RoCoC)	Critical Generator (Largest RoCoS)	Operating Point	Critical Generator (Largest RoCoC)	Critical Generator (Largest RoCoS)
Hour 1	G9	G9	Hour 13	G2	G15
Hour 2	G9	G9	Hour 14	G2	G9
Hour 3	G9	G9	Hour 15	N/A	N/A
Hour 4	G9	G9	Hour 16	G16	G14
Hour 5	G9	G9	Hour 17	G15	G14
Hour 6	G11	G15	Hour 18	G16	G14
Hour 7	G12	G14	Hour 19	G16	G15
Hour 8	G9	G9	Hour 20	G12	G9
Hour 9	G11	G9	Hour 21	G12	G13
Hour 10	G12	G14	Hour 22	G2	G14
Hour 11	G10	G10	Hour 23	G2	G13
Hour 12	G12	G16	Hour 24	G9	G9

Regarding the location of the critical generators, the topology of the modified IEEE 68-bus test system is illustrated again in Fig. 7.15 in which the locations of critical generators

are emphasised by rectangles of different colours.

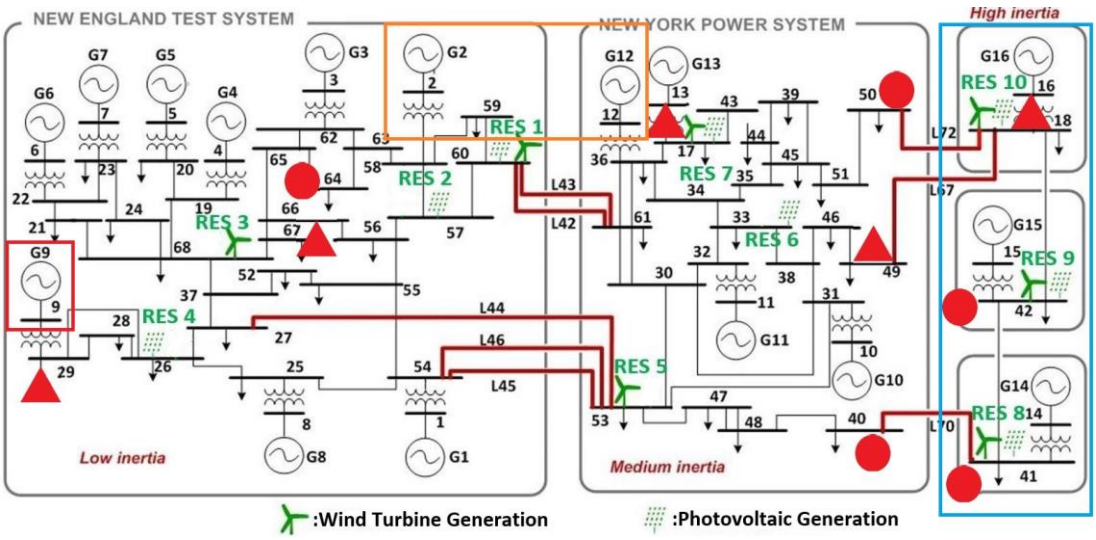

Figure 7.15 The modified IEEE 68-bus test system with the locations of the DSM (circles for large ICs and triangles for DNs) and the critical generator emphasised

Based on Table 7.4 and Fig. 7.15, the critical generator for operating points with relatively low demand (i.e., G9), marked by the red rectangle, is far from the main DSM assets (even though G9 is close to Bus 29, the DSM capacity of Bus 29 is only 3% of the total DSM capacity of the DN buses). The critical generator (G9) suffers from high RoCoC and RoCoS probably due to its low inertia time constant (H =3.14 s). Focusing on the operating points where large IC DSM assets are curtailed from the system to reduce peak demand (i.e., Hours 16 to 19), the critical generators identified by RoCoC and RoCoS are all in the high inertia equivalent areas emphasised by the blue rectangle in Fig. 7.15. These critical generators (i.e., G14 to G16) are close to 4/5 large IC DSM assets (Buses 40, 41, 42 and 50); their DSM capacity is 99.6% of the total DSM capacity of the large IC buses. At all remaining operating points, advanced DSM is only implemented at the DN buses, and it can be noted from Table 7.4 that either G2 or G12 has been identified as the critical generator by RoCoC at 9/13 (70%) operating points. These two generators, marked by the yellow rectangle, are close to the largest (about 65% of the total DSM capacity of the DN buses) DN-based DSM asset (Bus 17) and the cross-border transmission line between NETS and NYPS.

Therefore, it can be summarised from the discussions above that when system loading is relatively low, the generators with low inertia time constants are more likely to be

critical generators, but when the system loading is high, the generators close to the large load manipulations are more critical.

7.5.3 Possible Solutions to Improve the System Stability Performance During the Demand Side Management Activation Transient Period

Based on the finding that the power system can lose stability due to the implementation of DSM programs, this subsection introduces and discusses one of the possible solutions (i.e., introducing time delays between DSM programs) to improve the system stability performance during the DSM activation transient period. It is worth noting here that the optimisations of DSM implementation are outside the scope of this thesis.

7.5.3.1 Introducing Time Delays Between Load Reconnections

Focusing on Hour 4, when the system loses stability due to the simultaneous reconnection of large IC and DN DSM assets, the time responses of the rotor angle and terminal frequency of the critical generator (i.e., G9), based on a randomly selected iteration, are illustrated as blue solid lines in subplots (a) and (b), respectively, of Fig. 7.16.

A time delay of 30 seconds (because the rotor angle and terminal frequency oscillations caused by DN reconnection are almost settled after 30 seconds) is introduced between the reconnections of the large IC and DN DSM assets. The time responses of the critical generator when the DN DSM assets are reconnected before the large IC DSM assets are represented by red dashed lines in subplots (a) and (b) of Fig. 7.16, while the time responses of the critical generator when the large IC DSM assets are reconnected before the DN DSM assets are illustrated as black dotted lines in subplots (a) and (b) of Fig. 7.16.

It can be noted from subplots (a) and (b) of Fig. 7.16 that an introduced time delay (30 seconds) can stabilise power system transient and frequency stability regardless of the

reconnection order. When the large IC DSM assets are reconnected before the DN DSM assets (black dotted lines), the oscillations of the generator rotor angle and terminal frequency are poorly damped and exhibit more oscillatory responses, which leads to a longer settling time. However, when the DN DSM assets are reconnected first (red dashed lines), the oscillations of the generator rotor angle and terminal frequency can be well damped and settled within a reduced time interval.

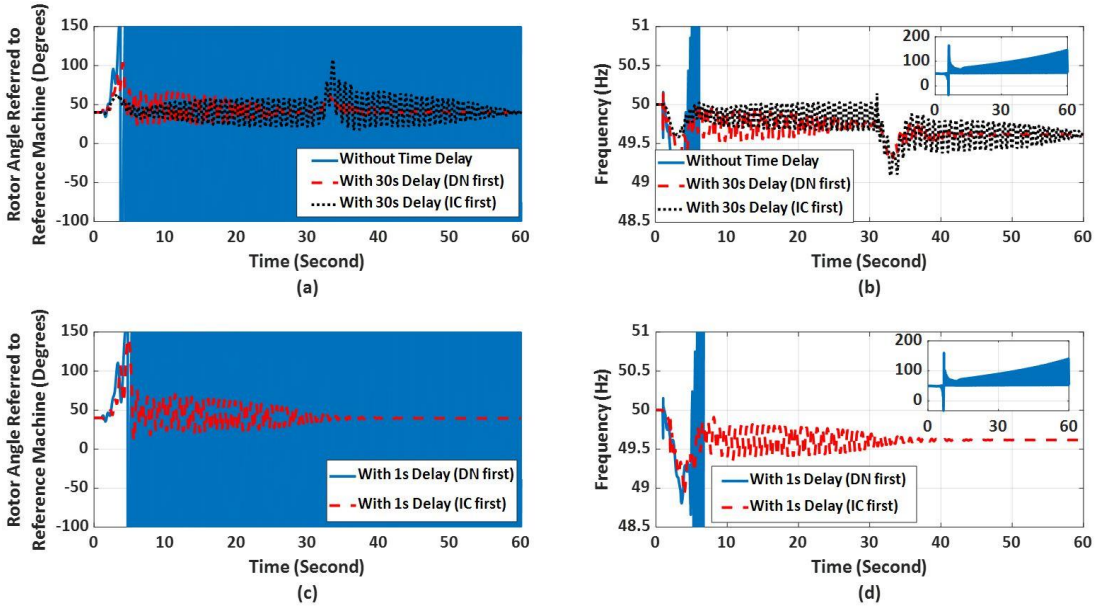

Figure 7.16 The time responses of the generator rotor angle ((a) and (c)) and terminal frequency ((b) and (d)) of the critical generator (G9) without/with different time delays between the DSM programs at Hour 4

The damping of rotor angle and frequency oscillations can be affected by a reduced time delay introduced between DSM programs. More specifically, subplots (c) and (d) of Fig. 7.16 focus on the time responses of the critical generator with a reduced time delay (i.e., 1 second). In subplots (c) and (d) of Fig. 7.16, the time responses when the DN DSM assets are reconnected first are represented by blue solid lines, and the time responses when the large IC DSM assets are reconnected first are illustrated by red dashed lines. It can be noted from red dashed lines that the system can still regain stability through the introduction of a significantly reduced time delay between the reconnections of the large IC DSM assets (first DSM program) and DN DSM assets (second DSM program), while the system is unstable when the DN DSM assets are reconnected before the large IC DSM assets, which is opposite from the case with 30 second delay.

According to Fig. 7.14, 480.71 MW (249.26 MW constant impedance load and 231.45 MW dynamic IM) of large IC DSM assets and 1003 MW (231.34 + 74.7 = 306.04 MW constant impedance load and 696.96 dynamic IM) of DN DSM assets are reconnected to the system at Hour 4. Hence, the reconnection of the large DSM assets before the small DSM assets (both in terms of capacity) is more beneficial even though a longer time delay between reconnections is required to stabilise the system in this case.

Another operating point (i.e., Hour 3), with load reconnections of both large IC and DN DSM assets, has been selected to analyse the impact of time delays between DSM programs. Similar to Hour 4, the time responses of the generator rotor angle and terminal frequency of the critical generator (G9) are illustrated in subplots (a) and (b) of Fig. 7.17, in which blue solid lines, red dashed lines and black dotted lines are used to represent the time responses without a time delay, with 30 seconds of time delay (when reconnecting the DN DSM assets first) and with 30 seconds of time delay (when reconnecting the large IC DSM assets first), respectively.

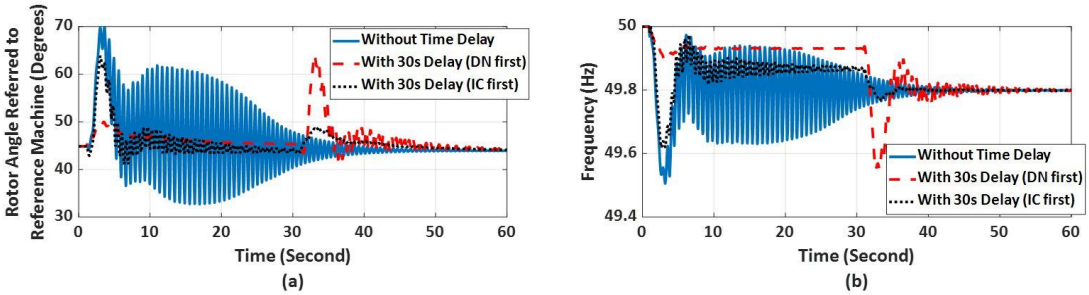

Figure 7.17 The time responses of the generator rotor angle (a) and terminal frequency (b) of the critical generator (G9) without/with time delays between the DSM programs at Hour 3

It can be noted from Fig. 7.17 that an introduced time delay results in less oscillatory responses of both rotor angle and terminal frequency, reduced maximum rotor angle deviation and increased frequency nadir regardless of reconnection order. Considering the order of reconnections, the black dotted lines exhibit a smaller maximum rotor angle deviation (18.9 degrees compared with 19.2 degrees in the red dashed line) and a larger frequency nadir (49.62 Hz compared with 49.55 Hz in the red dashed line); therefore, reconnecting the large IC DSM assets before the DN DSM assets is more beneficial to system stability performance. According to Fig. 7.14, 480.71 MW (249.26 MW constant impedance load and 231.45 MW dynamic IM) of large IC DSM assets and 306.04 MW

(231.34 + 74.7 = 306.04 MW constant impedance load) of DN DSM assets are reconnected at Hour 3; hence, the conclusion obtained based on Hour 3 (i.e., the reconnection of large DSM assets before small DSM assets, both in terms of capacity, is more beneficial) agrees with the previous finding at Hour 4.

By performing power system stability assessments for 60 seconds and introducing time delays of 30 seconds, the secondary and tertiary frequency controls, which aim to restore the rated frequency, are neglected in the study. In other words, frequency oscillations caused by activations of DSM can be settled only around a new value instead of the rated value (i.e., 50 Hz). Under such circumstances, a DSM program with a large capacity should be activated first because it will introduce a larger disturbance into the system. If the larger DSM program is activated after the smaller DSM program, the deteriorated system stability, as a consequence of the activation of the smaller DSM program, will be further deteriorated by a larger disturbance.

Moreover, Fig. 7.14 shows that large IC DSM assets are modelled as a combination of constant impedance loads and IMs, and all DN DSM assets are modelled as constant impedance loads at Hour 3. It can be noted from Fig. 7.17 that whenever large IC DSM assets are reconnected to the system, more oscillatory time responses can be observed for both the generator rotor angle and terminal frequency. Therefore, a DSM program contains IM should be carefully coordinated as it introduces more oscillatory responses, which usually exhibit large RoCoF and RoCoS and could trigger some sensitive relays, even though the system remains stable.

7.5.3.2 Introducing Time Delays Between Load Curtailments

The impact of time delays between load curtailments on system transient and frequency stability is investigated based on Hour 11, when only the DN DSM assets are curtailed from the system. In order to maintain the continuity of the analyses, a 30-second time delay is introduced between the curtailments of the largest DSM assets (678.6 MW at Bus 17) and all remaining DSM assets (365.4 MW in total at Buses 18, 29, 49 and 67). The time responses of the generator rotor angle and terminal frequency of the critical

generator (G10) are illustrated in subplots (a) and (b) of Fig. 7.18, in which blue solid lines, red dashed lines and black dotted lines are used to represent the time responses without time delay, with 30 seconds of time delay (when the largest DSM asset is curtailed first) and with 30 seconds of time delay (when the smaller DSM assets are curtailed first), respectively.

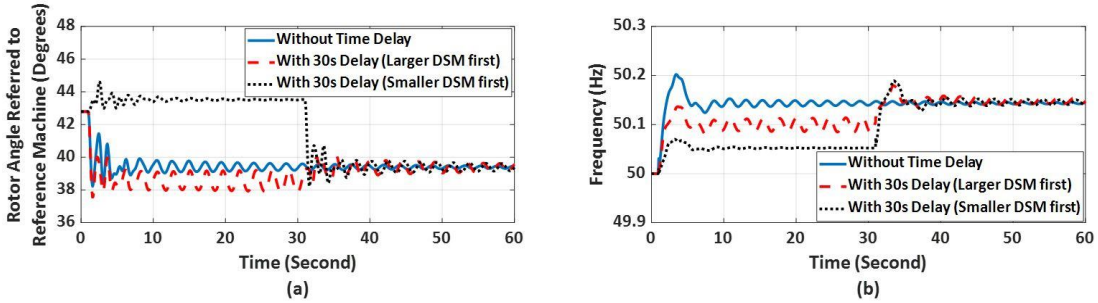

Figure 7.18 The time responses of the generator rotor angle (a) and terminal frequency (b) of the critical generator (G10) without/with time delays between the DSM programs at Hour 11

Based on Fig. 7.18, an introduced time delay can again reduce the maximum rotor angle deviation and frequency zenith regardless of the curtailment order. When the largest DSM asset is curtailed before other DSM assets, a smaller maximum rotor angle deviation (4.6 degrees compared with 5.3 degrees in the black dotted line) and a smaller frequency zenith (50.18 Hz compared with 50.19 Hz in the black dotted line) can be observed. Even though the improvements of stability indices are negligible, the finding that the system shows better stability performances when the largest DSM asset is curtailed first agrees with the conclusions obtained from previous investigations (i.e., Section 7.5.3.1). This conclusion though might be affected by the system, operating condition and the size of consecutive disturbances, hence detailed studies need to be carried out for a particular system if practical solution to the problem is to be proposed.

In summary, by assessing the impact of the activations of advanced DSM on power system transient and frequency stability, the following conclusions can be obtained:

- Synchronous generators with lower inertia time constants are more critical when the system demand is relatively low, while synchronous generators closer to large DSM assets are more sensitive to DSM activations when the system demand is high.

- Properly defined time delays between DSM activations can help the system transfer

from pre-DSM to post-DSM operating points with improved stability performance while avoiding the loss of stability. The sizes of the time delays can affect the damping of rotor angle and frequency oscillations.

- An accurate modelling of flexible DSM assets is essential, as the reconnection of IM leads to more oscillatory responses of the generator rotor angle and terminal frequency, which may trigger some speed-sensitive relays.

- If time delays are necessary to coordinate DSM implementations, it is better to activate the DSM with the larger capacity (in MW) first. Given that DSM activations with larger capacities usually lead to more severe oscillations, it is better to deploy them when the system is relatively healthier (i.e., closer to pre-DSM operating points).

7.6 Summary

This chapter assesses the impact of advanced DSM on combined system stability, which considers small disturbance, transient and frequency stability simultaneously, based on MCS-based probabilistic stability assessments. Critical factors (e.g., the modelling method of system demand) that affect the impact of advanced DSM on combined system stability are also identified by a range of case studies under different operating conditions.

First, the impact of advanced DSM and the potential critical factors on individual stability aspects are investigated by the percentage change of the corresponding stability index-based stability distance at each operating point. It has been found that advanced DSM could either improve or deteriorate a specific stability aspect and under certain circumstances, advanced DSM can stabilise an unstable operating point or lead to system instability. By investigating the impact of advanced DSM based on operating conditions with different RES baselines, locations of flexible DSM assets, DSM capacities and load models, it has been found that the system RES baseline and the modelling of demand are critical for assessing the DSM impact, as they both result in qualitative changes of

the result. The locations of flexible DSM assets and DSM capacity mostly affect the magnitude of the impact, while the direction of the impact remains the same. The impact of advanced DSM on the stability of a network with a low penetration of RES, small capacity of flexible DSM assets and limited DSM implementation is modest.

Then, the proposed composite stability index (i.e., PCICSI) is adopted to quantify the combined system stability performances due to its high accuracy and applicability. The impact of advanced DSM and the potential critical factors on combined system stability are quantified by the percentage change of the PCICSI at each operating point, and the overall impact of advanced DSM on a daily basis has been estimated by considering both beneficial and detrimental impacts. The impact of advanced DSM on combined system stability and the critical factors identified by the PCICSI agree with the findings based on individual stability aspects. This proves the accuracy and reliability of the combined system stability assessments using the PCICSI. The comprehensive assessment of the influence of advanced DSM on system angular and frequency stability is the fifth original contribution of this thesis.

Finally, by considering the activations of advanced DSM as system disturbances, this chapter emphasises the importance of system stability performance immediately after the system is subjected to DSM programs and introduces a possible solution (i.e., time delays between DSM programs) to improve stability performance. The locations of the critical generators are identified by MCS-based probabilistic stability assessments, and the impacts of time delays are studied by the time responses of the generator rotor angle and terminal frequency of the critical generator. It has been found that synchronous generators with lower inertia time constants are more sensitive to DSM activations when the system demand is relatively low and generators closer to large DSM assets are more critical when the system demand is high. Moreover, if time delays are required to stabilise unstable operating points or improve system stability performance, implementing DSM programs with larger capacities first can be more beneficial. Though it is only explanatory at this stage, emphasising the importance of the DSM activation transient period by assessing system transient and frequency stability, and indicating benefits of sequential (time delayed) deployment of DSM programs, is the sixth original contribution of this thesis.

8 Conclusions and Future Work

8.1 Conclusions

This thesis first proposes (in Chapter 2) and verifies (in Chapter 6) two composite stability indices, namely normalised Euclidean distance for stability (NEDS) and parallel circuit inspired composite stability index (PCICSI), to assess angular stability (including small-disturbance stability and transient stability) and frequency stability simultaneously. Based on the review of past work in power system stability assessment, traditional assessments of power system stability usually focus on the individual stability aspect and are evaluated by the corresponding stability indices. While stability indices have proved to be efficient in quantifying and evaluating system stability performance from a corresponding perspective, comprehensive understanding and assessment of system stability are limited by the fact that stability indices are usually derived and analysed separately. Although many composite stability indices, combining multiple stability indices from one stability aspect, have been developed to improve the accuracy of system stability assessment, a comprehensive evaluation of combined system stability has not been achieved yet because multiple stability aspects of system stability are affected simultaneously by new devices and technologies (e.g., RES-based generation and DSM).

To properly balance and combine different stability aspects, two proposed composite stability indices consider small disturbance stability, transient stability and frequency

stability simultaneously while each stability aspect is assessed by the corresponding normalised stability distance(s) which is/are calculated based on widely adopted stability indices. It is important to mention that the overall accuracy and applicability of proposed composite stability indices depends on reference values (either the most probable values for the NEDS or the maximum values for the PCICSI) adopted to normalise individual stability indices (distances). Although the most probable values can minimise the impact of extreme cases and provide a comparison between the current operating point and the most probable situation, they require a huge historical data base and regular updates. On the other hand, because the maximum values can be considered as extreme cases, the reference values of the PCICSI only need to be updated when new extreme events appear, which reduces the computational cost and increase the applicability of the PCICSI in real world power systems.

To verify the accuracy and efficiency of the proposed composite stability indices, the impact of RES-based generation and different load models on individual stability aspects and combined system stability are assessed by MCS-based probabilistic stability assessments based on three network models (two widely adopted IEEE test systems and an equivalent representation of four interconnected real networks), and quantified by individual stability distances and proposed composite stability indices, respectively. It has been found that both proposed composite stability indices can clearly indicate the distance of system operating points from the stability limits, the impacts on combined system stability performance and the most affected stability aspect for stable power systems. However, when power systems face the risk of losing stability, the NEDS becomes misleading and only the PCICSI can maintain the accuracy of assessments of combined system stability and identify unstable operating points. Therefore, the overall accuracy of PCICSI is higher than the NEDS.

As all stability distances are normalised to the most probable values in the case of NEDS, a comparison of combined stability performance is provided between the current operating point and the most probable situation encountered in the past, and thus NEDS is considered to be suitable to guide stability enhancements and improvements. On the other hand, PCICSI adopts extreme stability performances (i.e., the best individual system stability performance) as reference values, hence system stability enhancement

and improvement measures cannot be guided by PCICSI due to the lack of reasonable references.

As adopted stability aspects, stability indices and the setting of corresponding stability limits can be adjusted and substituted as required without significant loss of generality; proposed composite stability indices can be considered as frameworks that provide an efficient assessment and comprehensive measure of system stability performance and can facilitate the understanding of the impacts of existing and future technologies and stability enhancement solutions to the overall stability performance of the system. The indices can also be used to guide the optimisation of system stability performance with the objective of minimising/maximising the impacts of new devices, operational practices or control actions. The proposed framework and indices could be easily applied to other systems and studies beyond the power system. *The development of the proposed composite stability indices for combined system stability assessments and evaluation frameworks that can be applied to other power system analyses is the first original contribution of this thesis.*

Besides efficient and accurate measures to assess and quantify combined system stability, an appropriate analysis method and an accurate modelling of advanced DSM are also necessary to investigate the impact of advanced DSM on combined system stability of transmission networks. Even though the constant power load model is still the most widely adopted load model in power system dynamic studies, modelling of advanced DSM extends to the composite load model, which has been modelled as a parallel connection of static ZIP load and a dynamic IM in this thesis, as advanced DSM affects system dynamic responses and stability performances by manipulating both load consumption patterns and load compositions.

Based on the two transmission network models under study (i.e., modified IEEE 68-bus test system and 4TNE system modelled based on four interconnected real networks), several flexible DSM processes in large IC and DN buses are defined, and their capacities are determined based on either the annual utilisation rate and flexibility obtained from open literatures (modified IEEE 68-bus test system), or consultations with corresponding TSOs (4TNE system). Then, all flexible DSM processes are modelled by the corresponding

dominated load characteristic (either constant impedance load or IM) in the case of the composite load model, such that the implementations of advanced DSM change not only load magnitudes, but also load compositions. Moreover, demand payback effects, which have been modelled as reconnections of curtailed load, have also been considered in this thesis. Demand payback effects are modelled for each flexible DSM process based on corresponding payback parameters (i.e., payback hour and percentage of payback). Finally, the implementations of advanced DSM are developed based on individual flexible DSM processes considering corresponding capacities, flexible hours and maximum times of response per day. In the meantime, the implementations of advanced DSM aim to reduce the difference between the demand valley and demand peak without creating a new demand valley and peak.

The comprehensive modelling of DSM in this thesis is suitable for large-scale power system studies, including but not limited to, assessing the impacts of DSM on system stability performances, assessing the impacts of DSM on steady state system congestions, voltage regulation, losses and assessing the impact of DSM on operation of electricity market. *The comprehensive modelling of DSM for the purpose of system dynamic studies is the second original contribution of this thesis.*

Chapter 5 introduces and discusses the probabilistic analysis method adopted in this thesis to assess system stability performances at each operating point. Considering the high variability and uncertainty of modern and future power systems contributed by RES-based generation, load demand and system disturbance, an MCS-based probabilistic analysis method, which randomly samples input variables (in Matlab) and performs repeatable deterministic simulations for each input set (in DigSILENT PowerFactory), is adopted in this thesis to estimate distributions of adopted stability indices at each operating point (in Matlab). Even though the computational cost of the MCS-based probabilistic stability assessment is high, the accuracy of the results and the ability to cover high system operational variability and uncertainty is satisfying. Therefore, the adopted probabilistic framework is suitable for modern and future power system studies, especially when considering high integration levels of RES-based generation. Efficient sampling techniques for exploration of search space could be equally well used instead of MCS without affecting the proposed probabilistic framework. *The probabilistic*

framework of assessing the impact of advanced DSM, which has been modelled with the consideration of dominate load characteristics and demand payback effects, on system stability is the third original contribution of this thesis.

By applying the MCS-based probabilistic stability assessments and comparing system stability performances before/after the implementation of advanced DSM, it has been found that advanced DSM can either weaken or improve a particular aspect of system stability. More importantly, when the advanced DSM improves one stability aspect, it can weaken other aspect(s) of system stability. Due to the opposite impacts of advanced DSM observed from different system stability aspects, there is clearly a need to assess the impact of advanced DSM on combined system stability, which considers multiple aspects of system stability simultaneously, such that more efficient and comprehensive decisions of DSM planning and implementation can be made. Because the PCICSI has shown high accuracy and applicability in all operating conditions and it is able to identify unstable operating points, combined system stability performances before/after the implementation of advanced DSM are evaluated by the PCICSI. Furthermore, critical factors (e.g., modelling method of system demand) that affect the impact of advanced DSM on combined system stability are also identified by a range of case studies under different operating conditions. *The simultaneous assessment of angular and frequency stability of a power system using composite stability indices is the fourth original contribution of this thesis.*

By illustrating the daily combined system stability performance before/after the advanced DSM as daily PCICSI curves, it has been found that advanced DSM can either improve or weaken combined system stability at different operating points. Furthermore, advanced DSM can also stabilise an unstable operating point, and inappropriate demand payback effect can lead to system instability. By comparing the impacts of advanced DSM on combined system stability under different operating conditions (case studies), it has been found that the system RES baseline and modelling of demand are critical for assessing the impact of advanced DSM as they both result in quantitative and qualitative changes in the result. Therefore, they should be carefully and accurately defined in order to obtain desired changes of system stability performance through advanced DSM. Moreover, DSM capacity mostly affects the magnitude of the impact while the direction

of the impact (positive or negative) remains the same. Similarly, altered locations of flexible DSM assets lead to either increased or decreased DSM capacity and subsequently, quantitative changes of the impact of advanced DSM. However, the locations of system disturbance (i.e., reconnection of DSM assets) can also be changed due to altered locations of flexible DSM assets, which further affect combined system stability performance before/after the implementation of advanced DSM. Regarding the more realistic network model with low penetration of RES-based generation, small capacity of flexible DSM assets and limited DSM implementation, the impact of advanced DSM is modest. *The investigation of the impact of advanced DSM on combined system stability to identify critical factors that may affect the impact of advanced DSM is the fifth original contribution of this thesis.*

As discussed previously, advanced DSM affects system stability by manipulating both load consumption patterns and load compositions. Consequently, advanced DSM itself can be considered as system disturbances introduced to pre-DSM operating points. To safely implement advanced DSM and obtain economic and technical benefits from the implementations of advanced DSM, power systems are required to transfer from pre-DSM to post-DSM operating points without violating any stability limits. Unfortunately, the system dynamic responses immediately after the system is subjected to DSM activations are usually neglected in the planning and implementation processes of DSM programs, especially in the case of implicit DSM. Transient stability and frequency stability have been investigated in Chapter 7, focusing on the DSM activation transient period based on the advanced DSM developed in this thesis and the modified IEEE 68-bus test system with a high RES baseline and a composite load model.

The results illustrate that the system can lose stability due to demand payback effects around the demand valley, which emphasises the importance of the DSM activation transient period. As one of the potential solutions to improve system stability of the DSM activation transient period, introducing time delays between different DSM programs can help system to regain stability immediately after demand payback effects, and reduce the maximum angle deviation and the magnitude of frequency excursions. Furthermore, it also has been found that the DSM program (disturbance) with a larger capacity should be implemented before the DSM program (disturbance) with a smaller

capacity. Moreover, by ranking synchronous generators based on their dynamic responses during the DSM activation transient period, the generators with lower inertia time constants are found to be more critical during off-peak hours when load reconnections occur due to demand payback effects. However, generators closer to large DSM assets are more critical during peak hours when load curtailments are implemented to reduce peak demand. Accordingly, additional stability enhancement and improvement measures can be applied at these critical synchronous generators to improve the overall system stability during DSM events. *Though it is only explanatory at this stage, emphasising the importance of the DSM activation transient period by assessing system transient and frequency stability, and indicating benefits of sequential (time delayed) deployment of DSM programs, is the sixth original contribution of this thesis.*

8.2 Future Work

Although the overall aim and all the objectives stated in Chapter 1 have been achieved, some improvements can still be made to improve the accuracy and reliability of this research. The potential improvements of this research and future work are summarised below:

1. The combined system stability assessment including voltage stability. As one of the most important system stability aspects, voltage stability should be considered in proposed composite stability indices and combined system stability assessments. According to the definition of proposed composite stability indices, voltage stability indices (e.g., PV margins, voltage collapse index) can be integrated into the proposed composite stability indices as long as a proper voltage stability limit can be defined. They have been omitted in this study due to different time frames of system angular, frequency and voltage stability and the lack of general stability limit.

2. Probabilistic system stability assessments with reduced time steps. Performing MCS-based probabilistic stability assessments for multiple stability aspects is time consuming, especially in the case of transient and frequency stability. In order to

balance the accuracy of results and the computation cost of the research, MCS-based probabilistic stability assessments are performed hourly in this thesis. Even though the trend and indication of the variation of system stability performances can still be captured by hourly assessment, the accuracy and reliability of results can be significantly improved by performing dynamic simulations at reduced timescales (e.g., every 15 minutes or every 5 minutes) with more detailed and accurate modelling of operational uncertainties (e.g., wind speed). The resulting increase in the computational time could be addressed by using some of the advanced sampling techniques instead of conventional MCS [82, 183].

3. Development of appropriate weighting factors in composite stability indices to represent different importance of individual stability aspects (indices) and further improve the accuracy and applicability of proposed composite stability indices. Weighting factors can be developed and adjusted to reflect particular concerns of a system operator, and such are application specific and would be informed by system operator experience and/or past historic data processed using advanced machine learning and data analytics techniques.

4. Further investigations regarding the impact of different modelling parameters (e.g., locations of flexible demands, flexibility hours and payback hours) of advanced DSM on combined system stability performance. These parameters can help system operators to develop more efficient and beneficial implementations of DSM programs. The importance of different modelling parameters can be studied and ranked based on comprehensive sensitivity studies as described in e.g., [184].

5. Correlations between different stability aspects. To develop the NEDS, different system stability aspects have been considered as dimensions of a multi-dimensional space. Therefore, it is assumed that all system stability aspects are independent. In this research, different disturbances (i.e., three-phase to ground line faults for transient stability and disconnections of generator or reconnections of demand for frequency stability) have been modelled for different stability aspects. In real world power systems, different stability aspects are correlated. For instance, reconnections of demand lead not only to frequency excursions, but also to rotor angle excursions.

Further assessments of combined system stability using composite indices should investigate the correlation between different stability aspects when the system is subjected to a particular disturbance.

6. Updated multi-dimensional space for combined system stability. As mentioned previously, individual dimensions of a multi-dimensional space are supposed to be independent. The current multi-dimensional space, which adopts different stability aspects as dimensions, can be updated to a new space that adopts independent parameters (e.g., RES baselines, time and system loading level) as dimensions. Based on the extra simulations performed with different RES baselines and system loading levels, the proposed composite stability indices (i.e., NEDS and PCICSI) can be defined as functions of, for instance, time, RES baselines and system loading levels.

7. Development of general functions of composite stability indices. Current composite stability indices are obtained from MCS-based probabilistic stability assessments with huge computational costs. If a general function of the composite stability index is obtained, it can be used to rapidly assess the system combined stability performance for a given operating point and forecast system stability performances based on the estimations of system operating conditions. The general function of the composite stability index can be derived from historical data sets using machine learning [185, 186] and other appropriate data analysis methods.

8. Development of an analytical method of assessing the impact of advanced DSM. By manipulating load consumption patterns and load compositions, advanced DSM changes system loading level, which can be considered as a variable in the general function of composite stability indices. The impact of advanced DSM (i.e., changing system loading levels) can then be assessed from the variation of combined system stability performance (i.e., composite stability indices) without performing numerous simulations. Machine learning approaches could be used to facilitate this task [185, 186].

References:

[1] "International - U.S. Energy Information Administration (EIA)", *Eia.gov*, 2022. [Online]. Available: https://www.eia.gov/international/data/world/electricity/electricity-consumption?pd=2&p=0000002&u=0&f=A&v=mapbubble&a=-&i=none&vo=value&t=C&g=00000000000000000000000000000000000000000000000001&l=249-ruvvvvvfvtvnvv1vrvvvvfvvvvvvfvvvou20evvvvvvvvvvvnvvvs0008&s=315532800000&e=1546300800000&. [Accessed: 13-January-2022].

[2] H. Ritchie, M. Roser and P. Rosado, "Energy", *Our World in Data*, 2022. [Online]. Available: https://ourworldindata.org/energy-production-consumption. [Accessed: 13-January-2022].

[3] "Digest of UK Energy Statistics (DUKES): electricity", *GOV.UK*, 2022. [Online]. Available: https://www.gov.uk/government/statistics/electricity-chapter-5-digest-of-united-kingdom-energy-statistics-dukes. [Accessed: 13-January-2022].

[4] H. Nosair and F. Bouffard, "Energy-Centric Flexibility Management in Power Systems," *IEEE Transactions on Power Systems*, vol. 31, no. 6, pp. 5071-5081, January 2016.

[5] "Harnessing Variable Renewables: A Guide to the Balancing Challenge," Tech. Rep., International Energy Agency, OECD/IEA, Paris, France, 2011.

[6] C. W. Gellings, "The concept of demand-side management for electric utilities," *Proceedings of the IEEE*, vol. 73, no. 10, pp. 1468-1470, October 1985.

[7] A. Fattahi Meyabadi and M. H. Deihimi, "A review of demand-side management: Reconsidering theoretical framework," *Renewable and Sustainable Energy Reviews*, vol. 80, pp. 367-379, December 2017.

[8] S. Wang, S. Bi and Y. J. A. Zhang, "Demand Response Management for Profit Maximizing Energy Loads in Real-Time Electricity Market," *IEEE Transactions on Power Systems*, vol. 33, no. 6, pp. 6387-6396, April 2018.

[9] U.S. Department of Energy, "Benefits of Demand Response in Electricity Markets and Recommendations for Achieving Them – A Report to the United States Congress Pursuant to Section 1252 of the Energy Policy Act of 2005," P. 122, 2006.

[10] E. Kabalci, "Technical Challenges and Enhancements in Smart Grid Applications," in *Smart Grids and Their Communication Systems*, Springer, 2019.

[11] A. Barbato, A. Capone, L. Chen, F. Martignon and S. Paris, "A distributed demand-side management framework for the smart grid," Computer Communications, vol. 57, pp. 13-14, February 2015.

[12] A. S. Hopkins, *Best Practices in Utility Demand Response Programs*, Massachusetts, 2017.

[13] S. Gordon, C. Mcgarry, K. Bell and J. Tait, "Impact of Low Inertia and High Distributed Generation on the Effectiveness of Under Frequency Load Shedding Schemes," *IEEE Transactions on Power Delivery*, Early Access, December 2021.

[14] R. Vakili and M. Khorsand, "Enhancing Situational Awareness: Predicting Under

Frequency and Under Voltage Load Shedding Relay Operations," 2021 North American Power Symposium (NAPS), TX, USA, November 2021.

[15] C. Decker, "Chapter 5 – Energy transportation: electricity," *Handbook of Energy Economic and Policy*, pp. 193-238, 2021.

[16] "Electricity Distribution Systems Losses Non-technical Overview," *Ofgem*, May 2009. [Online]. Available: https://www.ofgem.gov.uk/publications/electricity-distribution-systems-losses-non-technical-overview. [Accessed: 15-January-2022].

[17] N. Hatziargyriou, J. V. Milanović, C. Rahmann, V. Ajjarapu, C. Cañizares, I. Erlich, D. Hill, I. Hiskens, I. Kamwa, B. Pal, P. Pourbeik, J. J. Sanchez- Gasca, A. Stanković, T. Van Cutsem, V. Vittal, C. Vournas, "Definition and Classification of Power System Stability – Revisited & Extended," *IEEE Transactions on Power Systems,* vol. 36, no. 4, pp. 3271-3281, July 2021.

[18] H. Abdullah, "Problem solving of Newton's second law through a system of total mass motion," *Asia-Pacific Forum on Science Learning and Teaching*, vol. 15, no. 2, Article 15, December 2014.

[19] P. Kundur, *Power System Stability and Control*, 2nd ed., vol. 1, New York: McGraw-Hill, 1994.

[20] J. Machowski, J. W. Bialek and J. R. Bumby, *Power System Dynamics and Stability*, John Wiley & Sons, 1997.

[21] J. Zhao, Y. Tang and V. Terzija, "Robust Online Estimation of Power System Center of Inertia Frequency," *IEEE Transactions on Power Systems*, vol. 34, no. 1, pp. 821-825, January 2019.

[22] M. Li, Y. Wang, N. Xu, Y. Liu, W. Wang, H. Wang and W. Lei, "A novel virtual synchronous generator control strategy based on improved swing equation emulating and power decoupling method," *2016 IEEE Energy Conversion Congress and Exposition (ECCE)*, WI, USA, September 2016.

[23] J. Zhou and Y. Ohsawa, "Improved Swing Equation and Its Properties in Synchronous Generators," *IEEE Transactions on Circuits and Systems I: Regular Papers*, vol. 56, no. 1, pp. 200-209, January 2009.

[24] R. Preece, "Improving the Stability if Meshed Power Networks: A Probabilistic Approach Using Embedded HVDC Lines," *Springer Theses*, 2013, [Online]. Available: https://link.springer.com/content/pdf/10.1007/978-3-319-02393-9.pdf. [Accessed: 15-January-2022].

[25] A. M. Lyapunov, *Stability of Motion*, English translation, Academic Press, Inc., 1967.

[26] M. H. Haque, "Improvement of first swing stability limit by utilizing full benefit of shunt FACTS devices," *IEEE Transactions on Power Systems*, vol. 19, no. 4, pp. 1894-1902, November 2004.

[27] S. Wang, J. Yu and W. Zhang, "Transient Stability Assessment Using Individual Machine Equal Area Criterion PART I: Unity Principle," *IEEE Access*, vol. 6, pp. 77065-77076, July 2018.

[28] S. Paudyal, G. Ramakrishna and M. S. Sachdev, "Application of Equal Area Criterion Conditions in the Time Domain for Out-of-Step Protection," *IEEE Transactions on Power Delivery*, vol. 25, no. 2, pp. 600-609, April 2010.

[29] Y. Dai, M. Noebels, M. Panteli and R. Preece, "Evaluating the Effect of Dynamic and Static Modelling on Cascading Failure Analysis in Power Systems," *2021 IEEE*

Madrid PowerTech, Madrid, Spain, July 2021.

[30] S. Odawara, S. Yamamoto, K. Sawatari, K. Fujisaki, Y. Shindo, N. Yoshikawa and T. Konishi, "Iron Loss Evaluation of Reactor Core With Air Gaps by Magnetic Field Analysis Under High-Frequency Excitation," *IEEE Transactions on Magnetics*, vol. 51, no. 11, November 2015.

[31] J. R. Linders, "Effects of Power Supply Variations on AC Motor Characteristics," *IEEE Transactions on Industry Applications*, vol. IA-8, no. 4, pp. 383-400, July 1972.

[32] M. Cheng, S. S. Same and J. Wu, "Benefits of using virtual energy storage system for power system frequency response," *Applied Energy*, vol. 194, pp. 376-385, May 2017.

[33] G. Frigo, A. Derviskadic, Y. Zuo and M. Paolone, "PMU-Based ROCOF Measurements: Uncertainty Limits and Metrological Significance in Power System Applications," *IEEE Transactions on Instrumentation and Measurement*, vol. 68, no. 10, pp. 3810-3822, October 2019.

[34] L. Meegahapola, A. Sguarezi, J. S. Bryant, M. Gu, E. R. Conde D. and R. B. A. Cunha, "Power System Stability with Power-Electronic Converter Interfaced Renewable Power Generation: Present Issues and Future Trends," *Energies*, vol. 13, no. 13, 3441, July 2020.

[35] H. Bevrani, *Robust Power System Frequency Control*, 2nd ed., Springer, 2014.

[36] Y. J. (A.) Zhang, C. Zhao, W. Tang and S. H. Low, "Profit-Maximizing Planning and Control of Battery Energy Storage Systems for Primary Frequency Control," *IEEE Transactions on Smart Grid*, vol. 9, no. 2, pp. 712-723, March 2018.

[37] E. Weitenberg, Y. Jiang, C. Zhao, E. Mallada, C. D. Persis and F. Dorfler, "Robust Decentralized Secondary Frequency Control in Power Systems: Merits and Tradeoffs," *IEEE Transactions on Automatic Control*, vol. 64, no. 10, pp. 3967-3982, October 2019.

[38] M. Perninge and R. Eriksson, "Optimal Tertiary Frequency Control in Power Systems with Market-Based Regulation," *IFAC-PapersOnLine*, vol. 50, no. 1, pp. 4374-4381, July 2017.

[39] K. Baltputnis, Z. Broka and A. Sauhats, "Analysis of the Potential Benefits from Participation in Explicit and Implicit Demand Response," *2019 54th International Universities Power Engineering Conference (UPEC)*, Bucharest, Romania, September 2019.

[40] P. Manner, J. Salmelin, S. Honkapuro, I. Alapera and S. Annala, "A novel method to utilize direct electrical space heating for explicit demand response purposes – proof of concept," *2020 IEEE PES Innovative Smart Grid Technologies Europe (ISGT-Europe)*, The Hague, Netherlands, October 2020.

[41] T. Freire-Barcelo, F. Martin-Martinez and A. Sanchez-Miralles, "A literature review of Explicit Demand Flexibility providing energy services," *Electric Power Systems Research*, vol. 209, 107953, August 2022.

[42] M. P. Lee, O. Aslam, B. Foster, D. Kathan and C. Young, "Assessment of Demand Response and Advanced Metering - Staff Report," *Federal Energy Regulatory Commission*, December 2014. [Online]. Available: https://www.ferc.gov/sites/default/files/2020-05/demand-response.pdf. [Accessed: 20-January-2022].

[43] S. E. D. Coalition, "Mapping demand response in Europe today," *Tracking*

Compliance with Article, vol. 15, 2014.

[44] "IMPLEMENTING DEMAND RESPONSE IN THE NATIONAL ELECTRICITY MARKET OF SINGAPORE – FINAL DETERMINATION PAPER", *Energy Market Authority of Singapore*, October 2013. [Online]. Available: Final_Determination_Demand_Response_28_Oct_2013_Final.pdf. [Accessed: 21-January-2022].

[45] "Bangladesh Power Development Board (BPDB) – Annual Report," [Online]. Available: http://www.bpdb.gov.bd/download/annual_report/Annual%20Report%202012-2013.pdf. [Accessed: 02-June-2015].

[46] "Customer Load Active System Services," *Electricity North West*, 2014. [Online]. Available: https://www.enwl.co.uk/globalassets/innovation/class/class-documents/class-closedown-report-master.pdf. [Accessed: 30-January-2022].

[47] "Ancillary service provision by RES and DSM connected at distribution level in the future power system," *SmartNet Project Deliverable*, vol. 1, 2016. [Online]. Available: http://smartnet-project.eu/wp-content/uploads/2016/12/D1-1_20161220_V1.0.pdf. [Accessed: 30-January-2022].

[48] C. Vivekananthan, Y. Mishra and F. Li, "Real-Time Price Based Home Energy Management Schedular," *IEEE Transactions on Power Systems*, vol. 30, no. 4, pp. 2149-2159, July 2015.

[49] N. Mohammad and Y. Mishra, "Demand-Side Management and Demand Response for Smart Grid," in *Smart Grids and Their Communication Systems*, Springer, 2019.

[50] N. G. Paterakis, O. Erdinc and J. P. S. Catalao, "An overview of Demand Response: Key-elements and international experience," *Renewable and Sustainable Energy Reviews*, vol. 69, pp. 871-891, March 2017.

[51] "COMMERCIAL AND INDUSTRIAL DEMAND RESPONSE", *CPS Energy*. [Online]. Available: https://www.cpsenergy.com/content/dam/corporate/en/Documents/EnergyEfficiency/requirements_demand_response.pdf. [Accessed: 30-January-2022].

[52] "Power Partner℠ Thermostats", *Savings.austinenergy.com*, 2022. [Online]. Available: https://savings.austinenergy.com/rebates/residential/offerings/cooling-and-heating/pp-thermostat/. [Accessed: 14-Febuary-2022].

[53] "Low Carbon London Project Closedown Report," Low Carbon London, 2015. [Online]. Available: https://innovation.ukpowernetworks.co.uk/wp-content/uploads/2019/05/Project-Closedown-Report-March-2015.pdf. [Accessed: 14-Febuary-2022].

[54] Endeavour Energy – Solutions for Community. [Online]. Available: https://www.endeavourenergy.com.au/wps/wcm/connect/EE/NSW/NSW+omepage/communityNav. [Accessed: 14-Febuary-2022].

[55] "Dynamic Regulation (DR) | National Grid ESO", *Nationalgrideso.com*, 2022. [Online]. Available: https://www.nationalgrideso.com/industry-information/balancing-services/Frequency-Response-Services/Dynamic-Regulation. [Accessed: 15-Febuary- 2022].

[56] "Dynamic Containment | National Grid ESO", *Nationalgrideso.com*, 2022. [Online]. Available: https://www.nationalgrideso.com/balancing-

services/frequency-response-services/dynamic-containment. [Accessed: 15-Febuary-2022].

[57] "Future of Frequency Response – Industry update," National Grid ESO. [Online]. Available: https://www.nationalgrideso.com/document/138861/download. [Accessed: 19-Febuary-2022].

[58] J. Meng, Y. Mu, J. Wu, H. Jia, Q. Dai and X. Yu, "Dynamic frequency response from electric vehicles in the Great Britain power system," *Journal of Modern Power Systems and Clean Energy*, vol. 3, no. 2, pp. 203-211, June 2015.

[59] S. Esmailnajad, "Demand Side Management in Swedish Industry – An investigation of load management in major Swedish industries," Master's Thesis, Chalmers University of Technology, 2014.

[60] S. Puranik, "Demand Side Management Potential in Swedish Households – A case study of dishwasher, laundry and water hearing loads," Master's Thesis, Chalmers University of Technology, 2014.

[61] Y. Liu, N. Eyre, S. Darby, M. Keay, D. Robinson and X. Li, "Assessment of Demand Response Market Potential and Benefits in Shanghai," July 2015. [Online]. Available: https://www.eci.ox.ac.uk/research/energy/downloads/Assessment%20of%20Demand%20Response%20Market%20Potential%20and%20Benefits%20in%20Shanghai.pdf. [Accessed: 20-Febuary-2022].

[62] "Demand side response in non-domestic sector – Final report for Ofgem," Elementenergy, July 2012. [Online]. Available: http://www.element-energy.co.uk/wordpress/wp-content/uploads/2012/07/Demand-Side-Response-in-the-non-domestic-sector.pdf. [Accessed: 21-Febuary-2022].

[63] "GB electricity demand – realising the resource," Sustainability First, April 2015. [Online]. Available: https://www.sustainabilityfirst.org.uk/images/publications/gbelec/Sustainability%20First%20-%20GB%20Electricity%20Demand%20%20Project%20-%20Infographic%20-%2011%20April%202015%20-%20FINAL.pdf. [Accessed: 21-Febuary-2022].

[64] "National Electricity Amendment (Classification of loads as ancillary service loads) Rule 2017," Australian Energy Market Commission, June 2017. [Online]. Available: https://www.aemc.gov.au/sites/default/files/content/d97f595d-5250-4f93-b52b-aacd07fee50c/ERC0221-Classification-of-Loads-as-Ancillary-Service-Loads-Consultation-Paper-FINAL.pdf. [Accessed: 21-Febuary-2022].

[65] G. Heffner, C. Goldman, B. Kirby and M. Kintner-Meyer, "Loads Providing Ancillary Services: Review of International Experience," Lawrence Berkeley National Laboratory, May 2007. [Online]. Available: https://www.energy.gov/sites/prod/files/oeprod/DocumentsandMedia/Loads_providing_Ancillary_Services_main_report_62701.pdf. [Accessed: 21-Febuary-2022].

[66] C. P. Steinmetz, "Power Control and Stability of Electric Generating Stations," *Transactions of the American Institute of Electrical Engineers*, vol. 39, no. 2, pp. 1215-1287, July 1920.

[67] A. Karimishad and T. t. Nguyen, "Probabilistic transient stability assessment using two-point estimate method," *8th International Conference on Advances in Power System Control, Operation and Management (APSCOM 2009)*, London,

UK, November 2009.

[68] R. Billinton, P. R. S. Kuruganty and M. F. Carvalho, “An Approximate Method for Probabilistic Assessment of Transient Stability,” *IEEE Transactions on Reliability*, vol. R-28, no. 3, pp. 255-258, August 1979.

[69] C. Dent, “Forecasting and Probabilistic Methods for Power Systems: A Review of UK Research,” The Institution of Engineering and Technology (IET), March 2015. [Online]. Available: https://www.pure.ed.ac.uk/ws/portalfiles/portal/31058015/4._IET_Educational_Chris_Dent_.pdf. [Accessed: 22-Febuary-2022].

[70] “Documentation | Probabilistic Analysis Overview”, *Rocscience.com*, 2022. [Online]. Available: https://www.rocscience.com/help/rocplane/documentation/probabilistic-analysis/probabilistic-analysis-overview. [Accessed: 22-Febuary-2022].

[71] M. R. Jannesar, A. Sedighi, M. Savaghebi, A. Anvari-Moghaddam and J. M. Guerrero, “Optimal probabilistic planning of passive harmonic filters in distribution networks with high penetration of photovoltaic generation,” *International Journal of Electrical Power & Energy Systems*, vol. 110, pp. 332-348, September 2019.

[72] R. L. Harrison, “Introduction to Monte Carlo Simulation,” *AIP Conference Proceeding*, vol. 1204, no. 17, January 2010.

[73] P. L. Bonate, “A Brief Introduction to Monte Carlo Simulation,” *Clinical Pharmacokinetics*, vol. 40, pp. 15-22, September 2012.

[74] K. N. Hasan, R. Preece and J. V. Milanovic, “Priority Ranking of Critical Uncertainties Affecting Small-Disturbance Stability Using Sensitivity Analysis Techniques,” *IEEE Transactions on Power Systems*, vol. 32, no. 4, pp. 2629-2639, July 2017.

[75] M. Fan, V. Vittal, G. T. Heydt and R. Ayyanar, “Probabilistic Power Flow Studies for Transmission Systems With Photovoltaic Generation Using Cumulants,” *IEEE Transactions on Power Systems*, vol. 27, no. 4, pp. 2251-2261. November 2012.

[76] Y. Chabane, A. A. Ladjici, A. Hellal and K. Dookhitram, “Cooperative coevolutionary algorithms for optimal PSS tuning based on Monte-Carlo Probabilistic small-signal stability assessment,” *International Transactions on Electricity Energy Systems*, vol. 30, no. 11, November 2020.

[77] L. Shi, S. Sun, L. Yao, Y. Ni and M. Bazargan, “Effects of wind generation intermittency and volatility on power system transient stability,” *IET Renewable Power Generation*, vol. 8, no. 5, pp. 509-521, 2014.

[78] P. N. Papadopoulos and J. V. Milanovic, “Probabilistic framework for transient stability assessment of power systems with high penetration of renewable generation,” *IEEE Transactions on Power Systems*, vol. 32, no.4, pp. 3078-3088, July 2017.

[79] J. Meng, Y. Mu, H. Jia, J. Wu, X. Yu and B. Qu, “Dynamic frequency response from electric vehicles considering travelling behaviour in the Great Britain power system,” *Applied Energy*, vol. 162, pp. 966-979, January 2016.

[80] O. Alizadeh Mousavi, R. Cherkaoui and M. Bozorg, “Blackouts risk evaluation by Monte Carlo Simulation regarding cascading outages and system frequency deviation,” *Electric Power Systems Research*, vol. 89, pp. 157-164, August 2012.

[81] H. Huang, C. Y. Chung, K. W. Chan and H. Chen, “Quasi-Monte Carlo Based

Probabilistic Small Signal Stability Analysis for Power Systems With Plug-In Electric Vehicle and Wind Power Integration," *IEEE Transactions on Power Systems*, vol. 28, no. 3, pp. 3335-3343, August 2013.

[82] R. Preece, J. V. Milanovic, "Efficient Estimation of the Probability if Small-Disturbance Instability of Large Uncertain Power Systems," *IEEE Transactions on Power Systems*, vol. 31, no.2, pp. 1063-1072, March 2016

[83] H. W. Qazi and D. Flynn, "Analysing the impact of large-scale decentralised demand side response on frequency stability," *International Journal of Electrical Power & Energy Systems*, vol. 80, pp. 1-9, September 2016.

[84] P. Sheikhzadeh-Baboli and M. Assili, "A Hybrid Adaptive Algorithm for Power System Frequency Regulation Based on Proposed Emergency Demand Side Management," *IETE Journal of Research*, DOI: 10.1080/03772063.2021.1942246, July 2021.

[85] Y. Dong, X. Xie, K. Wang, B. Zhou and Q. Jiang, "An Emergency-Demand-Response Based Under Speed Load Shedding Scheme to Improve Short-Term Voltage Stability," *IEEE Transactions on Power Systems*, vol. 32, no. 5, pp. 3726-3735, September 2017.

[86] R. M. Larik, M. W. Mustafa, M. N. Aman, T. A. Jumani, S. Sajid and M. K. Panjwani, "An Improved Algorithm for Optimal Load Shedding in Power Systems," *Energies*, vol. 11, no. 7, 1808, July 2018.

[87] S. Rai, Y. Kumar and G. Agnihotri, "Under Voltage Load Shedding for Contingency Analysis to Optimize Power Loss and Voltage Stability Margin," *Electrical and Electronics Engineering: An International Journal (ELELIJ)*, vol. 3, no. 4, pp. 57-64, November 2014.

[88] P. Gupta and Y. P. Verma, "Voltage profile improvement using demand side management in distribution networks under frequency linked pricing regime," *Applied Energy*, vol. 295, 117053, August 2021.

[89] J. Ponocko and J. V. Milanovic, "Multi-Objective Demand Side Management at Distribution Network Level in Support of Transmission Network Operation," *IEEE Transactions on Power Systems*, vol. 35, no. 3, pp. 1822-1833, May 2020.

[90] W. Hu, C. Wang, Z. Chen and B. Bak-Jensen, "Power system transient stability improvement using demand side management in competitive electricity markets," *2012 9th International Conference on the European Energy Market*, Florence, Italy, May 2012.

[91] X. Tang and J. V. Milanovic, "Assessment of the impact of demand side management on power system small signal stability," *2017 IEEE Manchester PowerTech*, Manchester, UK, June 2017.

[92] R. A. Biroon, Z. Abdollahi and R, Hadidi, "Frequency Control by Tariff Regulation: (A comparison between the MPC and Tariff Modification)," *2020 IEEE Texas Power and Energy Conference (TPEC)*, TX, USA, February 2020.

[93] C. Duan, P. Chakraborty, T. Nishikawa and A. E. Motter, "Hierarchical Power Flow Control in Smart Grids: Enhancing Rotor Angle and Frequency Stability with Demand-Side Flexibility," *IEEE Transactions on Control of Network Systems*, vol. 8, no. 3, pp. 1046-1058, September 2021.

[94] S. Ranjan, A. Latif, D. C. Das, N. Sinha, S. M. S. Hussain, T. S. Ustun and A. Iqbal, "Simultaneous analysis of frequency and voltage control of the interconnected hybrid power system in presence of FACTS devices and demand response

scheme," *Energy Reports*, vol. 7, pp. 7445-7459, November 2021.

[95] B. Qi, K. N. Hasan and J. V. Milanovic, "Identification of Critical Parameters Affecting Voltage and Angular Stability Considering Load-Renewable Generation Correlations," *IEEE Transactions on Power Systems*, vol. 34, no. 4, pp. 2859-2869, July 2019.

[96] Y. Zhu and J. V. Milanovic, "Identifying Critical Load Locations for Power System Voltage, Angular and Frequency Stability," *2019 IEEE PES Innovative Smart Grid Technologies Europe (ISGT-Europe)*, Bucharest, Romania, October 2019.

[97] N. Mithulananthan, C. A. Canzares, J. Reeve and G. J. Rogers, "Comparison of PSS, SVC, and STATCOM controllers for damping power system oscillations," *IEEE Transactions on Power Systems*, vol. 18, no. 2, pp. 786-792, May 2003.

[98] C. Guo, W. Jiang and C. Zhao, "Small-signal instability and supplementary coordinated damping-control of LCC-HVDC system with STATCOM under weak AC grid conditions," *International Journal of Electrical Power & Energy Systems*, vol. 104, pp. 246-254, January 2019.

[99] W. Dong, H. Xin, D. Wu and L. Huang, "Small Signal Stability Analysis of Multi-Infeed Power Electronic Systems Based on Grid Strength Assessment," *IEEE Transactions on Power Systems*, vol. 34, no. 2, pp. 1393-1403, March 2019.

[100] Y. Li, G. Geng and Q. Jiang, "A parallelized Contour Integral Rayleigh-Ritz Method for Computing Critical Eigenvalues of Large-Scale Power Systems," *IEEE Transactions on Smart Grid*, vol. 9, no. 4, pp. 3573-3581, July 2018.

[101] G. Rogers, *Power system oscillations*: Springer Science & Business Media, 2012.

[102] C. S. Saunders, M. M. Alamuti and G. A. Taylor, "Transient stability analysis using potential energy indices for determining critical generator sets," *2014 IEEE PES General Meeting*, MD, USA, July 2014.

[103] A. Sajadi, R. Preece and J. V. Milanovic, "Evaluation of Suitability of Different Transient Stability Indices for Identification of Critical System States," *arXiv:2001.03519*, January 2020.

[104] L. Shi, S. Dai, Y. Ni, L. Yao and M. Bazargan, "Transient stability of power systems with high penetration of DFIG based wind farms," *2009 IEEE PES General Meeting*, AB, Canada, July 2009.

[105] T. Su, Y. Liu, J. Zhao and J. Liu, "Probabilistic Stacked Denoising Autoencoder for Power System Transient Stability Prediction With Wind Farms," *IEEE Transactions on Power Systems*, vol. 36, no. 4, pp. 3786-3789, December 2020.

[106] A. Sajadi, R. Preece and J. V. Milanovic, "Identification of transient stability boundaries for power systems with multidimensional uncertainties using index-specific parametric space," *International Journal of Electrical Power & Energy Systems*, vol. 123, 106152, December 2020.

[107] J. Huang, L. Guan, Y. Su, H. Yao, M. Guo and Z. Zhong, "Recurrent Graph Convolutional Network-Based Multi-Task Transient Stability Assessment Framework in Power System," *IEEE Access*, vol. 8, pp. 93283-93296, April 2020.

[108] A. G. Phadke, J. S. Thorp and M. G. Adamiak, "A New Measurement Technique for Tracking Voltage Phasors, Local System Frequency, and Rate of Change of Frequency," *IEEE Transactions on Power Apparatus and Systems*, vol. PAS-102, no. 5, pp. 1025-1038, May 1983.

[109] "Grid Code | Nation Grid ESO". *Nationalgrideso.com,* 2021. [Online]. Available: http://www.nationalgrideso.com/industry-information/codes/grid-code-

old?code-documents=. [Accessed: 29/03/2021].

[110] M. Nedd, J. Browell, K. Bell and C. Booth, "Containing a Credible Loss to Within Frequency Stability Limits in a Low-Inertia GB Power System," *IEEE Transactions on Industry Applications*, vol. 56, no. 2, pp. 1031-1039, March-April 2020.

[111] R. Urban, S. Denis and M. Rafael, "Estimating frequency stability margin for flexible under-frequency relay operatoin," *Electric Power Systems Research*, vol. 194, 107116, May 2021.

[112] B. Sravan Kumar, M. Suryakalavathi and G. V. Nagesh Kumar, "Optiml location of thyristor Controlled Series Capacitor to improve power system performance using Line based composite index," *2016 IEEE 6th International Conference on Power Systems (ICPS)*, New Delhi, India, March 2016.

[113] I. Musirin and T. K. Adbul Rahman, "Novel fast voltage stability index (FVSI) for voltage stability analysis in power transmission system," *Student Conference on Research and Development*, Shah Alam, Malaysia, July 2002.

[114] A. N. Yadav and K. Pal, "Demand side maximum loading limit ranking based on composite index using ANN," *International Journal of System Assurance Engineering and Management*, November 2021.

[115] X. Ye and J. V. Milanovic, "Composite Index for Comprehensive Assessment of Power System Transient Stability," *IEEE Transactions on Power Systems*, Early Access, November 2021.

[116] S. Vyas and L. Kumaranayake, "Constructing socio-economic statues indices: how to use principal components analysis," *Health Policy and Planning*, vol. 21, no. 6, pp. 459-468, November 2006.

[117] E. Rakhshani, D. Gusain, V. Sewdien, J. L. R. Torres and M. A. M. M. V. D. Meijden, "A Key Performance Indicator to Assess the Frequency Stability of Wind Generation Dominated Power System," *IEEE Access*, vol. 7, pp. 130957-130969, September 2019.

[118] D. O. Villalba, C. Rahmann, R. Alvarez, C. A. Canizares and C. Strunck, "Practical Framework for Frequency Stability Studies in Power Systems with Renewable Energy Sources," *IEEE Access*, vol. 8, pp. 202286-202297, Novermber 2020.

[119] Y. Zou, W. Chen. M. Tong and S. Tao, "DEA Cross-Efficiency Aggregation with Deviation Degree Based on Standardized Euclidean Distance", *Mathematical Problems in Engineering*, vol. 2021, Article ID 6682499, 2021. https://doi.org/10.1155/2021/6682499.

[120] S. Chow, J. Shao and H. Wang, "A NOTE ON SAMPLE SIZE CALCULATION FOR MEAN COMPARISONS BASED ON NONCENTRAL t-STATISTICS," *Journal of Biopharmaceutical Statistics*, vol. 12, no. 4, pp. 441-456, 2002.

[121] Y. Zhu and S. Au, "Bayesian operational modal analysis with asynchronous data, part I: Most probable value," *Mechanical Systems and Signal Processing*, vol. 98, pp. 652-666, January 2018.

[122] W. J. Gil-Gpnzalez, A. Garces, O. B. Fosso and A. Escobar-Mejia, "Passivity-Based Control of Power Systems Considering Hydro-Turbine With Surge Tank," *IEEE Transactions on Power Systems*, vol. 35, no.3, pp. 2002-2011, May 2020.

[123] C. Li, Y. Wu, H. Zhang and Y. Liu, "Study of Modeling of Dynamic Components in STEPS," *IEEE Sustainable Power and Energy Conference*, Novermber 2020.

[124] S. Tsegaye and K. A. Fante, "Analysis of Synchronous Machine Excitation Systems: Comparative Study," *International Journal of Electrical, Computer, Energetic,*

Electronic and Communication Engineering, vol. 10, no. 12, pp. 1492-1496, 2016.

[125] S. Mohajeryami, A. R. Neelakantan, I. N. Moghaddam and Z. Salami, "Modeling of deadband function of governor model and its effect on frequency response characteristics," 2015 *North American Power Symposium (NAPS)*, October 2015.

[126] C. Duggan, P. Brogan, X. Liu, R. Best and J. Morrow, "Synchronisation Control Action for Very Low-Frequency Oscillations," *Irish Signals and Systems Conference (ISSC),* June 2021.

[127] S. Jin, S. G. Abhyankar, B. J. Palmer, R. Huang, W. A. Perkins and Y. Chen, "Toward a Numberically Robust and Efficient Implicit Integration Scheme for Parallel Power Grid Dynamic Simulation Development in GridPACK™," *Transactions on Computational Science and Computational Intelligence*, pp. 371-386, October 2021.

[128] S. Sumathi, L. A. Kumar and P. Surekha, *Solar PV and Wind Energy Conversion Systems*, Springer, 2015.

[129] *WECC Wind Power Dynamic Modelling Guide*. WECC Renewable Energy Modelling Task Force, Salt Lake City, UT, USA, 2014.

[130] *Wind Turbines-Part 27-I: Electrical Simulation Models – Wind Turbines*. IEC 61400-27-1, 2015.

[131] *WECC PV Power Dynamic Modelling Guide*. WECC Renewable Energy Modelling Task Force, Salt Lake City, UT, USA, 2014.

[132] M. Abdraman, A. Tahir, D. Lissouck, M. Kazet and R. Mouangue, "Wind Resource Assessment in the City of N'dhamena in Chad," *International Journal of Renewable Energy Research-IJRER*, vol. 6, no. 3, 2016.

[133] National Renewable Energy Laboratory, PVWatts Viewer [Online]. Available: https://pvwatts.nrel.gov/.

[134] Y. Zhu, J. V. Milanovic, "Automatic Identification of Power System Load Models Based on Field Measurements," *IEEE Transactions on Power Systems*, vol. 33, no. 3, pp. 3162-3171, May 2018.

[135] CIGRE WG C4.605: "Modelling and aggregation of loads in flexible power networks," J. V. Milanovic, (Convenor), (TB 566), ISBN: 978-2-85873-261-6, February 2014.

[136] L. Hajagos and B. Danai, "Laboratory Measurement of Modern Loads Subjected to Large Voltage Changes for Use in Voltage Stability Studeis," 1996.

[137] C. Taylor, Power System Voltage Stability. New York: McGraw-Hill, 1994.

[138] P. C. Krause, Analysis of Electric Machinery. New York: McGraw-Hill, 1986.

[139] S. M. Zali and J. V. Milanovic, "Generic model of active distribution network for large power system stability studies," IEEE Transactions on Power Systems, vol. 28, no. 3, pp. 3126-3133, August 2013.

[140] P. Regulski, D. Vilchis-Rodriguez, S. Djurovic and V. Terzija, "Estimation of composite load model parameters using an imporved particle swarm optimization method," IEEE Transactions on Power Delivery, vol. 30, no. 2, pp. 553-560, April 2015.

[141] J.-Y. Lim, J.-H. Kim, J.-O. Kim, and C. Singh, "Application of expert system to load composition rate estimation algorithm," *IEEE Transactions on Power Systems,* vol. 14, no. 3, pp. 1137-1143, August 1999.

[142] X. Liang, W. Xu, C. Y. Chung, W. Freitas and K. Xiong, "Dynamic Load Models for Industiral Facilities," *IEEE Transactions on Power Systems,* vol. 27, no. 1, pp. 69-

80, February 2012.
[143] I. Richardson, M. Thomson, D. Infield, and C. Clifford, “Domestic electricity use: A high-resolution energy demand model,” *Energy and Buildings,* vol. 42, no. 10, pp. 1878-1887, October 2010.
[144] National Grid. Demand Data [Online]. Available: https://www.nationalgrid.com/UK/Industry-information/Electricity-transmission-operational-data/Data-Explorer/.
[145] M. Starke, N. Alkadi and O. Ma, “Assessment of industrial load for demand response across U.S. regions of the Western Interconnect”, *Oak Ridge National Laboratory*, Oak Ridge, Tennessee, USA, 2013.
[146] "Monthly Hourly Load Values," entsoe.eu, 2019. [Online].Available: https://www.entsoe.eu/data/power-stats/hourly_load/. [Accessed: 14/10/2019].
[147] P. Pourbeik and A. Gaikwad, “A Summary of EPRI Load Modelling Efforts,” 2011.
[148] T. Muller and D. Most, “Demand Response Potential: Available when Needed?”, *ELSEVIER*, Energy Policy 115, pp. 181-198, 2018.
[149] H. C. Gils, “Assessment of the theoretical demand response potential in Europe”, *ELSEVIER*, Energy 67, pp. 1-18, 2014.
[150] Sweden Statisitcs. [Online]. Available: https://www.scb.se/en.
[151] DECC. Energy Consumpton in the UK (ECUK), Domestic data tables, 2013 Update, July 2013.
[152] DECC. Capturing the full electricity efficiency potential of the UK, November 2012.
[153] B. Drysdale, J. Wu and N. Jenkins, “Flexible demand in the GB domestic electricity sector in 2030”, *ELSEVIER*, Applied Energy 139, pp. 281-290, 2015.
[154] P. Bertoldi, B. Hirl and N. Labanca, “Energy efficiency status report 2012:, *European Commission, JRC, Scientific and Policy Reports* 136, 2012.
[155] A. Masood, A. Xin, S. A. A. Rizvi, H. S. Qazi, L. K. Qambrani and S. Khan, “Congestion Management in Local Market Considring the Payback Effect,” *Asia Conference on Power and Electical Engineering (ACPEE)*, April 2021.
[156] A. Esmat, J. Usaola and M. A. Moreno, “Congestion management in smart grids with flexible demand considering the payback effect,” *IEEE PES Innovative SMART Grid Technologies Conference Europe (ISGT-Europe)*, October 2016.
[157] R. Kollu, S. R. Rayapudi, SVL. Narasimham and K. M. Pakkurthi, “Mixture probability distribution functions to model wind speed distributions,” *International Journal of Energy and Environment Engineering*, October 2012.
[158] Y. M. Kantar, I. Usta, I. Arik and I. Yenilmez, “Wind speed analysis using the Extended Generalized Lindley Distribution,” *Elservier*, Renewable Energy, vol. 118, pp. 1024-1030, April 2018.
[159] J. Hossain, S. Sharma, V. V. N. Kishore, “Multi-peak Gaussian fit Applicability to wind speed distribution,” *Elsevier*, Renewable and Sustainable Energy Reviews, vol. 34, pp. 483-490, June 2014.
[160] C. Jung and D. Schindler, “Wind speed distribution selection – A review of recent development and progress,” *Elsevier*, Renewable and Sustainable Energy Reviews, vol. 34, October 2019.
[161] T. H. Yeh and L. Wang, “A Study on Generator Capacity for Wind Turbines Under Various Tower Heights and Rated Wind Speeds Using Weibull Distribution,” *IEEE*

Transactions on Energy Conversion, vol. 23, no. 2, pp. 592-602, June 2008.

[162] Z. Qin, W. Li and X. Xiong, "Generation System Reliability Evaluation Incorporating Correlations of Wind Speeds with Different Distributions," *IEEE Transactions on Power Systems*, vol. 28, no. 1, pp. 551-558, February 2013.

[163] A. Feijoo and D. Villanueva, "Wind Farm Power Distribution Function Considering Wake Effects," *IEEE Transactions on Power Systems*, vol. 32, no. 4, pp. 3313-3314, July 2017.

[164] S. Tewari, C. J. Geyer and N. Mohan, "A Statistical Model for Wind Power Forecast Error and its Application to the Estimation of Penalties in Liberalized Markets,' *IEEE Transactions on Power Systems*, vol. 26, no. 4, pp. 2031-2039, November 2011.

[165] L. Yang, M. He, J. Zhang and V. Vittal, "Support-Vector-Machine-Enhanced Markov Model for Short-Term Wind Power Forecast," *IEEE Transactions on Sustainable Energy*, vol. 6, no. 3, pp. 791-799, July 2015.

[166] D. D. Tung and T. H. Le, "A Statistical Analysis of Short-Term Wind Power Forecasting Error Distribution," *International Journal of Applied Engineering Research*, vol. 12, no. 10, pp. 2306-2311, 2017.

[167] S. Liu, P. X. Liu and X. Wang, "Stochasitc Small-Signal Stablity Analysis of Grid-Connected Photovoltaic Systems," *IEEE Transactions on Industrial Electronics*, vol.63, no. 2, pp. 1027-1038, February 2016.

[168] M. F. N. Khan, T. N. Malik and I. A. Sajjad, "A Novel Probabilistic Generation Model for Grid Connected PV Based Distributed Generation," *Journal of Engineering Reseach*, vol. 8, no. 1, pp. 231-247, March 2020.

[169] W. Li and R. Billinton, "Effect of bus load uncertainty and correlation in composite system adequacy evaluation," *IEEE Transactions on Power Systems*, vol. 6, no. 4, pp. 1522-1529, November 1991.

[170] P. Huang, G. Huang, G. Augenbore and S. Li, "Optimal configuration of multiple-chiller plants under cooling load uncertainty for different climate effects and building types," *Elsevier*, Energy and Buildings, vol. 158, pp. 684-697, January 2018.

[171] S. Zhang, Y. Cheng, J. Liu and Z. Lin, "Subzone control optimization of air distribution for thermal comfort and energy efficiency under cooling load uncertainty," *Elsevier*, Applied Energy, vol. 251, October 2019.

[172] J. L. Aznarte and N. Siebert, "Dynamic Line Rating Using Numerical Weather Predictions and Machine Learning: A Case Study," *IEEE Transactions on Power Delivery*, vol. 32, no. 1, pp. 335-343, February 2017.

[173] L. Kuipers and H. Niederreiter. *Uniform Distribution of Sequences*, Dover Publications, Inc. 2016.

[174] T. Guo and J. V. Milanovic, "Online Identification of Power System Dynamic Signature Using PMU Measuremnts and Data Mining," *IEEE Transactions on Power Systems*, vol. 31, no. 3, pp. 1760-1768, May 2016.

[175] R. Billinton and P. R. S. Kuruganty, "Probabilistic Assessment of Transient Stability in a Practical Multimachine System," *IEEE Transactions on Power Apparatus and Systems*, vol. PAS-100, no. 7, pp. 3634-3641, July 1981.

[176] J. P. Coelingh, A. J. M. van Wijk and A. A. M. Holtslag, "Analysis of wind speed observations over the North Sea," *Elsevier, Journal of Wind Engineering and Industrial Aerodynamics*, vol. 61, no. 1, pp. 51-69, June 1996.

[177] S. Tao, Y. Ruoting, Z. Linhzhi and G. Shan, “Power system probabilistic production simulation containing large-scale wind power and photovoltaic power,” *IEEE-PES Asia-Pacific Power and Energy Engineering Conference (APPEEC)*, December 2013.

[178] J. L. Rueda, D. G. Colome and I. Erlich, “Assessment and Enhancement of Small Signal Stability Considering Uncertainties,” *IEEE Transactions on Power Systems*, vol. 24, no. 1, pp. 198-207, February 2009.

[179] J. D. Morales, J. V. Milanovic, “Methodology for Optimal Deployment of Corrective Control Measures to Ensure Transient Stability of Uncertain Power Systems,” *IEEE Transactions on Power Systems*, vol. 36, no. 3, pp. 1677-1687, May 2021.

[180] K. N. Hasan and R. Preece, “Influence of Stochastic Dependence on Small-Disturbance Stability and Ranking Uncertainties,” *IEEE Transactions on Power Systems*, vol. 33, no. 3, pp. 3227-3235, May 2018.

[181] R. C. Burchett, H. H. Happ and D. R. Vierath, “Quadratically Convergent Oprimal Power Flow,” *IEEE Transactions on Power Apparatus and Systems*, vol. PAS-103, no. 11, pp. 3267-3275, November 1984.

[182] R. D. Zimmerman, C. E. Murillo-Sanchez and R. J. Thomas, “MATPOWER: Steady-state operations, planning and analysis tools for power system research and education,” *IEEE Trans. Power Systems*, vol. 26, no. 1, pp. 12-19, February 2011.

[183] R. Latpate, J. Kshirsagar, V. K. Gupta and G. Chandra, *Advanced Sampling Methods*, Springer, 2021.

[184] Y. Zhu and J. V. Milanovic, “Efficient identification of critical load model parameters affecting transient stability,” Electric Power Systems Research, vol. 175, October 2019.

[185] M. I. Jordan and T. M. Mitchell, “Machine learning: Trends, perspectives, and prospects,” *Science*, vol. 349, No. 6245, pp. 256-260, July 2015.

[186] O. A. Alimi, K. Ouahada and A. M. Abu-Mahfouz, “A Review of Machine Learning Approaches to Power System Security and Stability,” IEEE Access, vol. 8, pp. 113512-113531, June 2020.

Appendix A: Test Network Data

This appendix introduces modelling data of important system components (e.g., synchronous generators, loads and transmission lines) in all test networks.

A.1 Modified IEEE 9-Bus Test System

A.1.1 Synchronous Generator Data

The modelling data of synchronous generators in the modified IEEE 9-bus test system is presented in Table A.1 (basic information), Table A.2 (resistance and reactance), Table A.3 (time constants) and Table A.4 (cost coefficients).

Table A.1 Synchronous generators data for the modified IEEE 9-bus test system (basic information)

Generator	P (MW)	Q (Mvar)	Pmax (MW)	Pmin (MW)	Qmax (Mvar)	Qmin (Mvar)	Voltage (p.u.)	Power Base (MVA)
G1	0	0	178.82	0	300	-300	1	100
G2	28.33	0	30.83	0	300	-300	1	100
G3	28.33	0	30.83	0	300	-300	1	100
G4	28.33	0	30.83	0	300	-300	1	100
G5	54.33	0	66.67	0	300	-300	1	100
G6	54.33	0	66.67	0	300	-300	1	100
G7	54.33	0	66.67	0	300	-300	1	100

Table A.2 Synchronous generators data for the modified IEEE 9-bus test system (resistance & reactance)

Generator	Rotor Type	X_l (p.u.)	X_d (p.u.)	X_q (p.u.)	X'_d (p.u.)	X'_q (p.u.)	X''_d (p.u.)	X''_q (p.u.)
G1	Salient	0.083	0.361	0.240	0.150	N/A	0.1	0.1
G2	Round	0.095	1.680	1.610	0.332	0.320	0.2	0.2
G3	Round	0.095	1.680	1.610	0.332	0.320	0.2	0.2
G4	Round	0.095	1.680	1.610	0.332	0.320	0.2	0.2
G5	Round	0.100	1.720	1.660	0.330	0.378	0.2	0.2
G6	Round	0.100	1.720	1.660	0.330	0.378	0.2	0.2
G7	Round	0.100	1.720	1.660	0.330	0.378	0.2	0.2

Table A.3 Synchronous generators data for the modified IEEE 9-bus test system (time constants)

Generator	Rotor Type	T'_{d0} (s)	T'_{q0} (s)	T''_{d0} (s)	T''_{q0} (s)	H (s)
G1	Salient	8.960	N/A	0.075	0.150	9.552
G2	Round	5.890	0.600	0.058	0.080	2.770
G3	Round	5.890	0.600	0.058	0.080	2.770
G4	Round	5.890	0.600	0.058	0.080	2.770
G5	Round	6.000	0.535	0.058	0.095	4.320
G6	Round	6.000	0.535	0.058	0.095	4.320
G7	Round	6.000	0.535	0.058	0.095	4.320

Table A.4 Synchronous generators data for the modified IEEE 9-bus test system (cost coefficients)

Generator	C_2	C_1	C_0	Generator	C_2	C_1	C_0
G1	0.11	5	150	G5	0.085	1.2	600
G2	0.1225	1	335	G6	0.085	1.2	600
G3	0.1225	1	335	G7	0.085	1.2	600
G4	0.1225	1	335				

The modelling data of synchronous generator controllers in the modified IEEE 9-bus test system is summarised in Table A.5.

Table A.5 Synchronous generators data for the modified IEEE 9-bus test system (controllers)

Exciters	
IEEE ST1A (static exciter)	T_R=0.01, K_A^{ex}=200, E_{fd}^{min}=-5, E_{fd}^{max}=5
IEEE DC1A (DC exciter)	T_R=0.01, K_A^{ex}=40, E_{fd}^{min}=-10, E_{fd}^{max}=10, T_A^{ex}=0.02, T_E^{ex}=0.785, K_E^{ex}=1, A_E^{ex}=0.07, B_E^{ex}=0.91
Speed Governors	
IEEEG3 (hydro)	T_g=0.05, T_p=0.04, Sigma permanent droop=20, Delta temporary droop=0.2, T_r=10, a11=0.5, a13=1, a21=1.5, a23=1, T_w=0.75, U_c=-0.1, U_o=0.1, P_{min}=0, P_{max}=1
IEEEG1 (steam)	*K*=20, *T1*=0.2, *T2*=1, *T3*=0.6, *T4*=0.6, *T5*=0.5, *T6*=0.8, *T7*=1, *K1*=0.3, *K2*=0, *K3*=0.25, *K4*=0, *K5*=0.3, *K6*=0, *K7*= 0.15, *K8*=0, U_c=-0.3, U_o=0.3, P_{min}=0, P_{max}=1
GAST (gas fire)	*R*=20, *T1*=0.4, *T2*=0.1, *T3*=3, *AT*=1, *Kt*=2, V_{min}=0, V_{max}=1
AVR	
AVR (static exciter)	*K1*=200, *T1*=0.01, *y_min*=-5, *y_max*=5
AVR (DC exciter)	*K*=1, *K1*=40, *T*=0.785, *T1*=0.01, *T2*=0.02, *Ae*=0.07, *Be*=0.91, *y_min*=-10, *y_max*=10
PSS	
PSS	*Tw1*=10, *Tw2*=10, *T1*=0.05, *T2*=0.01, *T3*=0.05, *T4*=0.02, K_{pss}=10, *y_min*=-0.5, *y_max*=0.5

A.1.2 Load Data

The modelling data of loads in the modified IEEE 9-bus test system is summarised in Table A.6.

Table A.6 Loads data for the modified IEEE 9-bus test system

Load	Location	P (MW)	Q (Mvar)
1	Bus 5	90	30
2	Bus 7	100	35
3	Bus 9	125	50

A.1.3 Transmission Line Data

The modelling data of transmission lines (including transformers) in the modified IEEE 9-bus test system is summarised in Table A.7.

Table A.7 Transmission lines (including transformers) data for the modified IEEE 9-bus test system

From Bus	To Bus	R (p.u.)	X (p.u.)	B (p.u.)
1	4	0	0.058	0
4	5	0.017	0.092	0.158
5	6	0.039	0.17	0.358
3	6	0	0.059	0
6	7	0.012	0.101	0.209
7	8	0.009	0.072	0.149
8	2	0	0.063	0
8	9	0.032	0.161	0.306
9	4	0.01	0.085	0.176

A.2 Modified IEEE 68-Bus Test System

A.2.1 Synchronous Generator Data

The modelling data of synchronous generators in the modified IEEE 68-bus test system is presented in Table A.8 (basic information), Table A.9 (resistance and reactance), Table A.10 (time constants) and Table A.11 (cost coefficients).

Table A.8 Synchronous generators data for the modified IEEE68-bus test system (basic information)

Generator (Type)	P (MW)	Q (Mvar)	Pmax (MW)	Pmin (MW)	Qmax (Mvar)	Qmin (Mvar)	Voltage (p.u.)	Power Base (MVA)
G1 (gas fire)	250	0	297.5	29.75	280	-210	1.045	100
G2(gas fire)	545	0	637.5	63.75	600	-450	0.98	100
G3 (coal fire)	650	0	765	76.5	720	-540	0.983	100
G4 (nuclear)	632	0	765	76.5	720	-540	0.997	100
G5 (hydro)	505	0	595	59.5	560	-420	1.011	100
G6 (nuclear)	700	0	850	85	800	-600	1.05	100
G7 (coal fire)	560	0	680	68	640	-480	1.063	100
G8 (coal fire)	540	0	637.5	63.75	600	-450	1.03	100
G9 (hydro)	800	0	935	93.5	880	-660	1.025	100
G10 (coal fire)	500	0	595	59.5	560	-420	1.01	100
G11 (coal fire)	1000	0	1190	119	1120	-840	1.00	100
G12 (nuclear)	1350	0	1615	161.5	1520	-1140	1.016	100
G13 (coal fire)	3591	0	3570	357	3360	-2520	1.011	100
G14 (coal fire)	1785	0	2125	212.5	2000	-1500	1.00	100
G15 (coal fire)	1000	0	1190	119	1120	-840	1.00	100
G16 (coal fire)	4000	0	4717.5	471.75	4440	-3330	1.00	100

Table A.9 Synchronous generators data for the modified IEEE 68-bus test system (resistance & reactance)

Generator (Type)	Rotor Type	X_l (p.u.)	X_d (p.u.)	X_q (p.u.)	X'_d (p.u.)	X'_q (p.u.)	X''_d (p.u.)	X''_q (p.u.)
G1 (gas fire)	Round	0.044	0.350	0.242	0.109	0.098	0.088	0.088
G2(gas fire)	Round	0.263	2.213	2.115	0.523	0.450	0.375	0.375
G3 (coal fire)	Round	0.274	2.246	2.133	0.478	0.450	0.405	0.405
G4 (nuclear)	Round	0.266	2.358	2.322	0.392	0.360	0.315	0.315
G5 (hydro)	Round	0.189	2.310	2.170	0.462	0.420	0.350	0.350
G6 (nuclear)	Round	0.224	2.540	2.410	0.500	0.450	0.400	0.400
G7 (coal fire)	Round	0.258	2.360	2.336	0.392	0.360	0.320	0.320
G8 (coal fire)	Round	0.210	2.175	2.100	0.428	0.375	0.338	0.338
G9 (hydro)	Round	0.328	2.317	2.255	0.627	0.550	0.495	0.495
G10 (coal fire)	Round	0.139	1.183	0.805	0.320	0.315	0.280	0.280
G11 (coal fire)	Round	0.144	1.792	1.792	0.252	0.210	0.168	0.168
G12 (nuclear)	Round	0.418	1.919	1.805	0.589	0.532	0.475	0.475
G13 (coal fire)	Round	0.063	0.622	0.600	0.116	0.105	0.084	0.084
G14 (coal fire)	Round	0.043	0.450	0.433	0.072	0.063	0.058	0.058
G15 (coal fire)	Round	0.024	0.252	0.242	0.040	0.035	0.032	0.032
G16 (coal fire)	Round	0.114	0.988	0.927	0.197	0.167	0.153	0.153

Table A.10 Synchronous generators data for the modified IEEE 9-bus test system (time constants)

Generator (Type)	Rotor Type	T'_{d0} (s)	T'_{q0} (s)	T''_{d0} (s)	T''_{q0} (s)	H (s)
G1 (gas fire)	Round	10.20	1.50	0.050	0.035	12.000
G2(gas fire)	Round	6.56	1.50	0.050	0.035	4.027
G3 (coal fire)	Round	5.70	1.50	0.050	0.035	3.980
G4 (nuclear)	Round	5.69	1.50	0.050	0.035	3.178
G5 (hydro)	Round	5.40	0.44	0.050	0.035	3.714
G6 (nuclear)	Round	7.30	0.40	0.050	0.035	3.480
G7 (coal fire)	Round	5.66	1.50	0.050	0.035	3.300
G8 (coal fire)	Round	6.70	0.41	0.050	0.035	3.240
G9 (hydro)	Round	4.79	1.96	0.050	0.035	3.136
G10 (coal fire)	Round	9.37	1.50	0.050	0.035	4.429
G11 (coal fire)	Round	4.10	1.50	0.050	0.035	2.014
G12 (nuclear)	Round	7.40	1.50	0.050	0.035	4.858
G13 (coal fire)	Round	5.90	1.50	0.050	0.035	11.810
G14 (coal fire)	Round	4.10	1.50	0.050	0.035	12.000
G15 (coal fire)	Round	4.10	1.50	0.050	0.035	21.429
G16 (coal fire)	Round	7.80	1.50	0.050	0.035	8.108

Table A.11 Synchronous generators data for the modified IEEE 68-bus test system (cost coefficients)

Generator	C_2	C_1	C_0	Generator	C_2	C_1	C_0
G1	0.0193	6.9	0	G9	0.0071	3.7	0
G2	0.0111	3.7	0	G10	0.0090	3.9	0
G3	0.0104	2.8	0	G11	0.0050	4.0	0
G4	0.0088	4.7	0	G12	0.0040	2.9	0
G5	0.0128	2.8	0	G13	0.0019	2.5	0
G6	0.0094	3.7	0	G14	0.0033	3.3	0
G7	0.0099	4.8	0	G15	0.0050	3.8	0
G8	0.0113	3.6	0	G16	0.0014	9.5	0

The modelling data of synchronous generator controllers in the modified IEEE 68-bus test system is summarised in Table A.12.

Table A.12 Synchronous generators data for the modified IEEE 68-bus test system (controllers)

Exciters	
IEEE ST1A (static exciter)	T_R=0.01, K_A^{ex}=200, E_{fd}^{min}=-5, E_{fd}^{max}=5
IEEE DC1A (DC exciter)	T_R=0.01, K_A^{ex}=40, E_{fd}^{min}=-10, E_{fd}^{max}=10, T_A^{ex}=0.02, T_E^{ex}=0.785, K_E^{ex}=1, A_E^{ex}=0.07, B_E^{ex}=0.91
Speed Governors	
IEEEG3 (hydro)	T_g=0.05, T_p=0.04, Sigma permanent droop=20, Delta temporary droop=0.2, T_r=10, a11=0.5, a13=1, a21=1.5, a23=1, T_w=0.75, U_c=-0.1, U_o=0.1, P_{min}=0, P_{max}=1
IEEEG1 (steam)	*K*=20, *T1*=0.2, *T2*=1, *T3*=0.6, *T4*=0.6, *T5*=0.5, *T6*=0.8, *T7*=1, *K1*=0.3, *K2*=0, *K3*=0.25, *K4*=0, *K5*=0.3, *K6*=0, *K7*= 0.15, *K8*=0, U_c=-0.3, U_o=0.3, P_{min}=0, P_{max}=1

GAST (gas fire)	*R*=20, *T1*=0.4, *T2*=0.1, *T3*=3, *AT*=1, *Kt*=2, V_{min}=0, V_{max}=1
AVR	
AVR (static exciter)	*K1*=200, *T1*=0.01, *y_min*=-5, *y_max*=5
AVR (DC exciter)	*K*=1, *K1*=40, *T*=0.785, *T1*=0.01, *T2*=0.02, *Ae*=0.07, *Be*=0.91, *y_min*=-10, *y_max*=10
PSS	
PSS	*Tw1*=10, *Tw2*=10, *T1*=0.05, *T2*=0.01, *T3*=0.05, *T4*=0.02, K_{pss}=10, *y_min*=-0.5, *y_max*=0.5

A.2.2 Load Data

The modelling data of loads in the modified IEEE 68-bus test system is summarised in Table A.13.

Table A.13 Loads data for the modified IEEE 68-bus test system

Load	Location	P (MW)	Q (Mvar)	Load Category
1	Bus 17	6000	300	Distribution Network
2	Bus 18	2470	123	Distribution Network
3	Bus 20	680	103	Distribution Network
4	Bus 21	274	115	Distribution Network
5	Bus 23	248	85	Distribution Network
6	Bus 24	309	-92	Distribution Network
7	Bus 25	224	47	Distribution Network
8	Bus 26	139	17	Distribution Network
9	Bus 27	281	76	Distribution Network
10	Bus 28	206	28	Distribution Network
11	Bus 29	284	27	Distribution Network
12	Bus 33	112	0	Large Industrial Customer
13	Bus 36	104	-19.4	Large Industrial Customer
14	Bus 39	267	12.6	Distribution Network
15	Bus 40	65	23	Large Industrial Customer
16	Bus 41	1000	250	Large Industrial Customer
17	Bus 42	1150	250	Large Industrial Customer
18	Bus 44	267	4.84	Distribution Network
19	Bus 45	208	21	Distribution Network
20	Bus 46	150	28.5	Distribution Network
21	Bus 47	203	32	Distribution Network
22	Bus 48	241	2	Distribution Network
23	Bus 49	164	29	Distribution Network
24	Bus 50	100	-147	Large Industrial Customer
25	Bus 51	337	-122	Distribution Network
26	Bus 52	158	30	Large Industrial Customer
27	Bus 53	252	118	Distribution Network
28	Bus 55	322	2	Distribution Network
29	Bus 56	200	73.6	Large Industrial Customer
30	Bus 59	234	84	Large Industrial Customer
31	Bus 60	208	70	Large Industrial Customer
32	Bus 61	104	125	Large Industrial Customer

Load	Location	P (MW)	Q (Mvar)	Load Category
33	Bus 64	9	88	Large Industrial Customer
34	Bus 67	320	153	Distribution Network
35	Bus 68	329	32	Distribution Network

A.2.3 Transmission Line Data

The modelling data of transmission lines (including transformers) in the modified IEEE 9-bus test system is summarised in Table A.14.

Table A.14 Transmission lines (including transformers) data for the modified IEEE 68-bus test system

From Bus	To Bus	R (p.u.)	X (p.u.)	B (p.u.)
1	54	0	0.0181	0
2	58	0	0.0250	0
3	62	0	0.0200	0
4	19	0.0070	0.0142	0
5	20	0.0090	0.0180	0
6	22	0	0.0143	0
7	23	0.0050	0.0272	0
8	25	0.0060	0.0232	0
9	29	0.0080	0.0156	0
10	31	0	0.0260	0
11	32	0	0.0130	0
12	36	0	0.0075	0
13	17	0	0.0033	0
14	41	0	0.0015	0
15	42	0	0.0015	0
16	18	0	0.0030	0
36	17	0.0050	0.0045	0.3200
49	18	0.0076	0.1141	1.1600
68	19	0.0016	0.0195	0.3040
19	20	0.0007	0.0138	0
68	21	0.0008	0.0135	0.2548
21	22	0.0008	0.0140	0.2565
22	23	0.0006	0.0096	0.1846
23	24	0.0022	0.0350	0.3610
68	24	0.0003	0.0059	0.0680
54	25	0.0070	0.0086	0.1460
25	26	0.0032	0.0323	0.5310
37	27	0.0013	0.0173	0.3216
26	27	0.0014	0.0147	0.2396
26	28	0.0043	0.0474	0.7802
26	29	0.0057	0.0625	1.0290
28	29	0.0014	0.0151	0.2490
53	30	0.0008	0.0074	0.4800
61	30	0.0019	0.0183	0.2900
61	30	0.0019	0.0183	0.2900

From Bus	To Bus	R (p.u.)	X (p.u.)	B (p.u.)
30	31	0.0013	0.0187	0.3330
53	31	0.0016	0.0163	0.2500
30	32	0.0024	0.0288	0.4880
32	33	0.0008	0.0099	0.1680
33	34	0.0011	0.0157	0.2020
35	34	0.0001	0.0074	0
34	36	0.0033	0.0111	1.4500
61	36	0.0022	0.0196	0.3400
61	36	0.0022	0.0196	0.3400
68	37	0.0007	0.0089	0.1342
31	38	0.0011	0.0147	0.2470
33	38	0.0036	0.0444	0.6930
41	40	0.0060	0.0840	3.1500
48	40	0.0020	0.0220	1.2800
42	41	0.0040	0.0600	2.2500
18	42	0.0040	0.0600	2.2500
17	43	0.0005	0.0276	0
39	44	0	0.0411	0
43	44	0.0001	0.0011	0
35	45	0.0007	0.0175	1.3900
39	45	0	0.0839	0
44	45	0.0025	0.0730	0
38	46	0.0022	0.0284	0.4300
53	47	0.0013	0.0188	1.3100
47	48	0.0025	0.0268	0.4000
47	48	0.0025	0.0268	0.4000
46	49	0.0018	0.0274	0.2700
45	51	0.0004	0.0105	0.7200
50	51	0.0009	0.0221	1.6200
37	52	0.0007	0.0082	0.1319
55	52	0.0011	0.0133	0.2138
53	54	0.0018	0.0206	1.3974
54	55	0.0013	0.0151	0.2572
55	56	0.0013	0.0213	0.2214
56	57	0.0008	0.0128	0.1342
57	58	0.0002	0.0026	0.0434
58	59	0.0006	0.0092	0.1130
57	60	0.0008	0.0112	0.1476
59	60	0.0004	0.0046	0.0780
60	61	0.0017	0.0182	0.7608
58	63	0.0007	0.0082	0.1389
62	63	0.0004	0.0043	0.0729
64	63	0.0016	0.0435	0
62	65	0.0004	0.0043	0.0729
64	65	0.0016	0.0435	0
56	66	0.0008	0.0129	0.1382
65	66	0.0009	0.0101	0.1723
66	67	0.0018	0.0217	0.3660
67	68	0.0009	0.0094	0.1710
53	27	0.0320	0.3200	0.4100
50	18	0.0012	0.0288	2.0600

A.3 4TNE System

Due to the confidential reasons, this section only introduces the cost coefficients of synchronous generators in the 4TNE system. All cost coefficients are adopted from open literatures and summarised in Table A.15.

Table A.15 Synchronous generators data of the 4TNE system (cost coefficients)

Area	Location	C_2	C_1	C_0
Area 4	1GC	0.0128	2.8	0
	2GC	0.0071	3.7	0
	3GC	0.0094	3.7	0
	4GC	0.0193	6.9	0
	5GCX	0.0104	2.8	0
	6GC	0.0111	3.7	0
Area 3	7GS	0.0014	9.5	0
	8GS	0.0019	2.5	0
	9GS	0.0014	9.5	0
	10GS	0.0014	9.5	0
	11GS	0.0050	3.8	0
	12GS	0.0088	4.7	0
	13GS	0.0071	3.7	0
	14GS	0.0193	6.9	0
	15GS	0.0033	3.3	0
	16GS	0.0088	4.7	0
Area 2	17GB	0.0090	3.9	0
	18GB	0.0113	3.6	0
	19GB	0.0040	2.9	0
	20GBX	0.0113	3.6	0
	21GB	0.0019	2.5	0
	22GB	0.0090	3.9	0
	23GB	0.0104	2.8	0
	24GB	0.0040	2.9	0
	25GB	0.0050	4.0	0
	26GB	0.0099	4.8	0
	27GB	0.0033	3.3	0
	28GB	0.0099	4.8	0
Area 1	29GMX	0.0094	3.7	0
	30GMX	0.0111	3.7	0
	31GMX	0.0193	6.9	0

Appendix B: Publications

B.1 Thesis Based Publications

B.1.1 International Journal Papers

[B1] M. Wang and J. V. Milanovic, “Simultaneous Assessment of Multiple Aspects of Stability of Power Systems with Renewable Generation,” submitted to *IEEE Transactions on Power Systems*, manuscript number: TPWRS-00229-2022.

[B2] M. Wang and J. V. Milanovic, “The Impacts of Demand Side Management on Combined Frequency and Angular Stability of the Power System,” submitted to *IEEE Transactions on Power Systems*, manuscript number: TPWRS-00375-2022. (In second review)

B.1.2 International Conference Papers

[B3] M. Wang, K. N. Hasan and J. V. Milanovic, “Impact of Demand Side Management on Angular Stability of Power Systems with Renewable Generation”, published in *IEEE ISGT Europe 2018*, Sarajevo, 2018.

[B4] K. N. Hasan, M. Wang and J. V. Milanovic, “A Survey on Demand Side Management Potential in South-East Europe to Support Transmission Network Flexibility”, published in *IEEE ISGT Europe 2018*, Sarajevo, 2018.

[B5] K. N. Hasan, M. Wang and J. V. Milanovic, “A Survey on Electrical Energy Storage Potential in South-East Europe to Support Transmission Network Flexibility”, published in *IEEE ISGT Europe 2018*, Sarajevo, 2018.

[B6] M. Wang, J. Ponocko and J. V. Milanovic, “The Effect of the Type and Composition of Demand on the Influence of DSM on Power System Angular Stability”, published in *IEEE GTD Asia 2019*, Bangkok, 2019.

[B7] M. Wang and J. V. Milanovic, “Contribution of Advanced Demand Side Management to Angular Stability of Interconnected Transmission Networks”, published in *IEEE ISGT Europe 2019*, Bucharest, 2019.

[B8] J. Ponocko, M. Wang and J. V. Milanovic, “Assessing the Impact of Cross-border DSM on Power Transfers in Regional Transmission System”, published in *IEEE MELECON 2020*, Virtual Conference, 2020.

[B9] Z. Luburic, T. Tadin, A. Andre, J. Ponocko, M. Wang, J. V. Milanovic, O. Skrba and B. Rebic, “Provision of the Experiments by Coordination of Demand Side Response Units in the Region of Southeast Europe within the CROSSBOW Project – HOPS Case”, published in *HRO CIGRE 2020*, Virtual Conference, 2020.

[B10] M. Wang and J. V. Milanovic, “The Effect of the Type and Composition of Demand on DSM Contribution to System Frequency Stability”, published in *IEEE ISGT Europe 2020*, Virtual Conference, 2020.

[B11] M. Wang and J. V. Milanovic, “Assessment of the Impact of Load Modelling and DSM on Combined Power System Angular and Frequency Stability Using Composite Stability Index”, published in *IEEE ISGT Europe 2021*, Virtual Conference, 2021.

[B12] M. Wang, J. V. Milanovic and J. Ponocko, “The Influence of Deployment of DSM on Power System Angular and Frequency Transients and Stability,” submitted to *IEEE ISGT Europe 2022*, 2022.

B.2 Other Publications

B.2.1 International Conference Papers

[B13] S. Abdelrahman, M. Wang, J. V. Milanovic and E. Becirovic, “Study of Harmonic Propagation in Transmission Networks with High Penetration of Power Electronic Devices”, published in IEEE PowerTech 2017, Manchester, 2017.

B.2.2 Technical Reports

[B14] A. Parisio, M. Panteli, J. Ponocko, K. N. Hasan, M. Wang, J. V. Milanovic, et al., "CROSSBOW demo clusters formal analysis," Deliverable 2.3, EU H2020 Project "CROSS BOrder management of variable renewable energies and storage units enabling a transnational Wholesale market (CROSSBOW)", (H2020-773430), August 2018.

[B15] J. Ponocko, M. Wang, J. V. Milanovic, et al., "Practical Approaches to DSM for Wide Scale Roll Out," Deliverable 9.1, EU H2020 Project "CROSS BOrder management of variable renewable energies and storage units enabling a transnational Wholesale market (CROSSBOW)", (H2020-773430), April 2019.

[B16] J. Ponocko, M. Wang, J. V. Milanovic, et al., "DSM suitability for improving cross border issues with increased penetration of RES," Deliverable 9.2, EU H2020 Project "CROSS BOrder management of variable renewable energies and storage units enabling a transnational Wholesale market (CROSSBOW)", (H2020-773430), August 2019.

[B17] J. Ponocko, M. Wang, J. V. Milanovic, et al., "CROSSBOW DSM-IP platform V.1," Deliverable 9.3, EU H2020 Project "CROSS BOrder management of variable renewable energies and storage units enabling a transnational Wholesale market (CROSSBOW)", (H2020-773430), October 2019.

[B18] K. Almunem, M. Kuschke, K. S. J. Dolenc, B. Blazic, L. Herman, M. Hashempour, H. Liao, J. M. Alvarado, M. Wang, J. V. Milanovic, et al., "Mitigation of PQ Disturbances and Provision of Differentiated PQ," Deliverable 5.5, EU H2020 Project "Massive InteGRATion of power Electronic devices (MIGRATE)", (H2020-691800), December 2019.